SYNTHESIS, CHARACTERISATION AND DECOMPOSITION PROPERTIES OF MANGANESE-BASED BOROHYDRIDES FOR HYDROGEN STORAGE

by

RUIXIA LIU

A thesis submitted to the University of Birmingham
for the degree of
DOCTOR OF PHILOSOPHY

School of Metallurgy and Materials
College of Engineering and Physical Sciences
University of Birmingham
July 2012

SYNOPSIS

Manganese borohydride has a theoretical hydrogen content of 9.5 wt% and relatively low decomposition temperature of 130-180 ℃ , making it of interest for hydrogen storage. Mechanochemical milling is a viable synthesis route where alkali metal borohydrides react via a metathesis reaction with manganese chloride. In this work, a series of manganese-based borohydrides were synthesized by mechanochemical milling of the $x\mathrm{ABH_4}$-$\mathrm{MnCl_2}$ (A = Li, Na, K; $x = 2$ or 3) samples under argon. The structural and thermal decomposition properties of the borohydride compounds were investigated using XRD, Raman spectroscopy, FTIR, TGA-MS, DSC, *in-situ* XRD and *in-situ* Raman spectroscopy.

Samples prepared by ball-milling $x\mathrm{LiBH_4}$-$\mathrm{MnCl_2}$ ($x = 2$ or 3) resulted in the formation of $\mathrm{Mn(BH_4)_2}$ with a space group symmetry $P3_112$ and LiCl in a stoichiometric ratio, with excess $\mathrm{LiBH_4}$ observed when $x = 3$. Thermal decomposition of $\mathrm{Mn(BH_4)_2}$ was observed between 130 and 180 °C (in 1 bar flowing Ar) for milled $\mathrm{2LiBH_4}$-$\mathrm{MnCl_2}$ with mass loss of 8.4 wt %, and 105 and 145 °C for milled $\mathrm{3LiBH_4}$-$\mathrm{MnCl_2}$ with mass loss of 8.1 wt %, and both with the concurrent evolution of hydrogen and diborane (molar ratio of 9:1). Analysis of the decomposition products suggested the presence of amorphous boron, manganese metal and LiCl for both milled samples, and the formation of three as yet unidentified phases (320-400 °C) for the milled $\mathrm{3LiBH_4}$-$\mathrm{MnCl_2}$ sample.

When sodium borohydride was used as a reagent, $\mathrm{Mn(BH_4)_2}$ was also observed, however instead of NaCl a solid solution of $\mathrm{NaCl_x(BH_4)_{1-x}}$ and the ternary chloride $\mathrm{Na_6MnCl_8}$ were formed. After heating, $\mathrm{Mn(BH_4)_2}$ decomposed between 118 and 170 °C with a 6.4 wt% loss for milled $\mathrm{2NaBH_4}$-$\mathrm{MnCl_2}$, and between 110 and 160 °C with a 6.0 wt% loss for milled

$3NaBH_4$-$MnCl_2$; both occurred with the concurrent evolution of hydrogen and diborane. As part of the milled products, solid solutions of $NaCl_x(BH_4)_{1-x}$ were formed where $x = 0.77$ and 0.68 for milled $2NaBH_4$-$MnCl_2$ and $3NaBH_4$-$MnCl_2$, respectively. Following hydrogen desorption from $Mn(BH_4)_2$, thermal decomposition of these solid solutions by the interaction with the ternary chloride Na_6MnCl_8 occurred between 250 and 425 ºC ($2NaBH_4$-$MnCl_2$) and between 150 and 225 °C ($3NaBH_4$-$MnCl_2$) with the release of hydrogen. Analysis of both milled samples heated under flowing Ar showed that amorphous B and possibly Mn formed (110 to 170 °C); the reaction of the solid solutions $NaCl_x(BH_4)_{1-x}$ with the ternary chloride Na_6MnCl_8 (150 to 425 °C) resulted in the formation of NaCl; and, in the case of milled $3NaBH_4$-$MnCl_2$, unknown phases were observed after heating to above 380 °C.

When potassium borohydride was used as a reagent, $Mn(BH_4)_2$ was not observed (under the milling conditions investigated). Rather, mixed cation borohydride $K_2Mn(BH_4)_4$, ternary chloride $KMnCl_3$ and unreacted KBH_4 were observed. The mass losses for the milled sample were from 100 to 160 °C with a 1.6 wt% loss (with a release of majority hydrogen and trace diborane), associated with the decomposition of $K_2Mn(BH_4)_4$ to form KBH_4, boron, and finely dispersed manganese and from 165 to 260 °C with a 1.9 wt% loss (only hydrogen release), associated with the reaction of KBH_4 with ternary chloride to give KCl, boron, finely dispersed manganese. Simultaneously, the formed KCl can be dissolved into KBH_4 to yield a $K(BH_4)_xCl_{1-x}$ solid solution, and react with $KMnCl_3$ to form a new ternary chloride K_4MnCl_6 phase. The potential higher borane species decomposed to release a small amount of hydrogen between 270 and 380 °C.

This study has given a clearer understanding of the synthetic routes, structural characteristics and decomposition properties of manganese-based borohydrides formed by mechanical ball milling of ABH_4 (A = Li, Na, K) and $MnCl_2$ (with 2:1 and 3:1 molar ratios) for 360 minutes under argon. The dehydrogenation of the manganese-based borohydrides was irreversible under experimental conditions (100-150 bar H_2, 100-250℃).

Acknowledgments

Firstly, I express my sincere thanks to Dr. David Book for his help and advice during the supervision of this project. He provided me with many helpful suggestions and important advice during the course of this work.

I am grateful for the assistance offered by Dr. Dan Reed and other members of the hydrogen materials group, both past and present, for their useful discussions, contributions and friendship over the last 4 years.

I also gratefully acknowledge the financial support from EPSRC to fund my project, to MEGS for the conference travel funding.

Finally, a special thank to all my family members. Without their understanding, support and encouragement I could never have completed this PhD.

List of Abbreviations

ACs	Activated Carbons
ATR	Attenuated Total Reflectance
CCD	Charge-Coupled Device
CNTs	Carbon Nanotubes
DFT	Density Functional Theory
DME	Dimethylether
DOE	Department of Energy
DSC	Differential Scanning Calorimetry
ESDs	Estimated Standard Deviations
FTIR	Fourier Transform Infrared
GNFs	Graphite Nanofibers
IEA	International Energy Agency
MAS- NMR	Magic Angle Spinning-Nuclear Magnetic Resonance
MCAS	Mechano-Chemical Activation Synthesis
MOFs	Metal of Frameworks
MS	Mass Spectrometry
MWCNTs	Multiwalled Carbon Nanotubes
PCT	Pressure-Composition-Temperature
PEMFC	Proton Exchange Membrane Fuel Cell
PSD	Position Sensitive Detector
SR-PXD	Synchrotron Radiation Powder X-ray Diffraction
SWCNTs	Single-Walled Carbon Nanotubes
TGA	Thermogravimetric Analysis
THF	Tetrahydrofuran
TPD	Temperature Programmed Desorption
XRD	X-ray Diffraction

Contents

Chapter 1 Introduction

In modern society, energy demand and environmental problems are two major issues. Due to global economic growth and the linked rise in living standards around the world, there is an increasing demand for energy resources for electricity generation, heating and transportation. As reported by the International Energy Agency (IEA) in their 2011 World Energy Outlook: Executive Summary, “Despite uncertainty over the prospects for short-term economic growth, primary demand for energy in the New Policies Scenario grows strongly, increasing by one-third between 2010 and 2035” (IEA, 2011).

Nevertheless, the considerable demands on the energy supply are currently accompanied by damage to the eco-environmental system, by the burning of primary carbon-based fossil fuels. This leads to emissions of carbon dioxide, the main gas responsible for climate change, to the atmosphere. It is well-established that the higher concentration of greenhouse gases in the atmosphere is the primary cause of global warming (IPCC, 2007).

In addition, the use of global energy is expected to rise by 70% by 2020, much of it projected to be met by fossil fuels. The consumption of fossil fuels is currently 100,000 times faster than the rate at which they can regenerated by natural processes (Service, 2004). It is important to consider that fossil fuels are finite and the supply of hydrocarbon resources is becoming significantly reduced. Therefore, the long-term challenge is to utilize cleaner and more sustainable energy technologies.

Hydrogen is not a primary energy source, but is generally considered to have the potential to be an “energy carrier” of the future (Schlapbach, 2002; Winter and Nitsch, 1988). Depending on its production method, hydrogen is a very attractive and “green” fuel, producing near-zero emissions of greenhouse gases from renewable and nuclear power sources and potentially also from fossil fuel-based energy sources which incorporate carbon capture and storage. Hydrogen is compatible with high-efficiency fuel cells, combustion turbines and reciprocating engines to produce power, with only water as a combustion product, for all sectors of the economy (i.e. transportation, power, industry, and residential). In terms of hydrogen energy economies, the production, storage, distribution and utilization of hydrogen are all crucial considerations.

Hydrogen production is a large and growing industry. Hydrogen readily chemically binds with other elements, such as oxygen and carbon. To release hydrogen from these compounds, energy is needed to break the chemical bonds. Globally, hydrogen is produced from natural gas (48%), oil (30%), coal (18%) by steam reforming, partial oxidation, or gasification and from water by electrolysis (4%) (Sperling and Cannon, 2004). Clearly, the hydrogen production by traditional steam reforming (Rostrup-Nielsen, 1984), partial oxidation (Wanet et al., 2005; Zhang et al., 2005) and gasification process (Lin et al., 2002) leads to the release of the impurities, e.g. small amounts of CH_4, CO, NO_x and a significant quantity of CO_2, which results in adverse impacts on hydrogen end-use and the emission of greenhouse gases into the air. The electrolysis of water produces high purity hydrogen gas with no harmful pollutants, however, if the majority of the electricity used is generated from natural gas and fossil fuels, then the greenhouse gas emissions have only been relocated. Therefore, there is a need to focus on reducing the emission of carbon, improving efficiency and lowering cost. The potential solutions are: exploring carbon capture and sequestration technologies combined with traditional hydrogen production processes, developing biological production technique and using renewable sources (solar, hydropower, wind turbines, biomass) and nuclear power (Barbir, 2005; Janon and Andrews, 2008), to supply heat and electricity for water splitting.

Hydrogen distribution is totally dependent on the onsite hydrogen production or centrally based production (Quakernaat, 1995). With onsite hydrogen production, there is the significant issue of distribution and delivery to be considered. The produced hydrogen can be stored as a compressed gas, liquid or stored in a solid-state material. Hydrogen produced at a central location could also be distributed to the end user using a hydrogen pipeline or via the existing network of natural gas pipelines with the delivery of a mixture of hydrogen and natural gas. Liquefied hydrogen and compressed hydrogen trailers are also options for the transportation of hydrogen.

Hydrogen utilization can be divided into two categories: by direct combustion of hydrogen in specially designed turbines and engines, in the same manner as gasoline; or by using fuel cells where the chemical energy can be converted into electrical and thermal energy. In internal combustion engines (Jin and Ishida, 2000; Takahashi et al., 2003), when hydrogen burns with oxygen, the only by-product is water; no polluting substances are given off. As electrochemical reactions are more efficient than combustion for generating energy, fuel cells are expected to be the preferred choice for the utilization of hydrogen.

A fuel cell converts energy from chemical reactions directly into electrical energy. As shown in Figure 1.1, a fuel cell is composed of two electrodes (anode and cathode), sandwiched around an electrolyte. Molecular hydrogen is fed into the anode of the fuel cell where, with the help of a catalyst, hydrogen splits into electrons and protons. The protons pass through the electrolyte to the cathode whereas the electrons form a current around the external circuit to the cathode where the fed oxygen captures electrons and subsequently combines with protons to produce water. Meanwhile, the generated electron current can be utilized for various purposes. This process is clean and highly efficient, typically two to three times more efficient than burning hydrogen (Larminie and Dicks, 2000).

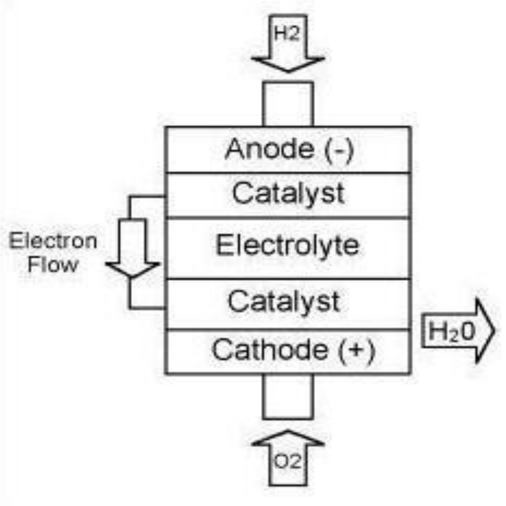

Anode: $2H_2 \rightarrow 4H^+ + 4e^-$

Cathode: $4e^- + O_2 \rightarrow 2O^{2-}$

Overall: $2H_2 + O_2 \rightarrow 2H_2O$

Figure 1.1 Schematic of a fuel cell converting H_2 *and* O_2 *into electrical energy*

Depending on the type of electrolyte materials, there are several promising varieties of fuel cells, such as proton exchange membrane (Dai et al., 2008b; Gerbec et al., 2008), phosphoric acid (Zervas et al., 2008), solid oxide (Laberty et al., 2007; Sayers et al., 2008) and alkaline (Tsivadze et al., 2008; Wan et al., 2008). Of these, the proton exchange membrane fuel cell (PEMFC) has received much attention as an efficient and promising candidate for mobile power generation. The advantages of PEMFCs include reduced weight and volume with good power-to-weight ratio, low temperature and pressure operation and a quick starting time with full power available in minutes or less. However, there are still some barriers to overcome for the widespread introduction of fuel cells as commercial power sources: prolonging durability, reducing cost and improving reliability. For PEMFCs to achieve a better performance, much effort has been devoted to the development of practical and inexpensive materials (membrane and catalyst), system engineering improvements and a greater fundamental understanding via the concurrent use of modelling simulations and experimental measurements (Dai et al., 2008b; Outeiro et al., 2008).

The utilization of hydrogen with fuel cell devices can be for either stationary or mobile applications (transportation and portable use) (Larminie and Dicks, 2000). The stationary applications primarily include combined heat and power systems for a range of end-uses e.g. industrial, commercial and residential needs, in which the fuel cell system can operate at temperatures from 60 to 1000 ℃ (depending on the fuel cell chemistry). For mobile applications, hydrogen fuel cells require lightweight, compact and flexible configurations, as well as high power densities and safe operation. Portable fuel cells can also be used in electronic equipment e.g. cellular telephones, portable computers, and video cameras to replace batteries. In the case of mobile applications particularly transportation, hydrogen may be produced from the on-board reforming of fuels, which needs an improved hydrogen storage approach for on-board application.

Hydrogen storage is playing a central role in both stationary and mobile applications. The storage for stationary application has focused on the initial cost, long-term maintenance and store efficiency rather than the size and mass of the unit that may occupy a large area with multi-step chemical charging/recharging cycles. The most important factors to be considered for transportation applications, however are the volume and mass of stored hydrogen, i.e. so that enough hydrogen (e.g. 5-10 kg) may be supplied to enable a 300 mile driving range with a 5 min charge/recharge (at room temperature). The US Department of Energy (DOE) has specified performance targets for an automotive hydrogen storage system of 5.5 wt% and 40 kg H_2/m^3 for 2015 (DOE, 2009). The conventional storage approach is to utilize cryogenic or compressed gaseous confinement of molecular hydrogen. However, in order to try to meet the DOE targets, there has been an extensive effort into developing dense and safe solid-state hydrogen storage materials with good thermodynamic properties. An effective hydrogen storage material will require: 1) high storage capacity and gravimetric/volumetric densities; 2) appropriate thermodynamics; 3) effective heat transfer; 4) long cycle lifetime for decomposition/recombination; 5) safety under normal use and acceptable risk under abnormal conditions. To date, no storage method satisfies all of these criteria.

The transition from hydrocarbon-based (currently fossil fuel) energy sources to a hydrogen-based economy will require major scientific, technological and socioeconomic challenges to be overcome. It has been shown that there are several barriers which must be addressed (Dixon, 2007): introducing CO_2–free technology for economical and sustainable hydrogen production; developing hydrogen storage systems for mobile and stationary applications including novel material development; establishing a safe and efficient infrastructure for hydrogen delivery and distribution and significantly improving the durability and tolerance to impurities of fuel cells in hydrogen applications.

Chapter 2 Literature Review: Hydrogen Storage

2.1 Introduction

Hydrogen storage is one of the key barriers to introduction of the hydrogen economy. Two kinds of storage functions with very different requirements are needed for efficient storage of hydrogen: stationary applications including residential heating, electrical generation and industrial application, where the storage can occupy a large area with multistep chemical charging/recharging cycles that operate at high temperature and pressure and compensate for slow charging/recharging kinetics with extra capacity; and mobile applications such as vehicles, where the volume, mass, safety and cost of the hydrogen storage system are very important factors to be considered.

In terms of vehicle applications, there are two ways to run a road car with hydrogen. One is direct burning hydrogen with air. A slightly higher efficiency for a hydrogen-air mixture (25%) than that of a petrol-air mixture is possible, but when using a richer mixture, NO_x will be produced. In the second method, hydrogen reacts electrochemically with O_2 (from the air) in a fuel cell, which produces electricity and drives an engine with the efficiency of 50-60%. For a driving range of 400 km it would require approximately 8 kg of hydrogen burnt using a combustion engine, or 4 kg of hydrogen using a PEM fuel cell to drive electric motor (Schlapbach and Züttel, 2001). At room temperature and standard pressure, 4 kg of hydrogen gas would occupy a volume of 48300 litres, which would be impractical for use in a car. Figure 2.1 shows the volume occupied in storing 4 kg of hydrogen by several storage methods, in comparison to the size of a typical passenger car. Significantly, the reduction in volume is achieved by compressing and liquefying hydrogen, or even better by storing hydrogen in a solid-state medium.

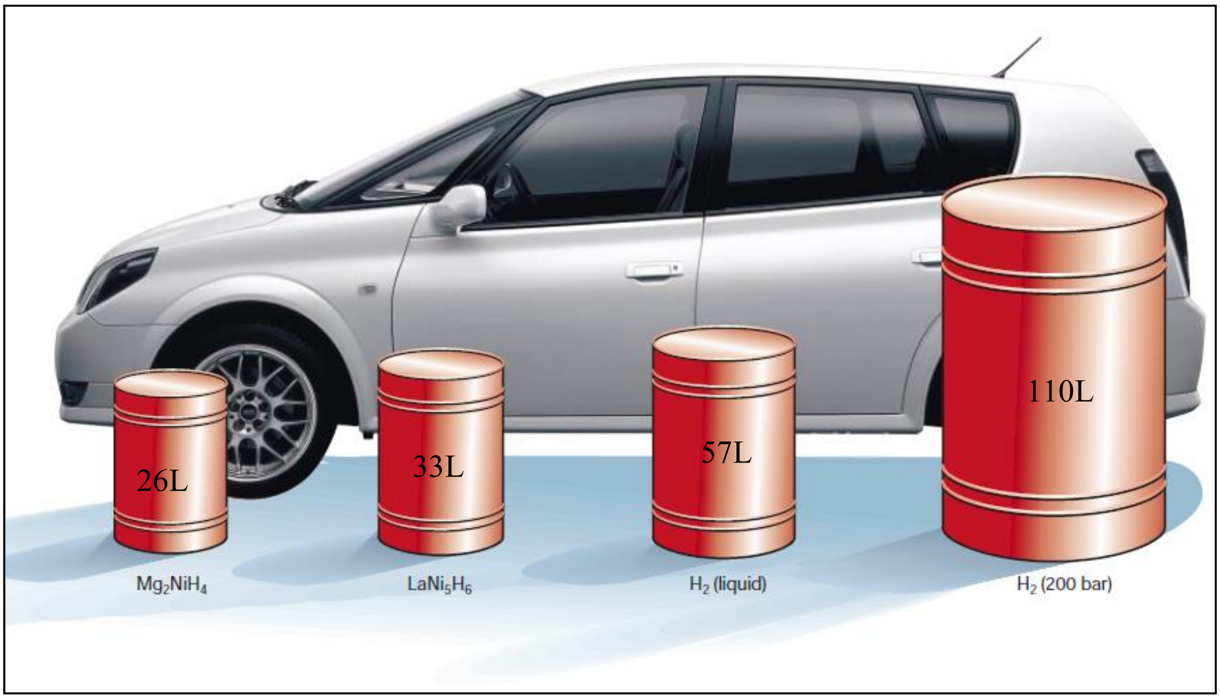

Figure 2.1 The volume of 4 kg of hydrogen stored in different ways (200 bar gas, liquid hydrogen and solid materials e.g.$LaNi_5H_6$*,* Mg_2NiH_4*), compared to a family car (Schlapbach and Züttel, 2001)*

Within the criteria for an effective hydrogen storage system, alongside appropriate thermodynamics, reasonable operational conditions, long life-time and safety issues, the gravimetric and volumetric densities are particularly important. A comparison of gravimetric and volumetric densities for hydrogen storage is shown in Figure 2.2. The compressed gaseous or liquid storage has a relative low volumetric density in comparison to solid-state storage. Metal hydrides such as $LaNi_5H_6$ and $BaReH_9$ have exceptional volumetric densities but poor gravimetric hydrogen densities as they consist of relatively heavy elements. The most effective materials should have both high gravimetric and volumetric storage densities. For instance, the complex hydrides e.g. $[BH_4]^-$, $[AlH_4]^-$ show high gravimetric and volumetric storage densities, and have considerable potential to meet the hydrogen storage system performance targets set by the US DOE (5.5 wt% or 40 kg H_2/m^3 for 2015). Overall, each hydrogen storage method or material has its own advantages and drawbacks. The following section will describe research into hydrogen storage, including storage methods and materials.

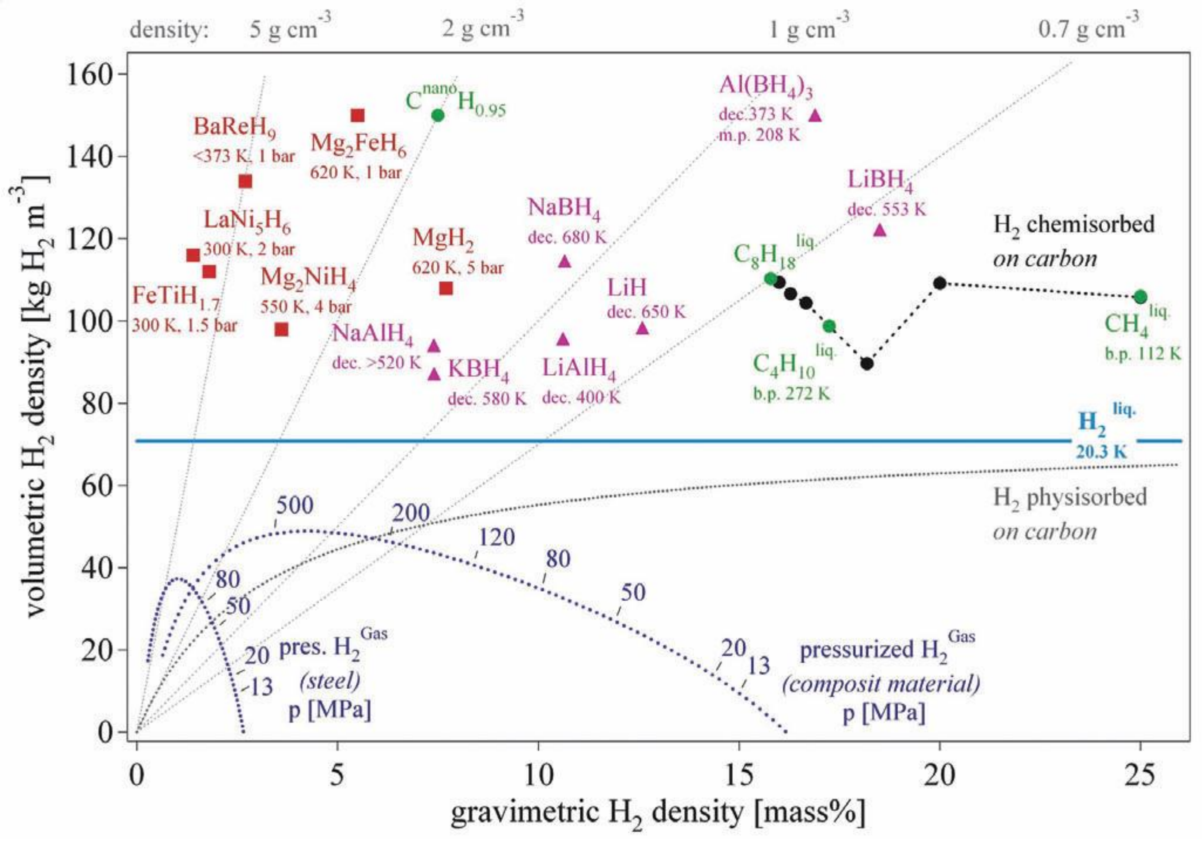

Figure 2.2 Gravimetric and volumetric hydrogen densities for selected hydrogen storage materials (Züttel, 2003)

2.2 Gaseous storage

Hydrogen gas has a high gravimetric energy density (120 MJ/kg), which is at least three times larger than that of other chemical fuels (liquid hydrocarbon, 44 MJ/kg) (Satyapal et al., 2007). At room temperature and atmospheric pressure, however, due to its low density of 0.0909 kg/m^3, hydrogen has a poor volumetric energy density (12.5 MJ/m^3). To increase energy density by volume, the hydrogen gas must be compressed to several hundred atmospheres and stored in a pressure vessel with reasonable volume. The development of pressure tank materials and design is playing a key role in this technique. Hydrogen storage tanks need to be made from lighter materials such as aluminium or carbon/graphite compounds. These materials should have high tensile strength, low density and good resistance to hydrogen absorption/reaction. Carbon fibre-reinforced 350 and 700 bar compressed hydrogen gas tanks have been recently developed to carry enough fuel for a reasonable driving distance of 400-500 km, increasing the hydrogen density to 30 kg/m^3 at 700 bar, which is about half that of liquid hydrogen (Ko et al., 2005; Schlapbach and Züttel, 2001). The promising composite tanks consist of three layers: an inner layer such as an aluminium film or high-molecular-weight polymer to prevent (or significantly reduce) hydrogen gas permeation; over-wrapped with carbon fibre materials, to produce a pressure stress-bearing component and an outer shell made from highly resistant materials, to prevent mechanical damage and corrosion, e.g. glass fibre and aramid-materials (Züttel, 2003).

Although extensive efforts have been made to develop high-pressure gas tanks, the gaseous storage of hydrogen in compressed tanks is relatively inefficient as the volumetric hydrogen storage density of system is still too low, i.e. the gas tank takes up too much space to carry enough hydrogen in the vehicle for a reasonable driving distance of 400-500 km. Additionally, safety concerns over the use of high-pressure vessels and the high energy requirement associated with the compression of hydrogen, are major limitations for its use for transportation.

2.3 Liquid storage

Cryogenic hydrogen has been used for several decades in the space programme. It can be produced by liquefaction of gaseous hydrogen and stored in cryogenic tank at temperature of -253 °C and ambient pressure (Shimko, 2005). Liquid hydrogen with 70 kg/m^3 density takes up less storage volume than compressed gas; thus it has a relatively high volumetric energy density at low pressure (Satyapal et al., 2007). There are, however, several practical problems: large amounts of energy are required for liquefaction, resulting in the loss of around 30% of the energy stored in hydrogen and 'boil-off' into gaseous high-pressure hydrogen occurs.

The typical liquefaction process of hydrogen is the Linde or Joule-Thomson cycle (Shimko, 2005; Züttel, 2003). Hydrogen gas is compressed to a high pressure with temperature rising, cooled in a heat exchanger, and then passed to a throttling valve for isenthalpic expansion. On expanding to the lower pressure, hydrogen gas pre-cooled below its inversion temperature (-71 °C, 0 atm) undergoes further cooling, which leads to liquid formation. Liquefaction by compressing and cooling to approximately -253 °C is an energy intensive process, associated with energy losses. Theoretically, the necessary energy to liquefy hydrogen gas at room temperature is 3.23 kWh/kg, however in practice, an energy around 4-5 times higher (15.2 kWh/kg) is required (von Ardenne et al., 1990).

For the storage of liquid hydrogen, special cryogenic tanks which are generally super-insulated, such as metallic double-walled tanks with insulation sandwiches between walls are needed to avoid thermal losses. As a result of large temperature differences between ambient and liquid hydrogen, thermal heat losses through these tanks inevitably occur during storing and handling, which causes hydrogen boil-off. The boil-off rate depends on the amount of hydrogen in the tank and the heat leakage, which is governed by the size and shape of the tanks, and the extent of the thermal insulation. The boil-off rate of liquid hydrogen typically is 0.127% per day. For double-walled, vacuum insulated spherical dewars, boil-off loss is 0.4% per day for 50 m^3 tanks (Züttel, 2003). As hydrogen has a low critical temperature (-240 °C) above which a distinct liquid does not exist, its continuous boil-off limits the possible use of liquid hydrogen storage systems.

2.4 Solid-state materials

2.4.1 Introduction

In terms of generic interaction mechanisms, hydrogen storage in solid materials can be divided into two categories: physisorption-based molecular hydrogen storage via weak van der Waals interactions between molecular hydrogen and solid surfaces and chemisorption-based atomic hydrogen storage by ‘chemical’ bonding of hydrogen atoms with the lattice of the storage medium or by the formation of new chemical compounds (Fichtner, 2005; Züttel, 2003). Physical adsorption exhibits several advantages, for example low operating pressure, good reversibility and sorption kinetic properties and relatively low cost of materials. The major drawbacks of these materials, however, are quite small gravimetric and volumetric hydrogen densities with low temperature. The currently investigated physisorption-based materials include carbon-based materials, zeolites, porous polymers and metal-organic framework materials. Chemical absorption materials can offer high hydrogen storage capacity but poor reversibility, thermodynamics and kinetics with high temperature and pressure as they chemically bind or release hydrogen atoms while forming the compounds. Figure 2.3 shows the observed hydrogen storage capacities, as a function of the temperature for hydrogen sorption or release for some well-known materials. The ideal storage and release should occur at 0-100 °C and 1-10 bar with a storage capacity > 5 wt% so as to meet U.S. DOE system targets for 2015 (see Figure 2.3). The most promising materials are metal hydrides, complex hydrides and other chemical storage materials.

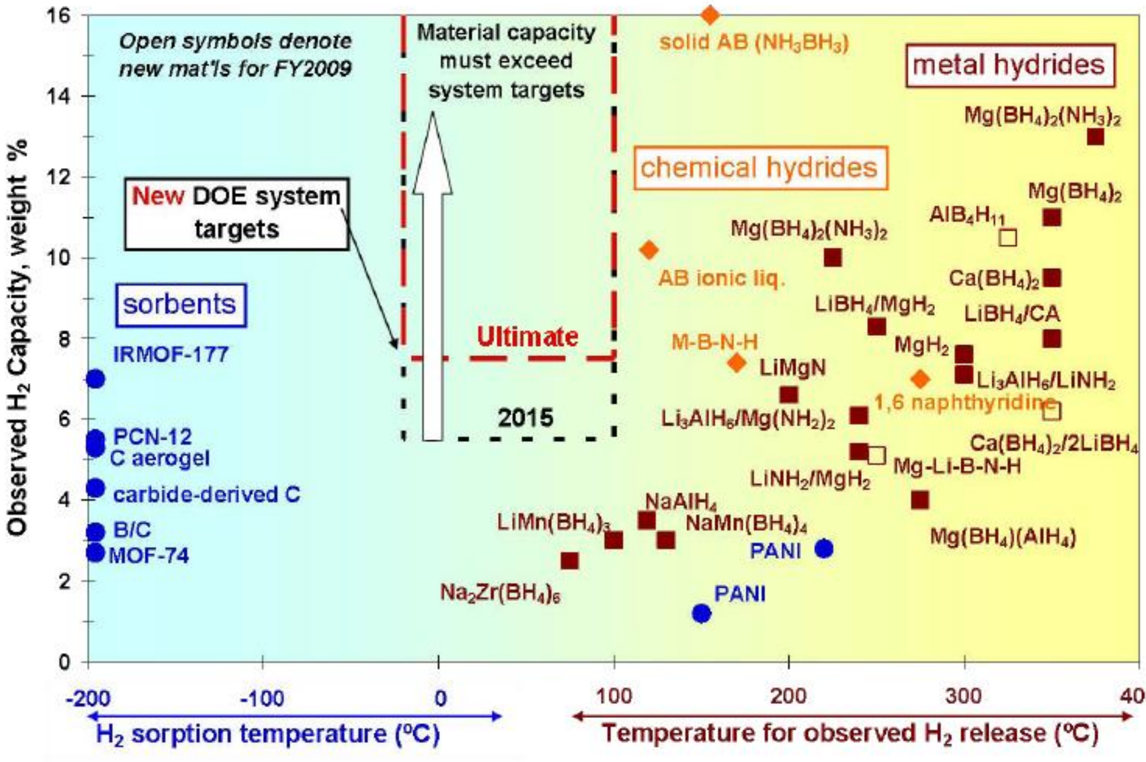

Figure 2.3 Observed hydrogen storage capacity against the temperature of hydrogen desorption/sorption for some solid-state materials (DOE, 2009)

2.4.2 Porous materials.

Carbon-based materials are lightweight and attractive for use in hydrogen storage. Early work in this area in the 1960s focused on a range of activated carbon materials with different carbon structures (Amankwah et al., 1989; Carpetis and Peschka, 1980; Kidnay and Hiza, 1967). Unfortunately, it is difficult to get activated carbon adsorbents with high-surface-area, which is significant effect factor on storage capacity.

Since first report on hydrogen storage in carbon nanotubes (CNTs) was published in 1997 by Dillon *et al.* (1997), considerable research has been carried out on hydrogen adsorption in such nano-structured carbon materials as graphite nanofibres, single-walled carbon nanotubes (SWCNTs), multiwalled carbon nanotubes (MWCNTs) and nanographite. Dillon's group reported that the hydrogen storage capacity on pure SWCNTs was estimated as much as 10 wt% at room temperature based on the measurement of hydrogen adsorption by thermal desorption spectroscopy on non-purified SWCNTs samples, where contained only 0.1 to 0.2 wt% of SWCNT (Dillon et al., 1997). A SWCNT sample, pre-soaked in hydrochloric acid and heat-treated in vacuum, exhibited hydrogen storage capacity of 4.2 wt% at room temperature under 100-120 bar pressure (Liu et al., 1999). Hydrogen storage in CNTs is dependent on many parameters such as their structure, pretreatment, purification, surface area and size as well as storage pressure and temperature. MWCNTs have a considerable wider diversity of shapes and configurations, basically consisting of layers of nested concentric cylinders of graphite with a hollow centre. It was reported that hydrogen storage values on MWCNTs ranged from 1.97 to 6.3 wt% at room temperature and at pressures of 40-150 bar (Hou et al., 2002; Lee et al., 2002; Li et al., 2001). However, a high hydrogen capacity at room temperature has not been reproduced by other workers (Smith et al., 2003; Ye et al., 1999; Züttel et al., 2002). The reasons why confirmation has not been forthcoming could be: 1) low purity of CNT samples, for example, a hydrogen storage capacity of ~ 10 wt% reported for SWCNTs was an extrapolation from a sample with only 0.1-0.2 wt% of nanotubes to achieve the value for a pure material (Dillon et al., 1997); 2) contamination of samples, for instance, a hydrogen storage capacity of ~ 4.2 wt% found for SWCNTs at 100 bar hydrogen and room temperature was due to the presence of synthetic catalyst residues (~ 40 wt% of Co, Ni and Fe) (Liu et al., 1999); and 3) inaccuracy of determining the hydrogen storage capacity, e.g. the result of Chen et al. (1999a) (up to 20 wt% uptake by alkali-doped CNTs) was most likely a consequence of the presence of water in the hydrogen gas supply. Therefore, for CNTs materials to be used for hydrogen storage in practice, some obstacles such as mass production with a controlled nanostructure at a reasonable cost and the methods of purification and pretreatment for opening the caps at the tube ends to improve their hydrogen storage capacity have to be overcome.

Graphite is an inexpensive material that is available on an industrial scale. However, as its small interlayer distance and low specific surface area, hydrogen storage in graphite is rather low. It has been shown that the hydrogen capacity based on physisorption is proportional to the specific surface area of materials. To improve the adsorption of hydrogen on graphite, nanostuctured graphite was prepared by ball milling techniques (Chen et al., 1999b; Orimo et al., 1999). After milling for 80 hours in 10 bar hydrogen, the graphite could store up to 7.4 wt % hydrogen at room temperature although the specific surface area was only on the order of 10 m^2/g. It was also noted that hydrogen desorption started at about 327 °C with maxima around 527 °C and 777 °C, accompanied by the release of a considerable amount of hydrocarbons such as methane and ethane. These results indicated the uptake of hydrogen during ball-milling was mainly attributed to the formation of covalent C-H bonds rather than to physisorption bonding onto designated binding sites (Orimo et al., 1999), which resulted in impractical rehydrogenation of the desorbed graphite materials under moderate condition of pressure and temperature.

Intercalated carbon materials may have modified hydrogen storage properties due to a change in structure e.g. expanding interlayer distances and electronic structure and configuration of carbon. The addition of alkali metals to graphite leads to an increase in the spacing between the layers, which therefore facilitates hydrogen diffusion into the material. MWNTs doped with lithium or potassium exhibited hydrogen adsorption of 20 wt% (200 to 400 °C) or 14 wt% (room temperature) under ambient pressure, however, high temperatures (e. g. >500 °C) were required to fully desorb hydrogen from these materials (Chen et al., 1999a). By infrared spectroscopy both Li-H and C-H species were confirmed to be formed on the sample surface, and the interaction between hydrogen and Li-MWNTs was suggested to be a dissociative mechanism, in which Li might act as a catalytic active centre for the hydrogen to dissociate into H atoms bound to carbon atoms. Mixing carbon materials with conductive metal particles such as Pt, Pd, Ni, Ti, Cu may cause a change in the electronic properties of carbon materials. A recent study using Density Functional Theory (DFT) methods has showed that a single Ni atom on the fullerene surface could store up to three H_2 molecules, thus, Ni-dispersed fullerenes would be novel hydrogen storage media capable of storing 6.8 wt% hydrogen (Shin et al., 2006). Experimental reports indicated that Ni nanoparticle-doped MWCNTs could release 2.8 wt% hydrogen at ambient conditions (Kim et al., 2005), and the presence of Ru, Pd and Pt nanoparticles in carbon material medium increased the hydrogen uptake by 2-5 fold compared with that of undoped carbon materials at room temperature and low or intermediate pressure, suggesting that the spillover process of hydrogen occurred from catalysts to the carbon receptor at the carbon surface (Anson et al., 2006; Wang and Yang, 2008; Wang et al., 2009).

Consequently, carbon-based materials for hydrogen storage are still a hot topic. However, the reliability of the experimental measurement to get hydrogen retained capacity on the carbon based materials is essential, and also it is far from certain that useful carbon materials can be economically and consistently synthesized. Additionally, the surface and bulk properties of these materials needed to achieve practical hydrogen storage at room temperature are not clearly understood, thus a better understanding of the microscopic characteristics of carbon materials that impact on hydrogen uptake, as well as the interaction mechanism between hydrogen and carbon surfaces are required so that optimal storage materials may be developed.

Zeolites are a large category of highly crystalline aluminosilicates; $M_{x/n}[(AlO_2)_x(SiO_2)_y]\cdot zH_2O$, where M is an exchangeable cation with valency n, e.g. Na^+, K^+, Ca^{2+}, Mg^{2+} and ratio y/x is any value greater than 1 (Barrer, 1978). There are over a hundred different zeolite framework types. The anionic skeleton of zeolites is penetrated by channels giving a honeycomb-like structure, as shown in Figure 2.4. The unique framework with a large of number of cages in these materials contributes to the hydrogen storage capacity. A variety of exchangeable cations in the framework channels and cavities are considered as hydrogen adsorption sites where the cations generate a strong electric field, resulting in the polarization of adsorbed hydrogen molecules and ion-dipole interactions (Reguera et al., 2008; Torres et al., 2007).

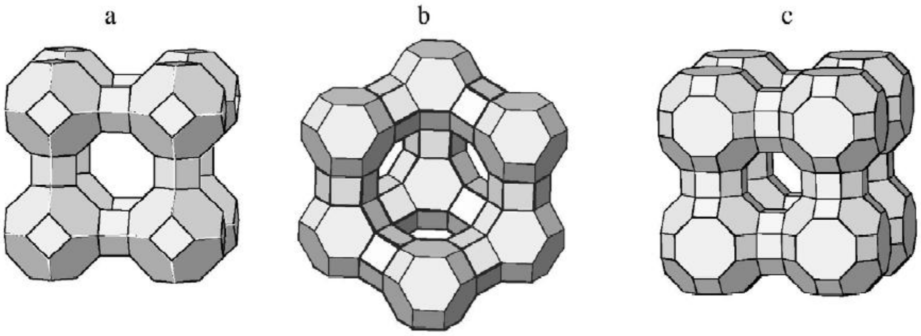

Figure 2.4 Zeolite structure, a) LTA (Zeolite-A), b) FAU (Zeolite-X, -Y), c) RHO (Zeolite-Rho) (Langmi et al., 2003)

The main exchangeable framework cations in zeolites are alkali and alkaline earth elements. It has been reported that NaA, NaX, NaY and CaX had hydrogen storage capacities of 1.54, 1.79, 1.81 and 2.19 wt% respectively at -196 °C and 15 bar hydrogen (Langmi et al., 2005). Yaremov and II'in (2008) reported that, at -196 °C and 1 bar hydrogen pressure, the cavity silicate zeolites of the LTA and FAU types (NaA and NaY) could retain c.a. 1 wt% of hydrogen. At cryogenic temperature and moderately high pressure a higher hydrogen storage capacity has been reached in NaX, up to 2.5 wt% (Du and Wu, 2006). Transition metals e.g. Ni, Co and Zn and noble metals e.g. Pd, Pt, Rh and Ru are known to have a high affinity for hydrogen. Efforts have been made to investigate hydrogen storage properties with transition and noble metal exchanged zeolites. It has been shown that the addition of these metals did not lead to an improvement in hydrogen physisorption capacity at cryogenic temperatures, but chemisorption might occur at room or higher temperature by forming hydrides with Pd, Ni and Ru metals (Nishimiya et al., 2001; Prasanth et al., 2008). Zeolites have low cost, high stability and a variety of porous structures, which may indicate potential for reversible hydrogen storage. However, low gravimetric hydrogen storage capacities of less than 2 wt% so far, are major problems for these materials to be used in practice.

Metal-organic frameworks (MOFs) are crystalline coordination polymers composed of mononuclear or polynuclear metal centres as the nodes and multi-dentate organic ligands as the linkers, forming vertices of a framework with a porous structure of metal-ligand complexes. Figure 2.5 shows three examples of X-ray crystal structures for A) MOF-5, B) IRMOF-6, and C) IRMOF-8 where inorganic $[OZn_4]^{6+}$ groups are joined to different organic linker units to form porous cubic frameworks (Rosi et al., 2003).

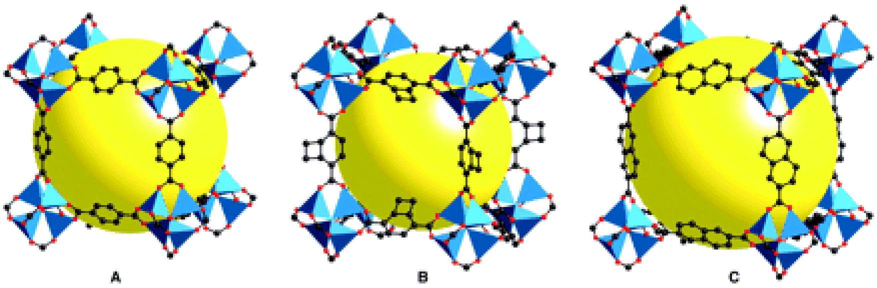

*Figure 2.5 Single-crystal X-ray structures of MOF-5 (**A**), IRMOF-6 (**B**), and IRMOF-8 (**C**) illustrated for a single cube fragment of their respective cubic three-dimensional extended structure. On each of the corners is a cluster $[OZn_4(CO_2)_6]$ of an oxygen-centred Zn4 tetrahedron that is bridged by six carboxylates of an organic linker (Zn, blue polyhedron; O, red spheres; C, black spheres). The large yellow spheres represent the largest sphere that would fit in the cavities without touching the van der Waals radii of the framework atoms. Hydrogen atoms have been omitted, reproduced from Rosi et al.'s work (2003).*

MOFs are relatively new materials for hydrogen storage. Since the first report on MOF-based hydrogen storage was published in 2003 (Rosi et al., 2003), hundreds of unique MOFs have been evaluated for their hydrogen storage capacities (Farha et al., 2008; Panella et al., 2006; Yang et al., 2011). The typical pore volume and surface areas of these types of materials were obtained respectively from 0.2 to1 cm^3/g, and 500 to 4600 m^2/g, and hydrogen uptake was up to 6-8 wt% at -196 °C and 70-90 bar hydrogen (Furukawa et al., 2007; Lupu et al., 2011; Wong-Foy et al., 2006). A positive roughly linear correlation between hydrogen adsorbed and pore volume and apparent surface area was reported in previous studies (Thomas, 2009; Wong-Foy et al., 2006). However, the drawback of MOF-based materials is that their weak interaction with hydrogen derived from physisorption results in very small amounts of hydrogen adsorbed, typically less than 2 wt% at ambient temperature and relatively high pressure. Extensive efforts have been made to increase the binding energy of hydrogen in MOF materials. The introduction of light metal ions such as Li, Na and Mg has been suggested by theoretical prediction for the enhancement of hydrogen adsorption (Dalach et al., 2008; Lochan and Head-Gordon, 2006) and enhanced hydrogen sorption has also been experimentally verified through different routes (Srepusharawoot et al., 2011; Yang et al., 2008). Recent studies have shown that MOFs with open metal sites exhibited significantly larger experimental heats of hydrogen adsorption than classical MOFs materials, in which the open metal sites contributed to the primary and strongest hydrogen binding sites (Sumida et al., 2011; Zhou et al., 2008). The major challenges for MOFs material are derived from their rational design and preparation processes which control crystal structure and pore texture properties e.g. pore connectivity, structure and dimension by the alternation of the linkers, ligands and metals as well as incorporation of variety of chemicals in the materials, giving different adsorption properties. Features such as rational design, extraordinary permanent porosity and a large pore volume make MOFs interesting for a large range of potential applications including chemical separations, catalysis, gas storage and release etc.

2.4.3 Metal hydrides

Metal hydrides may represent ideal storage systems. The reaction of hydrogen with metals can be described by the following chemical reaction:

$$M + x/2H_2 \leftrightarrow MH_x + \text{Heat} \tag{2.1}$$

The thermodynamic behaviour in forming hydrides is typically described by pressure-composition isotherms, as shown in Figure 2.6 (Züttel, 2003). Hydrogen molecules are adsorbed at the interface of metallic materials, and disassociated into individual hydrogen atoms that are absorbed or dissolved into the metal phase. The initial dissolution of hydrogen atoms in the metal phase is known as the α-phase. The hydrogen atoms are rearranged in a specific configuration by contributing their electrons to the band structure of the metal, forming a metal hydride (β-phase). The amounts of hydrogen which is reversibly stored at a certain temperature can be determined by the length of a plateau in the isotherms.

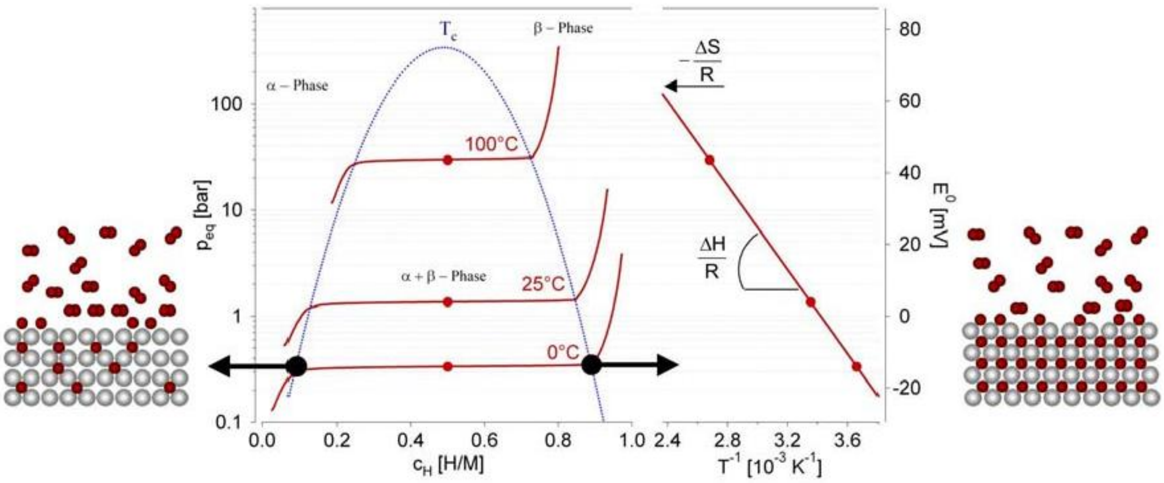

Figure 2.6 The pressure-composition isotherms of typical metal hydrides (Züttel, 2003)

Although the majority of elements are able to form elemental hydrides under appropriate conditions, most of them have poor pressure-composition-temperature (PCT) properties. Traditional metal hydrides are alloy hydrides, such as intermetallics of types AB, AB_2, AB_3, AB_5 and A_2B, combining a strong hydride forming element A with weak hydriding elements B to form alloys (Delogu and Mulas, 2009; Liao et al., 2006; Zhao et al., 2010), as well as solid solution alloys in which minor elements as solutes are dissolved in a primary element as a solvent (Yoo et al., 2009). The crystal structures and hydrogen storage properties of conventional metal hydrides are summarized in Table 2.1. These hydrides show that the gravimetric hydrogen density (GHD) is less than 3.6 wt% and the equilibrium hydrogen pressure (P_{eq}) and temperature (T) for hydrogen desorption are variable.

Table2.1 The key hydrogen storage properties of typical metallic hydrides (Bowman and Fultz, 2002; Chen and Zhu, 2008)

Type	Alloy	Hydride phase	Crystal structure	GHD* (wt%)	P_{eq} (bar)/ T (°C)**
AB_5	$LaNi_5$	$LaNi_5H_6$	Hexagonal	1.4	2 / 25
	$LaNi_{4.8}Sn_{0.2}$	$LaNi_{4.8}Sn_{0.2}H_6$	Hexagonal	1.2	1 / 39
AB_3	$CaNi_3$	$CaNi_3H_{4.4}$	Hexagonal	1.8	0.5 / 25
AB_2	ZrV_2	$ZrV_2H_{5.5}$	Hexagonal	3.0	10-8 / 50
	$ZrMn_2$	$ZrMn_2H_{3.6}$	Hexagonal	0.9	1 / 167
	$TiMn_{1.4}V_{0.62}$	$TiMn_{1.4}V_{0.62}H_{3.4}$	Hexagonal	1.1	1 / -5
AB	TiFe	$TiFeH_{1.8}$	Cubic	1.9	5 / 30
	ZrNi	$ZrNiH_3$	Cubic	1.1	1 / 300
A_2B	Mg_2Ni	Mg_2NiH_4	Cubic	3.6	1 / 282
Solid solution	Ti-V-based	Ti-V-H_4	Cubic	2.6	1 / 25

GHD: gravimetric hydrogen density

**Peq/T: equilibrium hydrogen pressure for hydrogen desorption at temperature T*

Light metals such as Mg, have shown promising levels of stored hydrogen; for instance, the stoichiometric compound MgH_2 provides a storage capacity of 7.6 wt% (Jain et al., 2010). However, due to the high stability of MgH_2 (ΔH_f = -78 kJ/mol), relatively high temperatures are needed for hydrogen absorption /desorption with impractical cycling kinetics, generally 50 hours for the recombination of Mg with H_2 to form full hydride MgH_2 at 300 °C and nearly 1 hour for dehydrogenation at 350 °C (Bogdanović et al., 1999; Jain et al., 2010). To improve the characteristics of Mg-hydride, a variety of approaches have been investigated including alloying with other transition metal and their oxides, the addition of catalysts, particle size reduction and tuning small ion mobility. The destabilization of Mg-hydride has been achieved by adding alloying additives e.g. Al (Andreasen, 2008; Crivello et al., 2009) and Ni (Kodera et al., 2007), via forming Mg_2Ni and Mg-Al alloys. Catalysts, e. g. transition metals, metal oxides, intermetallic compounds that absorb hydrogen in milder conditions and carbon materials, have been investigated, which showed an enhanced dissociation of hydrogen molecules and recombination of hydrogen atoms through catalytic mechanisms such as the “hydrogen pump” and “spillover effect” (Aguey-Zinsou et al., 2007; Dufour and Huot, 2007; Patah et al., 2009). With the addition of catalysts, hydrogen molecules more easily dissociate into hydrogen atoms on the surface of the catalyst particles. When the hydrogen concentration achieves a certain degree on the surface of catalysts, the migration and diffusion of hydrogen into the matrix can be accelerated through catalyst/matrix interface, where the catalysts actually work as a “hydrogen pump” during the hydrogenation (Hu et al., 2004) and “spillover effect” refers to the diffusion of surface hydrogen species from the catalyst sites into the matrix, leading to an enhanced hydrogenation kinetics (Lueking and Yang, 2004). The addition of Nb_2O_5 resulted in improvement of sorption/desorption kinetics of MgH_2 by decreasing sorption/desorption time to 60/90 seconds respectively with reversible hydrogen storage of 7 wt% at 300 °C and by lowering the desorption activation energy to 61 kJ/mol H_2 (Barkhordarian et al., 2004). Using the high-energy ball milling technique, the particle size of metal hydrides can be reduced, which is beneficial for enhancing the sorption kinetics by altering the surface properties and the microstructure of Mg-hydrides (Aguey-Zinsou et al., 2007). Magnesium nanowires with smallest diameters between 30-50 nm have been prepared by vapour-transport methods, indicating a reduced activation energy of hydiding/dehydriding for Mg (34/39 kJ/mol H_2) and a dehydrogenation enthalpy of 65.3 kJ/mol H_2 (Li et al., 2007c).

Although metal hydrides are safe and volume-efficient hydrogen storage materials, their low gravimetric densities up to 3.6 wt% except for Mg hydride, and the high temperature of hydrogen desorption and slow dehydriding kinetics for Mg-hydride are significant obstacles for practical on-board application.

2.4.4 Complex hydrides

Complex hydrides are relatively new for hydrogen storage. They have attracted growing interest in recent years due to their high gravimetric densities of hydrogen. Generally, complex metal hydrides have the formula $M_xL_yH_z$, where M is an alkali metal cation and L is a metal or metalloid. The well known examples, with the most stable structures, are alanates $[AlH_4]^-$, amides $[NH_2]^-$ and borohydrides $[BH_4]^-$ of alkali, alkaline earth or other cations, in which hydrogen is covalently bonded to a central atom in complex anions (Orimo et al., 2007; Züttel et al., 2007). The typical alkali and alkaline earth complex hydrides with hydrogen storage properties are summarized in Table 2.2.

The significant advantage for these types of materials is high theoretical total hydrogen capacities such as up to ca. 18 wt% with high volumetric densities of hydrogen up to 0.146

g/cm^3 H_2. The utilization of the materials for hydrogen storage depends on the kinetics and thermodynamics of decomposition and recombination, such as whether the materials can be conveniently dehydrided at a practical temperature and how the material can be recharged with hydrogen.

Table 2.2 Typical alkali and alkaline earth complex hydrides (Ares et al., 2009; Ares et al., 2008; Ashby and Kobetz, 1966; Bogdanović and Schwickardi, 1997; Chen et al., 2002; Orimo et al., 2007; Rafi-ud-din et al., 2011; Züttel et al., 2007)

Complex	Density (g/cm^3)	H capacity (wt%)	H density (g/cm^3)	T*(ºC)	ΔH_f (kJ/mol)
$LiAlH_4$	0.917	10.54	0.0974	150	-116
$NaAlH_4$	1.28	7.41	0.0956	178	-113
$KAlH_4$	1.08	5.71	0.0532	290	-
$Mg(AlH_4)_2$	1.29	9.27	0.0723	-	-
$Ca(AlH_4)_2$	1.12	7.84	0.0704	>230	-
$LiNH_2$	1.18	8.78	0.1036	372-400	-179.6
$NaNH_2$	1.39	5.15	0.0719	210	-123.8
KNH_2	1.62	3.66	0.0593	338	-128.9
$Mg(NH_2)_2$	1.39	7.15	0.0994	360	-
$Ca(NH_2)_2$	1.74	5.59	0.0973	-	-383.4
$LiBH_4$	0.66	18.36	0.1225	265	-194
$NaBH_4$	1.07	10.57	0.1131	505	-191
KBH_4	1.17	7.42	0.0871	585	-229
$Mg(BH_4)_2$	0.989	14.82	0.1465	320	-
$Ca(BH_4)_2$	-	11.47	-	260	-

* *T: onset decomposition temperature*

Alkali metal alanates thermally decompose to produce hydrogen through the following three reactions (Ares et al., 2009; Ares et al., 2008; Ashby and Kobetz, 1966; Bogdanović and Schwickardi, 1997; Morioka et al., 2003; Rafi-ud-din et al., 2011):

$$MAlH_4 \rightarrow 1/3M_3AlH_6 + 2/3Al + H_2 \quad (M = Li, Na, K) \tag{2.2}$$

(Li: 5.3 wt% H_2 at 150-175℃ ; Na: 3.7 wt% H_2 at 230℃ ; K: 2.9 wt% at 290-330℃)

$$M_3AlH_6 \rightarrow 3MH + Al + 3/2H_2 \quad (M = Li, Na, K) \tag{2.3}$$

(Li: 2.6 wt% H_2 at 180-220℃ ; Na: 1.8 wt% at 265 ºC; K: 1.4 wt% at 330-355℃)

$$MH + Al \rightarrow MAl + ½H_2 \quad (M = Li) \tag{2.4}$$

(Li: 2.6 wt% H_2 at 400-420℃)

Equation (2.4) is not considered to be available for most practical applications as it takes place above 400 ℃ . Although the decomposition temperature is relatively low for equations (2.2) and (2.3), the dehydrogenation kinetics is a major barrier. In recent years, many research groups have explored various approaches to try to enhance the dehydrogenation kinetics and reversibility of $MAlH_4$. For instance, various additives have been investigated for their roles in the decomposition and hydrogenation process (Bogdanović and Schwickardi, 1997; Guo et al., 2011; Ismail et al., 2011; Rafi-ud-din et al., 2011; Sun et al., 2008).

Doped rare earth element catalysts helped to speed-up the decomposition reaction rate of $LiAlH_4$ and improved the dehydriding properties of $LiAlH_4$; for example, reducing the dehydriding start temperature of $LiAlH_4$ by about 25 ºC (Guo et al., 2011). A $LiAlH_4$/SWCNT composite system resulted in both a decreased decomposition temperature and enhanced desorption kinetics compared to pure $LiAlH_4$. The decomposition onset temperature of the 5 wt% SWCNT-added $LiAlH_4$ sample was reduced to 80 ºC for equation (2.2) and 130 ºC for equation (2.3). In terms of the desorption kinetics, the 5 wt% SWCNT-added $LiAlH_4$ sample released about 4.0 wt% hydrogen at 90 ºC after 40 minutes dehydrogenation, while the as-milled $LiAlH_4$ sample released less than 0.3 wt% hydrogen for the same temperature and time. The apparent activation energy for hydrogen desorption was decreased from 116 kJ/mol for as-received $LiAlH_4$ to 61 kJ/mol by the addition of 5 wt% SWCNTs (Ismail et al., 2011). Nickel-based catalysts possess satisfactory catalytic activity. $LiAiH_4$, milled with $NiCl_3$ for 30 min, released 4.2 wt% hydrogen at 100 ℃ within 3 hours. The mixture exhibited a greatly reduced decomposition temperature (by 50 ℃) and improved desorption kinetics (Sun et al., 2008). However, there has been no successful data reported about reversibility of dehydrogenated $LiAlH_4$ so far, although $LiAlH_4$ doped with 2 mol% $LaCl_3$ exhibited rehydrogenation amount only 0.8 wt% at 180 ℃ under 80 bar H_2 after dehydriding at 270 ℃ (Zheng et al., 2007). Further effort focused on the destabilized $LiAlH_4$ system combined with nano-particles of MgH_2 demonstrated 5.0 wt% hydrogen reversibe with moderate kinetics at 300 and 350 ℃ (Vittetoe et al., 2009). A significant improvement on the hydrogen absorption properties of the $LiAlH_4$-MgH_2 composite was obtained by the addition of TiF_3. A hydrogen absorption capacity of 2.68 wt% under 300 ℃ and 20 bar H_2 pressure was reached after 5 minutes in the $LiAlH_4$-MgH_2-TiF_3 composite, compared to 1.75 wt% for $LiAlH_4$-MgH_2 (Mao et al., 2011). This finding provided many possibilities for the improvement of reversible hydrogen storage in the $LiAlH_4$ system.

In 1997, Bogdanović and Schwickardi (1997) first reported that, by doping Ti-catalysts e.g. b-$TiCl_3$, $Ti(OBu^n)_4$ into a $NaAlH_4$ suspension followed by evaporation, the dehydrogenation of $NaAlH_4$ could be kinetically enhanced and its reversible reaction could be achieved under moderate conditions. They found that the dehydriding of $NaAlH_4$ occurred at 150 ℃ and the rehydrogenation process was accomplished within 5 hours at 170 ℃ and 152 bar hydrogen pressure. However, this system indicated cyclic instability, with hydrogen capacity decreased from 5.6 wt% to 3.1 wt% after 31 cycles. Doping catalysts has demonstrated thermodynamic and kinetic enhancement for $NaAlH_4$, compared with Bogdanovic's original findings. The catalytic efficiency depends on not only the doping techniques but also dopant precursors. Ti-species are the most frequently used catalyst, the nature of which is an important factor in the catalyst efficiency. Ti halides e.g.$TiBr_4$, $TiCl_4$, $TiCl_3$ and TiF_3 have been proposed to be high effective catalysts for de-/hydrogenation of $NaAlH_4$ at considerably reduced temperature and/or pressure conditions (Bogdanović and Schwickardi, 1997; Nielsen et al., 2011; Wang et al., 2005). Besides Ti-based doping catalysts, lanthanide oxides and salts e.g. $LaCl_3$, $Ce(NO_3)_2$, $ScCl_3$, $CeCl_3$ and PrCl, doped into $NaAlH_4$ have been investigated recently (Bogdanović et al., 2006; Lee et al., 2007; Zheng et al., 2011). It was found that $NaAlH_4$ with lanthanide oxides except for CeO_2 could reversibly store hydrogen, of which Sm_2O_3 showed the best catalytic performance in both hydrogenation kinetics and cyclic stability (Lee et al., 2007). $NaAlH_4$ ball milled with 2 mol% $ScCl_3$, exhibited a greater reversible hydrogen storage capacity than that of the Ti-catalyst system at 130-140 °C and 100-110 bar hydrogen pressure, and had improved kinetic cycling stability. The hydrogenation time of the Sc- and Ce-doped $NaAlH_4$ systems decreased by a factor of 2 at 100 bar and by a factor of 10 at 50 bar compared to that of Ti-doped system (Bogdanović et al., 2006).

The main advantage of $KAlH_4$ over sodium and lithium alanates is that $KAlH_4$ exhibits a rapid reversible hydrogen decomposition reaction without the aid of any external catalysts. The homogeneous doping of the transition metal catalyst is essential for the reversibility and fast kinetics. The reversible dehydrogenation and hydrogenation of $KAlH_4$ were clearly demonstrated over a temperature range 250-340 °C under <10 bar of hydrogen. The hydrogen storage capacity was above 3.5 wt% (Morioka et al., 2003). Addition of $TiCl_3$ to $KAlH_4$ reduced the decomposition temperatures (by 50℃) of $KAlH_4$, which benefits its utilization as a hydrogen storage material at moderate temperatures in the near future (Ares et al., 2009).

Amide systems (of alkali or alkaline earth metals) hold great potential for hydrogen storage except for the slow hydrogen desorption kinetics. In 2002, encouraging progress had made by Chen et al. (2002), where they demonstrated that the hydrogenation of lithium nitride (Li_3N) occurred reversibly with a two-step reaction, expressed as follows:

$$LiNH_2 + 2LiH \leftrightarrow Li_2NH + LiH + H_2 \leftrightarrow Li_3N + 2H_2 \qquad (2.5)$$

Although the $LiNH_2$-LiH system could theoretically store up to 10.3 wt% H_2, for practical applications only the first decomposition step can be used (6.5 wt% H_2) as the required temperatures for the second step (above 350 °C) are too high. An alternative approach is to partially substitute LiH by MgH_2 which reduces the decomposition temperature while the storage capacity (of the first step) decreased to 5.2 wt% at 200 °C with a desorption equilibrium pressure of about 30 bar (Luo and Ronnebro, 2005). The 2 $LiNH_2$-MgH_2 system was shown to be reversible over nine cycles at 200 °C and 32 bar H_2 with a gravimetric capacity of 4.6 wt% (Luo, 2004). The first step reaction (equation 2.6), where $Li_2Mg(NH)_2$ and hydrogen form, had a reduced reaction enthalpy compared with the equivalent $LiNH_2$-LiH equation (2.5) (Janot et al., 2007; Luo, 2004).

$$2LiNH_2 + MgH_2 \rightarrow Li_2Mg(NH)_2 + 2H_2 \leftrightarrow Mg(NH_2)_2 + 2LiH \qquad (2.6)$$

In addition, mixtures of amides and borohydrides (Chater et al., 2007b; Chater et al., 2006; Niemann et al., 2009), amides and alanates (Luo et al., 2009) or addition of Si and Ti-based catalysts to amides (Palade et al., 2010; Teng et al., 2011) have been investigated during the last few years. In some cases the thermodynamic destabilization effects in the amide system from additives were observed as the alteration of reaction pathways resulted in lower reaction enthalpies.

The optimization of the amide system is very important for improving the hydrogen desorption reaction. For example, replacing $LiNH_2$ in the $LiNH_2$-2LiH system with $Mg(NH_2)_2$ resulted in a significant decrease in the desorption enthalpy change. The system exhibited favourable thermodynamics, good reversibility, and a relatively high reversible hydrogen capacity (5.6 wt%) through the following reaction (Liang et al., 2011; Xiong et al., 2004):

$$Mg(NH_2)_2 + 2LiH \leftrightarrow Li_2Mg(NH)_2 + 2H_2 \qquad (2.7)$$

In order to optimize the hydrogen storage properties of the Li–Mg–N–H system, investigations of the $Mg(NH_2)_2$-LiH system with different stoichiometric ratios were conducted by several research groups. It was found that 3.0 wt% of hydrogen was released from the 1:1 $Mg(NH_2)_2$-LiH mixture along with significant ammonia evolution, and that a higher content of LiH facilitated a reduction in ammonia release (Xiong et al., 2006); the 3:8 $Mg(NH_2)_2$-LiH mixture could reversibly store 6.9 wt% of hydrogen (Leng et al., 2004), but only when heated to 450 ℃ .

In contrast, $NaNH_2$ has received relatively little attention as, unlike Li and Mg, sodium imide is unknown at present, which limits possible destabilization of reaction pathways. In spite of this, there were a few studies of $NaNH_2$-containing systems such as $NaNH_2$-$NaBH_4$ (Chater et al., 2007a; Somer et al., 2010), $NaNH_2$-$NaAlH_4$ (Dolotko et al., 2007), $NaNH_2$-$LiAlH_4$ (Chua et al., 2010) and $NaNH_2$-MgH_2 (Dolotko et al., 2010; Sheppard et al., 2011). In these cases, desorption experiments indicated severe kinetic limitations and further investigation of the reaction mechanism(s) in such mixed systems may lead to new destabilization pathways, so as to improve the sorption kinetics and thermodynamic properties.

Borohydride compounds are a relatively new category of complex hydride (in the context of hydrogen storage) containing boron and hydrogen covalently bonded in a tetrahedral structure. Borohydride compounds will be reviewed in detail in the next section.

Chapter 3 Literature Review: Borohydrides

3.1 Introduction

Borohydrides contain boron and hydrogen covalently bonded in a tetrahedral structure with boron in the center and the hydrogen located at the four corners, as shown in Figure 3.1. The charge on the $[BH_4]^-$ unit is compensated by metal cations (M).

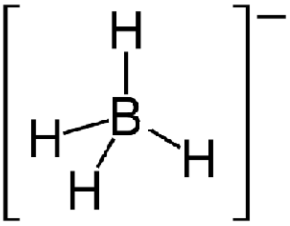

Figure 3.1 Schematic tetrahedral structure of $[BH_4]^-$ unit

Through hydrogen bridging atoms, hydrogen can bind to different metal cations with ionic or covalent bonds in three different orientations: monodentate, one bond; bidentate, two bonds; and tridentate, three bonds (see Figure 3.2). The coordination mode and physicochemical properties of borohydrides strongly depend on the nature of the metal and its oxidation state, which affect the thermodynamic stability of the borohydride compound.

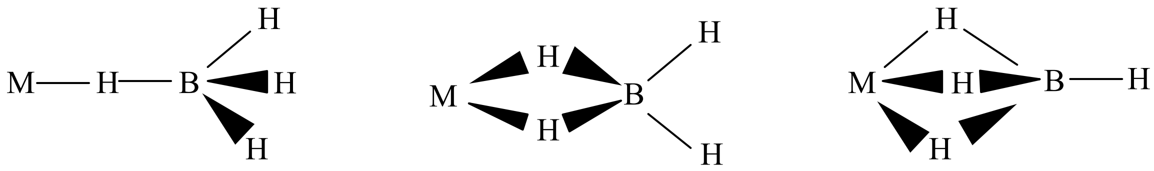

Monodentate coordination Bidentate coordination tridentate coordination

Figure 3.2 Covalent bonding configurations (Reed, 2009)

Historically, metal borohydrides have been employed as reducing agents in organic synthetic chemistry and precursors for the synthesis of organometallic derivatives and the production of borides, hydrides as well as other inorganic materials. Over the last ten years, borohydride complexes have been regarded as one of the most promising candidates for hydrogen storage in mobile applications due to their intrinsically high gravimetric and volumetric hydrogen capacities (Li et al., 2011a; Orimo et al., 2007; Züttel et al., 2007). The material properties of typical single cation borohydrides are shown in Table 3.1. Within this class of compound, alkali metal or alkaline earth metal borohydrides exhibit the higher hydrogen densities, e. g. 18.5 wt% and 121.5 kg H_2/m^3 for $LiBH_4$. However, these materials have decomposition temperature greater than 300 °C and exhibit poor reversibility.

Table 3.1 The properties of typical borohydrides (Li et al., 2011a; Nakamori and Orimo, 2008; Züttel et al., 2007)

Compounds	**Theoretical storage capacity (wt%)**	**Hydrogen density (kg/m^3)**	**Decomposition temperature (°C)**	**Heat of formation (kJ/mol)**
$LiBH_4$	18.5	121.5	400	-194
$NaBH_4$	10.7	114.5	565	-191
KBH_4	7.47	87.8	640	-229
$RbBH_4$	4.0	76.8	-	-
$CsBH_4$	2.7	65.3	-	-
$BeBH_4$	20.8	146.0	-	-
$Mg(BH_4)_2$	14.9	147.4	260-280	-
$Ca(BH_4)_2$	11.6	124.1	320	-
$Sc(BH_4)_3$	13.5	-	162	-
$Ti(BH_4)_3$	13.1	-	< 25	-
$Zr(BH_4)_4$	10.7	126.2	<250	-
$Hf(BH_4)_4$	6.78	112.2	< 250	-
$Mn(BH_4)_2$	9.5	117.8	-	-
$Zn(BH_4)_2$	8.49	-	85	-
$Al(BH_4)_3$	16.9	133.5	< 25	-

For any chemical reaction, the reaction temperature (T) depends on the Gibbs free energy:

$$\Delta G = \Delta H - T\Delta S \tag{3.1}$$

where ΔH enthalpy change, ΔS entropy change. The thermodynamic stability of borohydride compounds, one of most important hydrogen storage properties, can be evaluated by enthalpy change (ΔH_{dec}) of their thermal decomposition reaction. ΔH_{dec} is the difference in the heat of formation (ΔH_{f}) between the decomposed products and the borohydride compound, described as follows (Li et al., 2011a):

$$\Delta H_{\mathrm{dec}} = \Delta H_{\mathrm{fprod}} - \Delta H_{\mathrm{fboro}} \tag{3.2}$$

This equation (3.2) indicates that apart from those of the decomposed products, the stability of borohydride compounds determines the enthalpy change (ΔH_{dec}) of thermal decomposition. First-principles calculations, combined with experimental measurements have shown a good inverse relationship between the thermal decomposition temperature (T_{d}) of single cation homoleptic borohydrides and the Pauling electronegativity (χ_{p}) of the cation through the enthalpy of formation (Nakamori et al., 2007; Nakamori et al., 2006), as shown in Figure 3.3. In this work, assuming that the dehydrogenation reaction of borohydrides occurred via the following equation:

$$\mathrm{M(BH_4)_n} \rightarrow \mathrm{MH_m} + \mathrm{nB} + \{(4\mathrm{n}-\mathrm{m})/2\}\mathrm{H_2} \tag{3.3}$$

The enthalpy change for this reaction, ΔH_{des} , can be estimated using the predicted $\Delta H_{\mathrm{fboro}}$ for $\mathrm{M(BH_4)_n}$ and experimental data for $\mathrm{MH_m}$, ΔH_{fMHm}. A good correlation between ΔH_{des} and T_{d} was also obtained (see inset in Figure 3.3), which indicated that χ_{p} is a useful indicator to estimate the thermodynamic stability of borohydride compounds. Hence borohydrides with cation χ_p between 1.2 and 1.5 were suggested as promising candidates for hydrogen storage.

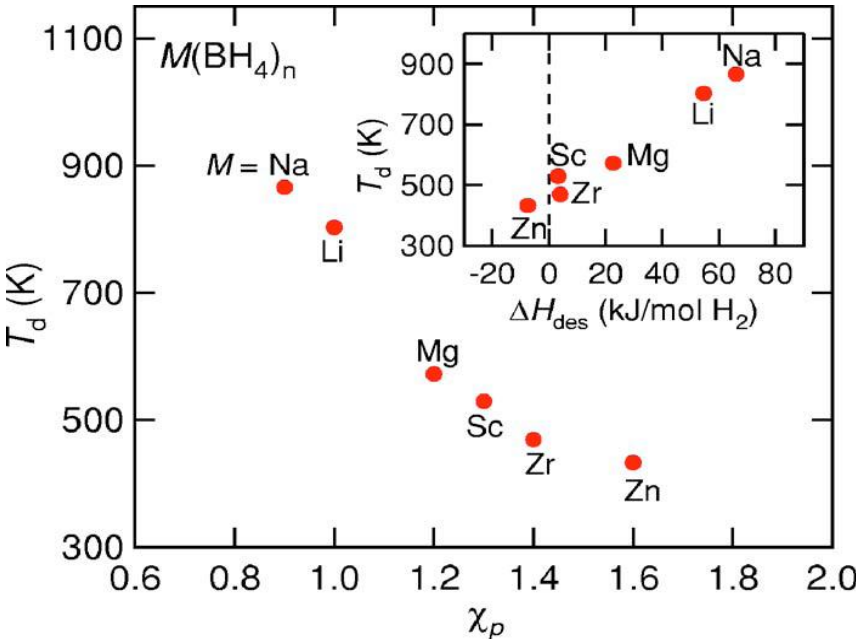

Figure 3.3 The decomposition temperature (T_d) as a function of the Pauling electronegativity χ_p (inset shows the correlation between T_d and estimated ΔH_{des} for the desorption reaction) (Nakamori et al., 2007)

To obtain borohydride complexes with improved thermodynamic properties, one approach is to synthesise borohydride compounds with appropriate cation χ_p (1.2-1.5) e.g. transition metals, including $Zr(BH_4)_4$, $Hf(BH_4)_4$, $Y(BH_4)_3$ and $Mn(BH_4)_2$ (Bird and Churchill, 1967; Broach et al., 1983; Černý et al., 2009; Jensen, 2003a; b; Ravnsbaek et al., 2010a; Sato et al., 2008). The other approach is to prepare mixed cation borohydrides by thermodynamic tuning, which allows the borohydride-based compounds to be synthesised selectively. Combining appropriate cations has been an effective method for adjusting the thermodynamic stability of borohydrides so as to have decomposition temperatures within the desired range for hydrogen storage applications; several examples – such as $LiK(BH_4)_2$, $ZrLi(BH_4)_5$, $ZrLi_2(BH_4)_6$,

$LiSc(BH_4)_4$ and $NaZn_2(BH_4)_5$ – have been reported so far (Hagemann et al., 2008; Li et al., 2007b; Nickels et al., 2008; Ravnsbaek et al., 2009).

A recently developed method for modifying the thermodynamic properties of borohydrides is anion substitution between halide anions: F^-, Cl^-, Br^-, I^- in alkali or alkaline earth salts and BH_4^- in metal borohydride structure to form a solid solution. Dissolution of ACl into ABH_4 (A = Li, Na or K) has been observed through ball-milling, annealing or combination of ball-milling and annealing of ABH_4-ACl mixture, to form solid solutions such as $Na(BH_4)_{1-x}Cl_x$ (Ravnsbaek et al., 2011), $Li(BH_4)_{1-x}Cl_x$ (Arnbjerg et al., 2009; Mosegaard et al., 2008). The formation of the solid solutions may alter the decomposition pathways and the structural flexibility and reactivity of ABH_4. During the thermal decomposition of $ASc(BH_4)_4$ (A = Na, K) the solid solutions: Na or $K(BH_4)_{1-x}Cl_x$ also formed (Černý et al., 2010b; Černý et al., 2010c). Therefore, the anion substitution to form a solid solution might play an important role in the modification of the thermal decomposition of borohydride compounds.

3.2 Alkali metal borohydride systems

3.2.1 $LiBH_4$

3.2.1.1 Synthesis

Pure lithium borohydride ($LiBH_4$) was first reported by Schlesinger and Brown (1940) who prepared $LiBH_4$ using the reaction of ethyl-lithium with diborane and found the reaction completed at room temperature in 5 hours. Their further research found a higher yield of borohydrides through the reaction of the corresponding metal hydrides with diborane in diethyl ether solvent under suitable conditions, followed by heating to release the solvent (Schlesinger et al., 1953a):

$$2LiH + B_2H_6 + \text{diethyl ether} \rightarrow 2LiBH_4\text{- diethyl ether} \qquad (3.4)$$

Additionally, a conventional production of $LiBH_4$ is through a metathesis reaction between $NaBH_4$ and Li halides in the presence of ether or isopropyl amine as shown below (Brown et al., 1981):

$$Na(BH_4) + LiCl \text{ or } LiBr \rightarrow Li(BH_4) + NaCl \text{ or } NaBr \qquad (3.5)$$

Obviously, these methods require the removal of solvent and any byproduct e.g. NaCl, NaBr from the mixture. Even so there is still a trace amount of solvent in the desired product (Brown et al., 1981; Schlesinger and Brown, 1940).

Direct synthesis of borohydrides from the elements, producing solvent-free product, has some advantages over wet chemical reactions using a solvent. Although the direct synthesis of $LiBH_4$ is thermodynamically favoured (formation enthalpy of $\Delta H_{\mathrm{fboro}} = -194.2$ kJ), the formation of $LiBH_4$ requires high temperatures and pressures. A German patent in 1958 reported that alkali metal borohydrides were produced directly from metal and boron with hydrogen at 30-150 bar and 550-700 ℃ :

$$Li + B + 2H_2 \rightarrow LiBH_4 \qquad (3.6)$$

which can be extended to preparation of group IA and IIA metal borohydrides (Goerrig, 1958). To reproduce this result, most recently Friedrichs et al. (2008) have prepared pure $LiBH_4$ or $LiBD_4$ directly from the elements first through pre-milling lithium and boron at a temperature of 330 ℃ for 60 hours in argon atmosphere and heating up to 450 ℃ for another 60 hours and then followed by exposing the Li-B pre-milled mixture to a hydrogen or deuterium atmosphere at 150 bar and 700 ℃ . A similar synthetic process was applied to form $LiBH_4$

using lithium and boron as the starting elements by means of a solid phase reaction under an argon atmosphere then under 60 bar hydrogen (Cakanyildirim and Guru, 2008). Due to the chemical inertness of the solid boron preventing its reaction with lithium and hydrogen, the direct synthesis of $LiBH_4$ from the elements no doubt demands a high temperature and high hydrogen pressure, which is a major drawback.

In 2005, Orimo et al. (2005) showed that the dehydrogenation of $LiBH_4$ was reversible, as the end products lithium hydride (LiH) and boron (B) absorbed hydrogen at 600 ℃ under a hydrogen pressure of 350 bars for over 12 hours to form $LiBH_4$. The formation of $LiBH_4$ (~ 27 wt% yield) was demonstrated by high-energy ball milling a mixture of LiH and crystalline B in a hydrogen atmosphere for over 138 hours (Agresti and Khandelwal, 2009). The production of $LiBH_4$ from lithium hydride and boron is kinetically hindered by the need to break the rigid boron lattice, and subsequently react with lithium hydride to form boron-hydrogen (B-H) bonds (Züttel et al., 2007). By preparing a homogenous dispersion of lithium and boron at an atomic level, such as by forming a binary LiB_x compound, improved reaction kinetics of $LiBH_4$ formation was obtained (Friedrichs et al., 2008). Starting from AlB_2 instead of B strongly enhanced the kinetics of forming $LiBH_4$ from lithium hydride for a synthetic process at 450 ℃ under 13 bar hydrogen (Friedrichs et al., 2009b):

$$2LiH + AlB_2 + 3H_2 \leftrightarrow 2LiBH_4 + Al \quad (3.7)$$

Low-temperature synthesis of $LiBH_4$ was first presented by using a gas-solid reaction between lithium hydride and diborane at 120 ℃ under ambient pressure, in which diborane was generated from the decomposition of a milled $LiBH_4$-$ZnCl_2$ mixture (Friedrichs et al., 2009a). However, the formation yield of $LiBH_4$ was limited to about 74 wt%. A further study showed that a core shell structure of the grains existed (see Figure 3.4), in which $LiBD_4$

formed a passivation layer on the surface of the LiD grains. The formation of a core shell structure hindered ionic diffusion through the surface (Friedrichs et al., 2010a).

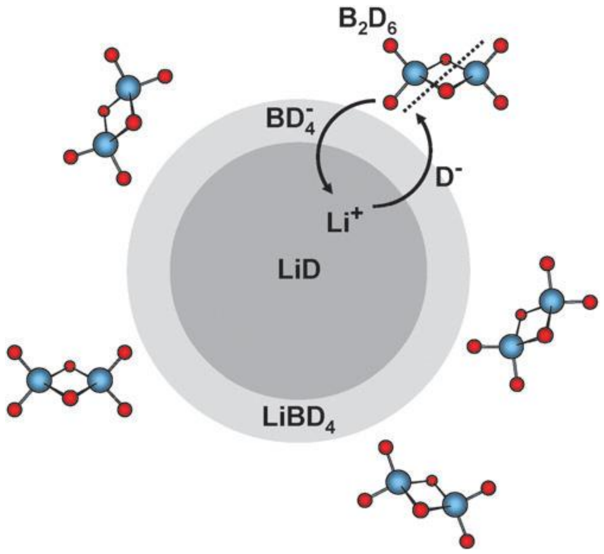

Figure 3.4 Schematic presentation of the core shell formation on LiD due to surface reaction with diborane.

To remove the passivation layer, a ball milling technique was needed to produce almost pure $LiBH_4$ with a 94 mol% yield achievable at room temperature by milling LiH in a diborane/hydrogen atmosphere, providing fresh reactive surfaces and enhancing interdiffusion (Friedrichs et al., 2010b). This work claimed that during formation and decomposition of borohydrides, diborane might be the key for reversible hydrogen absorption and desorption reaction under moderate conditions. The synthesis mechanism of $LiBH_4$ through solid-gas reaction of LiH and diborane gas was investigated by H/D isotope labelling of the reaction educts (Gremaud et al., 2011). Clear evidence of the heterolytic splitting of diborane on the LiH surface was found, where the entire BH_4^- unit formed from the diborane then transferred to LiH, subsequently exchanged with the H^- ions of the underlying hydride. A reaction pathway might be expressed as follows:

$$LiH + B_2H_6 \leftrightarrow LiH + BH_4^- BH_2^+ \leftrightarrow LiBH_4 + BH_3 \qquad (3.8)$$

3.2.1.2 Structure

The structure of $LiBH_4$ has been extensively investigated using varieties of analytical instruments such as X-ray diffraction (XRD), nuclear magnetic resonance (NMR) and Raman spectroscopy (Epp and Wilkening, 2010; Fillinchuk et al., 2008; Gomes et al., 2002; Hagemann et al., 2009; Harris and Meibohm, 1947; Racu et al., 2008; Soulié et al., 2002). The first report on the crystal structure of $LiBH_4$ was published in 1947, where the unit cell of $LiBH_4$ as orthorhombic with space group *Pmna* was suggested with each lithium ion associated with four borohydride ions (Harris and Meibohm, 1947). This result was confirmed by Soulié et al (2002) using powder synchrotron XRD technique, who claimed that at room temperature the same orthorhombic symmetry with same space group (*Pnma*, a = 7.17858(4) Å, b = 4.43686(2) Å, c = 6.80321(4) Å) was demonstrated; the tetrahedral BH_4^- units were aligned along two orthogonal directions and distorted in bond lengths and angles. They also suggested that a structure transition to a hexagonal phase with space group $P6_3mc$, (a = 4.27631(5) Å, c = 6.94844(8) Å) occurred at 135 ℃ . Theoretical modelling has been used to try to predict the structure(s) and properties of $LiBH_4$ (Feankcombe et al., 2005; Łodziana and Vegge, 2004; Miwa et al., 2004). All of the models consistently found the orthorhombic *Pnma* structure to be the ground-state phase in $LiBH_4$, in agreement with diffraction experiments at room temperature. However, none of the calculations predicted the hexagonal structure for the high temperature phase; for instance, a monoclinic *Cc* symmetry has been predicted for the high-temperature structure of $LiBH_4$ by modelling calculations using DFT and a quasiharmonic approximation (Łodziana and Vegge, 2004). In order to resolve ambiguities between experimental and theoretical studies of $LiBH_4$, synchrotron XRD was performed for determining the crystal structure of the low- and high-temperature polymorphs of $LiBH_4$ (Fillinchuk et al., 2008). Experimental data from this study showed that the high-temperature structure was hexagonal indeed, space group *P6₃mc*, not monoclinic *Cc* symmetry; tetrahedral BH_4^- anions were undistorted and geometrically very similar in both polymorphs, and furthermore the phase change at 108 ℃ was preceded by a highly anisotropic lattice expansion. These results suggested that the phase transition of $LiBH_4$ between low- and high-temperature was a reconstructive order–disorder transformation (Callear et al., 2011).

The crystallographic study of $LiBH_4$ was supported by Raman spectroscopy measurement, where it was shown that the Raman active modes at room temperature were consistent with the presence of a BH_4^- anion having a distorted tetrahedral configuration; the structural phase change led to a higher local symmetry of the BH_4^- tetrahedron, indicating a complex dynamical behaviour for $LiBH_4$ over a broad temperature (Gomes et al., 2002; Hagemann et al., 2009; Racu et al., 2008).

The electronic structure and microscopic diffusion parameters of the hexagonal and orthorhombic forms of $LiBH_4$ were investigated by temperature and frequency dependent NMR spectroscopy (Epp and Wilkening, 2010). This study revealed that hexagonal layer-structured $LiBH_4$ showed a low-dimensional diffusion process and the spatial confinement of Li hopping might be responsible for the very high ionic conductivity for the hexagonal polymorph.

3.2.1.3 Dehydrogenation and rehydrogenation

$LiBH_4$ has a high gravimetric hydrogen density of 18.5 wt% and a volumetric hydrogen density of 121 kgH_2/m^3. Züttel et al investigated the hydrogen decomposition properties of $LiBH_4$ by thermogravimetric methods (Züttel et al., 2003a; Züttel et al., 2003b). It was found that at temperatures between 100 and 200 ℃ a structural transition occurred with slight hydrogen desorption of 0.3 wt%, and at around 270 ℃ the material started melting without hydrogen evolution. More hydrogen was liberated with 1 wt% at 320 ℃ and with a larger amount of hydrogen at 400-600 ℃. During the decomposition, a maximum amount of hydrogen 13.8 wt% was released from $LiBH_4$ when the temperature reached 900 ℃. The decomposition reaction of $LiBH_4$ can be schematically described as follows:

$$\text{100-200 ℃ :} \quad LiBH_4 \rightarrow LiBH_{4-x} + x/2H_2 \tag{3.9}$$

$$\text{320 ℃ :} \quad LiBH_{4-x} \rightarrow LiBH_2 + (1+x/2)H_2 \tag{3.10}$$

$$\text{400-600 ℃ :} \quad LiBH_2 \rightarrow LiH + B + \tfrac{1}{2}H_2 \tag{3.11}$$

Orimo et al (2005) also found two sharp and one broad endothermic DSC peaks for $LiBH_4$, which respectively corresponded to the structural transition at 107 ℃, melting at 280 ℃ and decomposition around 327-427 ℃. On heating to 600 ℃, $LiBH_4$ decomposed to form final products: LiH, B and H_2, and theoretically releases 13.9 wt% hydrogen.

In terms of this process (described in equations (3.9)-(3.11)), reversibility has been demonstrated at 600 ℃ and 155-350 bar hydrogen by showing B-H atomistic vibrations in Raman spectroscopy (Orimo et al., 2005) and the presence of the $LiBH_4$ crystalline phase in the XRD pattern of the rehydrogenated compound (Mauron et al., 2008).

Possible intermediate analysis for the decomposition of borohydrides may help to improve their reversibility properties. By first-principle calculations, the stabilities of possible intermediates (e. g. LiB_3H_8, $Li_2B_nH_n$: n = 5-12) during the decomposition of $LiBH_4$ have been reported (Ohba et al., 2006); among them $Li_2(B_{12}H_{12})$ was predicted to be the most stable product. Thus the following dehydrogenation-rehydrogenation process of $LiBH_4$ was proposed (equation (3.12)) with 10 or 4 wt % hydrogen release:

$$LiBH_4 \xrightarrow{10\text{ wt\%}} 1/12Li_2(B_{12}H_{12}) + 5/6LiH_2 + 13/12H_2 \xrightarrow{4\text{ wt\%}} LiH + B + 3/2H_2 \qquad (3.\ 12)$$

Successive experimental studies were conducted to confirm the intermediate $[B_{12}H_{12}]^{2-}$ compound during the decomposition of $LiBH_4$ by using ex-situ Raman, and Magic Angle Spinning (MAS)-NMR (Hwang et al., 2008; Orimo et al., 2006). These studies showed the presence of $Li_2(B_{12}H_{12})$ when the $LiBH_4$ sample was heated above 400 ℃ . Apart from $Li_2(B_{12}H_{12})$ detected by in situ XRD, an amorphous (by lab-based XRD) $Li_2(B_{10}H_{10})$ species was also identified by NMR spectroscopy during the reaction of $LiBH_4$ with diborane at 200 ℃ (Friedrichs et al., 2010c); the mechanism for the formation of $Li_2(B_{12}H_{12})$ and $Li_2(B_{10}H_{10})$ during the desorption of hydrogen from $LiBH_4$ could be explained as a result of the reaction(s) of partial diborane or higher borane species derived from decomposition of $LiBH_4$ with the remaining $LiBH_4$.

As a result of the thermodynamic stability of $LiBH_4$, its dehydrogenation and rehydrogenation reactions must be performed under extreme conditions, and so attempts have centred on reducing the dehydriding temperature and making the material reversible at reduced pressures and temperatures.

3.2.1.4 Destabilization and kinetic modification

According to equation (3.2), one approach for reducing the enthalpy change ΔH_{dec} of the decomposition reaction (as called destabilization) is to reduce the stability of the borohydride compound, for example, by producing multi-cation borohydride compounds $LiM(BH_4)_n$, in which metal M has a higher electronegativity than that of lithium. In this case, several samples – such as $LiK(BH_4)_2$, $ZrLi(BH_4)_5$, $ZrLi_2(BH_4)_6$, $LiSc(BH_4)_4$ and $NaZn_2(BH_4)_5$ – have been synthesized so far (Hagemann et al., 2008; Li et al., 2007b; Nickels et al., 2008; Ravnsbaek et al., 2009). The other approach for reducing ΔH_{dec} is to increase the stability of decomposed products. In this case, efforts have been focused on doping additives, including metals, oxides, metal halides, metal hydrides, alanates, amides, and borohydride mixtures, to try to lower the dehydrogenation temperature and improve the hydrogen sorption kinetics of $LiBH_4$; the hydrogen storage properties of $LiBH_4$ with typical doping additives are summarized in Table 3.2.

A reduction in hydrogen desorption temperature to 300 ℃ was found for $LiBH_4$ mixed with 75 wt% SiO_2 by Züttel's group. They reported that based on the weight of $LiBH_4$ in the mixture, around 9 wt% of hydrogen was released through the reaction: $LiBH_4 \rightarrow LiH + B + H_2$. This reaction was demonstrated to be partially reversible (Züttel et al., 2003a; Züttel et al., 2003b). By ball milling with metal oxides e.g. TiO_2, SnO_2, ZrO_2, V_2O_3 and metal chlorides $TiCl_3$, $LiBH_4$ can be modified, reducing the dehydriding onset temperatures from 400 to 200 ℃ with 9 wt% hydrogen evolution. The rehydrogenation conditions were moderated from 650 ℃ under 150 bar hydrogen to 600 ℃ under 70 bar hydrogen with 7-9 wt% hydrogen recombined (Au and Jurgensen, 2006). A further study revealed that $LiBH_4$ mixed with 25 mol% TiO_2 desorbed 9 wt% hydrogen from 100 to 600 ℃ and absorbed 8 wt% hydrogen at 600 ℃ under 70 bar hydrogen, whereas the $LiBH_4$-$0.20MgCl_2$-$0.1TiCl_3$ system released 5 wt% hydrogen from 60 to 450 ℃ and absopbed 4.5 wt% hydrogen at 600 ℃ under 70 bar hydrogen (Au et al., 2008b). Mixtures of $LiBH_4$ with 50 wt% mesoporous silica-gel liberated hydrogen at 260 ℃ , but were accompanied by the evolution of gaseous diborane (Kostka et al., 2007). The composite based on 6 $LiBH_4$-CaF_2 showed a slightly reduced thermodynamic stability compared with pure $LiBH_4$ (Yuan et al., 2011).

Table 3.2 Hydrogen storage properties of $LiBH_4$ with additives

Additives	**Hydrogen (wt%)**		**Conditions: temp (°C)/pressure (bar)**		**References**
	Obs (First dehyd)	**Obs (Rehyd)**	**First dehyd**	**Rehyd**	
SiO_2	9-10		200-600		(Au and Jurgensen, 2006; Au et al., 2008b; Yu et al., 2009; Züttel et al., 2003a; Züttel et al., 2003b)
TiO_2	8-9	~ 8	100-600	600/70	
V_2O_3	8-9	~ 8	200-600	600/70	
SnO_2	8-9		200-600		
ZrO_2	8-9		200-600		
Fe_2O_3	6-9		100-600		
Nb_2O_5	~ 9		100-600		
TiF_3	~12	3-6	100-500	500/70	(Au et al., 2008a; Gennari et al., 2011; Yuan et al., 2011)
$TiCl_3$	~ 9	3.4	100-600	500/70	
$CeCl_3$	~ 5.5	2.5	220-400	400/60	
CaF_2	9.3	6-9	400-600	450/92	
MgH_2	8-10	8.5	350-580	400/100	(Kou et al., 2011; Mao, 2011; Shim et al., 2010; Vajo et al., 2005; Yang et al., 2007)
CaH_2	5.1		~ 395		
YH_3	7.2	5	~ 350	350/90	
TiH_3	6-15		300-600		
Al	~ 9		280-600		(Puszkiel and Gennari, 2009; Yang et al., 2007; Zhang et al., 2009a; Zhang et al., 2009b)
Ti	2.5		400-500		
V	4.4		400-500		
Sc	2.9		400-500		
Mg	~ 9		60-600		
Cr	4.4		400-500		

Hydrogen-containing materials such as metal hydrides and complex hydrides, have resulted in improved hydrogen storage properties when doped with (or reacted with) $LiBH_4$ (Johnson et al., 2005). A typical example is the $LiBH_4$-MgH_2 system that has shown greatly improved reversibility by changing the chemical reaction pathway, as shown in equation (3.13):

$$2LiBH_4 + MgH_2 \rightarrow 2LiH + MgB_2 + 4H_2 \tag{3.13}$$

In this case, the formation of MgB_2 stabilized the dehydrogenated state and effectively destabilized the $LiBH_4$ (Vajo et al., 2005). The study of the reaction mechanism indicated that the formation process of MgB_2 included an incubation period and nucleus growth process; the incubation period was increased by increasing the initial dehydrogenation pressure at constant temperature, and was also influenced greatly by dehydrogenation temperature (Kou et al., 2011).

The $LiBH_4$-MgH_2 system doped with $TiCl_3$ exhibited 8-10 wt% reversible hydrogen capacity with a dehydrogenation/rehydrogenation enthalpy reduced by 25 kJ/mol of H_2 (Vajo et al., 2005). The addition of Al to the $LiBH_4$-MgH_2 composite improved not only the reversibility of the reaction but also the dehydrogenation kinetics by the formation of Mg-Al alloys (via the reaction of MgH_2 with metallic Al), followed by the formation of $Mg_{(1-x)}Al_{(x)}B_{(2)}$ (via the reaction of the Mg-Al alloys with $LiBH_4$) (Li et al., 2011b). $2LiBH_4$-MgH_2 nanoconfined by melt infiltration within an inert nanoporous resorcinol-formaldehyde carbon aerogel scaffold material has shown significantly enhanced kinetics when compared to bulk 2 $LiBH_{(4)}$-MgH_2 (Gosalawit-Utke et al., 2011). For instance, at 450 °C under 3.4 bar hydrogen, the nanoconfined $2LiBH_4$-MgH_2 released 90% of the total hydrogen storage capacity within 90 minutes, whereas the bulk material released only 34%. Additionally, other metal hydride-doped additives in $LiBH_4$ such as CaH_2, YH_3, CeH_2 were also investigated, suggesting that in

$LiBH_4$-metal hydride composites the formation of metal boride played a crucial role in the reversible hydrogen storage property, and hydrogen back-pressure promoted the formation of metal boride during dehydrogenation (Pinkerton and Meyer, 2008; Shim et al., 2010).

The eutectic composition between $LiBH_4$ and $Mg(BH_4)_2$ or $Ca(BH_4)_2$ was found by physically mixing two borohydride compounds (Bardaji et al., 2011; Fang et al., 2010a; Lee et al., 2009). It was revealed that these physical mixtures had much lower decomposition temperature, for example, at 270 °C $LiBH_4$-$Mg(BH_4)_2$ composite (with molar ratio of 1:1) released about 7.0 wt% of hydrogen.

In summary, although $LiBH_4$ exhibits the highest available gravimetric hydrogen storage capacity (18.5 wt%), the high decomposition temperature and poor kinetics hinder its practical application. To improve its hydrogen storage properties, in terms of both thermodynamics and kinetics, thermodynamic tuning to form mixed cation borohydrides, by considering the electronegativity of the elemental addition and adding elements or compounds which react with $LiBH_4$ to form new reaction pathway(s), have been shown to be effective.

3.2.2 NaBH$_4$

3.2.2.1 Synthesis

Sodium borohydride ($NaBH_4$) can be produced using several methods. In 1953, Schlesinger et al. successfully prepared $NaBH_4$ by reacting diborane with either sodium trimethoxyhydride, sodium tetramethoxyborohydride or sodium methoxide, respectively (Schlesinger et al., 1953d):

$$B_2H_6 + 2NaBH(OCH_3)_3 \rightarrow 2NaBH_4 + 2B(OCH_3)_3 \tag{3.14}$$

$$2B_2H_6 + 3NaB(OCH_3)_4 \rightarrow 3NaBH_4 + 4B(OCH_3)_3 \qquad (3.15)$$

$$2B_2H_6 + 3NaOCH_2 \rightarrow 3NaBH_4 + B(OCH_3)_3 \qquad (3.16)$$

The first reaction (equation (3.14)) had the advantage of requiring the least diborane. Continuation of Schlesinger et al's work (1953b) resulted in the development of an improved synthesis route for borohydride compounds that did not require diborane. The preparation of the $NaBH_4$ compound was afforded by the rapid reaction of methyl borate with sodium hydride (NaH) at 225-275 ℃ , followed by extraction of $NaBH_4$ from the products using isopropylamine:

$$4NaH + B(OCH_3)_3 \rightarrow NaBH_4 + 3NaOCH_3 \qquad (3.17)$$

where methyl borate might be replaced by sodium trimethoxyborohydride or tetramethoxyborohydride as well as esters. The reaction of NaH with boric oxide has been used for the commercial production of $NaBH_4$ (James and Wallbridge, 1970):

$$4NaH + 2B_2O_3 \rightarrow NaBH_4 + 3NaBO_2 \qquad (3.18)$$

Since the 2000's, sodium metaborate and borax have been used as boron sources for thermochemical reactions under hydrogen to prepare $NaBH_4$. For instance, by using ball milling through the reaction of Mg or MgH_2 with $NaBO_2$, $NaBH_4$ can be formed at different temperatures under 10-70 bar hydrogen (Kojima and Haga, 2003; Li et al., 2007d; Liu et al., 2008):

$$NaBO_2 + 2Mg + 2H_2 \rightarrow NaBH_4 + 2MgO\ (\Delta G^o = -342\ \text{kJ/mol}\ NaBH_4) \qquad (3.19)$$

As the temperature and the pressure increased, the yield of $NaBH_4$ increased to a maximum value (97-98%) at 550 °C under 70 bar hydrogen, and some additions of transition metals such as Ni, Fe and Co promoted the $NaBH_4$ formation (Kojima and Haga, 2003). $NaBH_4$ was synthesized by ball-milling anhydrous borax ($Na_2B_4O_7$) with Mg or MgH_2 (Li et al., 2003b). In order to improve the yield of $NaBH_4$, Na_2CO_3 was added to compensate for the insufficient Na:

$$8MgH_2 + Na_2B_4O_7 + Na_2CO_3 \rightarrow 4NaBH_4 + 8MgO + CO_2 \qquad (3.20)$$

At 550 °C and 25 bar hydrogen, $NaBH_4$ was formed with a 93% yield via a reaction between $Na_2B_4O_7$ and Mg, in which the amount of Mg played a key role in the $NaBH_4$ yield; increasing the Mg content resulted in an appreciable increase in $NaBH_4$ formation (Kayacan et al., 2011):

$$4Mg + 4H_2 + Na_2B_4O_7 \rightarrow 2NaBH_4 + 4MgO + B_2O_3 \qquad (3.21)$$

In this case, aqueous ammonia was used to extract $NaBH_4$ from the reaction mixture.

3.2.2.2 Structure

The crystal structures of borohydride materials are highly dependent on pressure and temperature. $NaBH_4$ exhibited a face-centred cubic structure in the *Fm3m* space group under ambient conditions (Kumar and Cornelius, 2005). At around -83 °C, the cubic $NaBH_4$ phase transformed into a tetragonal structure (Sundqvist and Andersson, 2006). Through XRD measurements the high-pressure phases of $NaBH_4$ at room temperature were investigated: tetragonal (space group $P\text{-}42_1c$) and orthorhombic (space group *Pnma*) structures for $NaBH_4$ were obtained respectively above 63000 and 89000 bar pressure (Lee et al., 2006).

Vibrations of $NaBH_4$ existed in the bending region with the $\nu_2(E)$ symmetric bending mode and the $\nu_4(F_2)$ asymmetric bending mode visible from 1050 to 1300 cm^{-1}, and the bond stretching region with the $\nu_1(A_1)$ symmetric stretching mode and the $\nu_3(F_2)$ asymmetric stretching mode from 2100 to 2500 cm^{-1} (Harvey and McQuaker, 1971; Renaudin et al., 2004). The phase transition of $NaBH_4$ with temperature and pressure can be confirmed by Raman spectroscopy. At room temperature, the eight Raman frequencies for $NaBH_4$ were obtained under ambient pressure (Renaudin et al., 2004), and with increasing pressure the single strong B-H stretch mode split into three above the transition pressure, indicating that the BH_4 anion became less symmetric in the high pressure phase (Moysés Araújo et al., 2005). The spectrum of the low-temperature phase was found to be similar to that found at room temperature, as expected for a phase transition due to the order-disorder type (Harvey and McQuaker, 1971) .

3.2.2.3 Solid-state dehydrogenation and rehydrogenation

Compared to $LiBH_4$, the thermal decomposition properties of $NaBH_4$ and other alkaline metal borohydrides have not been investigated in much detail, due to the higher decomposition temperature and the relatively slow kinetics. The earlier work showed that no significant mass loss was observed on heating solid $NaBH_4$ sample up to 400 °C but its thermal decomposition occurred at 565 °C with significant hydrogen evolution after melting at 505 °C (Schlesinger et al., 1953c; Steryladkina et al., 1965).

Recently the hydrogen release processes and the thermodynamic properties for the thermal decomposition reaction of $NaBH_4$ were investigated by a combination of computational and experimental methods (Urgnani et al., 2008). It was found that a multi-step decomposition reaction occurred: the evolution of hydrogen started at lower temperatures (150 °C), showing a peak at 240 °C with 1 wt% of H_2 loss and continued by several steps at different temperature; the main hydrogen release was observed after 500 °C with two desorption peaks at 510 and 580 °C. During the decomposition of $NaBH_4$, an intermediate compound (i.e. $[B_{12}H_{12}]^{2-}$ species) was not observed by lab-based XRD analyses. Thus, $NaBH_4$ undergoes irreversible thermal decomposition.

Several attempts have been made to destabilize $NaBH_4$ by reacting it with light elements or with other hydrides (Czujko et al., 2007; Mao et al., 2009). Of these systems, a $2NaBH_4$-MgH_2 composite was found to be promising. The presence of MgH_2 could accelerate the decomposition of $NaBH_4$ by decreasing the dehydrogenation temperature by about 40 ℃ compared with pure $NaBH_4$ using a heating rate of 1°C/min in 0.2 bar hydrogen. The process followed a two-step reaction (Mao et al., 2009):

$$2NaBH_4 + MgH_2 \rightarrow 2NaBH_4 + Mg + H_2 \rightarrow 2NaH + MgB_2 + 4H_2 \qquad (3.22)$$

When doped with a TiF_3 catalyst, this system showed that 5.89 wt% hydrogen could be rehydrogenated within 12 hours at 600 °C under an initial hydrogen pressure of 40 bar, forming $NaBH_4$ and MgH_2 phases.

3.2.2.4 Aqueous dehydrogenation and regeneration

To utilize a high hydrogen capacity of $NaBH_4$, its hydrolysis reaction may be considered an attractive approach (Schlesinger et al., 1953c). The dispersed aqueous solution is a safe method for liberating hydrogen from $NaBH_4$ at ambient conditions in a controllable way:

$$NaBH_4 + 2H_2O \rightarrow NaBO_2 + 4H_2 \qquad (3.23)$$

Based on the exothermic reaction shown in equation (3.23), considerable excess water is required so as to produce hydrogen efficiently, owing to the solubility limitation of $NaBO_2$ in aqueous solution and the hydrated forms of $NaBO_2{\cdot}xH_2O$, which consumes additional water, making less water available for $NaBH_4$ hydrolysis and dissolution.

The rate of the $NaBH_4$ hydrolysis reaction (equation 3.23) is dependent on reactant concentration, temperature, the pH value of solution and the type of catalyst used. There have been extensive investigations into suitable catalyst materials for the hydrolysis of aqueous, alkaline-stabilized $NaBH_4$, including both noble and non-noble metal catalysts (Amendola et al., 2000; Dai et al., 2011; Yu and Matthews, 2011). Noble metal catalysts have superior activity with good cyclic stability but high cost. Non-noble metal catalysts are by far the more economically preferable option for hydrogen storage systems, in spite of their lower specific activity. In terms of regeneration of $NaBH_4$, a cyclic system design is the key issue for overcoming the inherent solubility limitations imposed by the by-product ($NaBO_2$) which prevents the $NaBH_4$ concentration from being high enough for releasing hydrogen (Kojima and Haga, 2003).

3.2.3 KBH_4

3.2.3.1 Synthesis and structure

In 1953, Schlesinger et al (1953d) firstly prepared potassium borohydride (KBH_4) through the reaction of potassium tetramethyoxyborohydride with diborane. Without using diborane, KBH_4 can be made by a reaction of $NaBH_4$ with KOH as shown in equation (3.24) (Banus and Bragdon, 1955) or by a mechano-chemical reaction of magnesium hydride (MgH_2) with potassium borate (KBO_2) (equation 3.25), followed by extraction using anhydrous ethylenediamine under an Ar atmosphere (Li et al., 2003a):

$$NaBH_4 + KOH \rightarrow KBH_4 + NaOH \tag{3.24}$$

$$2MgH_2 + KBO_2 \rightarrow KBH_4 + 2MgO \tag{3.25}$$

The yield of KBH_4 from equation (3.25) reached 100% when an excess amount (35%) of MgH_2 was added.

Potassium borohydride shows similar structural characteristics to $NaBH_4$. At room temperature a cubic phase with space group *Fm*-3*m* symmetry has been determined by single crystal XRD and neutron powder diffraction (Luck and Schelter, 1999; Renaudin et al., 2004). The phase transformation of KBH_4 from cubic into a tetragonal structure with *P42/nmc* symmetry took place at -203 °C, in which the disordered BH_4^- has become ordered. This disorder-ordered phase change was also observed in the form of vibrational spectra of KBH_4 (Harvey and McQuaker, 1971).

3.2.3.2 Dehydrogenation

The theoretical hydrogen content of KBH_4 is 7.5 wt%. Earlier work on the thermal decomposition of KBH_4 was done by Mikheeva et al. (1962), who showed that KBH_4 started to melt at 590 °C, followed by mass loss at 640 °C up to 700 °C due to the evolution of hydrogen, as shown in equation (3.26):

$$2KBH_4 \rightarrow 2KH + 2B + 3H_2 \tag{3.26}$$

Under hydrogen atmosphere, the melting and decomposition temperature of KBH_4 were reported to be 607 and 584 °C respectively (Orimo et al., 2004), with slow evolution of hydrogen.

3.2.3.3 K-based bialkali borohydrides

In terms of the thermal decomposition temperature, the degree of charge transfer between the metal cation and the BH_4^- anion within borohydride compounds is a key factor (Nakamori et al., 2006). Therefore, it is hoped that bialkali borohydrides may be found with suitable thermodynamics, leading to a low decomposition temperature.

Potassium-based bialkali borohydrides have been synthesized, for example $LiK(BH_4)_2$ (Nickels et al., 2008), $NaK(BH_4)_2$ (Seballos et al., 2009). The single phase $LiK(BH_4)_2$ was identified as an orthorhombic structure having the space group *Pnma* and lattice parameters *a* = 7.9134 Å , *b*=4.4907 Å and *c* = 13.8440 Å. The decomposition temperature of this new compound was between those of Li- and K- borohydride compounds. Using XRD, Raman and MAS-NMR measurements, the new phase $NaK(BH_4)_2$ was confirmed, exhibiting a new crystal structure with rhombohedral symmetry, most likely in the space group *R3*. This was distinct from the starting materials $NaBH_4$ and KBH_4, although the new material decomposed to the starting materials at room temperature after 14 hours. The successful synthesis of the dual-cation borohydrides demonstrates the possibility of compositional control on the decomposition temperature of these potential hydrogen storage media.

3.2.4 Other alkali metal borohydrides

The conventional production of rubidium and caesium borohydrides was reported by dissolving metal hydroxides (RbOH and CsOH) and excess sodium borohydride ($NaBH_4$) in alcohol or methanol solutions at room temperature by equation (3.27) (Mikheeva and Arkhipev, 1966):

$$AOH + NaBH_4 \rightarrow ABH_4 + NaOH \quad (A = Rb, Cs) \tag{3.27}$$

Simultaneously, the mixture was cooled to -5 ℃ , and the product was filtered to obtain pure rubidium or caesium borohydride.

The room temperature structures of ABH_4 (A = Rb, Cs) have cubic symmetry (*Fm*-3*m*), similar to KBH_4; at low temperature ABH_4 compounds exhibit insignificant structural phase transition, distinct with KBH_4. However, evidence for a partial ordering in ABH_4 (A = Rb, Cs) compounds was not sufficient for a full structural characterization by lab-based XRD and neutron diffraction (Renaudin et al., 2004).

ABH_4 (A = Rb, Cs) compound has relatively higher decomposition temperature than that of $LiBH_4$: 600 and 660 ℃ in an inert atmosphere, and 560 and 570 ℃ under vacuum for $RbBH_4$ and $CsBH_4$, respectively. The decomposed products were found to be the alkali metal, amorphous boron and metal borate (Mikheeva and Arkhipev, 1966).

3.3 Alkaline earth metal borohydride systems

3.3.1 $Mg(BH_4)_2$

3.3.1.1 Synthesis

Magnesium borohydride may be a promising material for hydrogen storage with a 14.9 wt% hydrogen storage density. The first report on the synthesis of $Mg(BH_4)_2$ was published in the 1950's, where the process of synthesis was afforded by the reaction of organo-magnesium

($MgEt_2$) with diborane in ether as a solvent (equation 3.28) (Wiberg and Bauer, 1950). Although diborane or its derivatives e.g. alkyldi-boranes, amine-borane as starting materials can be reacted with magnesium or its compounds to yield $Mg(BH_4)_2$, it is impractical as a result of the high toxicity of diborane and its derivatives (Wiberg and Bauer, 1950):

$$3MgEt_2 + 4B_2H_6 \rightarrow 3Mg(BH_4)_2 + 2B(Et)_3 \qquad (3.28)$$

Another approach for the synthesis of $Mg(BH_4)_2$ was to use $NaBH_4$ or $LiBH_4$, and by exchange reaction with $MgCl_2$ in a solvent, produce solvated $Mg(BH_4)_2$ (equation 3.29):

$$MgCl_2 + Na/LiBH_4 \rightarrow Mg(BH_4)_2 + Na/LiCl \qquad (3.29)$$

This liquid-liquid reaction is quite an efficient synthetic approach, but desolvation is necessary for the production of pure $Mg(BH_4)_2$. Some efforts have been made for desolvation of solvated $Mg(BH_4)_2$ complexes. For instance, the triethylamine adduct of $Mg(BH_4)_2$ prepared by the reaction of pre-milled MgH_2 and triethylamine borane under an argon atmosphere was desolvated through drying the adduct for 17 hours at various stages to obtain high purity $Mg(BH_4)_2$ (Chlopek et al., 2007). With the exchange reaction of $LiBH_4$ and $MgCl_2$ (shown in equation (3.29)) in boiling diethyl ether, followed by vacuum heat-treatment for complete removal of the solvent, desolvated $Mg(BH_4)_2$ was produced with a 30% yield (Černý et al., 2007). Based on the exchange reaction of $MgCl_2$ with $LiBH_4$ or $NaBH_4$ in various solvents, the different preparation methods of desolvated $Mg(BH_4)_2$ were evaluated by Soloveichik et al. (2009a), who found that ball-milling a mixture of $MgCl_2$ and $NaBH_4$ in diethyl ether for 1-3 days was the optimal method for the generation of the target compound, and a heating programme (under vacuum) was developed for the desolvation of solvated $Mg(BH_4)_2$.

Solid-solid reaction by mixing $MgCl_2$ and $Li/NaBH_4$ in the solid state through heat treatment or mechano-chemical ball milling of starting mixture to synthesize solvent-free $Mg(BH_4)_2$ has also been investigated. Mixing $LiBH_4$ and $MgCl_2$ (2:1 mole ratio) followed by heat treatment in 100 bar hydrogen, can produce $Mg(BH_4)_2$ as well as byproducts e.g. $LiBH_4$, B, MgH_2 (Matsunaga et al., 2008). A mixture of $MgCl_2$ and $NaBH_4$ was processed by mechano-chemical activation synthesis (MCAS) using ball-milling to form $Mg(BH_4)_2$, NaCl, and possibly $Na\text{-}Mg\text{-}BH_4$ (Varin et al., 2008). Therefore, a subsequent processing step(s) would be required to obtain pure $Mg(BH_4)_2$.

A direct synthetic route for $Mg(BH_4)_2$ from both elements: magnesium and boron at 650℃ under 150 bar hydrogen was reported by Goerrig (1958). However, a recent attempt to prepare $Mg(BH_4)_2$ by mechanically milling pure Mg and B powder, followed by heat-treatment under hydrogen, was not successful (Zhang et al., 2010), which may be due to the barriers against breaking the B–B atomic bonds and the migration of the B atoms. Thus this process has to be reproduced by further work.

Solid–gas reaction by high pressure (100 bar hydrogen) ball milling of MgB_2 and hydrogen was performed to form amorphous $Mg(BH_4)_2$ phase with a yield of approximately 50% (Pistidda et al., 2010); the measurement by solid-state NMR showed the characteristic features of $Mg(BH_4)_2$ together with other $Mg(B_nH_m)_y$ species such as $MgB_{12}H_{12}$.

3.3.1.2 Structure

The crystal structure of $Mg(BH_4)_2$ is extremely complex and high quality experimental data is crucial for an accurate crystal structure determination. As reported by Černý et al (2007), the low temperature phase of $Mg(BH_4)_2$ have hexagonal symmetry with space group $P6_1$

measured by synchrotron and neutron powder diffraction. This polymorph structure was supported by a study from an independent group (Her et al., 2007), who suggested the $Mg(BH_4)_2$ phase had complex networks of corner-sharing tetrahedra consisting of a central Mg atom and four BH_4^- units.

A first principle computational calculation with density functional theory (DFT) was performed to optimise the experimentally obtained $P6_1$ structure of $Mg(BH_4)_2$, indicating the low temperature phase could be described with a higher symmetry, space group $P6_122$ (Dai et al., 2008a). This agrees with experimental results reported by Filinchuk et al (2009a), where they contended that the symmetry of single phase $Mg(BH_4)_2$ should be $P6_122$, after locating the position of the hydrogen atoms accurately. The low temperature hexagonal phase of $Mg(BH_4)_2$ was stable until 180 °C, then transformed to the orthorhombic *Fddd* phase, which was not reversible when subsequently cooled (Filinchuk et al., 2009a; Her et al., 2007).

At room temperature, infrared and Raman vibrational spectra of pure $Mg(BH_4)_2$ showed the B-H stretching modes around 2300 cm^{-1} and the BH_4 bending modes between 1000 and 1400 cm^{-1}, which can be assigned to the bidentate binding of the BH_4^- units to the Mg^{2+} ions (Filinchuk et al., 2009a).

3.3.1.3 Dehydrogenation and rehydrogenation

As the Pauling electronegativity of Mg (1.31) is greater than that of Li (0.98), $Mg(BH_4)_2$ is expected to be less stable than $LiBH_4$ (Nakamori et al., 2007). Many studies have been carried out into the thermal decomposition of $Mg(BH_4)_2$: it can be described as following a two-step reaction (equation (3.30)) to desorb 14.9 wt% (theoretical) of hydrogen (Chlopek et al., 2007; Matsunaga et al., 2008) in the temperature range 250~550 ℃ :

$$Mg(BH_4)_2 \rightarrow MgH_2 + 2B + 3H_2 \rightarrow Mg + 2B + 4H_2 \quad (3.30)$$

However, multiple endothermic reactions were observed in the DTA curve between 300 and 370 ℃ when $Mg(BH_4)_2$ was heated (Li et al., 2008). This observation suggested the possible formation of intermediate phases. This work also reported that the dehydrogenation reaction of $Mg(BH_4)_2$ began at approximately 230 ℃, accompanied with 14.4 wt% total hydrogen desorbed at temperatures up to 530 ℃. A multi-step reaction was suggested as equation (3.31):

$$Mg(BH_4)_2 \rightarrow \text{“some intermediates”} \rightarrow MgH_2 + 2B + 3H_2 \rightarrow Mg + 2B + 4H_2 \quad (3.31)$$

The intermediate compounds formed during decomposition of $Mg(BH_4)_2$ have been identified as polyborane intermediates, including amorphous $MgB_{12}H_{12}$ and $Mg(B_3H_8)_2$ (Chong et al., 2011; Li et al., 2009; Newhouse et al., 2010; Soloveichik et al., 2009b).

Soloveichik et al. (2009b) used solid-state NMR to confirm the formation of amorphous $MgB_{12}H_{12}$ as a dehydrogenation intermediate phase. Hydrogen released from $Mg(BH_4)_2$ was found to occur in at least four steps via the formation of several polyborane intermediate species including an exothermic reaction yielding crystalline MgH_2 as an intermediate (Figure 3.5). The decomposed products might be only partially recharged after the very first step and also via the hydrogenation of Mg metal.

With a combination of experimental and theoretical studies, the formation of the intermediate compound $MgB_{12}H_{12}$ was confirmed during the decomposition of $Mg(BH_4)_2$. The full dehydrogenation and partial rehydrogenation reaction occurred based on the following multistep reaction (Li et al., 2009):

$$Mg(BH_4)_2 \rightarrow 1/6MgB_{12}H_{12} + 5/6MgH_2 + 13/6H_2 \tag{3.32}$$

$$\leftrightarrow MgH_2 + 2B + 3H_2 \tag{3.33}$$

$$\leftrightarrow Mg + 2B + 4H_2 \tag{3.34}$$

In this investigation, about 6.1 wt% of hydrogen could be rehydrided at 270 ℃ in 400 bar H_2 through the formation of the intermediate compound $MgB_{12}H_{12}$, as shown in equations (3.33) and (3.34).

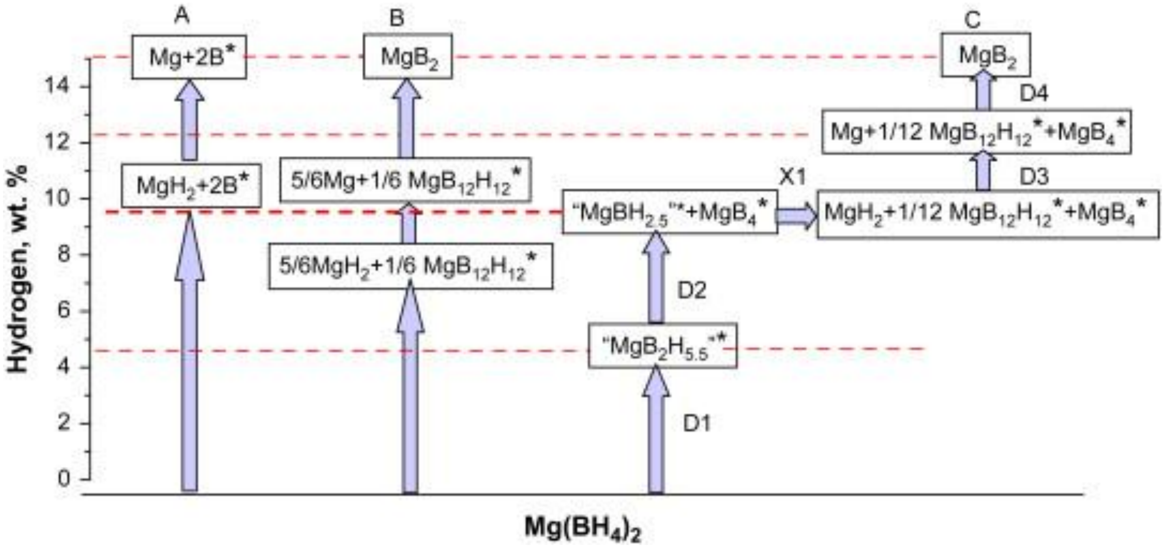

Figure 3.5 Decomposition pathways of $Mg(BH_4)_2$ (amorphous phases denoted by asterisk, observed hydrogen evolution steps marked by dashed lines) (Soloveichik et al., 2009b).

Using Raman and NMR spectroscopy, the stable amorphous $Mg(B_xH_y)_n$ intermediates, possibly including $[B_{12}H_{12}]^{2-}$ and related species were proved, further revealing that the desorbed $Mg(BH_4)_2$ sample at 300 ℃ showed an "early stage intermediate" similar to but distinct from $MgB_{12}H_{12}$, that played a key role as a precursor for its final product formation at higher temperatures, i.e. at 600 ℃ ; the material decomposed to form MgB_2 (Newhouse et al., 2010).

Using PCT, TGA/MS and NMR spectroscopy, the dominant species, $Mg(B_3H_8)_2$ as intermediate of decomposed $Mg(BH_4)_2$ was found at 200 °C although poly-borane structures ranging from the triborane anion to the dodecaborane dianion were suggested at higher temperature (>300 ℃) under a constant argon flow of 1 bar. The conversion from $Mg(BH_4)_2$ to $Mg(B_3H_8)_2$ was reversible at 250 ℃ under 122 bar H_2 (Chong et al., 2011).

A direct rehydrogenation of MgB_2 to $Mg(BH_4)_2$ with a 75 % yield was achieved at 400 ℃ under 400 bar then increasing to 950 bar of hydrogen for 108 hours, demonstrating 11 wt% of hydrogen was reversible (Severa et al., 2010b). However, further work is needed to evaluate reproducibility.

Conclusively, the decomposition pathway or mechanism of $Mg(BH_4)_2$, in particular, decomposed intermediates e.g. MgH_2, $Mg(B_xH_y)_n$, final products within Mg, B, MgB_2, depends on the temperature and atmosphere. Partial rehydrogenation can be achieved at certain temperatures under high pressure hydrogen. If thermodynamics and kinetics can be improved, $Mg(BH_4)_2$ is a promising candidate for hydrogen storage, although its decomposition mechanism(s) needs to be investigated further.

3.3.1.4 Destabilization and kinetic modification

Reducing the enthalpy of borohydride formation is critical for developing this type of material. By adding a second component, the enthalpy can be decreased by forming different decomposition products. The composites, $x\mathrm{LiBH_4}$-$(1-x)\mathrm{Mg(BH_4)_2}$ (x ranging from 0 to 1) were proposed and experimentally proved, as physical mixtures, to have a decomposition temperature much lower than those of the pure borohydrides. At $0.50 < x < 0.60$, the eutectic composition formed, starting to melt at 180 °C, followed by decomposition to release about 7 wt% of hydrogen below 270 ℃ (Bardaji et al., 2011). A theoretical study of the thermodynamics has been performed to predict the reaction enthalpy of the composites, e. g. $5Mg(BH_4)_2$-$2LiBH_4$ and $5Mg(BH_4)_2$-$Ca(BH_4)_2$ with ideal reaction enthalpies of 24.4 and 25.7 kJ/mol H_2 respectively at room temperature, and 40 kJ/mol H_2 for $Mg(BH_4)_2$ alone (Ozolins et al., 2009).

The additives can improve the kinetics and lower decomposition temperature. Compared with the as-synthesized $Mg(BH_4)_2$, a significantly reduced decomposition temperature was observed after adding $TiCl_3$ (Li et al., 2007a). Nanoconfinement and infiltration of materials into a nanoframework – e.g. $Mg(BH_4)_2$ infiltrated in scaffolds and activated carbon (Sartori et al., 2009) – is an approach that is being pursued to try to enhance sorption kinetics and thermodynamics.

3.3.2 $Ca(BH_4)_2$

3.3.2.1 Synthesis

Through the reaction of calcium chloride ($CaCl_2$) and sodium borohydride ($NaBH_4$) at room temperature in THF, an adduct $Ca(BH_4)_2\cdot(THF)_2$ was synthesized (Titov, 1964):

$$CaCl_2 + 2NaBH_4 + 2THF \rightarrow Ca(BH_4)_2\cdot(THF)_2 + 2NaCl \qquad (3.35)$$

This method has been used for the commercial production of $Ca(BH_4)_2\cdot(THF)_2$. Adduct-free $Ca(BH_4)_2$ can be obtained by heating $Ca(BH_4)_2\cdot(THF)_2$ at 160 ℃ under vacuum (Miwa et al., 2006).

The solid-state preparation method of $Ca(BH_4)_2$ has been demonstrated by either a metathesis reaction between $CaCl_2$ and Na/$LiBH_4$ using ball-milling to form a mixture of $Ca(BH_4)_2$ and Na/LiCl (Nakamori et al., 2007; Rongeat et al., 2011) or the hydrogenation of a CaH_2-MgB_2 composite at 350 °C and 140 bar hydrogen for 24 h to produce $Ca(BH_4)_2$ and MgH_2, as shown in equation (3.36) (Barkhordarian et al., 2008).

$$CaH_2 + MgB_2 + 4H_2 \rightarrow Ca(BH_4)_2 + MgH_2 \tag{3.36}$$

Nevertheless, this method produced Na/LiCl or MgH_2 as byproducts, which would then need to be separated in a second step.

A direct solid-state reaction between CaB_6 and CaH_2 was suggested for the production of $Ca(BH_4)_2$ under different conditions, with a yield of 60% at 440 ℃ under 700 bar hydrogen for 48 hours (Ronnebro and Majzoub, 2007), or with a yield of 19% at room temperature under 140 bar hydrogen for 24 hours (Rongeat et al., 2010). These studies found that catalysts e.g. TiF_3 were crucial to enhance reaction kinetics.

3.3.2.2 Structure

There are different structure modifications for the as-synthesized $Ca(BH_4)_2$, α, β or γ polymorph, depending on synthesis route and conditions. By desolvation of $Ca(BH_4)_2\cdot(THF)_2$, α-$Ca(BH_4)_2$ was presented from lab-based XRD data with space group *Fddd* (Miwa et al., 2006). However, from high-quality synchrotron powder diffraction, an actual space group of this orthorhombic structure was *F2dd* (Filinchuk et al., 2009b). As increasing temperature to about 225 ℃ , a second order transition to tetragonal *I-42d* phase occurred.

Rikto et al. (2007) found two polymorphs at room temperature: β-$Ca(BH_4)_2$ and γ-$Ca(BH_4)_2$ having tetragonal and orthorhombic unit cells. A phase transition from the low temperature γ-$Ca(BH_4)_2$ to β-$Ca(BH_4)_2$ at about 330-380 ℃ was reported. Additionally, another phase was observed during heating, possibly 'δ- $Ca(BH_4)_2$', which decomposed at 440-480 ℃ with hydrogen release.

Similar to $Mg(BH_4)_2$, the phase structure of $Ca(BH_4)_2$ is highly dependent on the synthesis route and experimental conditions. The true crystal structure of $Ca(BH_4)_2$ might not be accurately described until a single crystal of $Ca(BH_4)_2$ is available.

3.3.2.3 Dehydrogenation and rehydrogenation

The decomposition of $Ca(BH_4)_2$ was reported by Miwa et al. (2006) by equation (3.37). They found that the enthalpy change of this decomposition reaction was 32 kJ/mol H_2 according to a first-principles calculation, and a mass loss was 9.2 wt% up to 527 ℃ (by thermogravimetric analysis).

$$Ca(BH_4)_2 \rightarrow 2/3CaH_2 + 1/3CaB_6 + 10/3H_2 \tag{3.37}$$

The decomposition mechanism of $Ca(BH_4)_2$ (equation 3.37) was investigated, suggesting that $Ca(BH_4)_2$ underwent two step decomposition processes between 350 and 500 °C, as described in equation (3.38) (Kim et al., 2008b):

$$Ca(BH_4)_2 \rightarrow CaH_2 + \text{“intermediate”} \rightarrow CaH_2 + 3H_2 + 2B \text{ and/or } \alpha\text{-}CaB_6 \tag{3.38}$$

where CaH_2 and an unknown intermediate compound formed in the first step at 350-390 ℃ . The intermediate compound(s) then decomposed to form CaH_2 and amorphous B or CaB_6 in the temperature range of 400-500 ℃ , with a total mass loss about 9.0 wt%.

Due to the amorphous character of some decomposition products, it is difficult to identify all the decomposed species by a single technique, e.g. XRD. So far all the investigations show the presence of CaH_2, but have not conclusively identified the other decomposition products. Using Raman spectroscopy, the formation of CaB_6 was shown by heating $Ca(BH_4)_2$ at 330 and 480 ℃ under a static vacuum (Kim et al., 2009b). NMR measurements also indicated the presence of CaB_6 and another intermediate, possibly $CaB_{12}H_{12}$, during the decomposition of $Ca(BH_4)_2$ at 320 and 450 ℃ under vacuum (Ronnebro and Majzoub, 2007).

After $Ca(BH_4)_2$ containing $TiCl_3$ (molar ratio: 1:0.05) as a catalyst was dehydrogenated at 420 ℃ under vacuum, it was possible to rehydrogenate the material under 90 bar hydrogen at 350 ℃ for 24 hours to give a 3.8 wt% hydrogen content (Kim et al., 2008a). If doped with NbF_5, the rehydrided hydrogen content increased to about 5.0 wt% at 420 ℃ under 90 bar hydrogen for 24 hours (Kim et al., 2008c). After the decomposition of $Ca(BH_4)_2$ at 360 ℃ , without additives, only 1 wt% of hydrogen was rehydrogenated at 350 ℃ under 120 bar hydrogen; with catalysts, however, up to 3.5 wt% of hydrogen was rehydrogenated within an hour at 350 ℃ under 120 bar hydrogen (Ronnebro and Majzoub, 2008). Therefore, it can be said that the experimental conditions and use of catalysts are important for controlling the reversibility of $Ca(BH_4)_2$.

3.3.2.4 Destabilization and kinetic modification

Lee et al (2009) reported a systematic study of the $x\mathrm{LiBH_4}$-$(1\text{-}x)\mathrm{Ca(BH_4)_2}$ composite system (x ranges from 0 to 1). Their study found that the post-milled samples were physical mixtures of the constituent phases, which underwent a eutectic melting at ~ 200 ℃ and eutectic composition lies between $x = 0.6$ and 0.8. The decomposition temperature was lower than those for both the pure $LiBH_4$ and $Ca(BH_4)_2$. For example, the composite with $x = 0.4$

decomposed at below 400 °C releasing 10 wt% of hydrogen. Mechanically milling a 1:1 $LiBH_4$-$Ca(BH_4)_2$ mixture formed a dual-cation borohydride, $Li_{0.9}Ca(BH_4)_{2.9}$, which then transformed to stoichiometric $LiCa(BH_4)_3$ in the heating process. $LiCa(BH_4)_3$ exhibited improved de/rehydrogenation properties relative to both binary phases, indicating the effectiveness of dual-cation combinations for destabilizing the binary $LiBH_4$ and $Ca(BH_4)_2$ phases (Fang et al., 2010a).

It is well known that additives can enhance the thermodynamics and kinetics of the de/re-hydrogenation process. At 360 ℃ with 2 mol% dopant, $Ca(BH_4)_2$ decomposed rapidly (within 20 min) with about 7 wt% hydrogen evolution, but only released 5.5 wt% without additives (Ronnebro and Majzoub, 2008). Adding a small amount of Ti and Nb halides into $Ca(BH_4)_2$ lowered the decomposition temperature by forming different decomposition products, e.g. if doped with NbF_5 the decomposition product was $CaH_{2-x}F_x$, not CaH_2, and improved rehydrogenation properties of $Ca(BH_4)_2$ were also observed (Kim et al., 2008c).

3.4 Typical transition metal borohydrides

3.4.1 Introduction

Transition metals are classified as the metals in the d-block of periodic table. Borohydrides formed from transition metals with an electronegativity between 1.2 and 1.6 are expected to be promising candidates for hydrogen storage (Nakamori et al., 2007). The following review will focus on the most actively studied transition metal borohydride compounds that have been considered for hydrogen storage.

A typical synthetic route to transition metal borohydrides in early works (1940's-1980's) is based on a metathesis reaction between Li/$NaBH_4$ and MCl_n in an appropriate solvent such as diethyl ether or THF. However, unlike alkaline earth metal borohydrides, the removal of solvent by heat treatment tends to cause the decomposition of these transition metal borohydrides due to their relatively low dissociation temperatures.

3.4.2 Scandium-based borohydride

The solid scandium borohydride-solvent adduct ($Sc(BH_4)_2.THF$) has been prepared by the treatment of anhydrous $ScCl_3$ with a slight excess of $LiBH_4$ in THF at room temperature, and it was found that the volatile product readily sublimed at 80 ℃ (Marks and Kolb, 1977). $Sc(BH_4)_2\cdot DME$ prepared via a two-stage process (equations (3.39) and (3.40)) was reported by Makhaev et al (1984), where $ScCl_3$ and $NaBH_4$ in dimethylether (DME) were stirred for 10 h at room temperature, then heated to 100 ℃ for 5 h:

$$ScCl_3 + 4NaBH_4 + 4DME \rightarrow NaSc(BH_4)_4\cdot 4DME \tag{3.39}$$

$$\rightarrow NaBH_4 + Sc(BH_4)_3\cdot DME + 3DME \tag{3.40}$$

They found that the product melted at 97-107 ℃, accompanied by solvent loss and thereafter decomposed at 162 ℃.

Ball-milling has been employed to synthesize scandium borohyride by Nakamori et al (Nakamori et al., 2007; Nakamori et al., 2006). They proposed that the product from metathesis reaction between $3LiBH_4$ and $ScCl_3$ was the borohydride compound ($Sc(BH_4)_3$) and the thermal decomposition of the resulting product occurred at around 256 ℃ with a mass loss of 4.2 wt% which was less than the theoretical gravimetric hydrogen density of the mixture (5.6 wt%). Using vibrational spectrascopy and high-resolution synchrotron powder X-ray diffraction (SR-PXD) combined with theoretical calculations, the resulting product was suggested to be the ternary borohydride ($LiSc(BH_4)_4$) instead of $Sc(BH_4)_3$, and the crystal structure of $LiSc(BH_4)_4$ obtained by high-resolution SR-PXD revealed a tetragonal unit cell with a = 6.076 Å and c = 12.034 Å space group *P-42c* (Hagemann et al., 2008). This ternary borohydride ($LiSc(BH_4)_4$) was also identified by magic angle spinning (MAS) NMR technique (Hwang et al., 2008). Further study on this borohydride compound showed a modified formation reaction process as follows:

$$4ScCl_3 + 12LiBH_4 \rightarrow 3LiSc(BH_4)_4 + Li_3ScCl_6 + 6LiCl \qquad (3.41)$$

Upon heating this material to 400 °C, this material released about 6.4 wt% of the initial hydrogen content, and the identified desorption products (by NMR) were mainly amorphous ScB_2, B, ScH_2, and $Li_2(B_{12}H_{12})$ compounds besides LiCl (Kim et al., 2009a).

Two other scandium-based borohydrides ($NaSc(BH_4)_4$ and $KSc(BH_4)_4$) were successfully prepared by Černý et al through ball-milled mixtures of ABH_4 (A=Na, K) and $ScCl_3$, and the formation reaction was proposed as follows (Černý et al., 2010b; Černý et al., 2010c):

$$4ABH_4 + 2ScCl_3 \rightarrow ASc(BH_4)_4 + A_3ScCl_6 \qquad (3.42)$$

These new compounds $ASc(BH_4)_4$ crystallized in the orthorhombic crystal system with the space group symmetry *Cmcm* (a = 8.170(2) Å, b = 11.875(3) Å, c = 9.018(2) Å, V = 874.9(3) $Å^3$) for $NaSc(BH_4)_4$ and with space group symmetry *Pnma* (a = 11.856(5) Å, b = 7.800(3) Å, c = 10.126(6) Å, V = 936.4(8) $Å^3$) for $KSc(BH_4)_4$. The $NaSc(BH_4)_4$ compound was found to be stable up to 140 °C, where it started melting, followed by the evolution of hydrogen in two rapidly occurring steps between 170-220 and 225-370 °C. Similarly, $KSc(BH_4)_4$ was stable from RT up to about 130 ℃, where the compound melted and then released hydrogen in two rapid steps approximately at 190-230 ℃ and 240-320 ℃. Furthermore, the hydrogen release involved the formation of KBH_4, which reacted with K_3ScCl_6 and formed a solid solution, $K(BH_4)_{1-x}Cl_x$. Therefore, the bimetallic alkaline (Li, Na, and K) scandium borohydrides allow the hydrogen desorption temperature of the stable alkali metal borohydrides to be decreased.

3.4.3 Yttrium-based borohydride

Earlier work to prepare yttrium borohydride was centred on a wet chemical reaction between $LiBH_4$ and YCl_3 in THF, producing $YCl(BH_4)_2$ that can be decomposed to form $Y(BH_4)_3$ at 100-200 ℃ (Marks and Kolb, 1977).

Yttrium borohydride ($Y(BH_4)_3$) has been synthesized via metathesis reaction (equation (3.43)) in a solvent free-crystalline phase with *Pa-3* cubic symmetry (Sato et al., 2008):

$$YCl_3 + 3LiBH_4 \rightarrow Y(BH_4)_3 + 3LiCl \tag{3.43}$$

In this structure, Y^{3+} cation, in a highly distorted octahedral environment, was coordinated to six nearest neighbours.

Jaron and Grochala (2010) have recently tested fourteen different synthetic approaches towards pure solvent-free $Y(BH_4)_3$, including wet chemical methods with different initial reaction agents in variety solvents, as well as mechanochemical solid/solid reaction approaches with different precursors. Only the solid-state reaction between $LiBH_4$ and YCl_3 led to the expected product and LiCl. An attempted separation of $Y(BH_4)_3$ from the mixture, however, has failed to deliver the pure compound .

By using SR-PXD and MAS NMR spectroscopy, it was found that under moderate hydrogen pressure, heat treatment at 180 ℃ led to the phase transformation of $Y(BH_4)_3$ from a primitive cubic room-temperature phase (α-$Y(BH_4)_3$) to a high-temperature phase (β-$Y(BH_4)_3$) with a cubic crystal structure in the *Pm-3m* space group (Ravnsbaek et al., 2010a).

An attempt has been made to form new mixed metal borohydrides ($LiY(BH_4)_4$) by ball-milling and cryo-milling YCl_3-$LiBH_4$ with a 1:4 molar ratio, rather $Y(BH_4)_3$ was obtained according to equation (3.43) with unreacted $LiBH_4$ (Frommen et al., 2010), which existed in a low temperature modification. This study reported that the phase transition of the prepared $Y(BH_4)_3$ compound to a high-temperature phase (space group *Fm-3c*) took place at 202 ℃ under 100 bar deuterium.

The thermal decomposition process of the $Y(BH_4)_3$ compound has been investigated by a number of research groups. The dehydrogenation reaction of $Y(BH_4)_3$ isolated from the mixture ($Y(BH_4)_3$-3LiCl) by solvent started at appropriately 187 ℃ , with a total mass loss of 7.8 wt% observed up to 500 ℃ with only hydrogen evolution. The reaction proceeded via multistep dehydriding processes, accompanied by the formation of intermediate phases (Yan et al., 2009). Another study showed that the slow thermal decomposition of $Y(BH_4)_3$ started slightly above 145 ℃ with a significant acceleration of hydrogen evolution above 200 ℃ . Hydrogen release during thermal decomposition was accompanied by various boron hydrides, which were identified by mass spectroscopy and IR spectroscopy (Jaron and Grochala, 2010).

Investigation of the decomposition mechanism showed that, upon heating to 190 ℃ , $Y(BH_4)_3$ decomposed to YH_3, which transformed to YH_2 at 270 ℃ . The final decomposition product was found to be YB_4 and amorphous boron containing compounds (Ravnsbaek et al., 2010a). In-situ SR-PXD measurements showed the occurrence of an intermediate phase during the thermal decomposition in the temperature range of 200-250 ℃ with presumed orthorhombic symmetry (Frommen et al., 2010).

3.4.4 Titanium-based borohydride

Titanium borohydride ($Ti(BH_4)_3$) was prepared by the reaction of a two-fold excess of $LiBH_4$ with $TiCl_4$ vapour, as described in equation (3.44) (Hoekstra and Katz, 1949) or by the mechanochemical reaction of solid $LiBH_4$ with $TlCl_3$, as shown in equation (3.45) (Volkov and Myakishev, 1992).

$$2TiCl_4 + 8LiBH_4 \rightarrow 2Ti(BH_4)_3 + 8LiCl + B_2H_6 + H_2 \qquad (3.44)$$

$$TiCl_3 + 3LiBH_4 \rightarrow Ti(BH_4)_3 + 3LiCl \qquad (3.45)$$

There are few reports regarding the structure of the $Ti(BH_4)_3$ compound, as this compound was reported to be volatile and highly air sensitive, and decomposed autocatalytically at room temperature even under inert atmosphere (Hoekstra and Katz, 1949; Marks and Kolb, 1977).

3.4.5 Zirconium-based borohydride

Zirconium borohydride ($Zr(BH_4)_4$) was first produced in 1949 by the reaction of aluminium borohydride with an excess of double salt $NaZrF_5$ in ether solution via the reaction (equation 3.46) (Hoekstra and Katz, 1949):

$$2Al(BH_4)_3 + NaZrF_5 \rightarrow Zr(BH_4)_4 + 2AlF_2BH_4 + NaF \qquad (3.46)$$

Another formation procedure for $Zr(BH_4)_4$ was proposed by Reid et al (1957) using $ZrCl_4$ and an excess of $LiBH_4$ as precursors based on the equation (3.47), with 75% yield:

$$ZrCl_4 + 4LiBH_4 \rightarrow Zr(BH_4)_4 + 4LiCl \qquad (3.47)$$

However, experimental attempts to synthesize $Zr(BH_4)_4$ by this procedure were unsuccessful (Reid et al., 1957). This synthetic method was developed by Volkov et al (1999) who indicated that $Zr(BH_4)_4$ could be formed from $LiBH_4$ or $NaBH_4$ by an exchange reaction (equation 3.47) using rotational mills: very fast formation kinetics and a 90% yield for $Zr(BH_4)_4$ were achieved when $LiBH_4$ was used instead of $NaBH_4$. In recent years, by mechanochemical reaction between $NaBH_4$ and $ZrCl_4$, the $Zr(BH_4)_4$ compound was produced at room temperature under vacuum, reaching yields of 55% (Gennari et al., 2009).

It was found that $Zr(BH_4)_4$ was volatile and had a melting point around room temperature (28-32 ℃). On heating this compound decomposed at 160 ℃ from the gas-phase, indicating the evolution of B_2H_6 with H_2, and a thermal decomposition can be described as follows (Gennari et al., 2009):

$$Zr(BH_4)_4\ (s, g) \rightarrow Zr(BH_4)_4\ (l, g) \tag{3.48}$$

$$\rightarrow ZrB_2(s) + B_2H_6\ (g) + 5H_2\ (g) \tag{3.49}$$

The vapour-phase IR spectra was performed to investigate the structure of $Zr(BH_4)_4$ compound, indicating the borohydride groups were bonded to the Zr metal atom by bridging hydrogen atoms, which was deduced from the presence of a band at 2200-2000 cm^{-1} in the IR spectrum (James et al., 1966).

3.4.6 Hafnium-based borohydride

Hafnium borohydride has very similar physicochemical properties to the $Zr(BH_4)_4$ compound, such as high volatility, and a low melting point of 29 °C (Hoekstra and Katz, 1949; Marks and Kolb, 1977). The bonding in $Hf(BH_4)_4$ involving bridging hydrogen atoms, is expected to be in the chemical character between the ionic $NaBH_4$ and the covalent borohydride $Al(BH_4)_3$ (James et al., 1966).

Although the first synthesised $Hf(BH_4)_4$ compound was reported in 1949 (Hoekstra and Katz, 1949), unfortunately, the thermal decomposition of this compound could not be performed due to its low boiling point of 118 ℃ (Nakamori et al., 2006). When allowed to stand at room temperature the material, similar to $Zr(BH_4)_4$, slowly decomposed, releasing hydrogen.

3.4.7 Zinc-based borohydride

The preparation of zinc borohydride $Zn(BH_4)_2$ has been reported by mixing $ZnCl_2$ and $LiBH_4$ (molar ratio of 1:2) in diethylether at room temperature (Wiberg and Henle, 1952), and by mechanically milling $NaBH_4$ with $ZnCl_2$ under an inert atmosphere (Maltseva et al., 1989). The synthetic route (equation (3.50)) has recently been further developed (Jeon and Cho, 2006; Srinivasan et al., 2008).

$$ZnCl_2 + 2NaBH_4 \rightarrow Zn(BH_4)_2 + 2NaCl \tag{3.50}$$

It was shown that the $Zn(BH_4)_2$ within the milled material (which also contained NaCl), started to decompose at 85 °C and completed at 140 °C with a total mass loss of 12.1 wt%, which was much higher than the expected 3.8 wt% based on the complete dehydrogenation (shown in equation 3.51) of $Zn(BH_4)_2$ in the milled mixture. By combination with mass spectrometric results, it was shown that hydrogen evolution was accompanied by a significant amounts of diborane. Decomposition was suggested via equation (3.52) (Jeon and Cho, 2006):

$$Zn(BH_4)_2 \rightarrow Zn + 2B + 4H_2 \tag{3.51}$$

$$Zn(BH_4)_2 \rightarrow Zn + B_2H_6 + H_2 \tag{3.52}$$

A slightly lower mass loss of 8.4 wt% was observed at 100 °C for $Zn(BH_4)_2$ within the milled material prepared according to equation (3.50), and this mass loss reduced with increasing milling duration, probably owing to the partial release of hydrogen during the milling process (Srinivasan et al., 2008). In addition, this study showed that Ni-nanocatalyzed $Zn(BH_4)_2$ exhibited a decrease in thermal decomposition temperature at least by 20-40°C.

There is no structural information on $Zn(BH_4)_2$ though unknown XRD peaks were assigned to $Zn(BH_4)_2$ in a previous study (Jeon and Cho, 2006). Recent studies have shown that, based on ball milling of $ZnCl_2$ and ABH_4 (A = Li, Na or K) with different molar ratios, a series of zinc-based borohydride compounds can be prepared with a variety of compositions and structures (Černý et al., 2010a; Ravnsbaek et al., 2009; Ravnsbaek et al., 2010b). The formation can be described by equations (3.53)-(3.55):

$$2ZnCl_2 + 5ABH_4 \rightarrow AZn_2(BH_4)_5 + 4ACl \ \ (A=Li, Na) \tag{3.53}$$

$$ZnCl_2 + 3NaBH_4 \rightarrow NaZn(BH_4)_3 + 2NaCl \tag{3.54}$$

$$ZnCl_2 + KBH_4 \rightarrow KZn(BH_4)Cl_2 \tag{3.55}$$

In equation (3.53), the formation of the ternary chloride A_2ZnCl_4 from ACl and $ZnCl_2$ was also observed. In these studies, authors reported that the crystal structure and thermal decomposition properties had large diversity between these compounds. SR-PXD was performed to identify the crystal structure of these materials as $LiZn_2(BH_4)_5$ in space group *Cmca*, $NaZn_2(BH_4)_5$, $NaZn(BH_4)_3$ and $KZn(BH_4)Cl_2$ in space group $P2_1/c$.

Additionally, these investigations showed that the decomposition of $AZn_2(BH_4)_5$ occurred at 127 °C for $LiZn_2(BH_4)_5$ and 95 °C for $NaZn_2(BH_4)_5$ through several coupled reactions:

metallic zinc and ABH_4 formed, then simultaneous reaction of ABH_4 with A_2ZnCl_4 to form metallic zinc and ACl, which overall could be described by the reaction below (equation (3.56)) (Ravnsbaek et al., 2009):

$$2AZn_2(BH_4)_5 + A_2ZnCl_4 \rightarrow 5Zn + 4ACl + 5B_2H_6 + 5H_2 \qquad (3.56)$$

In terms of the $KZn(BH_4)Cl_2$ compound, it was found that the decomposition occurred at 110 °C to form metallic Zn, K_2ZnCl_4 and an intermediate phase that existed within a narrow temperature range between 110 and 130 ℃ , then dissociated to metallic Zn and K_2ZnCl_4 at 130 °C, with a higher observed mass loss than the equivalent theoretical hydrogen content. Thus a total thermal decomposition reaction of $KZn(BH_4)Cl_2$ was expressed as follows (Ravnsbaek et al., 2010b):

$$2KZn(BH_4)Cl_2 \rightarrow K_2ZnCl_4 + Zn + 2/n(BH_3)_n + 2H_2 \qquad (3.57)$$

3.5 Manganese -based borohydride

Manganese borohydride ($Mn(BH_4)_2$) has a theoretical hydrogen content of 9.5 wt% and manganese has an electronegativity of 1.55, which is a little lower than that of zinc (1.6). It is predicted that manganese borohydride may have satisfactory thermodynamic properties for hydrogen storage (Nakamori et al., 2007), such as stability at room temperature, a low decomposition temperature, but less diborane release during thermal decomposition.

Earlier work on the synthesis of manganese borohydride was based on exchange reactions in solvent solution, for example through the reaction of manganese chloride with lithium borohydride in anhydrous ether to form $Mn(BH_4)_2$ solution (Monnier, 1957) or with sodium borohydride in THF solution to form $Mn(BH_4)_2(THF)_3$ (Makhaev et al., 1987). However, attempts to desolvate $Mn(BH_4)_2(THF)_3$ resulted in decomposition, as the removal of the THF occurred at nearly the same temperature.

The solvent-free synthesis of the materials through ball-milling appears to be a very simple and efficient approach. As with other transition metal borohydrides, this preparation involves a complete or incomplete exchange reaction between alkali borohydrides and manganese chloride ($MnCl_2$), as shown in equation (3.58):

$$MnCl_2 + (2+x)ABH_4 \rightarrow A_xMn(BH_4)_{2+x} + 2ACl \quad \text{(A: alkali metals)} \tag{3.58}$$

Assuming a complete exchange reaction in equation (3.58), Nakamori et al. (2007) reported the thermodynamic stability of a series of metal borohydrides, in which manganese borohydride $Mn(BH_4)_2$ was presumed to have formed. The decomposition temperature for the proposed $Mn(BH_4)_2$ compound, formed from a $MnCl_2$-$LiBH_4$ mixture, started at around 130 °C and finished at 180 °C with a larger mass loss than the theoretical hydrogen density of the $Mn(BH_4)_2$-LiCl mixture, due to the release of both hydrogen and diborane.

In the FY 2007 annual progress report of the DOE hydrogen program, Jensen et al. (2007) reported that, according to the reaction in equation (3.58), alkali manganese borohydrides such as $AMn(BH_4)_3$ (A = Li, Na) could be prepared by mechanochemical synthesis. These complexes were stable at room temperature and released hydrogen at about 100 °C with little or no diborane production. These findings were supplemented by Choudhury et al. (2009b), who proposed the formation of $LiMn(BH_4)_3$ through the ball milling of $LiBH_4$ and $MnCl_2$ in the molar ratio of 3:1 for 20-30 minutes under nitrogen in spite of no direct evidence for this structure. This compound was reported to release 8.0 wt% of hydrogen between 135 and 155 °C in a single dehydrogenation reaction step with no mention of the evolution of diborane.

However, an investigation on the crystallographic and spectroscopic characteristics by Černý et al. (2009) showed that the material resulted from ball milling of $MnCl_2$ and $LiBH_4$ could be formulated as $Mn(BH_4)_2$ with a trigonal crystal structure, (space group $P3_112$) and existed between -183 and 177 °C (as shown in Figure 3.6). By using SR-PXD, together with Raman and IR spectroscopy, the authors observed that $Mn(BH_4)_2$ had a similar structure and bonding to that of α-$Mg(BH_4)_2$.

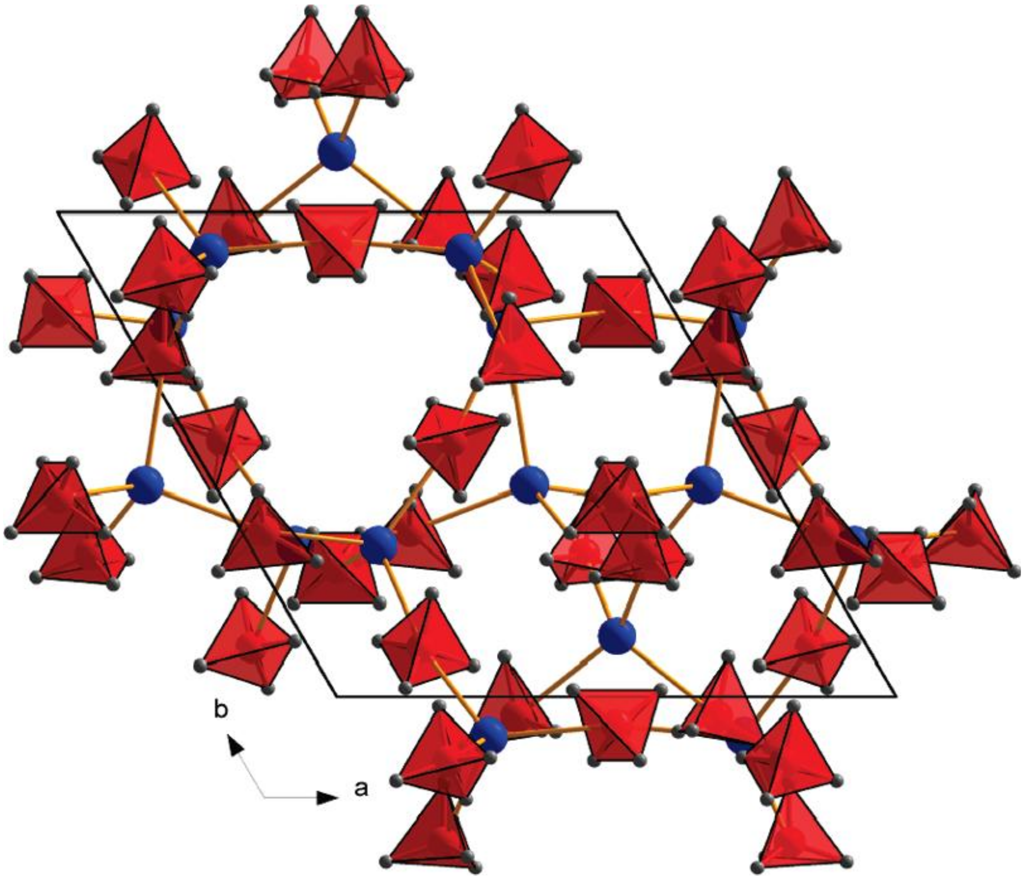

Figure 3.6 Crystal structure of $Mn(BH_4)_2$ viewed along the c-axis, showing the coordination of Mn atoms (blue) by BH_4 tetrahedra (red) (Černý et al., 2009).

Calculation for $Mn(BH_4)_2$ using DFT (Figure 3.7) (Choudhury et al., 2009a), suggested that a structure *I-4m2* symmetry was stable for this compound with an estimated formation enthalpy of -28.93 kJ/f.u. at -273 °C, which is not in agreement with the experimental results reported by Černý et al (2009). In addition, according to the calculated Gibbs energy, the most energetically favourable dehydrogenation of $Mn(BH_4)_2$ should follow equation (3.59), which was endothermic reaction at decomposition, releasing hydrogen without diborane:

$$Mn(BH_4)_2 \rightarrow Mn + 2B + 4H_2 \tag{3.59}$$

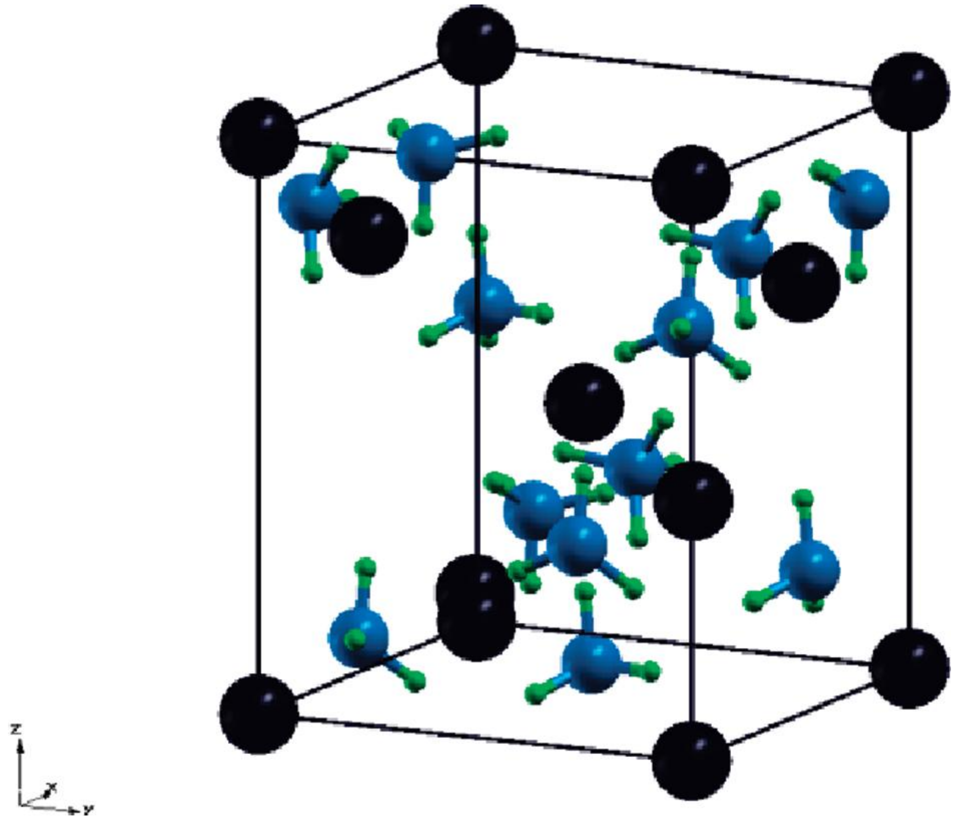

Figure 3.7 Three-dimensional crystal structures of $Mn(BH_4)_2$ with space group I-4m2 (black, blue, and green spheres represent Mn, B, and H atoms, respectively) (Choudhury et al., 2009a)

Further efforts have been made to clarify the nature of manganese-based borohydride prepared from the mechanochemical reaction between ABH_4 and $MnCl_2$, including the structure and thermal decomposition properties. Varin and Zbroniec (2010) reported that a $3LiBH_4$-$MnCl_2$ mixture, milled for 30 minutes in ultra-high purity hydrogen, only showed XRD peaks for LiCl, suggesting that an amorphous or disordered borohydride had formed.

Under 1 bar hydrogen, the milled mixture desorbed 4.0 wt% H_2 at 100 °C in 6 h, and 4.5 wt% H_2 at 120 ℃ in 2 h. They also claimed that a weak X-ray diffraction peak at around 20° 2θ was due to an impurity in the commercial $LiBH_4$.

A study of manganese-based borohydrides by thermal desorption, vibrational spectroscopy in conjunction with DFT calculations supported the results obtained by Černý et al (2009). They revealed that the reaction of $LiBH_4$ with $MnCl_2$ produced $Mn(BH_4)_2$ rather than $LiMn(BH_4)_3$, whereas the mechanochemical reaction of $NaBH_4$ with $MnCl_2$ led to the formation of a species that was chemically distinct from $Mn(BH_4)_2$. A comparison of the calculated and experimental IR spectra suggested that the product was an amorphous $Na_2Mn(BH_4)_4$ compound with bidentate binding of BH_4^- to the Mn center, or possibly another species (Severa et al., 2010a).

In summary, the formation process, structural characteristics and hydrogen storage properties of manganese-based borohydride complexes as a function of different precursors are unclear. Therefore, in order for the hydrogen storage potential of manganese-based borohydride materials to be evaluated, manganese-based borohydrides need to be prepared with different precursors, and their structural and decomposition properties need to be understood in detail so as to try to facilitate the development of reversible hydrogen sorption reaction pathways.

3.6 Aims and objectives of the project

The purpose of this project is to develop transition metal borohydride compounds for use as solid state hydrogen storage media in vehicular hydrogen stores. There are three specific objectives:

- To synthesize manganese-based borohydride compounds via the metathesis reaction between available alkali metal borohydrides ABH_4 (A = Li, Na, K) and manganese chlorides using a mechanochemical ball milling process. The preparation parameters such as starting materials, reactant ratio and reaction time, will be evaluated and optimized. The characterization of the milled products by various analytical techniques will be performed to identify crystal structure and molecular vibration properties of the newly developed borohydride materials.
- To investigate thermal decomposition behaviour in terms of thermogravimetric and calorimetric properties so as to understand the mechanism of decomposition. The comparison of hydrogen storage properties including decomposition temperature and gravimetric hydrogen density within a series of manganese-based compounds will be undertaken. The additives to the material system will be chosen to improve the dehydrogenation kinetics and thermodynamics of the materials.
- To identify the decomposition products of the milled materials in depth by *in-situ* measurement techniques. In conjunction with thermal decomposition properties, models for the dehydrogenation mechanism(s) of the milled materials will be presented so as to assist in the design and optimization of synthetic routes to obtain modified materials with superior properties.

Chapter 4 Experimental Techniques

This chapter is divided into five sections: 4.1) preparation of manganese-based borohydride compounds; 4.2) characterization of prepared materials; 4.3) thermogravimetric and calorimetric analysis; 4.4) investigation of decomposition processes; and 4.5) possible recombination of decomposed borohydride compounds. The employed techniques and the five experimental sections are shown in Figure 4.1.

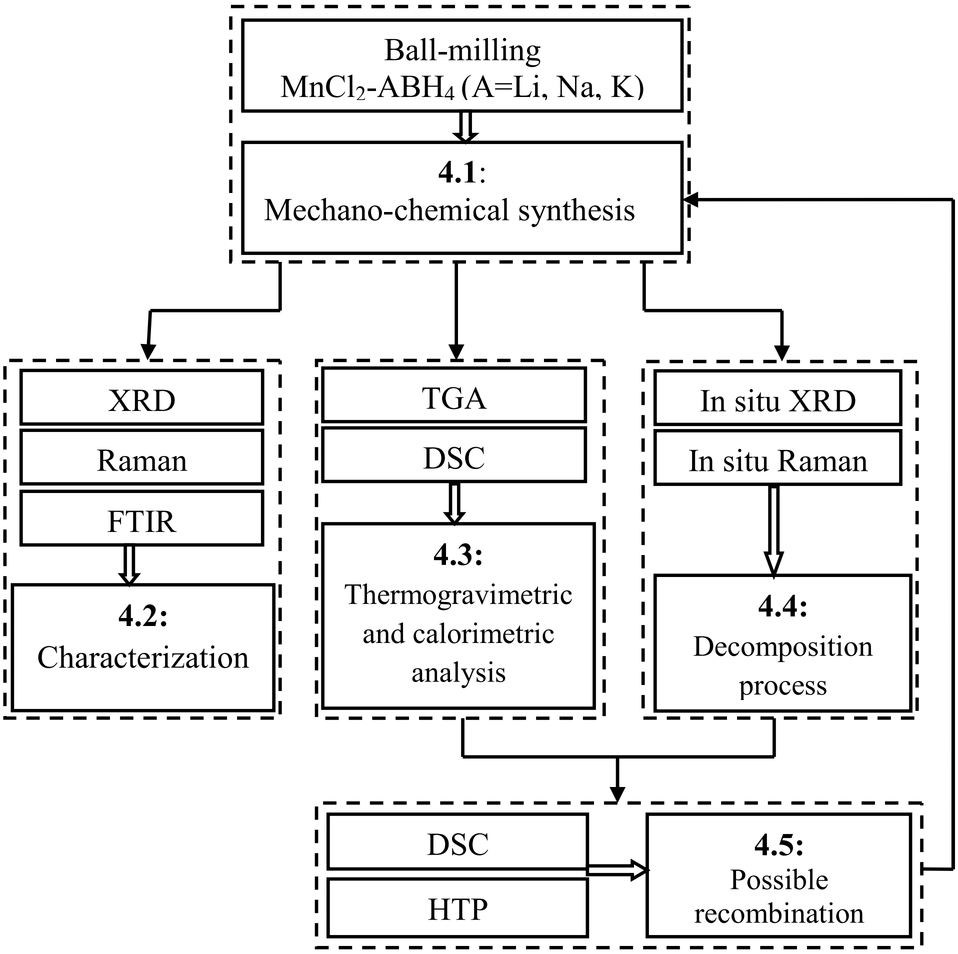

Figure 4.1 Diagram of experimental sections and techniques used

All the materials and prepared samples were stored and handled in an argon (99.99% purity) filled glovebox. The level of water and oxygen in the glovebox was kept below 0.1 ppm, and the hydrogen level less than 0.1%. All the operations were performed in a glovebox, as the materials are sensitive to air. The precursor materials and catalytic additives (Table 4.1) were used without pre-treatment or further purification.

Table 4.1 Starting materials and catalytic additives

Materials	Purity	Description		Manufacturer
$LiBH_4$	95 %	Powder, 30 mesh, MW 21.78	Precursor materials	Sigma-Aldrich
$NaBH_4$	99.99 %	Granular, MW 37.83		Sigma-Aldrich
KBH_4	≥98%	Powder, MW 53.94		Sigma-Aldrich
Anhydrous $MnCl_2$	99.999%	Beads, 10 mesh, MW 125.84		Sigma-Aldrich
Manganese (Mn)	≥99%	Powder, 50 mesh, MW 54.94	Catalytic additives	Sigma-Aldrich
Nickel (Ni)	99.99%	Powder, <150 μm, MW 58.69		Sigma-Aldrich
Titanium (Ti)	99.7%	Powder, 100 mesh, MW 47.87		Sigma-Aldrich
Titanium chloride ($TiCl_3$)	99.995 %	Powder, MW 154.23		Sigma-Aldrich
Niobium fluoride (NbF_5)	98%	Powder, MW 187.90		Sigma-Aldrich

4.1 Synthesis of Mn-based borohydrides

Attempts were made to synthesize Mn-based borohydride compounds according to the complete or incomplete exchange reaction between alkali borohydrides and manganese chloride, as shown in equation (3.58), by mechano-chemical ball-milling.

The planetary ball-mill is a horizontal rotating device transmitted by the outer gear. A grinding bowl sits on a grinding platform and rotates in a direction opposite to the direction of the base fixture. The centrifugal force drives the balls through superimposed rotational movements to impact with the materials. The schematic cross-section diagram of the planetary ball-mill is illustrated in Figure 4.2. The difference in speeds between the balls and grinding bowl results in an interaction between frictional and impact forces, which produces high dynamic energies for size reduction, mixing and particle shape change.

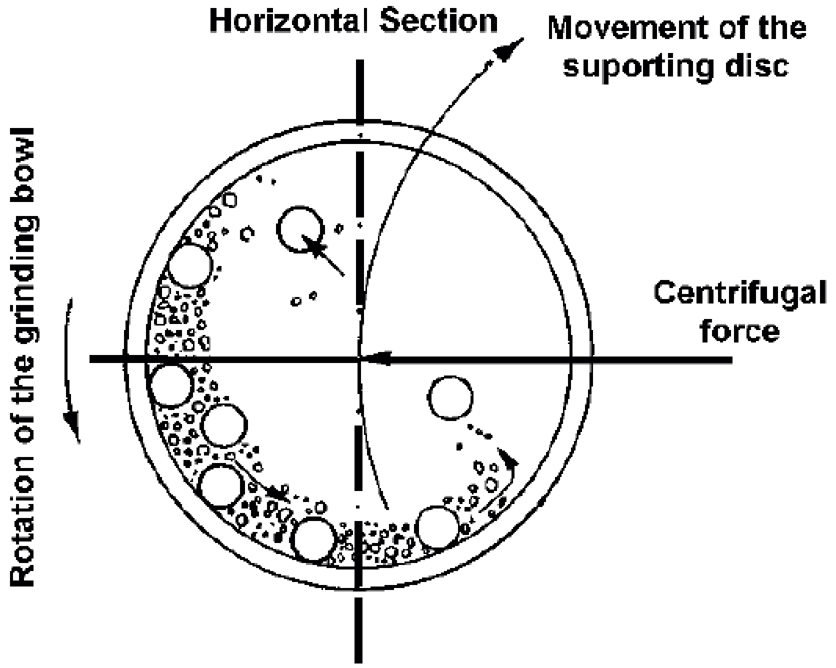

Figure 4.2 Schematic cross-section of a planetary ball mill (ILPI, 2012)

A 6 g mixture of ABH_4 (A=Li, Na or K) and $MnCl_2$ in 2:1 or 3:1 molar ratios was put in a stainless steel milling bowl (250 ml) and sealed under argon with a lid using a Viton O-ring. The mass ratio of the stainless steel balls (14 mm diameter) to powder was approximately 32:1. At room temperature, the mixture was milled using a Retsch PM400 Planetary Ball Mill at 175 rpm. In order to reduce the heating of the powder mixture due to friction during the milling process, milling was carried out in N×10 (N = 1, 3, 6, 12, 24, 36 or 60) minute durations separated by 10 minute rest intervals, giving total milling times of 10, 30, 60, 120, 240, 360 and 600 minutes. A small amount of milled samples from each milling time was taken for further characterization.

Additives of 2 mole % of Ni, Ti, $TiCl_3$ or NbF_5 were added to $2LiBH_4$-$MnCl_2$ mixture prior to milling for 360 minutes, in an attempt to influence the thermal decomposition properties of the materials. The prepared samples are summarized in Table 4.2.

Table 4.2 Summary of all ball-milled samples

Milling time (minutes)	xLiBH$_4$-MnCl$_2$		xNaBH$_4$-MnCl$_2$		xKBH$_4$-MnCl$_2$	Techniques used
	$x = 2$	$x = 3$	$x = 2$	$x = 3$	$x = 2$	
10	V	V				XRD, Raman, TGA, DSC
30	V	V	V	V	V	XRD, Raman, TGA, DSC
60	V	V	V	V	V	XRD, Raman, TGA, DSC
120	V	V	V	V	V	XRD, Raman, TGA, DSC
240	V	V	V	V	V	XRD, Raman, TGA, DSC
360 without additives	V	V	V	V	V	XRD, Raman, TGA, DSC, *in-situ* XRD, FTIR, *in-situ* Raman
360 with additives	V					XRD, Raman, TGA, DSC
600			V			XRD, Raman, TGA, DSC

4.2 Characterization of milled samples

4.2.1 X-ray diffraction

X-ray Powder Diffraction (XRD) is a powerful analytical technique to characterize and identify the crystallographic structure of phases in a material. It is based on the constructive interference of monochromatic X-rays from a crystalline material. X-rays are electromagnetic radiation with a much shorter wavelength than UV light and longer than gamma rays. X-rays are generated in a cathode ray tube by heating a filament to produce electrons that can be accelerated by high voltage towards a metal target. When electrons have sufficient energy to dislodge inner shell electrons of the metal target material, X-rays are produced, then filtered to produce monochromatic radiation, collimated to create a parallel beam and directed toward the sample.

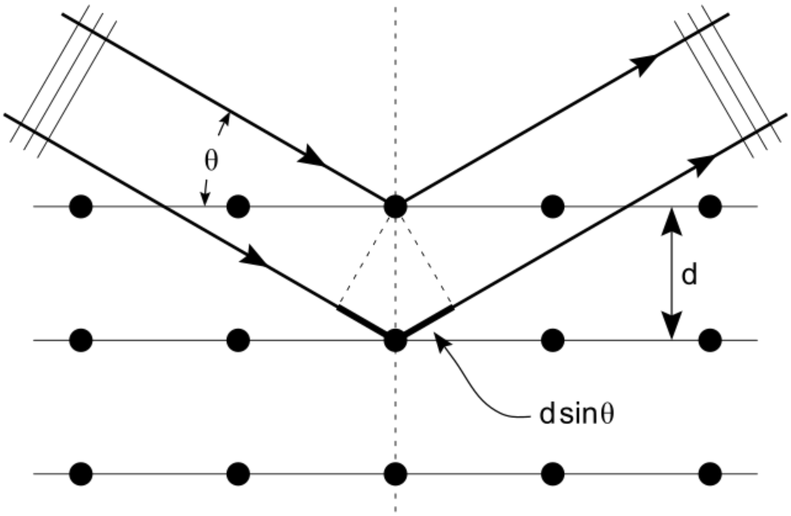

Figure 4.3 Diffraction of X-rays

Figure 4.3 shows the diffraction of X-rays by a crystal lattice. The principle of XRD analysis is based on Bragg's law. To obtain diffraction (constructive interference), the path length difference of two parallel beams, which is $2 \cdot d \cdot \sin\theta$, must be a multiple of the wavelength λ, given by Bragg's equation (4.1):

$$2 \cdot d \cdot \sin\theta = n \cdot \lambda \tag{4.1}$$

where n is an integer, λ is the wavelength of the incident X-ray, d is the spacing between the lattice planes, and θ is the angle between the incident x-ray and lattice planes.

In this work, the crystalline properties of mechano-chemically milled samples were investigated using a Bruker D8 Advance Diffractometer, as shown in Figure 4.4.

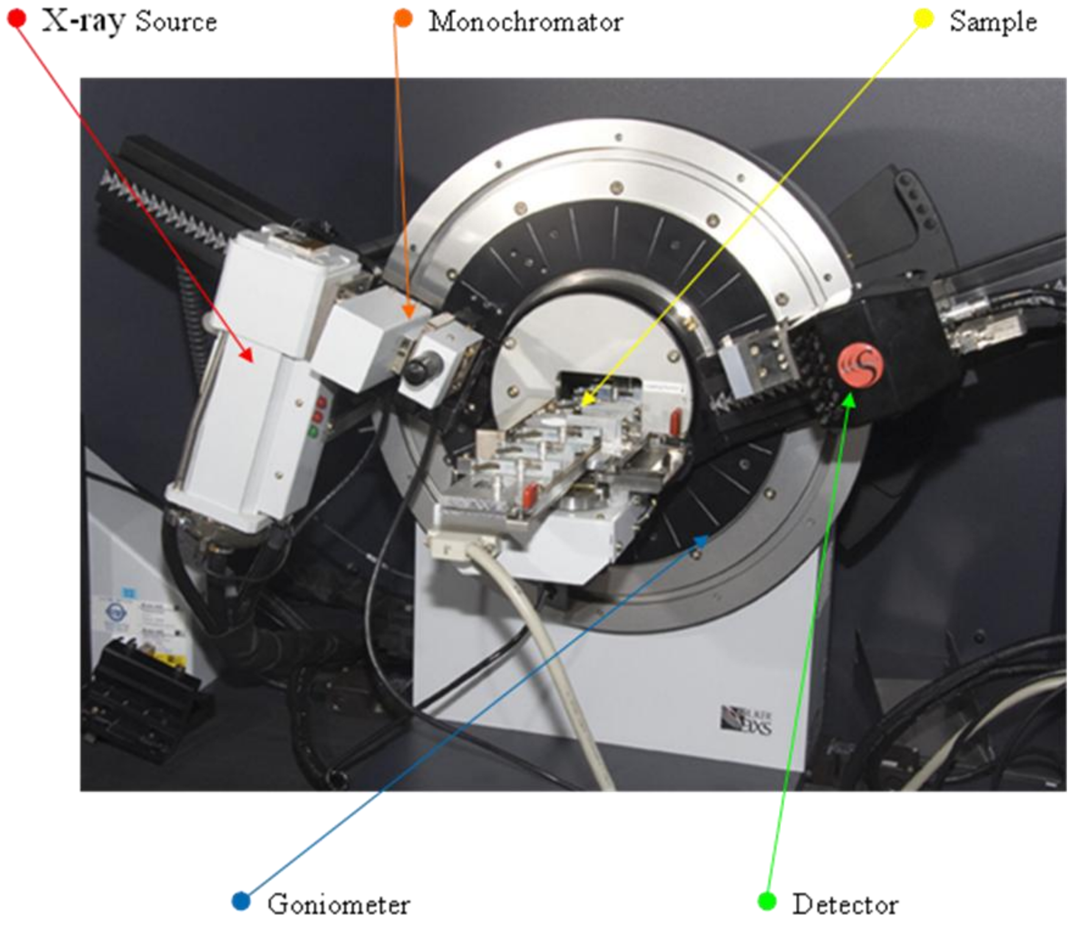

Figure 4.4 Bruker D8 advanced XRD

A source of monochromatic radiation using Cu $K\alpha$ (λ = 1.54Å) with a Göbel mirror or Cu $K\alpha1$ radiation with a two bounce germanium monochromator and X-ray detector using a Vantec position sensitive detector (PSD) are situated on the circumference of a graduated circle centred on the powder specimen. By moving the source and detector through a range of angles, the diffraction was measured with varying X-ray intensity at the detector. The diffractometer produces a pattern where the diffracted radiation intensity was associated with the angle 2θ. To prevent the reaction between samples and air during the measurement, powder samples were placed inside (and the powder flattened with a glass slide) an airtight dome-shaped sample holder made from Perspex.

TOPAS software supplied by Bruker AXS (Coelho, 2004), jEdit obtained from Durham University website managed by Prof. John Evans (Evans, 2009) and Crystallographic Information Files (.cif) from the Chemical Crystal Database (CDS, 2009) were used for the qualitative and semi-quantitative analysis of the phases present in the measured XRD pattern of prepared samples.

4.2.2 Raman and FTIR

Molecular vibrational information of materials can be obtained through Raman spectroscopy and infrared (IR) absorption spectroscopy, which are unique tools for assessing molecular motion and fingerprinting species.

A molecular vibration occurs when atoms in a molecule are in periodic motion while the molecule as a whole has constant translational and rotational motion. The typical frequencies of molecular vibrations (vibrational energy) are from less than 10^{12} to approximately 10^{14} Hz, which corresponds to radiation in the infrared region. At room temperature, most molecules are in the lowest energy state, the so called ground state, with a few at a higher level. Such a molecule can be excited to a higher vibrational mode when the molecule absorbs a quantum of energy (E), which corresponds to a vibrational frequency (v), according to the relation as shown in equation (4.2):

$$E = h\nu \qquad 4.2$$

where h is Planck's constant. Thus the most direct way to observe a molecular vibration is through IR spectroscopy as vibrational transitions typically require an amount of energy that corresponds to the infrared region of the spectrum (10^{12} - 10^{14} Hz).

Another possibility to probe molecular vibrations is based on an inelastic scattering process. The interaction between incident photons and the molecules of the sample will put the molecule into virtual state. When the molecule relaxes it emits a photon and returns to a vibrational state. The majority of photons emitted have the identical frequency to that of the incident light, a process referred to as elastic scattering, so called Rayleigh scattering. If the emitted photons have a different frequency to that of the incident light, inelastic scattering occurs. There are two types of inelastic scattering (Raman scattering), Stokes scattering and anti-Stokes scattering. The process, in which a photon is emitted with a lower energy than the incident radiation, is called Stokes scattering. A simplified energy diagram is shown in Figure 4.5. In Raman scattering, the difference in energy between the absorbed and re-emitted photons corresponds to the energy required to excite a molecule to a higher vibrational mode.

Figure 4.5 illustrates the difference between IR absorption and Raman scattering spectroscopy. In IR, the molecule is excited to a discrete (not virtual) energy level by the light with the energy equal to energy difference between the levels; the intensity of the transmitted light is compared with that of the incident light. While in Raman, the molecule is excited to a virtual state by much higher energy photons, e.g. laser source; the energy difference between absorbed and emitted photons is measured. IR and Raman spectroscopy both measure the vibrational energies of molecules but these methods have different selection rules (Nakamoto, 1997). For a vibrational motion to be IR active, the dipole moment of the molecule must change during the vibration. Therefore, the vibration of a heteropolar diatomic molecule is IR-active, while that of a homopolar diatomic molecule is IR-inactive. For a vibration to be Raman active, the polarizability of the molecule must change during the vibration. Thus, the combination of IR and Raman data is more conclusive than only one of these, for identifying molecular structures. In general, Raman spectroscopy favours symmetric vibrations of non-polar groups while IR spectroscopy is best at the asymmetric vibrations of polar groups; i.e. they provide complementary vibrational structural information.

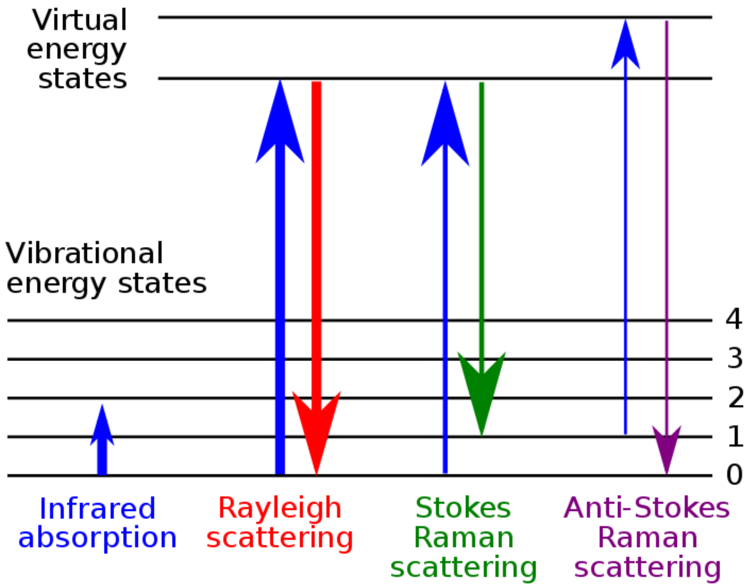

Figure 4.5 Energy diagram of Rayleigh and Raman scattering processes

IR spectroscopic measurements were performed with a Nicolet 8700 Fourier Transform Infrared (FTIR) spectrometer (Figure 4.6) using an attenuated total reflectance (ATR) attachment (also known as a 'Golden Gate') that allowed inert loading of samples. The spectrometer was purged with high-purity nitrogen for 30 minutes prior to measurements in order to try to minimize the carbon dioxide and water level within the spectrometer. The spectral resolution was 4 cm^{-1}, and a spectral range of 500 to 4000 cm^{-1} was selected. For FTIR measurements, the powder samples were pressed onto the crystal (of the 'Golden Gate') with a calibrated torque, and sealed in the sample holding cell in the glove box.

Figure 4.6 Nicolet 8700 FTIR spectrometer (left) with Golden Gate ATR attachment (right)

The principle of ATR is that if the radiation angle of incidence is exceeding the critical angle at the interface of the two media, total internal reflection will occur. However, there is still some penetration into the material setting up an evanescent wave that will be partially absorbed by the material based on the chemical bonding, causing an attenuation of the reflected radiation. Figure 4.7 shows a schematic of single reflection ATR used in this work.

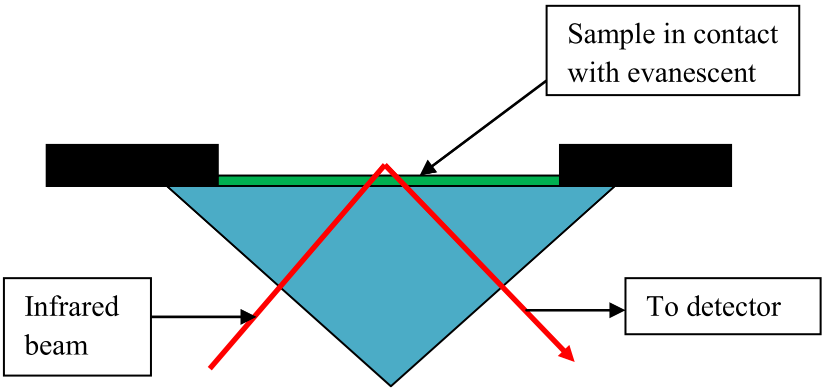

Figure 4.7 Schematic of single reflection ATR

Raman spectra were obtained using a Renishaw inVia Raman Microscope with Ar ion laser power (2 mW, 488 nm). As shown in Figure 4.8, a laser (blue) is focused on the sample and the emitted light is then channeled back through the objective (green) where a holographic notch filter removes the Rayleigh scattering. Remaining photons, stokes and anti-stoke scattering photons (yellow) are focused through a series of lenses and separated by a grating before detection using charge-coupled device (CCD). In this work, a microscope objective was used to focus the laser beam onto the sample with a ~50 µm diameter spot. The Raman scattered light ranged between 100 and 4000 cm^{-1} was collected using a 2400 grooves/mm grating. The spectral resolution was 2-4 cm^{-1}. The number of scans was optimized for each sample to obtain high intensity and well-resolved Raman spectra. In an Ar glovebox, samples were loaded into an Instec HCS621V sample cell, preventing contact between the sample and the air.

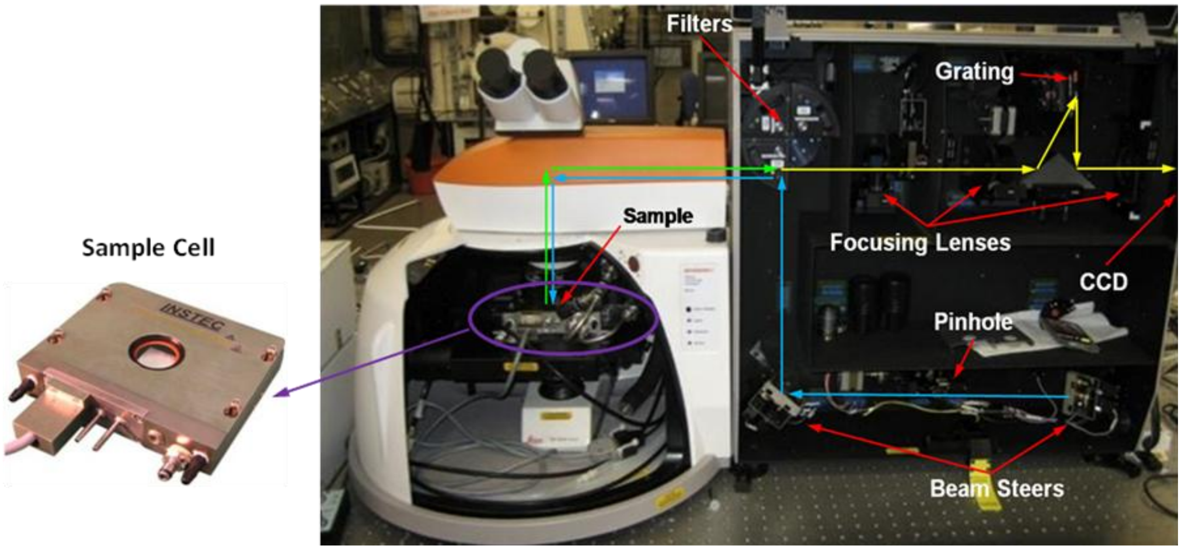

Figure 4.8 Renishaw inVia Raman Microscope with Instec HCS621V sample cell (Reed, 2009)

4.3 Thermogravimetric and calorimetric analysis

4.3.1 Thermogravimetric analysis

Thermogravimetric analysis (TGA) is an analytical technique used to determine the thermal stability of a material by monitoring the weight change due to dehydration, decomposition, or oxidation that occurs when a specimen is heated. The measurement is normally carried out in an inert atmosphere, such as argon and the weight is recorded as a function of increasing temperature. Characteristic thermogravimetric curves occur for specific materials due to unique sequences of physicochemical reactions occurring over the temperature ranges and heating rates. The specific TGA used in this work was a Netzsch TG209 coupled with a mass spectrometer (MS, Hiden Analytical HAL IV quadrupole mass spectrometer). The coupled technique was used to determine the mass change and the released chemical species during the sample heating process. A schematic diagram is shown in Figure 4.9.

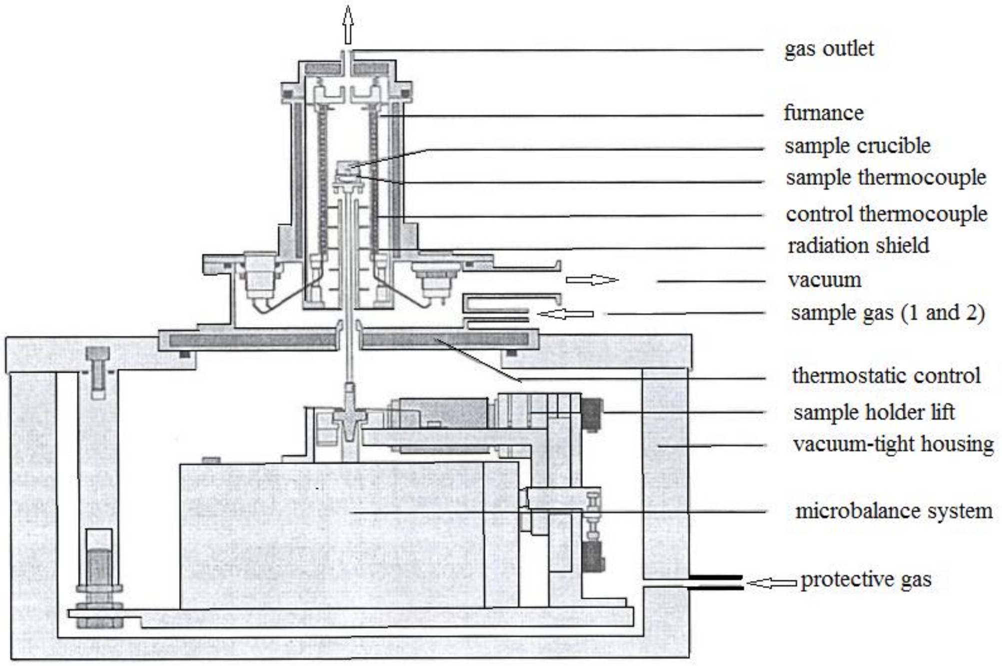

Figure 4.9 Schematic cross-sectional diagram of Netzsch TG209 (Reed, 2009)

Calibration of the TGA was carried out using six metal standards – In, Bi, Sn, Zn, Al and Ag with melting points over the operational temperature range of the instrument. Approximately 10-15 mg of sample was placed in an aluminium oxide crucible and covered with a lid. The sample was heated up from 30 to 500 °C with heating rate of 2 ºC/min under 1.5 bar argon flowing at 40 ml/min. Before a sample measurement, a baseline was run using an empty crucible under the same conditions to a sample measurement, so as to subtract any buoyancy effects on heating.

A mass spectrometer is designed to perform with five steps for a sample measurement: the vaporization of chemical species in the sample, the ionization of components to form charged fragments, the acceleration and separation of these fragments according to their mass-to-charge ratio (*m/z*), the detection of ions, and the transformation of ion signal into mass spectra. A Hiden Analytical HAL IV quadropole mass spectrometer was used in this work and a simplified schematic is shown in Figure 4.10.

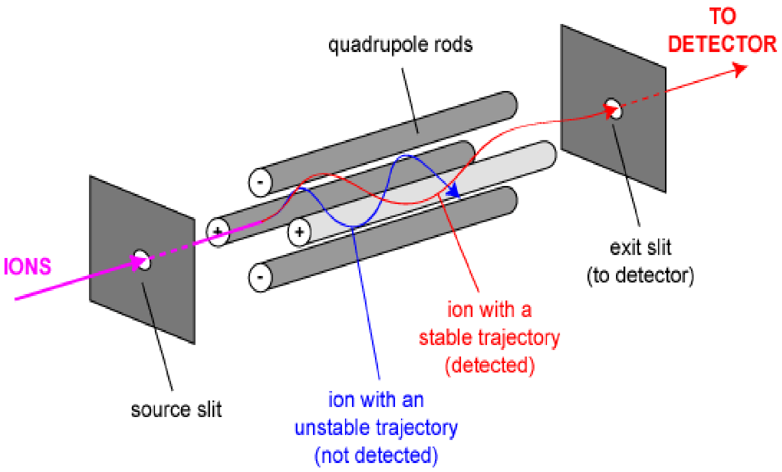

Figure 4.10 Simplified schematic of a mass spectrometer (MSR, 2012)

The desorbed gaseous molecules from the TGA enter the ion source to be ionized into ions using electron impact. The positively charged ions or fragments are accelerated in a vacuum through a quadrupole ion analyzer and are separated on the basis of mass-to-charge ratio by using electromagnetic fields with opposite pairs of four parallel rods. Only ions that stream a along certain direction can successfully pass through into the detector which is a Faraday cup.

Borane species (B_xH_y) are possible decomposition intermediates or final products from borohydride compounds in addition to hydrogen. The most common boranes are gaseous phase e.g. diborane B_2H_6 and tetraborane B_4H_{10}, liquid phase, e.g. pentaborane B_5H_9, as well as solid phase, e.g. decaborane $B_{10}H_{14}$. A significant amount of diborane released from the decomposition of zinc-based borohydrides (Jeon and Cho, 2006). The intermediate $[B_{12}H_{12}]^{2-}$, $[B_{10}H_{10}]^{2-}$ and/or $[B_3H_8]^{2-}$ species were observed during the decomposition of $LiBH_4$ (Friedrichs et al., 2010c) and $Mg(BH_4)_2$ (Chong et al., 2011). In this work, to try to identify possible species of the released gaseous phase and to determine their concentration from decomposition process, the MS for H_2 (m/z = 2), B_2H_6 (m/z = 26), B_4H_{10} (m/z= 53.3), and B_5H_9 (m/z=63) were set up to record the evolution dependence of different gases on the decomposition temperature.

4.3.2 Differential scanning calorimetry

Differential scanning calorimetry (DSC) is a thermoanalytical technique that can measure the difference in the energy required to increase the temperature of a sample and reference as a function of temperature. Both the sample and reference are subjected to identical temperature and pressure regimes throughout the experiment. The fundamental principle of this technique is that when the sample undergoes a physical transformation or chemical reaction, greater or less heat will be required to flow into it, compared to the reference, in order to maintain both at the same temperature.

A Netzsch DSC204HP, a heat flux DSC, was used to measure the energy required for any processes during the sample heating up and cooling down. Figure 4.11 gives a schematic cross-sectional diagram of the Netzsch DSC204HP, where the sample and reference are connected by a metal disc-made path with low resistance heat flow, assembled in a single furnace.

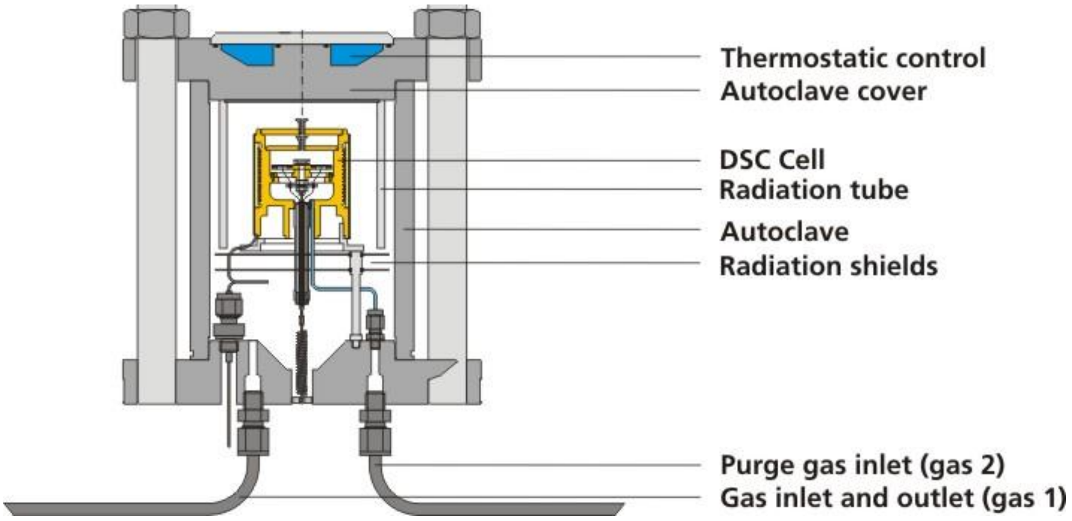

Figure 4.11 Schematic cross-sectional diagram of the Netzsch DSC204HP (NETZSCH, 2012)

A pre-weighed sample of approximately 10 mg was loaded into an aluminium DSC pan and heated from 30 to 500 ºC, and then cooled down to 50 ºC. A temperature ramp rate of 2 ºC/min, 4 bar argon or hydrogen atmosphere and a flow rate of pure argon at 100 ml/min were used for all the measurements. Before the sample measurement, a baseline was conducted using an empty Al pan under the same conditions to the sample measurement to reduce the effect of background on the sample measurement.

4.4 Analysis of the decomposition processes

4.4.1 *In-situ* XRD

A D8 XRD unit fitted with an Anton Parr XRK900 high temperature attachment (as shown in Figure 4.12) was used to determine the crystallisation behaviour of decomposition product in the temperature range from 30 to 500 °C then cooling down to 30 °C.

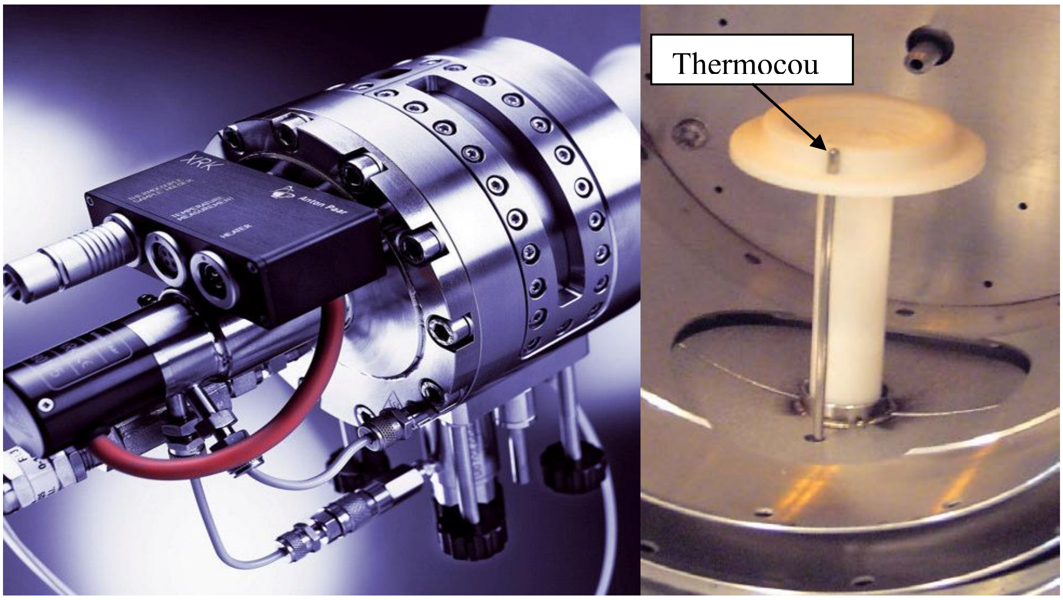

Figure 4.12 Anton Parr XRK900 high temperature stage (left) and sample holder with thermocouple (right)

The sample was loaded in an aluminium oxide crucible, fixed and sealed into the stage in the glove box to prevent contact with air. *In-situ* measurement was performed by heating the sample at a rate of 2 °C/ min under 100 ml/min of 2-3 bar flowing He. Each XRD pattern was recorded after the temperature reached the selected temperature in 2θ range of 5-90 °C (step size 0.0151°, step time 0.5 s, time range: 55 min).

4.4.2 *In-situ* Raman

To investigate the dependence of the vibration information during the decomposition of the sample against the temperature, *in-situ* Raman measurements were carried out using an Instec HCS621V sample cell. The sample was loaded in an aluminium crucible and sealed in the sample cell in the glove box. Ar gas flow and cooling water system, as well as heating units were connected into the cell. The sample was heated up from 30 to 500 °C at a ramp heating rate of 2 °C/min with 100 ml/min of 1-2 bar flowing Ar. After the temperature achieved a set point, the spectra were collected continually with six 10 s scans from 100 to 4000 cm^{-1}.

4.4.3 Raman and IR

A stainless steel reactor (Figure 4.13) was used to obtain samples decomposed at different temperatures. The milled sample was loaded into a borosilicate glass test tube that was put into the reactor in the glove box. The primary experiment indicated that no reaction occurred between the test tube and the samples under operational conditions. The sealed vessel was placed into a temperature-controlled oven, connected with the cooling water, argon flowing system and thermocouple. The sample was heated to a selected temperature at heating rate of 5 °C/min with 3 bar Ar flowing at 100 ml/min, then cooled to room temperature after reaching a set-temperature, ready for Raman and IR measurements.

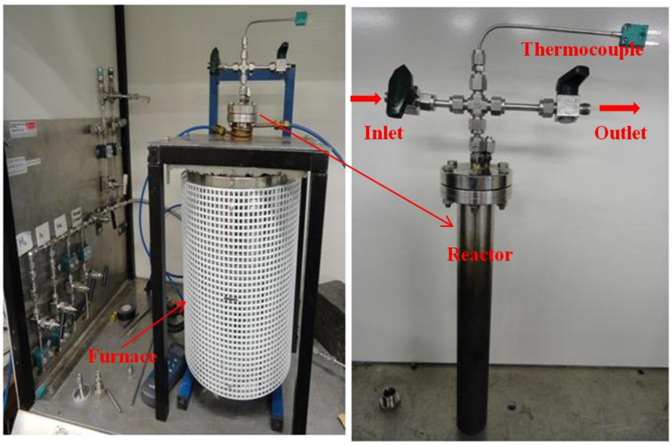

Figure 4.13 The reactor and heating system for the decomposition of samples

4.5 Reversibility

The milled sample ($2LiBH_4$-$MnCl_2$ milled for 360 minutes) firstly was decomposed in a DSC by heating to 200 ºC under 1.5 bar Ar flowing at 40 ml/min. An attempt was made to re-hydrogenate the desorbed sample using the DSC, which was heated from 30 to 200 ºC in 100 bar of H_2 flowing at 100 ml/min. The thermal decomposition properties of the rehydrogenated sample were then measured again by DSC and TGA.

Another attempt for the recombination was performed using a Hiden Isochema HTPS-2 volumetric system to measure the reversibility of $2KBH_4$-$MnCl_2$ sample milled for 360 minutes. The HTP system is able to measure the hydrogen sorption isotherms up to elevated pressures of 500 bar over a range of temperatures. The desorption was performed by heating the milled sample through temperature programmed desorption (TPD) from room temperature to 250℃ at a heating rate of 5℃ /min under 3 bar He flowing at 100 ml/min. The absorption was conducted by setting a hydrogen pressure of 150 bar and a temperature of 225℃ over 72 hours, then monitoring any pressure drop. The TGA (coupled with MS) measurement and Raman spectroscopy respectively were also performed on the rehydrogenated sample to assess the extent of reversibility.

Chapter 5 Results and Discussion: $LiBH_4$-$MnCl_2$ System

5.1 Synthesis and characterization

5.1.1 Crystallographic characterization

Powder XRD measurements were performed on samples of $2LiBH_4$-$MnCl_2$ and $3LiBH_4$-$MnCl_2$ which were ball-milled for different durations (Figures 5.1 and 5.2). For both the 10 min samples, X-ray diffraction peaks with significant intensities are attributed to the starting material $MnCl_2$ and to the resulting product LiCl. There are also weak reflections (labelled "unknown") which overlap with a broad band due to the Kapton sample holder at around 20° 2θ. Small intensity reflections for $LiBH_4$ can be found only for the 10-minute milled $3LiBH_4$-$MnCl_2$ sample. After milling for 30 minutes, the diffraction peaks of $MnCl_2$ disappear. Apart from weak reflections at around 20° 2θ, all the peaks are associated with LiCl, indicating an exchange reaction between $LiBH_4$ and $MnCl_2$ occurs via equation (3.58). In both the milled samples, it should be noted that the weak reflections which overlap with the background from the silica Kapton dome (at around 20° 2θ) are present for all the milled samples.

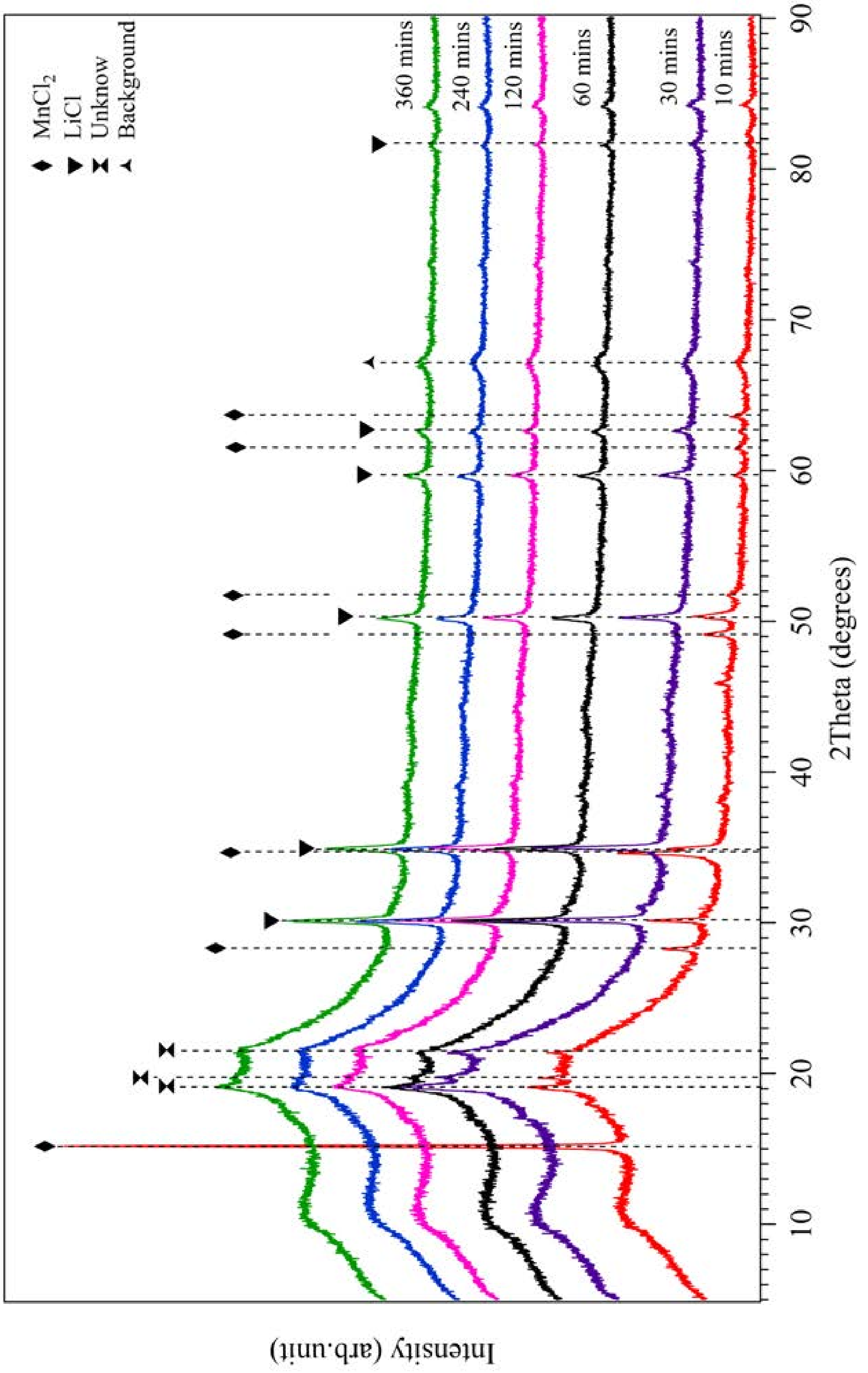

Figure 5.1 XRD patterns (Kapton dome) of $2LiBH_4$-$MnCl_2$ milled for different durations

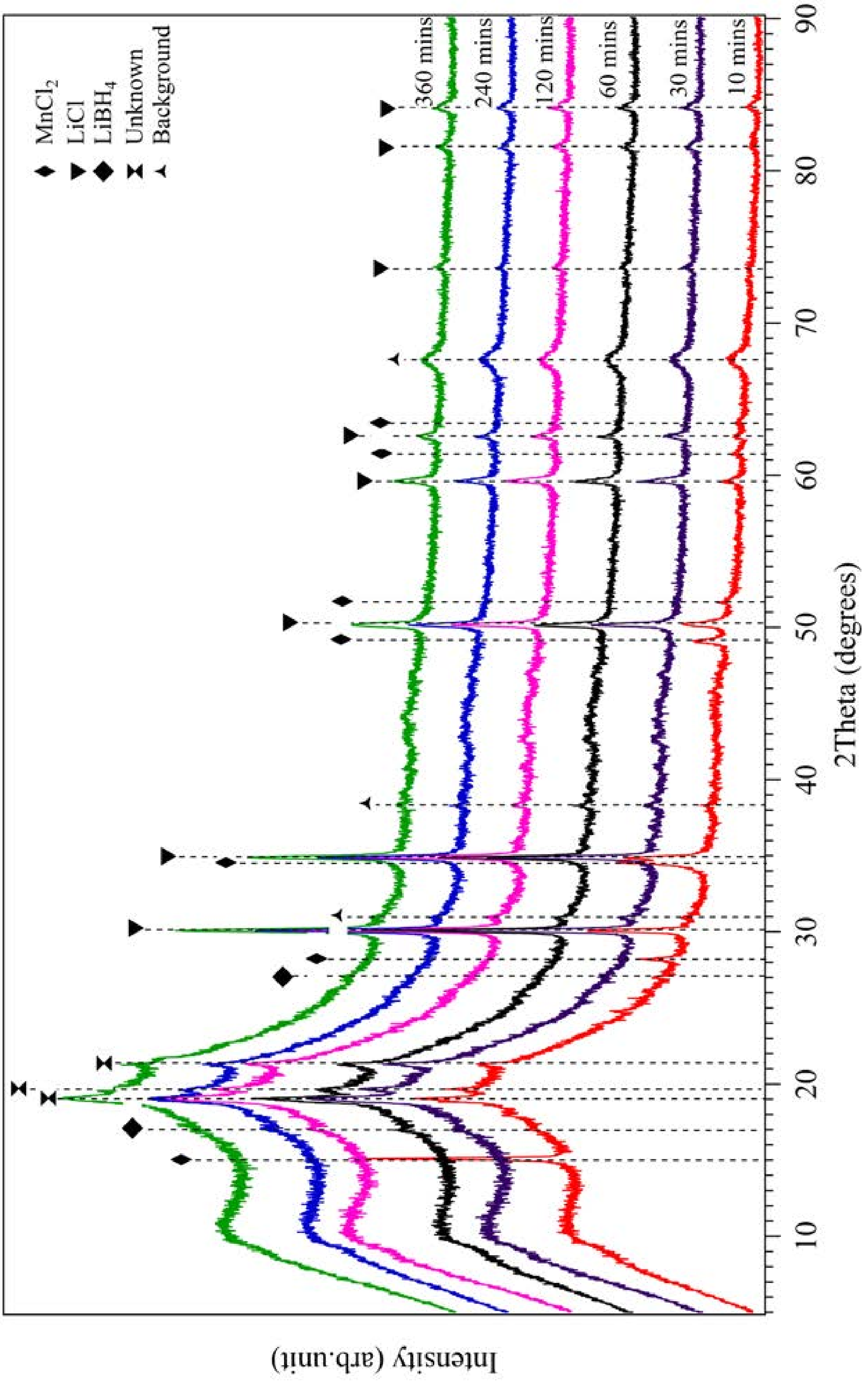

Figure 5.2 XRD patterns (Kapton dome) of $3LiBH_4$-$MnCl_2$ milled for different durations

In order to clarify the nature of the small peaks at ~ 20° 2θ, powder XRD was also performed on the 360-minute milled $2LiBH_4$-$MnCl_2$ and $3LiBH_4$-$MnCl_2$ samples using an Anton Parr XRK900 cell, which has a Be window (instead of Kapton). As shown in Figure 5.3, the diffraction peaks of milled $2LiBH_4$-$MnCl_2$ and $3LiBH_4$-$MnCl_2$ samples are attributed to LiCl and to the $P3_{1}12$ structure of $Mn(BH_4)_2$ proposed by Černý et al (2009), with no residual $LiBH_4$ or $MnCl_2$ present for either sample. This indicates that a metathesis reaction has occurred as follows:

$$2LiBH_4 + MnCl_2 \rightarrow Mn(BH_4)_2 + 2LiCl \tag{5.1}$$

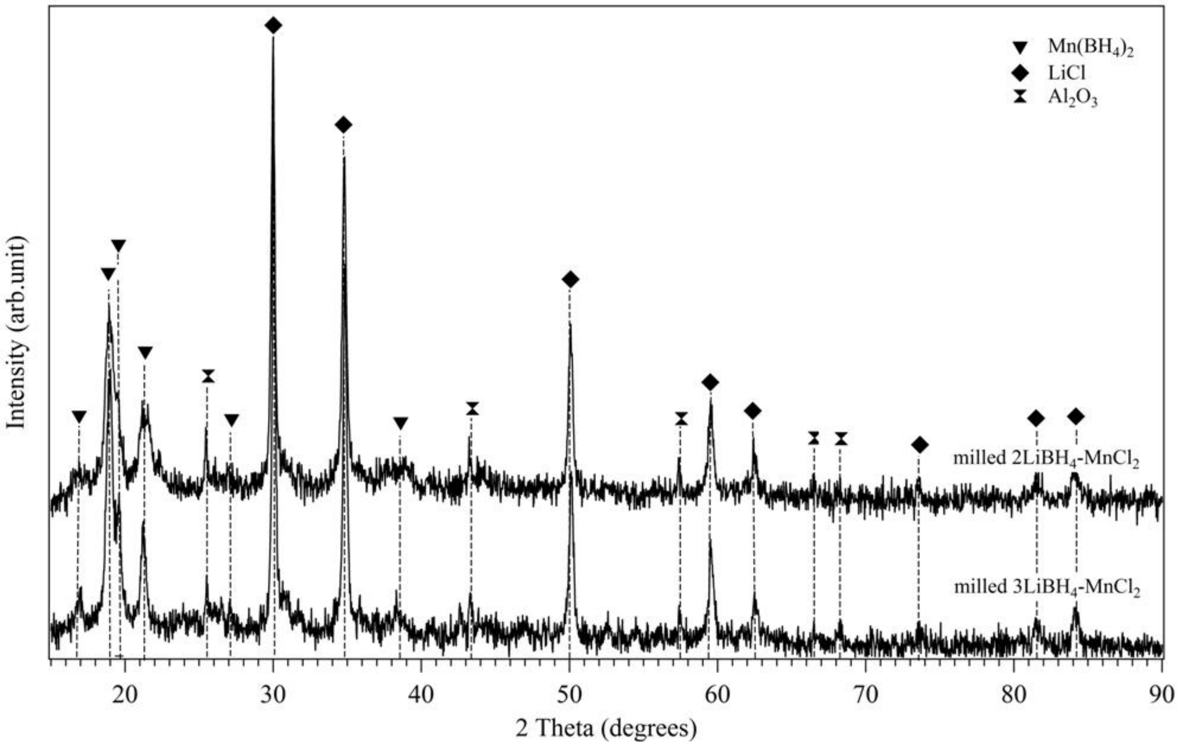

Figure 5.3 XRD patterns (Anton Parr cell) of x$LiBH_4$-$MnCl_2$ (x = 2 or 3) samples ball-milled for 360 minutes

In the case of the milled $3LiBH_4$-$MnCl_2$ sample, an 11.4 wt% excess of $LiBH_4$ would be expected if equation (5.1) is followed. However, this is not observed by XRD. This may originate from the comparatively small concentration of $LiBH_4$. The lattice parameters of

$Mn(BH_4)_2$ were found to be a = 10.48(1) Å and c = 10.82(1) Å for the milled $2LiBH_4$-MnCl2 sample and a = 10.42(1) Å and c = 10.81(1) Å for the milled $3LiBH_4$-$MnCl_2$ sample, using the structure proposed by Černý et al. (2009). The reduction in lattice parameter a between the two samples could be due to the substitution of some of the $[BH_4]^-$ anions by Cl^- anions. Such a substitution was also discussed as a possible explanation for the decrease in volume during heating between -183 and 127 °C by Černý et al. (2009).

An attempt was made to try to improve the crystalline properties of the formed $Mn(BH_4)_2$ from the milled $2LiBH_4$-$MnCl_2$ sample, by changing the conditions to milling for 90 or 180 times for 2 minute durations (separated by 2 minute rest intervals), giving total milling durations of 180 or 360 minutes; the XRD patterns of these milled samples are shown in Figure 5.4.

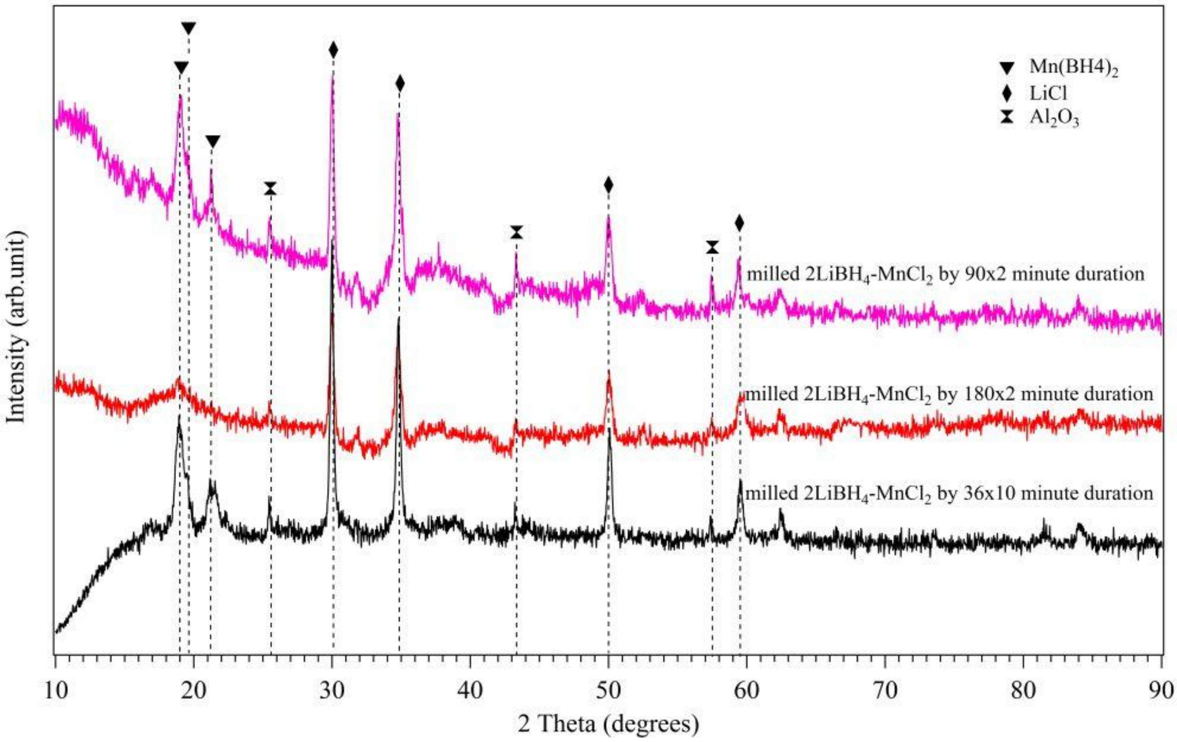

Figure 5.4 XRD patterns of $2LiBH_4$-$MnCl_2$ samples ball-milled for 90×2, 180×2 and 36×10 minute durations, giving total milling times of 180, 360, and 360 minutes.

For the same total milling time (360 min), the sample with the shorter milling period (2 min) appears to be less crystalline, (compared to the 10 min period), with broad and weak diffraction peaks for $Mn(BH_4)_2$ (at ~ 20° 2θ). This may be due to a reduction in the crystallite size of the formed $Mn(BH_4)_2$, as a result of an increased ball milling efficiency (using shorter milling duration intervals). This explanation can be confirmed by the crystallization of $Mn(BH_4)_2$ from the 180×2 min milling duration sample with an increased temperature (Figure 5.5), where the intensity of diffractions from $Mn(BH_4)_2$ are significantly increased when the sample was heated to 80 and 120 °C.

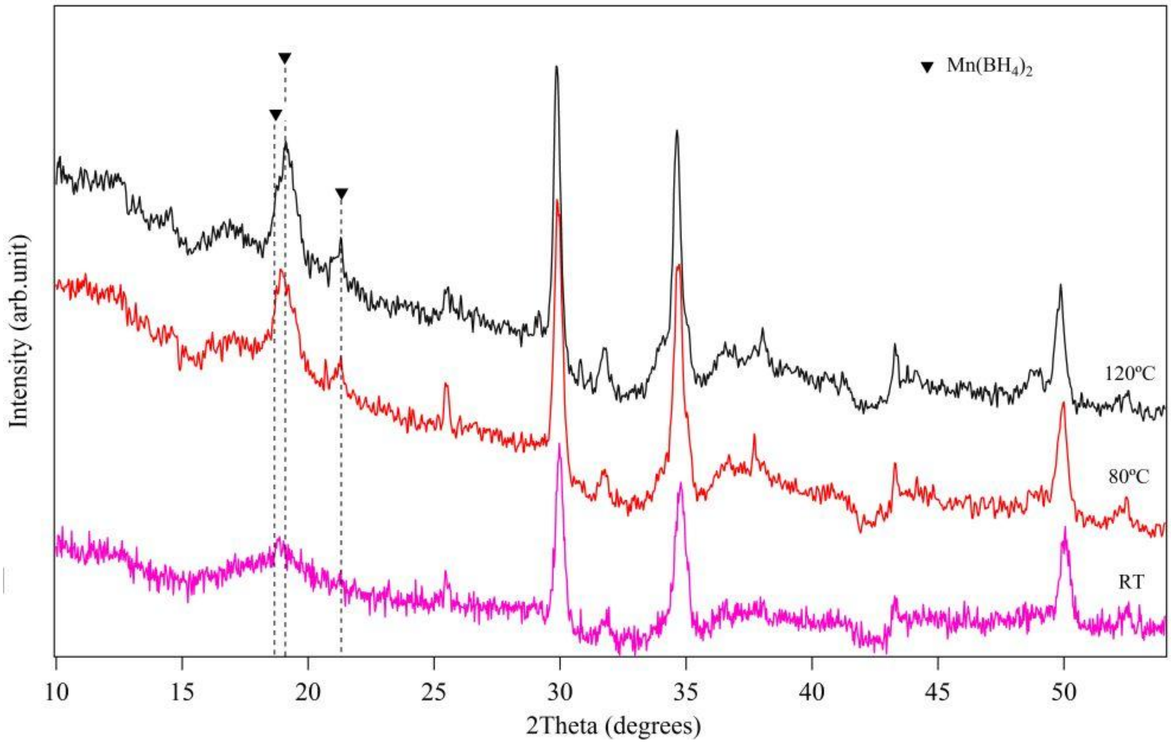

Figure 5.5 XRD patterns of 2$LiBH_4$-$MnCl_2$ samples ball-milled for 180×2 minute durations, heated at 2 ℃ /min under 4 bar He flowing at 100 ml/min

Therefore, to obtain good crystalline target compound the total milling period can be decreased, through the use of short duration milling intervals. Consequently, X-ray peaks consistent with reflections for $Mn(BH_4)_2$ with a *$P3_112$* structure are observed for both the

36×10 and 90×2 min milling duration samples, whereas only one broad low-intensity peak is observed for the 180×2 min milling duration sample. Thus, the milling duration interval is one of important factors for controlling the formation of a crystalline compound, and a 10 minute duration separated by 10 minute rest interval was used thereafter in this work.

5.1.2 Spectroscopic characterization

Raman spectroscopy can be used to identify the nature of the bonding of the borohydride to the metal centre, as the ionic, mono-, bi- and tridentate configurations have characteristic modes (Marks and Kolb, 1977). Among the four configurations, the vibrational spectra of borohydride molecules differ. The differences in the Raman spectra of the four bonding configurations of borohydrides have been given by Marks and Kolb (1977). Monodentate borohydrides should exhibit A_1 terminal hydrogen-boron stretching mode (νB-H_t) at around 2300-2440 cm^{-1} and the bridging hydrogen-boron stretching mode (νB-H_b) at ~ 2000 cm^{-1} both with strong intensity. The vibration of the metal-hydrogen (M-H) bond would occur in the region of 1700-2000 cm^{-1}, however, this would be a broad peak and at room temperature this vibration may be so broad that it is not observed. The strong A_1 mode due to the deformation of BH_3 would be observed with a frequency between 1000 and 1150 cm^{-1}. In the bidentate configuration of borohydrides, the strong B-H_t stretching vibration (symmetric A_1) with a possible shoulder is observed in the region 2400-2600 cm^{-1}. The A_1 B-H_b stretching mode is predicted to be at 1650-2150 cm^{-1}. A strong broad band associated with the bridge expansion and M-H_b stretching vibration is typically observed at 1300-1500 cm^{-1} and a doublet band due to the deformation of BH_2 is observed at 1050-1200 cm^{-1}. The principal difference between the Raman spectra of mono- and bi-dentate borohydrides occurs in the B-H_b stretching region and the B-H deformation region. For tridentate borohydrides, the B-H_t

stretching region has a single A_1 band at 2450-2600 cm^{-1}. The A_1 B-H_b modes typically appear as a strong singlet with a possible shoulder at 2100-2200 cm^{-1}. The band with significant intensity at 1100-1200 cm^{-1} is due to the bridge deformation. Ionic borohydrides should only exhibit two bands in the Raman spectrum, a B-H stretching mode (symmetric A_1) at 2200-2300 cm^{-1} and a BH_2 deformation mode (symmetric E) at 1050-1150 cm^{-1}. When the BH_4 group has symmetry lower than T_d, broadening or splitting of these bands may occur (Marks and Kolb, 1977; Reed, 2009).

Figures 5.6 and 5.7 show the room temperature Raman spectra of $2LiBH_4$-$MnCl_2$ and $3LiBH_4$-$MnCl_2$ samples milled for different time. There are three regions in the Raman spectra (Marks and Kolb, 1977): external vibrations (140-300 cm^{-1}), which are mainly due to translational and librational motions of the borohydride compound; internal bending bands (1000-1400 cm^{-1}); and internal stretching modes (2100-2400 cm^{-1}) of the $[BH_4]^-$ group.

The region between 1000 and 2500 cm^{-1} contains the bands involved in the deformation of the B-H bond and some M-H bonding, allowing chemical structure determination. In this case, the most relevant vibrations for the identification of the bonding mode are the νB-H_t and νB-H_b vibrations. The Raman peak positions and the assignment for $2LiBH_4$-$MnCl_2$ and $3LiBH_4$-$MnCl_2$ samples milled for different times are summarized in Table 5.1.

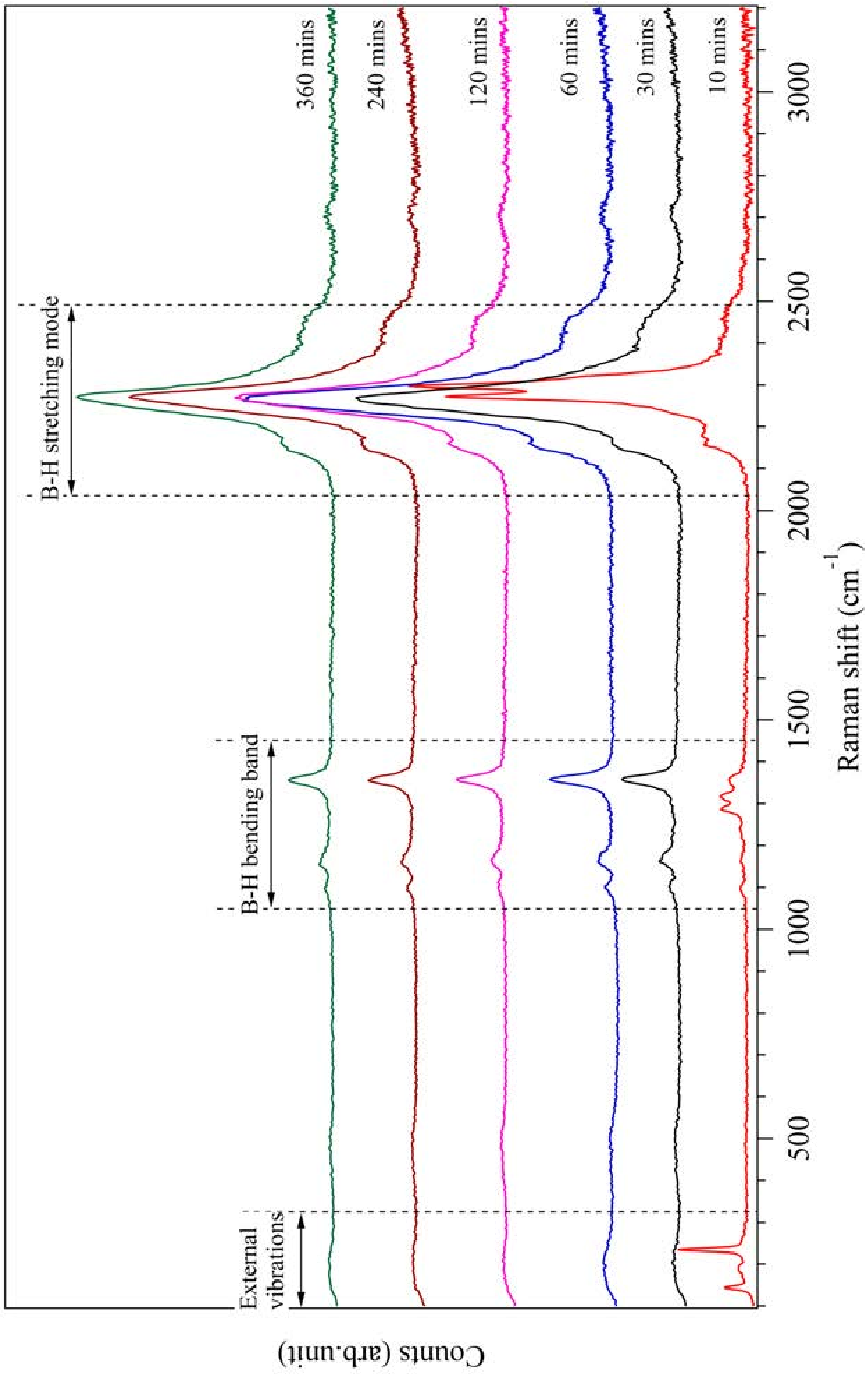

Figure 5.6 Raman spectra of 2LiBH$_4$-MnCl$_2$ samples milled for different durations

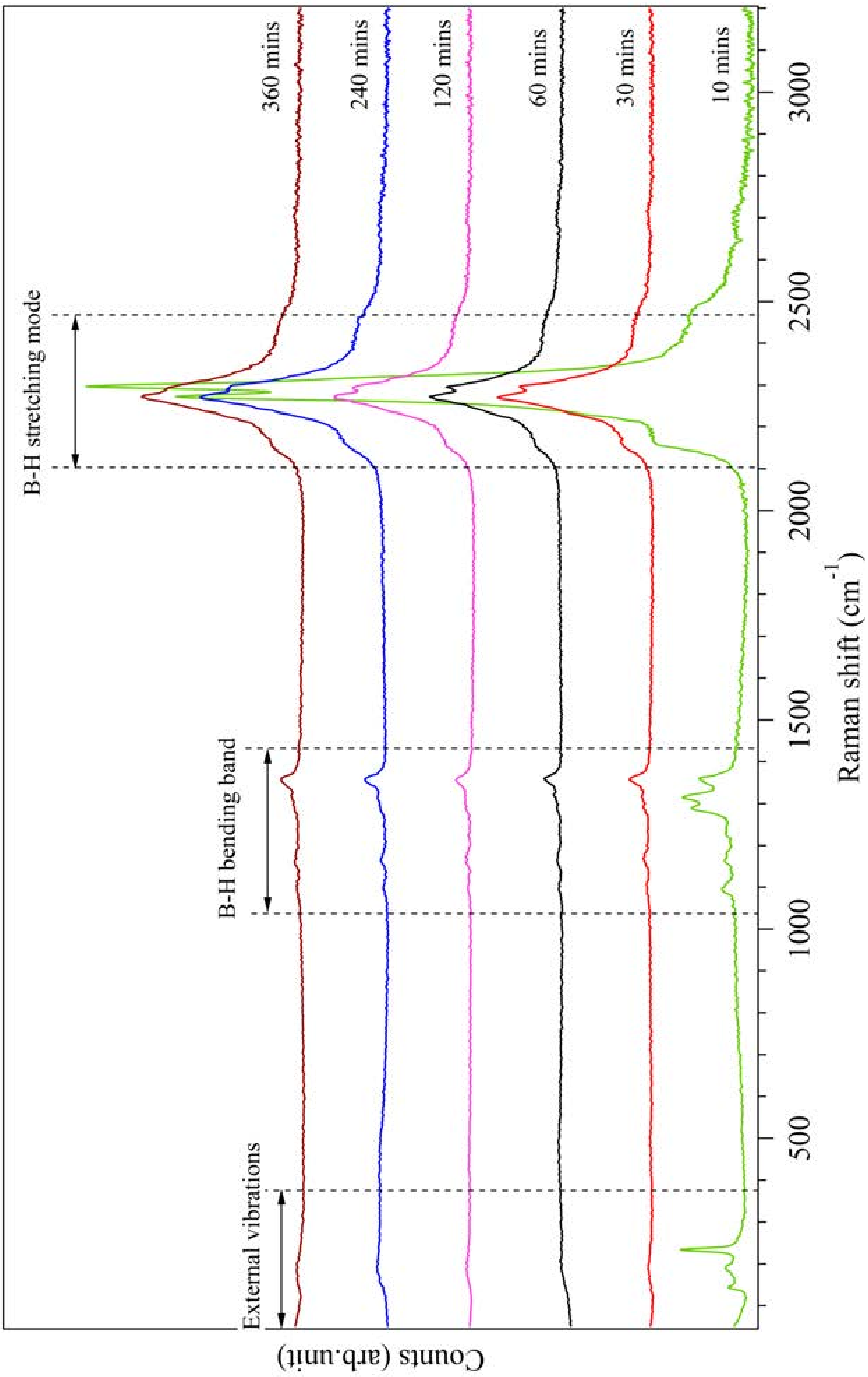

Figure 5.7 Raman spectra of $3LiBH_4$-$MnCl_2$ samples milled for different durations

Table 5.1 Raman shift (cm^{-1}) for $xLiBH_4$-$MnCl_2$ (x=2 or 3) milled for different durations

Raman shift (cm^{-1})							
xLiBH$_4$-MnCl$_2$ (x =2 or 3) samples with different milling time (minutes)						Assignment	Comment*
10	30	60	120	240	360		
144	-	-	-	-	-	External modes	*w*
(143)	(-)	(-)	(-)	(-)	(-)		
189	-	-	-	-	-		*w*
(190)	(-)	(-)	(-)	(-)	(-)		
234	-	-	-	-	-		*w*
(235)	(-)	(-)	(-)	(-)	(-)		
1098	1094	1093	1094	1095	1094	B-H bending modes	*vw*
(1091)	(1090)	(1083)	(1086)	(1090)	(1092)		
1162	1157	1155	1159	1154	1155		*w*
(1159)	(1158)	(1155)	(1155)	(1156)	(1155)		
-	1173	1173	1175	1176	1175		*sh*
(1171)	(1172)	(1173)	(1175)	(1175)	(1172)		
1287	-	-	-	-	-		*w*
(1286)	(1281)	(1279)	(1280)	(1276)	(1281)		
1317	-	-	-	-	-		*w*
(1312)	(1311)	(1306)	(1310)	(1313)	(1310)		
1356	1353	1355	1353	1353	1353		*m*
(1358)	(1354)	(1357)	(1355)	(1354)	(1353)		
2157	2158	2157	2156	2156	2157	B-H stretching modes	*w*
(2154)	(2155)	(2151)	(2154)	(2154)	(2155)		
2271	2274	2271	2270	2272	2270		*vs*
(2271)	(2267)	(2266)	(2267)	(2268)	(2269)		
2297	-	-	-	-	-		*s*
(2296)	(2293)	(2289)	(2296)	(2293)	(2295)		
2480	2472	2465	2461	2460	2460		*w*
(2481)	(2470)	(2464)	(2460)	(2460)	(2460)		

* *w-weak, vw-very weak, sh-shoulder, m-medium strong, vs-very strong, s-strong*

After milling for 10 minutes, external vibrations can be observed in the low-frequency Raman spectra of $2LiBH_4$-$MnCl_2$ and $3LiBH_4$-$MnCl_2$ samples, indicating the modification of the Li and BH_4 structure. These external vibrations disappear for samples milled for longer durations. The internal bending and stretching modes for both samples as a function of milling time are shown in Figures 5.8 and 5.9, respectively. With respect to the bending modes, which are dominated by symmetric and asymmetric vibrations, the $2LiBH_4$-$MnCl_2$ sample milled for 10 minutes shows five vibration modes at 1098, 1162, 1287, 1313 and 1356 cm^{-1}. With increased milling time the Raman vibrations at 1287 and 1313 cm^{-1} disappear, and a new peak at around 1173-1176 cm^{-1} appears for the samples milled for 30 to 360 minute durations. In the case of all of the milled $3LiBH_4$-$MnCl_2$ samples, there are six B-H bending modes, appearing at around 1083-1192, 1155-1159, 1171-1175, 1276-1286, 1306-1313 and 1353-1358 cm^{-1}. The very strong peaks situated at higher Raman frequencies are associated with B-H stretching modes. For both the $2LiBH_4$-$MnCl_2$ and $3LiBH_4$-$MnCl_2$ samples, with increased milling time: the vibration modes at ~ 2297 cm^{-1} reduce in intensity, until they disappear in the case of the milled $2LiBH_4$-$MnCl_2$ sample for a milling duration greater than 10 minutes; and the combination mode at 2480 cm^{-1} shift towards a lower frequency. A significant increase in intensity can be observed in both samples for the vibration modes at around 2270 cm^{-1} with increasing milling, which is accompanied by peak broadening for milling durations greater than or equal to 30 minutes.

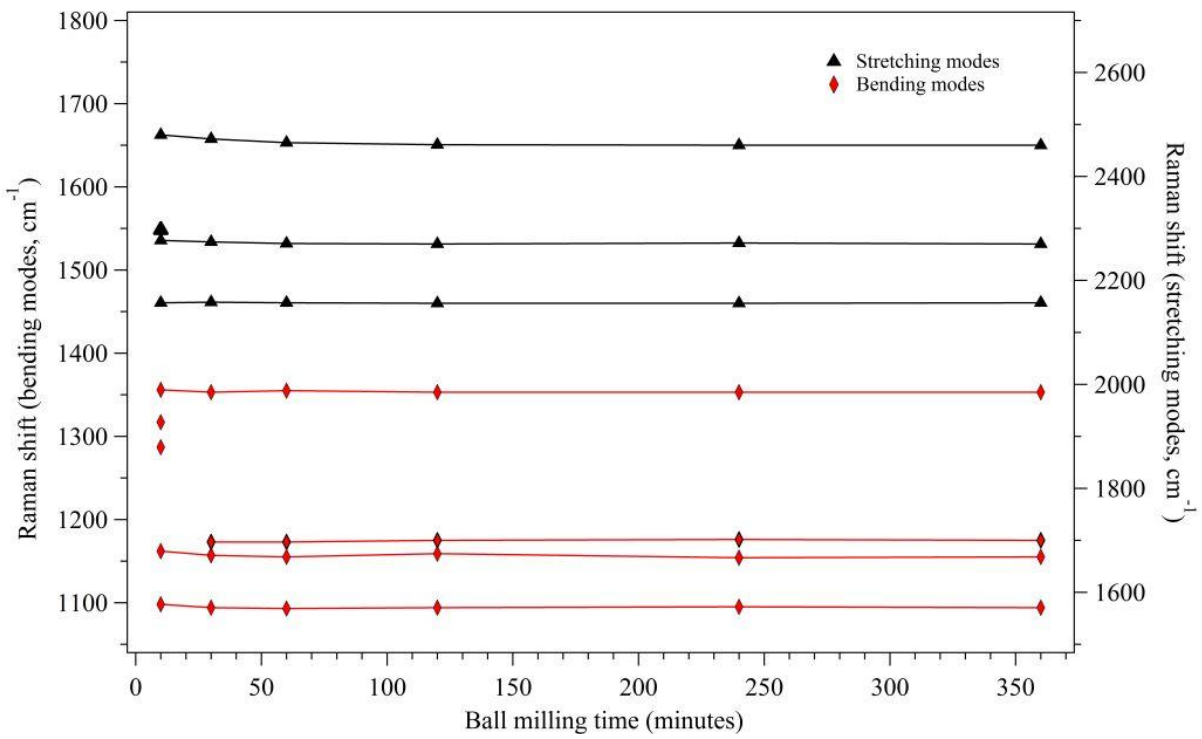

Figure 5.8 Bending and stretching vibration modes for $2LiBH_4$-$MnCl_2$ sample as a function of milling time

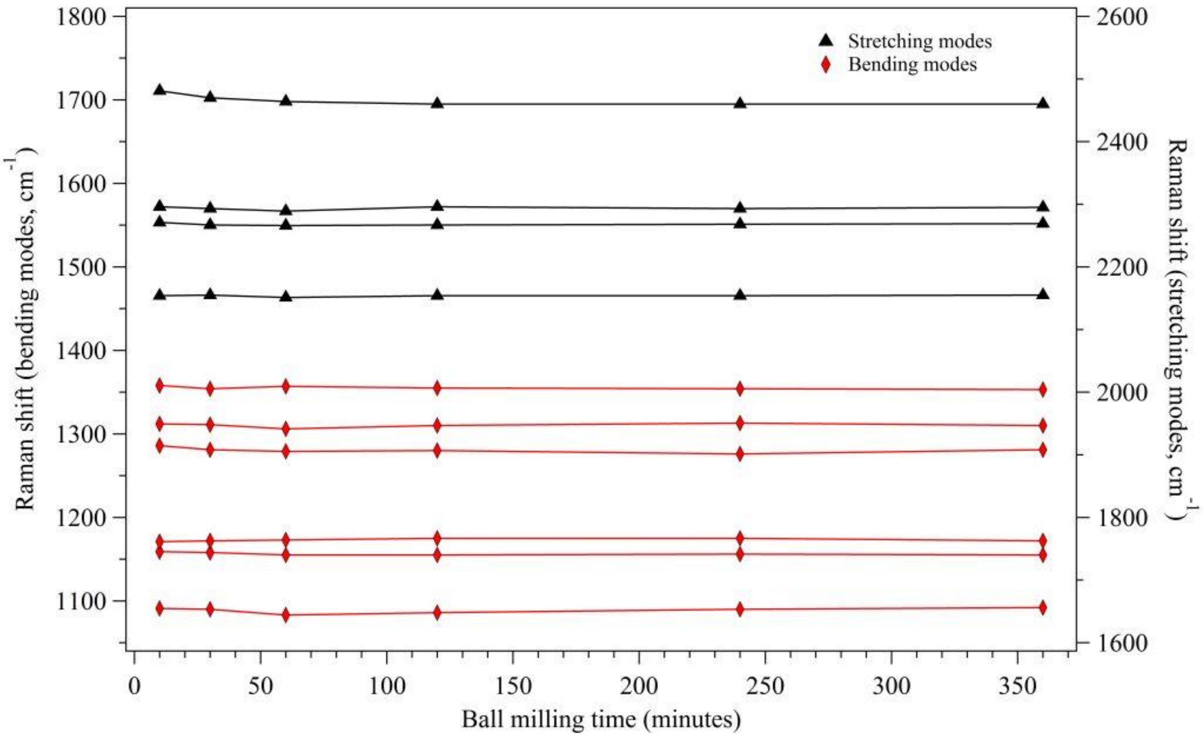

Figure 5.9 Bending and stretching vibration modes for $3LiBH_4$-$MnCl_2$ sample as a function of milling time

A comparison of the Raman spectra for as-received $LiBH_4$ (as a reference), $2LiBH_4$-$MnCl_2$ and $3LiBH_4$-$MnCl_2$ samples milled for 360 minutes, is shown in Figure 5.10 (with peak positions summarised in Table 5.2). For both the $LiBH_4$-$MnCl_2$ samples, the spectra are dominated by five fundamental Raman vibrations, B-H bending modes occurring at 1092(1094), 1155, 1172(1175) and 1353 cm^{-1}, and B-H stretching modes at 2269(2270) cm^{-1} with combination modes at 2155(2157) and 2460 cm^{-1}. Of these, the modes at 1155, 1172(1175) and 1353 cm^{-1} are not observed for as received $LiBH_4$. The difference between both the milled $LiBH_4$-$MnCl_2$ samples is that Raman active modes at 1281, 1310 and 2295 cm^{-1} occur only for the milled $3LiBH_4$-$MnCl_2$ sample.

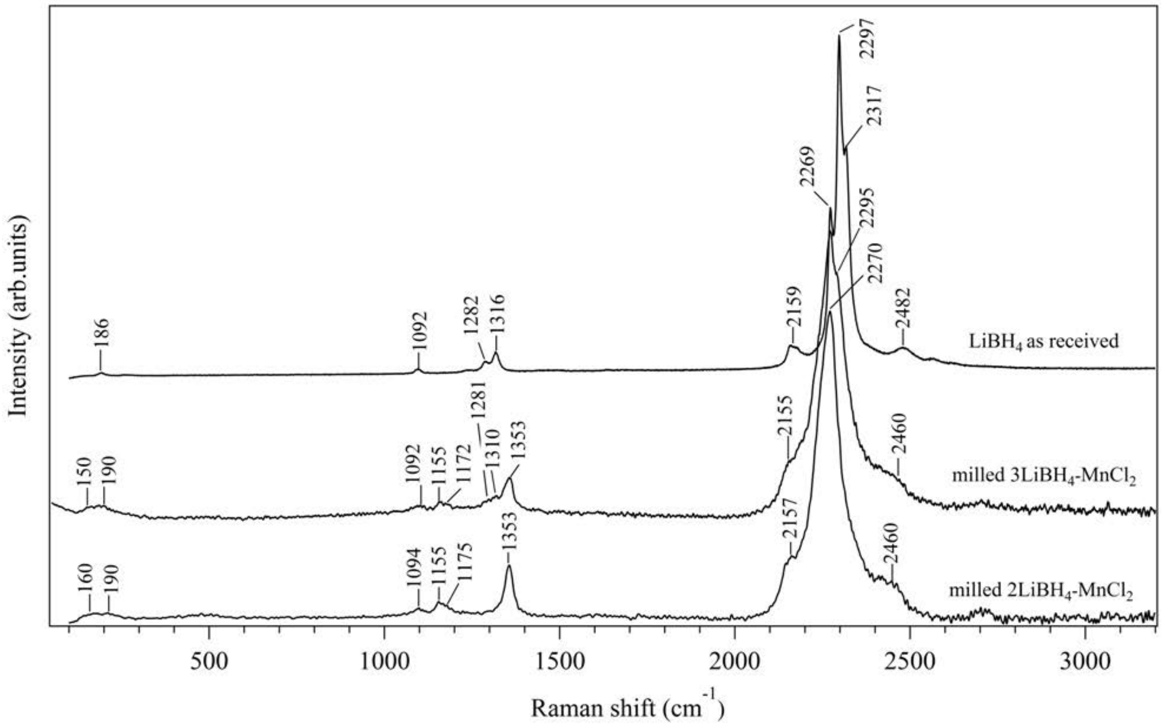

Figure 5.10 Raman spectra of $xLiBH_4$-$MnCl_2$ (x = 2 or 3) samples ball-milled for 360 minutes, with $LiBH_4$ as a reference

The milled $2LiBH_4$-$MnCl_2$ sample has a spectrum consistent with an ionic $[BH_4]^-$ (Marks and Kolb, 1977), although the bonds in the B-H stretching region (2100-2400 cm^{-1}) move to lower

Raman shifts compared to $LiBH_4$. This may have been induced by both a lengthening of the B-H bond and also the change in the force constant due to the interaction with the divalent Mn ion. The spectrum from the $3LiBH_4$-$MnCl_2$ sample exhibits the same ionic modes as the $2LiBH_4$-$MnCl_2$ sample, with additional modes (1281, 1310 and 2295 cm^{-1}) confirming the presence of excess $LiBH_4$ in this sample. The absence of extensive splitting of the B-H bending modes (1000-1330 cm^{-1}) indicates that the $[BH_4]^-$ ions occupy relatively high-symmetry sites with all the $[BH_4]^-$ ions existing in similar environments.

Table 5.2 Summary of Raman shift (cm^{-1}) of the resulting products from both ball-milled $LiBH_4$-$MnCl_2$ mixtures, compared to values from the literature for $LiBH_4$ and $Mn(BH_4)_2$

$LiBH_4$ (Racu et al., 2008)	$LiBH_4$ (this work)	$Mn(BH_4)_2$ (Černý et al., 2009)	(this work)		assignment
			$2LiBH_4$ -$MnCl_2$	$3LiBH_4$-$MnCl_2$	
189	186		160-190	150-190	external mode
255	-		-	-	
283	-		-	-	
1090	1092*w*	1102	1094*vw*	1092*vw*	B-H bending modes
1099	-	-	-	-	
-	-	1164	1155*w*	1155*w*	
-	-	1175	1175*s*	1172*sh*	
1235	-	-	-	-	
1286	1282*sh*	-	-	1281	
1316	1316*sh*	-	-	1310*sh*	
-		1359	1353*s*	1353*m*	
2157	2159*m*	2161	2157*w*	2155*w*	B-H stretching modes
2177	-	-	-	-	
2275	2269*sh*	2271	2270*vs*	2269*vs*	
2301	2297*vs*	-	-	2295*sh*	
2321	2317*sh*	-	-	-	
2391	-	-	-	-	
2491	2482*w*	-	2460*w*	2460	
2572	-	-	-	-	

On cooling the 360-minute milled $2LiBH_4$-$MnCl_2$ sample to -190 °C, an increase in the intensities of the vibration peaks is observed, as shown in Figure 5.11. This refinement in Raman vibration modes has insignificantly occurred for the milled $3LiBH_4$-$MnCl_2$ sample (see figure 5.12) in addition to all vibration modes at room temperature slightly change to higher Raman shift at -193 °C for both the samples. The room temperature Raman active mode at around 2270 cm^{-1} for milled $2LiBH_4$-$MnCl_2$ (2269 cm^{-1} for milled $3LiBH_4$-$MnCl_2$) splits into bands at 2258 and 2282 cm^{-1} (2235 and 2279 cm^{-1}) after cooling to -193 °C. The Raman frequency shift and the peak splitting at low temperature is due to the reduction of the thermal expansion and fluctuation within a lattice; the thermal vibration causes uniform displacement of molecules and coupling between vibrations within the molecules (Racu et al., 2008; Reed and Book, 2011).

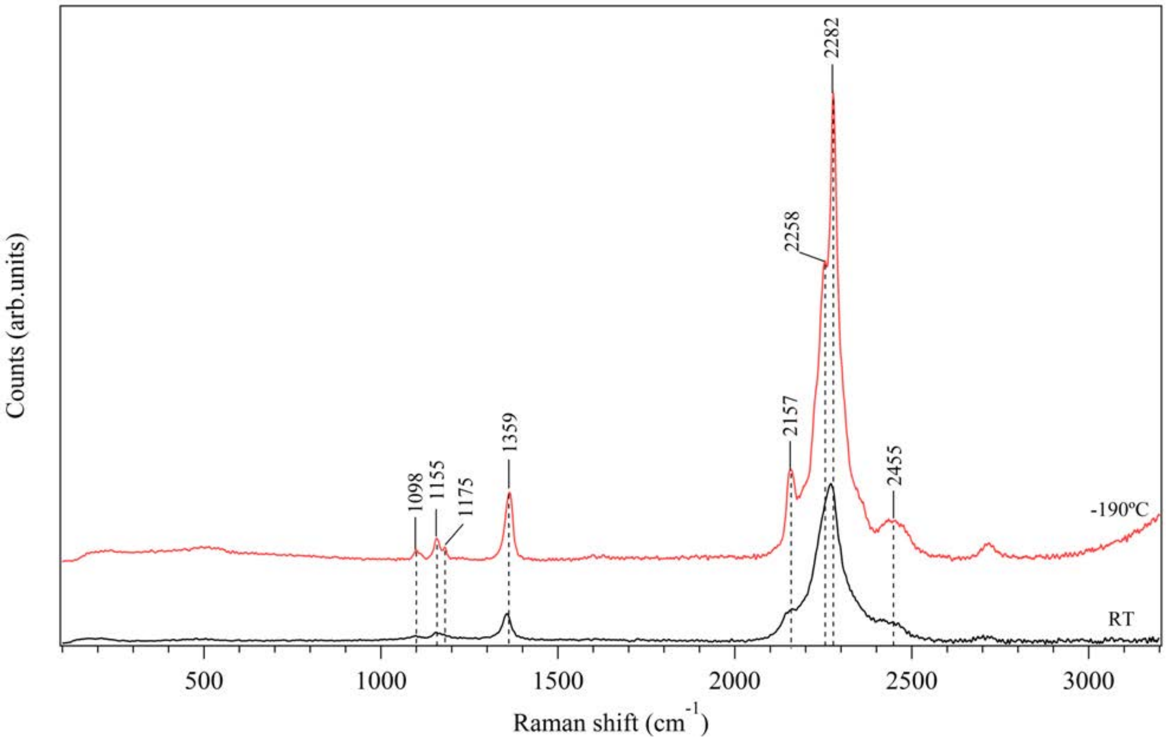

Figure 5.11 Raman spectrum of $2LiBH_4$-$MnCl_2$ sample milled for 360 minutes at -190 °C, with RT Raman spectrum as a reference

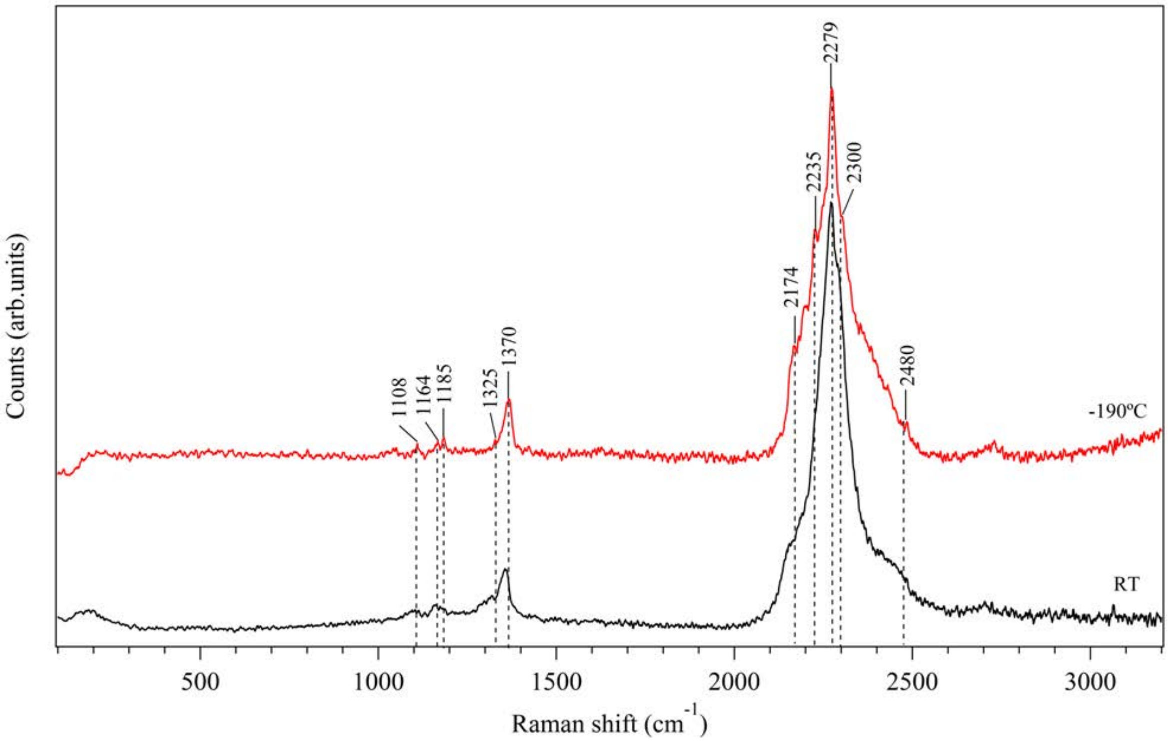

Figure 5.12 Raman spectrum of $3LiBH_4$-$MnCl_2$ sample milled for 360 minutes at -190 °C, with RT Raman spectrum as a reference

In addition, FTIR measurements show vibrations at 2230(2229), 1352(1354), 1203(1204), 1091(1092) cm^{-1} in both milled samples ($2LiBH_4$-$MnCl_2$ or $3LiBH_4$-$MnCl_2$), which may be associated with the $[BH_4]^-$ tetrahedra of $Mn(BH_4)_2$, as shown in Figure 5.13. Vibrations at 2305 and 964 cm^{-1} in the milled $3LiBH_4$-$MnCl_2$ sample confirm the presence of excess $LiBH_4$ in this sample, compared with the FTIR spectrum of $LiBH_4$ as received.

The XRD, Raman and FTIR results appear to confirm that the metathesis reaction has taken place according to equation (5.1).

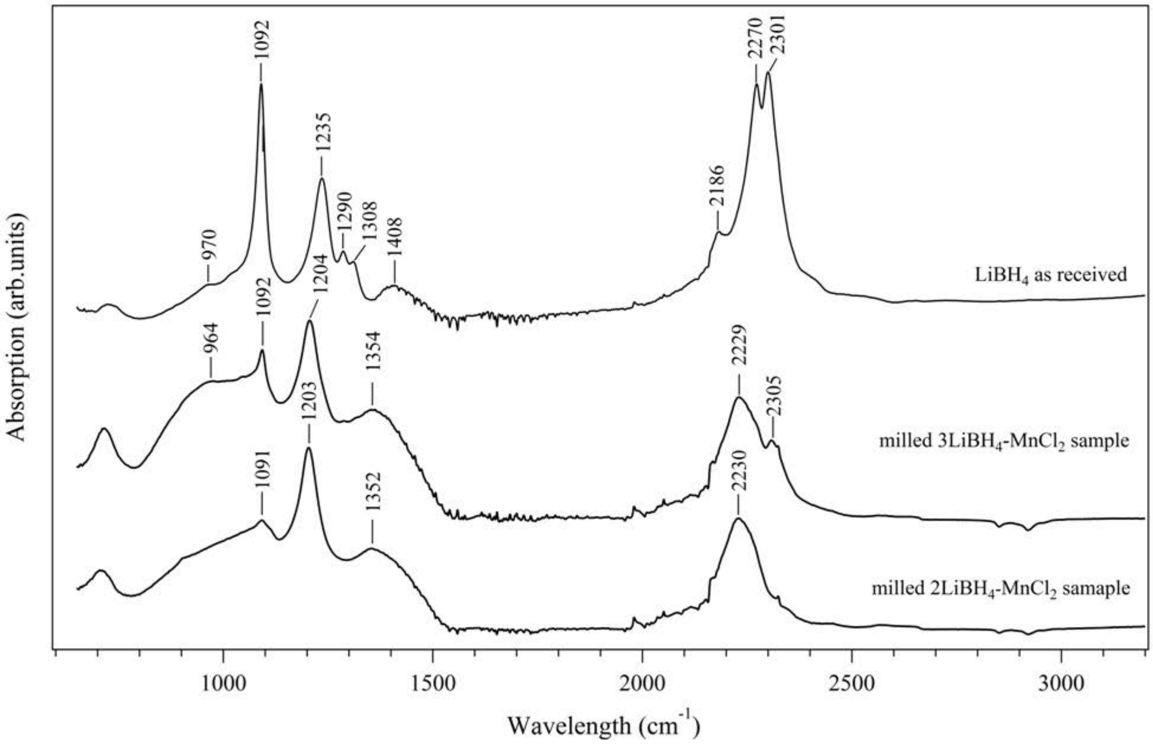

Figure 5.13 FTIR spectra of x$LiBH_4$-$MnCl_2$ (x = 2 or 3) samples ball-milled for 360 minutes, with $LiBH_4$ as a reference

5.2 Thermal decomposition properties

5.2.1 Thermogravimetric analysis

TGA profiles of $2LiBH_4$-$MnCl_2$ samples milled from 10 to 360 minutes are presented in Figure 5.14, with mass losses and decomposition temperatures summarized in Table 5.3. Onset decomposition temperatures slightly increase from 115 to 130 °C for the samples milled from 10 to 60 minutes, and remain constant afterward; whereas an increased milling time reduces the end temperature of decomposition from 310 ℃ for the 10-minute milled sample to 181 ℃ for the 360-minute milled sample, which implies an increased rate of the decomposition reaction for the samples that were milled for longer. The total mass losses in the mixture ($2LiCl$-$Mn(BH_4)_2$) are in the range of 7.8 ± 0.3 to 8.6 ± 0.1 wt%, which would be equivalent to mass losses from 15.7 to 16.9 wt% for the $Mn(BH_4)_2$ phase alone (i.e. by subtracting the mass due to LiCl, according to equation (5.1). These experimental values are much higher than the theoretical hydrogen contents of the 2LiCl-$Mn(BH_4)_2$ mixture (4.76 wt%) and the $Mn(BH_4)_2$ phase (9.53 wt%).

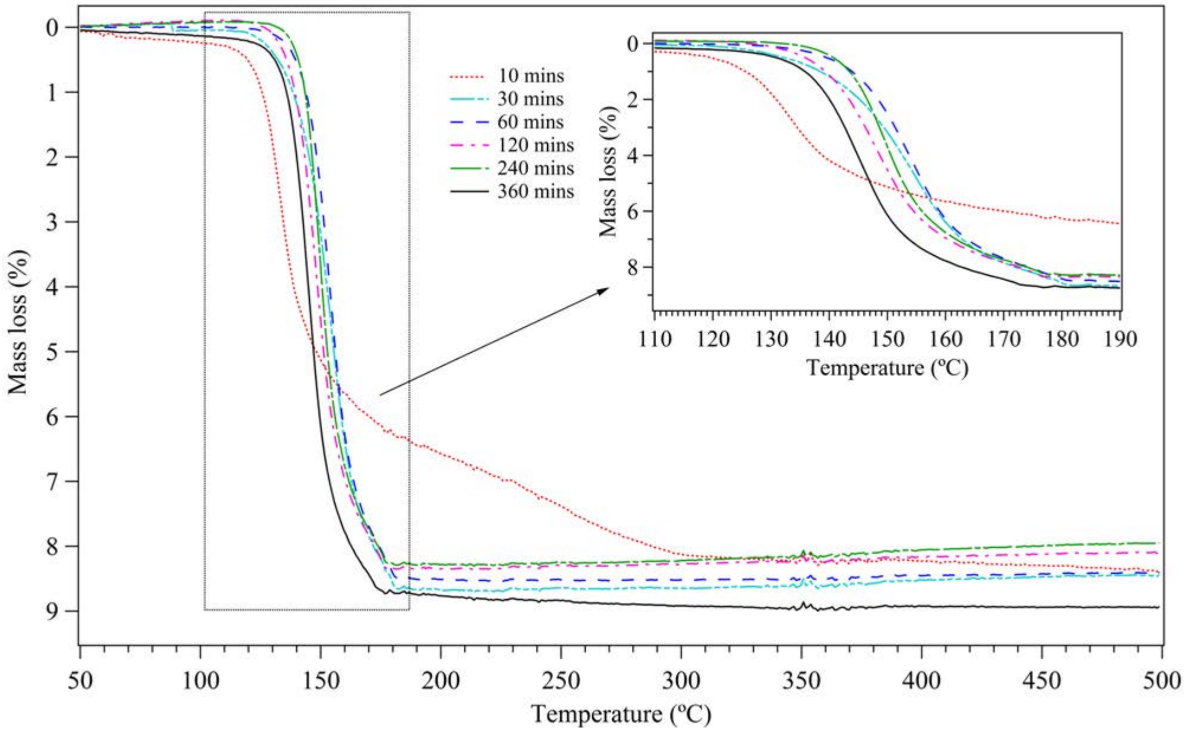

Figure 5.14 TGA profiles of $2LiBH_4$-$MnCl_2$ samples ball-milled for 10 to 360 minutes, heated at 2 ℃ /min under 1.5 bar Ar flowing at 40 ml/min

Table 5.3 Summary of TGA profiles for the milled 2$LiBH_4$ -$MnCl_2$ samples

	Milling time (minutes)					
TGA properties	10	30	60	120	240	360
Onset decomposition temperature (ºC)	115	120	130	128	130	130
End decomposition temperature (℃)	310	192	190	188	185	181
Total observed mass loss (wt%)	7.8±0.3	8.6±0.1	8.5±0.2	8.4±0.3	8.4±0.2	8.4±0.2
Theoretical H content of the mixture 2LiCl-$Mn(BH_4)_2$ (wt%)	4.76					
Calculated mass loss from the $Mn(BH_4)_2$ phase alone (wt%) *	15.7	17.1	16.9	16.9	16.9	16.9
Theoretical H content of the $Mn(BH_4)_2$ phase (wt%)	9.53					

* *Total observed mass loss* × ($M_{Mn(BH_4)_2}$+2M_{LiCl})/ $M_{Mn(BH_4)_2}$, *where M is molecular mass.*

Thermogravimetric analysis coupled with mass spectrometry of the 360-minute milled 2$LiBH_4$-$MnCl_2$ sample (Figure 5.15) shows that the onset of decomposition is 130 °C and is complete by 181 °C with a mass loss of 8.4 ± 0.2 wt%. This mass loss is not consistent with any of the proposed reactions (equations (5.2)-(5.6)):

$$Mn(BH_4)_2 \rightarrow Mn + 2B + 4H_2 \tag{5.2}$$

$$Mn(BH_4)_2 \rightarrow Mn + H_2 + B_2H_6 \tag{5.3}$$

$$Mn(BH_4)_2 \rightarrow MnB_2 + 4H_2 \tag{5.4}$$

$$Mn(BH_4)_2 \rightarrow MnH_2 + 2B + 3H_2 \tag{5.5}$$

$$Mn(BH_4)_2 \rightarrow MnH_2 + B_2H_6 \tag{5.6}$$

Mass spectrometry shows that there is a concurrent evolution of hydrogen and diborane with an onset temperature of 133 °C, reaching a peak at 148 °C. Gaseous borane compounds other than diborane are not detected by MS in this study. In addition, the MS shows a second, smaller hydrogen evolution peak at around 175 °C corresponding to a small change in the gradient of the TGA. The presence of a second decomposition step indicates that either there are two distinct mechanisms for decomposition, or that the decomposition involves a two-step process proceeding via an intermediate species.

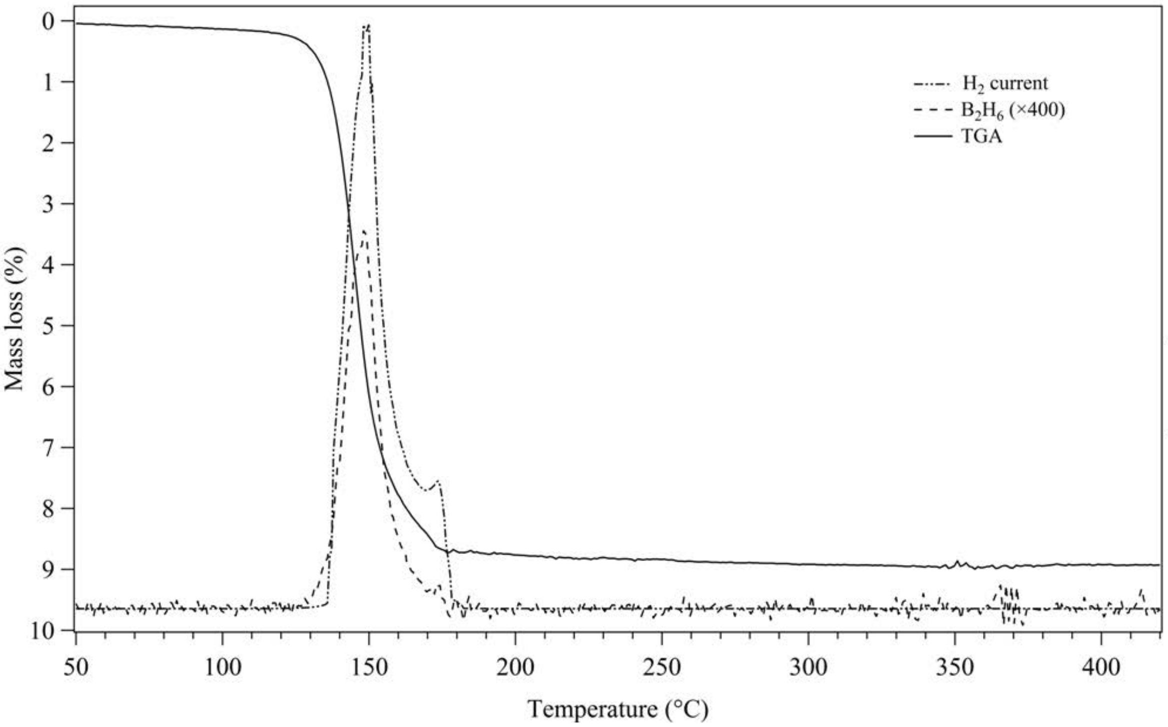

Figure 5.15 TGA profile for $2LiBH_4$ -$MnCl_2$ sample milled for 360 minutes, coupled with MS for evolved H_2 and B_2H_6 gases, heated at 2 ℃ /min under 1.5 bar Ar flowing at 40 ml/min

The TGA-MS profile for the $2LiBH_4$-$MnCl_2$ sample milled for 10 minutes shows a multi-step decomposition process (see Figure 5.16), where the first major peak of released hydrogen is accompanied by diborane (130-140 °C), which is attributed to the decomposition of Mn-based borohydride, probably ternary borohydride (Li-Mn-BH_4) formed from an incomplete metathesis reaction based on equation (3.58), or physically mixed $Mn(BH_4)_2$ and unreacted $LiBH_4$. The minor hydrogen peaks at ~ 200-300 °C are related to the subsequent decomposition of the reaction intermediates. The chemical composition and decomposition of the formed Mn-based borohydride with shorter milling period should be further investigated by in situ XRD measurement. In this case, it is not possible to measure the amount of diborane evolved accurately, because a proportion of this gas most probably sublimed onto the inner surface of the heated pipe connecting the TGA exhaust to the mass spectrometer inlet (a white film was subsequently observed when the pipe was cleaned).

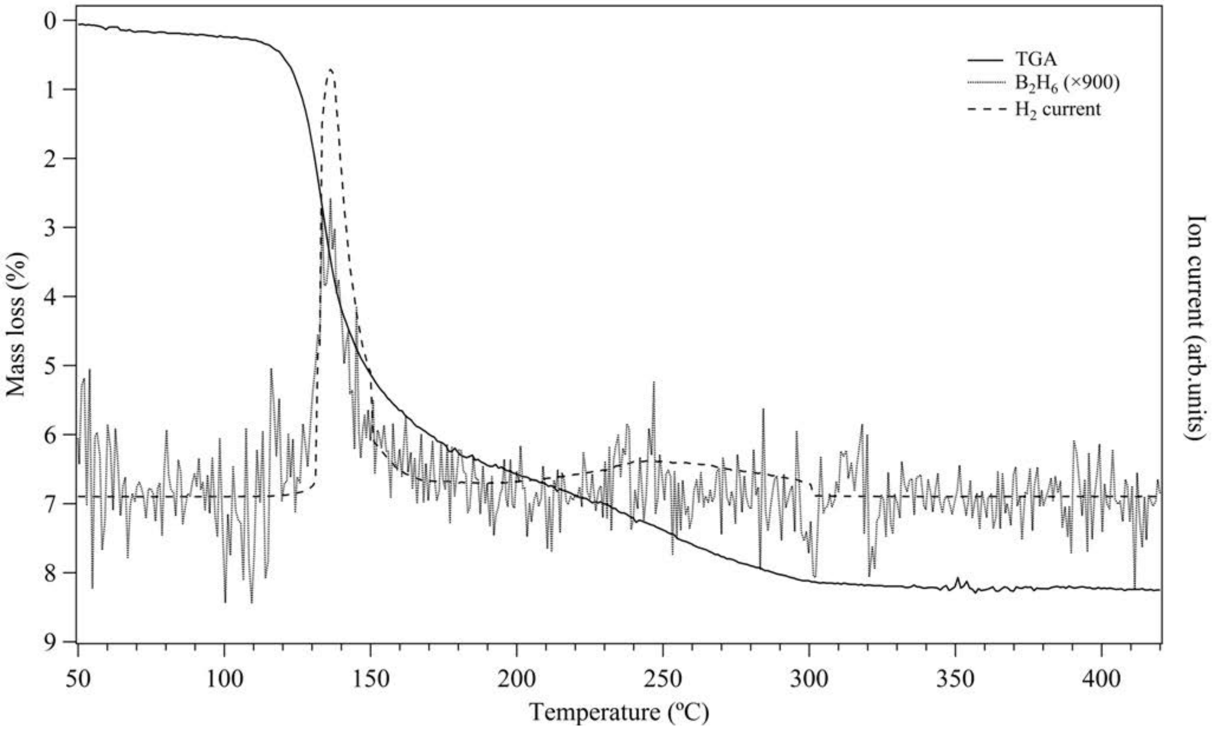

Figure 5.16 TGA profile for 2$LiBH_4$-$MnCl_2$ sample milled for 10 minutes, coupled with MS for evolved H_2 and B_2H_6 gases, heated at 2 ℃ /min under 1.5 bar Ar flowing at 40 ml/min

Figure 5.17 shows the TGA results from the 3$LiBH_4$-$MnCl_2$ samples milled for 10 to 360 minutes. There are two mass loss regions: at 105 to 180 ℃ corresponding to 7.3-8.2 wt%

(Table 5.4), and 320 to 420℃ corresponding to 0.7-0.9 wt%. This second mass loss region was not observed for the milled 2LiBH$_4$-MnCl$_2$ samples. The onset decomposition temperatures for the 3LiBH$_4$-MnCl$_2$ samples are lower (105-115 °C) than those for 2LiBH$_4$-MnCl$_2$ (115-130 °C). While with increasing milling duration from 10 to 360 minutes, the onset and end decomposition temperatures of the 3LiBH$_4$-MnCl$_2$ samples are reduced from 115 and 180 ℃, to 105 and 145 ℃, respectively. This indicates that the rates of decomposition increase for longer milling periods. The mass losses of 7.3 to 8.2 wt% (in the 105 to 180 ℃ region) are slightly lower than those for the milled 2LiBH$_4$-MnCl$_2$ samples (7.8-8.6 wt%).

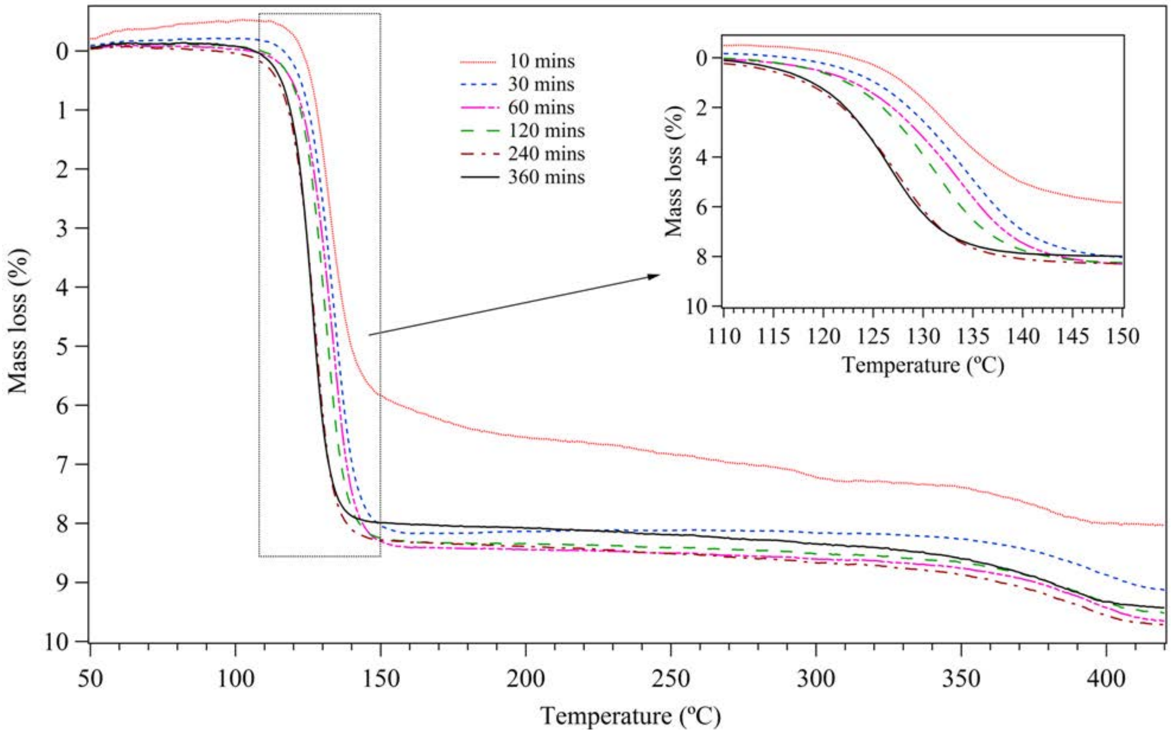

Figure 5.17 TGA profiles of 3LiBH-MnCl$_2$ samples milled for different time period, heated at 2 ℃ /min under 1.5 bar Ar flowing at 40 ml/min

Table 5.4 Summary of TGA profiles for the milled $3LiBH_4$-$MnCl_2$ samples

TGA properties	Milling time (minutes)					
	10	30	60	120	240	360
First onset decomposition temperature (ºC)	115	113	112	110	106	105
First end decomposition temperature (ºC)	180	155	150	149	145	145
First observed mass loss (wt%)	7.3±0.2	8.2±0.1	8.2±0.3	8.2±0.3	8.1±0.2	8.1±0.2
First calculated mass loss from $Mn(BH_4)_2$ phase alone (wt%) *	16.5	18.6	18.4	18.5	18.2	18.1
Theoretical H content of $Mn(BH_4)_2$ (wt%)	9.53					
Second onset decomposition temperature (ºC)	340	340	320	320	320	320
Second end decomposition temperature (ºC)	400	420	415	415	415	410
Second observed mass loss (wt%)	0.7±0.1	0.8±0.2	0.9±0.1	0.9±0.2	0.9±0.1	0.9±0.2
Total observed mass loss (wt%)	8.0	9.0	9.1	9.1	9.0	9.0

**Observed mass loss × $(M_{LiBH_4} + M_{Mn(BH_4)_2} + 2M_{LiCl}) / M_{Mn(BH_4)_2}$, where M is molecular mass.*

Thermogravimetric analysis coupled with MS of the $3LiBH_4$-$MnCl_2$ sample milled for 360 minutes (Figure 5.18) shows that the first decomposition between 105 and 145 °C with a mass loss of 8.1 ± 0.2 wt% is accompanied by the concurrent evolution of hydrogen and diborane, which is attributed to the decomposition of $Mn(BH_4)_2$. The second decomposition of 0.9 ± 0.2 wt% between 320 and 410 °C is accompanied only by the hydrogen evolution, which is in the range consistent with a 9 wt% (1.0 wt% of total system) decomposition of residual $LiBH_4$ (Züttel et al., 2003b). Unlike for the milled $2LiBH_4$-$MnCl_2$ sample, no hydrogen MS peak is observed at 170 °C. The 25 °C reduction in the decomposition temperature of $Mn(BH_4)_2$ for the milled $3LiBH_4$-$MnCl_2$ sample could be due to: a change in decomposition mechanism; a change in microstructure brought about by a different milling behaviour as a result of the presence of the remnant $LiBH_4$; and/or some form of catalytic effect of the $LiBH_4$ (Fang et al., 2010b).

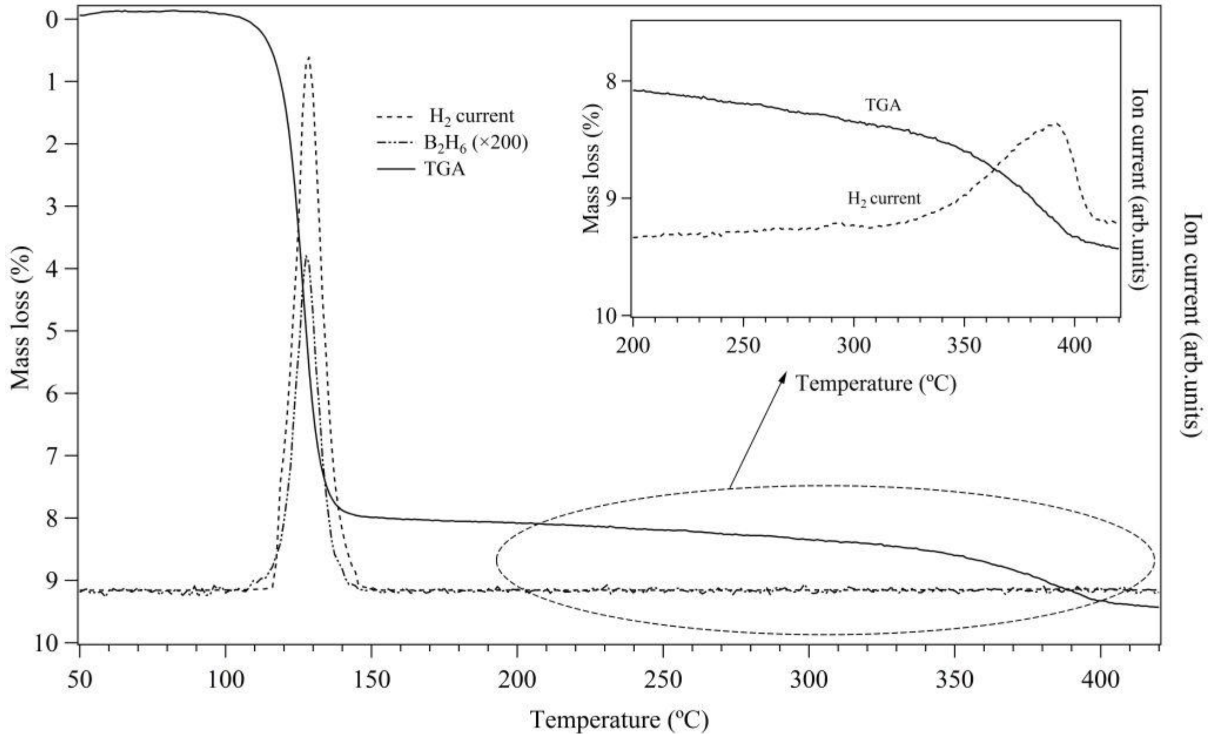

Figure 5.18 TGA profile for $3LiBH_4$-$MnCl_2$ sample milled for 360 minutes, coupled with MS data for evolved H_2 and B_2H_6 gases, heated at 2 ℃ /min under 1.5 bar Ar flowing at 40 ml/min

In the case of the $3LiBH_4$-$MnCl_2$ sample milled for 10 minutes, TGA coupled with MS shows a multi-step decomposition process (Figure 5.19), where the first major peak of released hydrogen along with diborane is located at 133 ℃ . The following minor hydrogen evolution with insignificant release of diborane is between 210 and 290 ℃ . These peaks are possibly related to a multi-step decomposition of the formed Mn-based borohydride although the composition of this complex borohydride is still unknown. In the temperature range of 300-400 ℃ , there are two hydrogen evolution peaks, which is due to the unreacted $LiBH_4$.

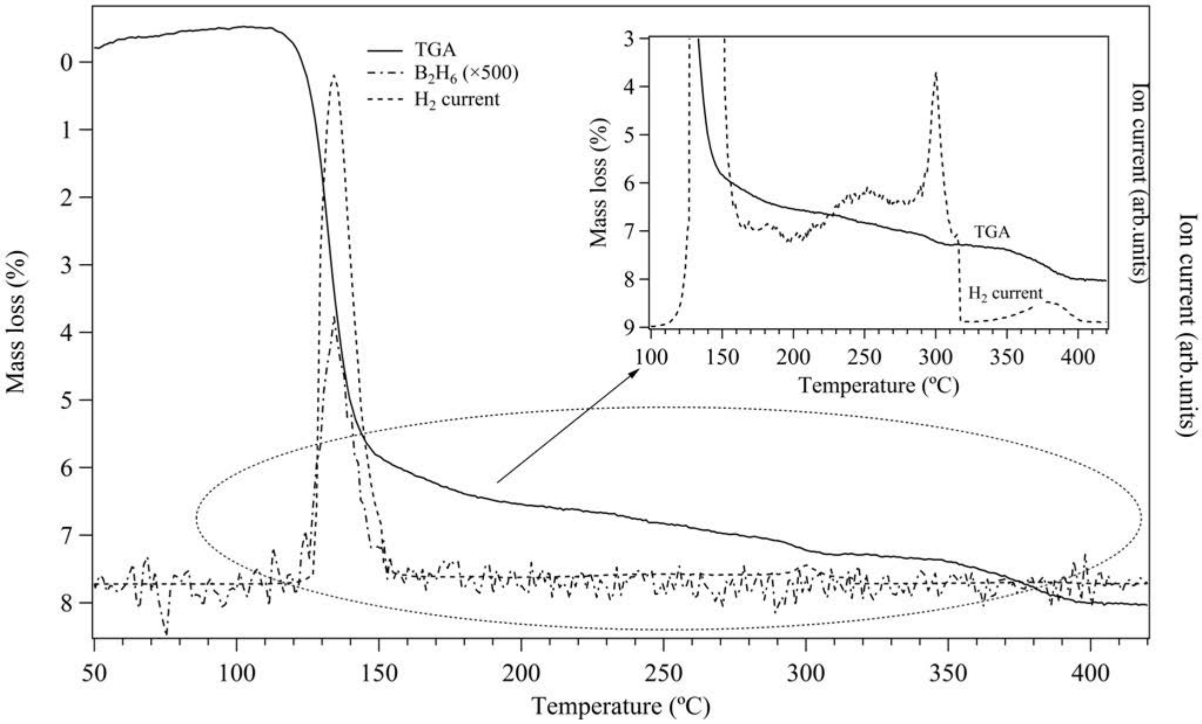

Figure 5.19 TGA profile for $3LiBH_4$-$MnCl_2$ sample milled for 10 minutes, coupled with MS for evolved H_2 and B_2H_6 gases, heated at 2 °C/min under 1.5 bar Ar flowing at 40 ml/min

5.2.2 Differential scanning calorimetric analysis

Differential scanning calorimetry of the $2LiBH_4$-$MnCl_2$ samples milled for different durations (Figure 5.20) shows a number of peaks. The most significant peaks for the samples milled for 30 to 360 minutes are endothermic peaks between 130 and 170 °C, which correspond to the temperatures of the mass losses observed in the TGA (Figure 5.14) for the thermal decomposition of $Mn(BH_4)_2$. The position of these endothermic peaks slightly reduces in temperature from 158 to 149 °C as the milling duration is increased from 30 to 360 minutes. This improvement in decomposition kinetics may be due to the reduction in particle size of $Mn(BH_4)_2$ with increased milling time (Varin et al., 2006). Moreover, there are visible endothermic shoulders occurring around 175 ℃ for the $2LiBH_4$-$MnCl_2$ samples with 30 to 360 minutes milling time, further suggesting that either there are two distinct mechanisms for decomposition or that the decomposition involves a two-step process proceeding via an intermediate species; these processes produce a small amount of hydrogen, as shown in MS data in Figure 5.15.

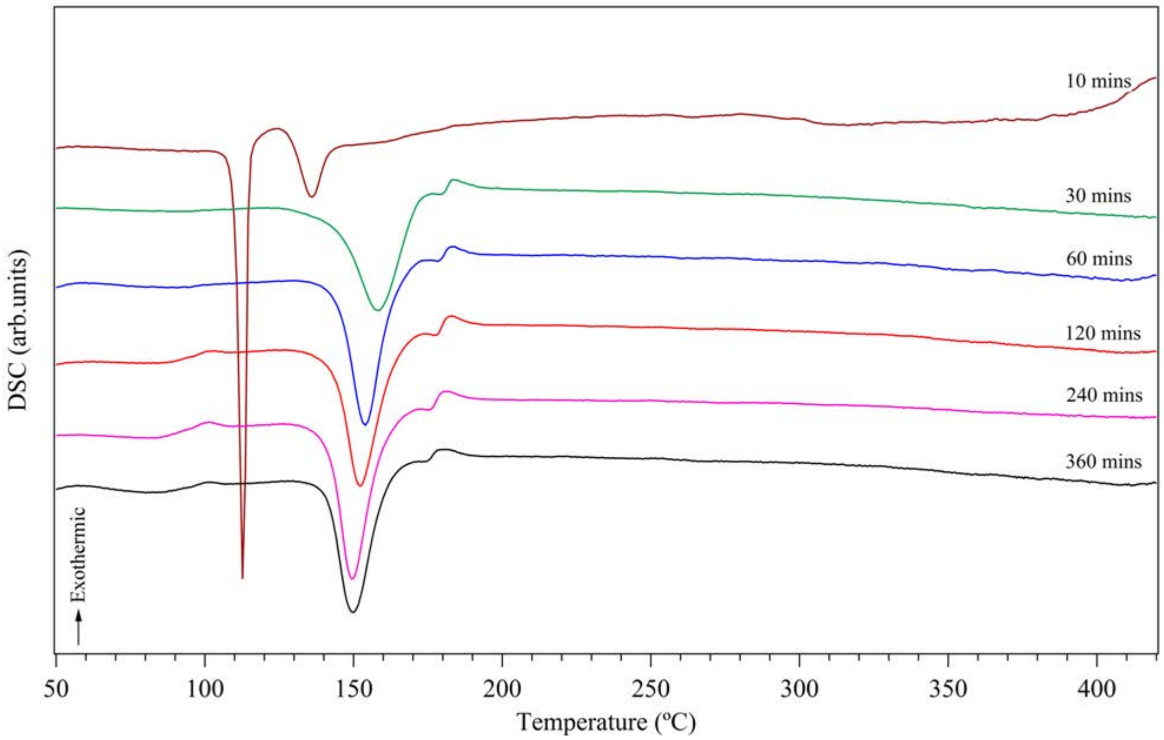

Figure 5.20 DSC profiles of 2LiBH$_4$-MnCl$_2$ samples milled for different durations, heated at 2 °C/min under 3 bar Ar flowing at 100 ml/min

The DSC for the 10-minute milled $2LiBH_4$-$MnCl_2$ sample appears rather different. There is a broad endothermic peak at ~ 135 ℃ associated with the decomposition of manganese borohydride which is accompanied by the evolution of hydrogen and diborane (Figure 5.16), and a large sharp peak at approximately 112 ℃ which is not accompanied by any mass loss or gas release (Figure 5.16).

After heating the 10-minute milled $2LiBH_4$-$MnCl_2$ sample to 120 °C, an exothermic peak is observed at around 94 °C during cooling to room temperature (see Figure 5.21). It has been reported that the phase change of $LiBH_4$ occurring at 117.5 °C when the samples is heated at 2

°C/min in 3 bar Ar flowing is fully reversible over several cycles to 200 °C with an exothermic DSC peak around 105 °C during cooling to room temperature (Reed, 2009).

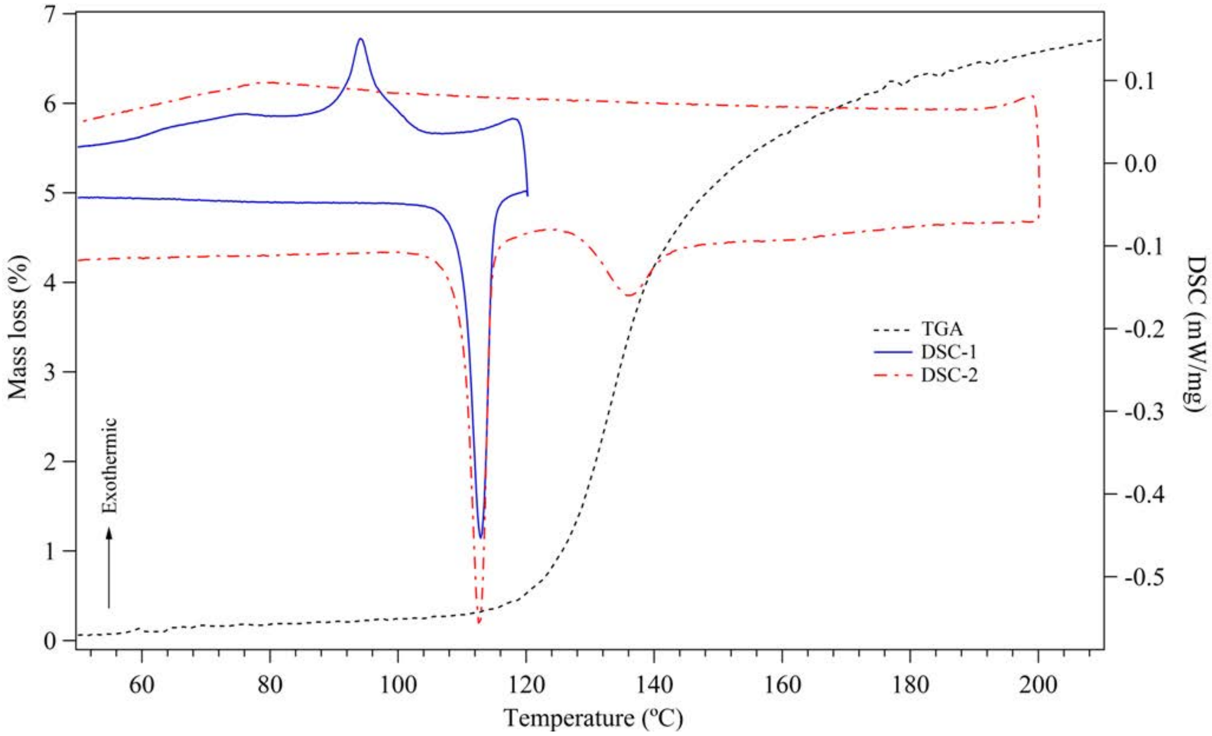

Figure 5.21 DSC profile of the 10-minute milled $2LiBH_4$-$MnCl_2$ sample heated to 120 (DSC-1) and to 200 °C (DSC-2) then cooled to RT at 2 °C/min under 3 bar Ar flowing at 100 ml/min, coupled with TGA data

In this study, however, there is no reversibly exothermic DSC peak for the sample heated up to 200 °C and then cooled down. Through another cycle of heating and cooling for the sample, no DSC peaks can be found (not shown here). Furthermore no other distinct calorimetric reactions are observed from $LiBH_4$ when heated to 420 ℃ (see Figure 5.20), for instance, no melting point at 290 ℃ for $LiBH_4$ and at 297°C for Cl^- ions substituted $LiBH_4$, and also no expected decomposition at 400 ℃ for $LiBH_4$ or Cl^- substituted $LiBH_4$ (Arnbjerg et al., 2009). These results indicate that the sharp endothermic peak at 112 ℃ for the $2LiBH_4$-$MnCl_2$ sample milled for 10 minutes is not associated with $LiBH_4$ or Cl^- substituted $LiBH_4$, but is related to the phase change of a Mn-based borohydride (Li-Mn-BH_4) that is formed via an incomplete exchange reaction (equation (3.58)) although the composition and structure of this complex borohydride is still unknown, which should be further investigated by *in-situ* XRD.

Figure 5.22 shows the DSC profiles of the $3LiBH_4$-$MnCl_2$ samples milled for different durations. The milled $3LiBH_4$-$MnCl_2$ samples show several DSC peaks. The decomposition of manganese borohydride $Mn(BH_4)_2$ occurs with an endothermic peak at around 128-137 °C, which slightly decreases (137 to 128 °C) with increased milling from 10 to 360 minutes. A sharp peak at 112 °C for the sample milled for 10 minutes disappears gradually and a new peak can be found at the lower temperature e.g. 99 °C for the sample milled for 360 minutes.

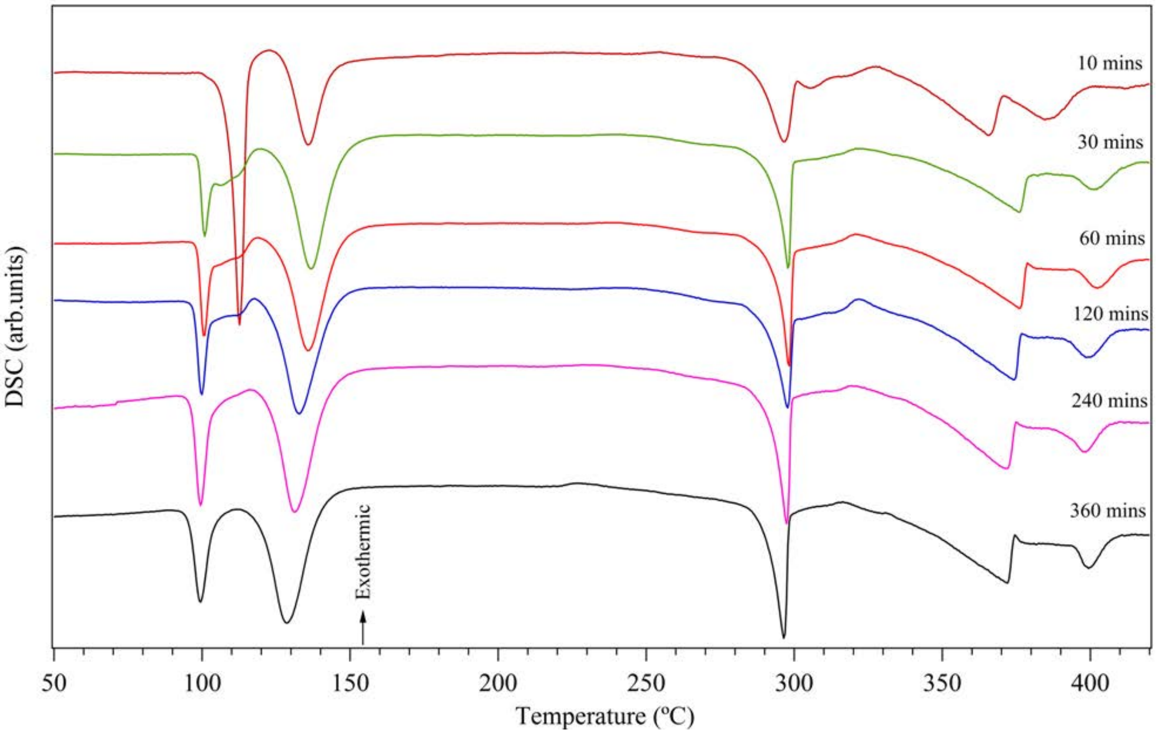

Figure 5.22 DSC profiles of $3LiBH_4$-$MnCl_2$ samples milled for different durations, heated at 2 °C/min under 3 bar Ar flowing at 100 ml/min

The significant difference between the milled $2LiBH_4$-$MnCl_2$ and $3LiBH_4$-$MnCl_2$ samples is that the milled $3LiBH_4$-$MnCl_2$ samples show DSC features associated with $LiBH_4$. For instance the endothermic peak occurring at ~ 100 °C for the 360-minute milled sample is attributed to the orthorhombic to hexagonal phase change in the excess $LiBH_4$ although this value is significantly lower than in pure $LiBH_4$ (118 °C) possibly due to Cl^- substitution for $[BH_4]^-$ ions (Arnbjerg et al., 2009; Oguchi et al., 2009). An endothermic peak at 298 °C is due to the melting of $LiBH_4$. There then follows a series of peaks typical of the decomposition of $LiBH_4$ (Arnbjerg et al., 2009; Pendolino et al., 2009). These DSC features show a very good agreement with TGA and MS results.

After heating the 360-minute milled $3LiBH_4$-$MnCl_2$ sample to 110 and 200 ℃ , exothermic peaks are observed at 72 and 67 ℃ , respectively, during cooling to room temperature (Figure 5.23). This is due to the reversible hexagonal to orthorhombic transition for the $LiBH_4$ phase (Reed, 2009).

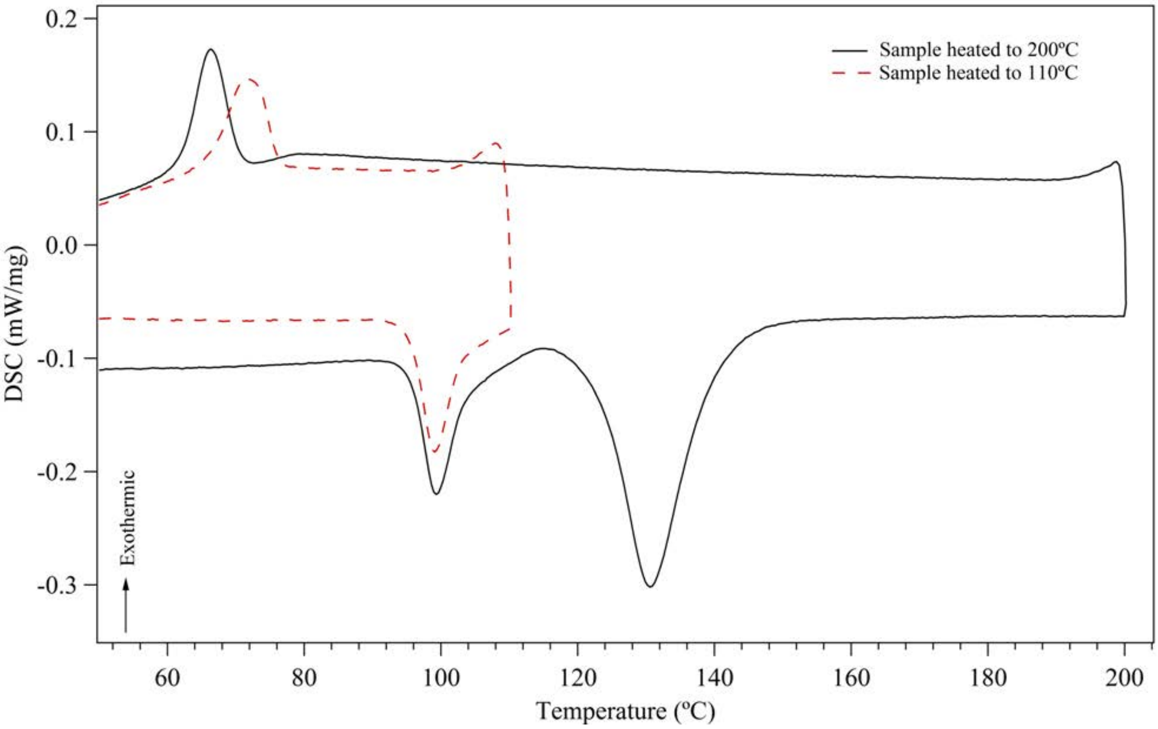

Figure 5.23 DSC profiles of $3LiBH_4$ -$MnCl_2$ samples milled for 360 minutes, heated to 110 and 200 °C then cooled to RT at 2 °C/min under 3 bar Ar flowing at 100 ml/min

The DSC profiles of the 10-minute milled $3LiBH_4$-$MnCl_2$ and $2LiBH_4$-$MnCl_2$ samples which were heated to 120 ℃ then cooled to room temperature, are shown in Figure 5.24. The milled $3LiBH_4$-$MnCl_2$ sample exhibits a lower peak onset temperature (100 ℃) compared to $2LiBH_4$-MnCl (105 °C), and a significant overlap of endothermic peaks around 100-116 ℃. An exothermic peak at around 94 ℃ is present in both milled samples. While a weak and broad exothermic peak at around 72 ℃ during cooling is only observed for the $3LiBH_4$-$MnCl_2$ sample on cooling, suggesting that the endothermic reaction around 100-116 ℃ is associated with the phase change of both the Mn-based borohydride(Li-Mn-BH_4) and a small amount of unreacted $LiBH_4$ or Cl^- substituted $LiBH_4$.

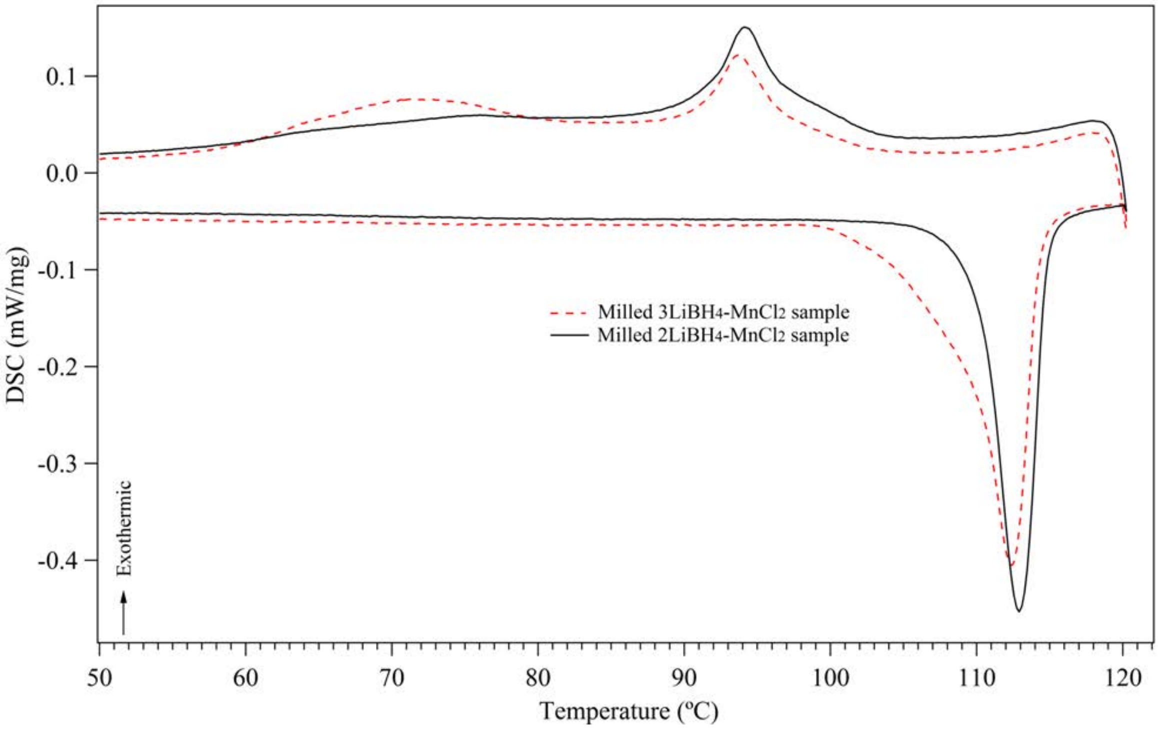

Figure 5.24 DSC profiles for $3LiBH_4$ -$MnCl_2$ and $2LiBH_4$ -$MnCl_2$ samples milled for 10 minutes, heated to 120 °C then cooled to RT at 2 °C/min under 3 bar Ar flowing at 100 ml/min

5.3 Decomposition behaviour

5.3.1 Milled $2LiBH_4$-$MnCl_2$

In-situ XRD heating from room temperature to 400°C in an inert atmosphere was performed to monitor any changes in the crystalline phases as a function of temperature. Samples were loaded in Al_2O_3 crucibles and therefore small reflections due to the crucible are observed in all patterns. Figure 5.25 shows the patterns from the $2LiBH_4$-$MnCl_2$ sample milled for 360 minutes. At room temperature reflections due to the reaction products LiCl and $Mn(BH_4)_2$ are observed. On heating to 130 °C the $Mn(BH_4)_2$ phase starts to decompose and the diffraction peaks for this compound are no longer present between 150 and 160 °C. The unit cell parameters of $Mn(BH_4)_2$ with the space group symmetry $P3_112$ are plotted as a function of temperature, as shown in Figure 5.26. Between 50 and 150 °C, the *a* lattice parameter increases while the *c* parameter decreases, which is similar to the anisotropic trend reported by Černý et al (2009). This change in lattice cell parameters follows the deformation of the $Mn(BH_4)_2$ structure with increasing temperature. After further heating to 400 °C there are no diffraction peaks corresponding to decomposition products, e.g. metallic manganese or boron-containing species, only LiCl. The shape and intensity of the diffraction peaks for LiCl are similar to those at lower temperatures, apart from a slight shift in peak position as a result of thermal expansion with increased temperature. The absence of diffraction peaks suggests the formation of amorphous manganese and/or boron phases.

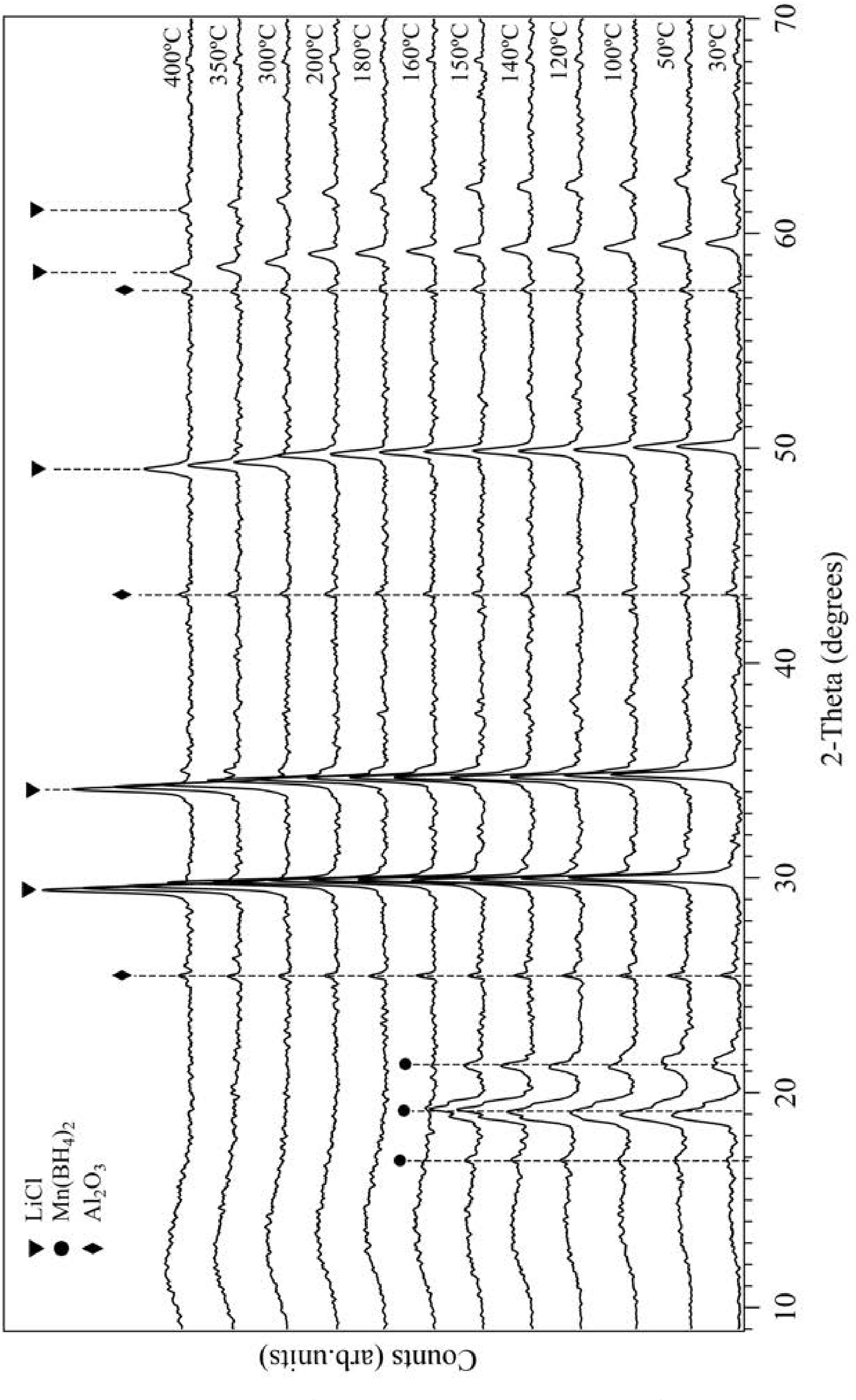

Figure 5.25 In-situ XRD patterns of $2LiBH_4$-$MnCl_2$ sample milled for 360 minutes, heated at 2 °C/min in 4 bar He flowing at 100 ml/min

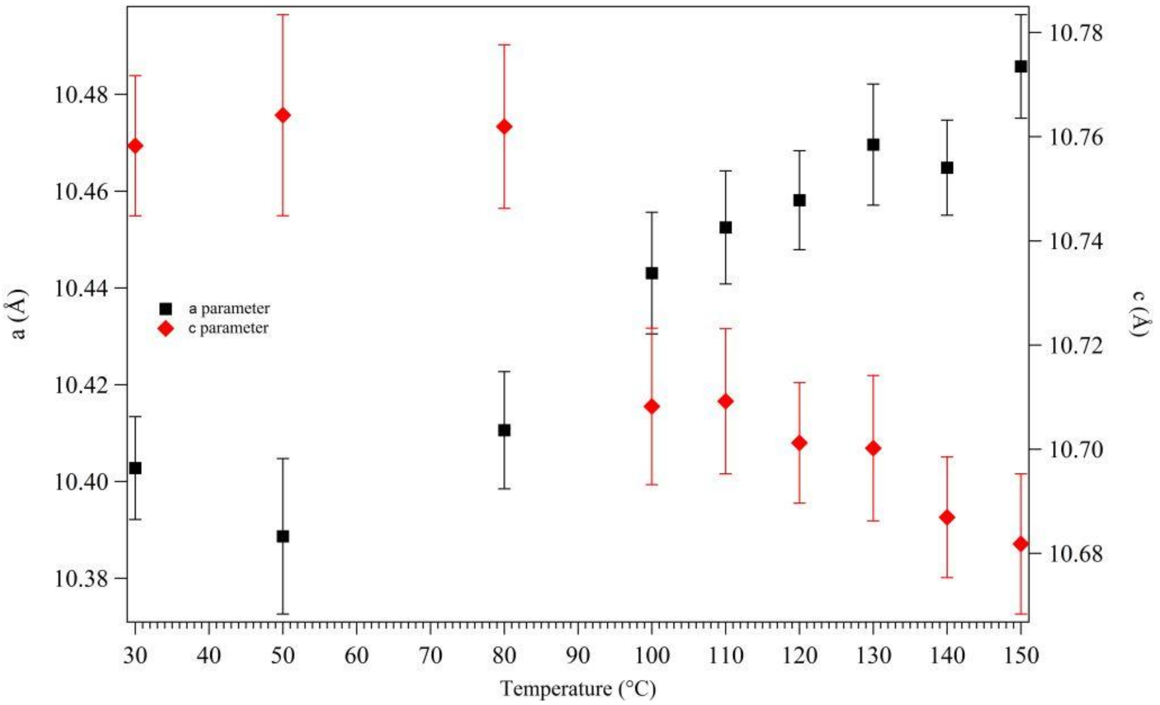

Figure 5.26 Effect of temperature on the lattice parameters of the $Mn(BH_4)_2$ compound in the 360-minute milled $2LiBH_4$-$MnCl_2$ sample; error bars show 3ESDs

In-situ Raman spectroscopy of the 360-minute milled $2LiBH_4$-$MnCl_2$ sample (Figure 5.27) shows a reduction in intensity of the B-H stretching modes (2269, 2155 and 2460 cm^{-1}) and bending bands (1092, 1155, 1172 and 1353 cm^{-1}) at 120 °C with no B-H stretching or bending modes present at 150 °C; this corresponds to the thermal decomposition of $Mn(BH_4)_2$ with the loss of H_2 and B_2H_6. On the other hand, after the decomposition of the milled $2LiBH_4$-$MnCl_2$ sample there are very weak and broad bands formed around 350-450, 700-900 and 1050-1150 cm^{-1} for the reaction products from the milled sample, as shown in Figure 5.28, which are in fairly reasonable agreement with Raman vibrations for amorphous boron (Sigma Aldrich) although the intensity of the peak of the milled sample is much lower.

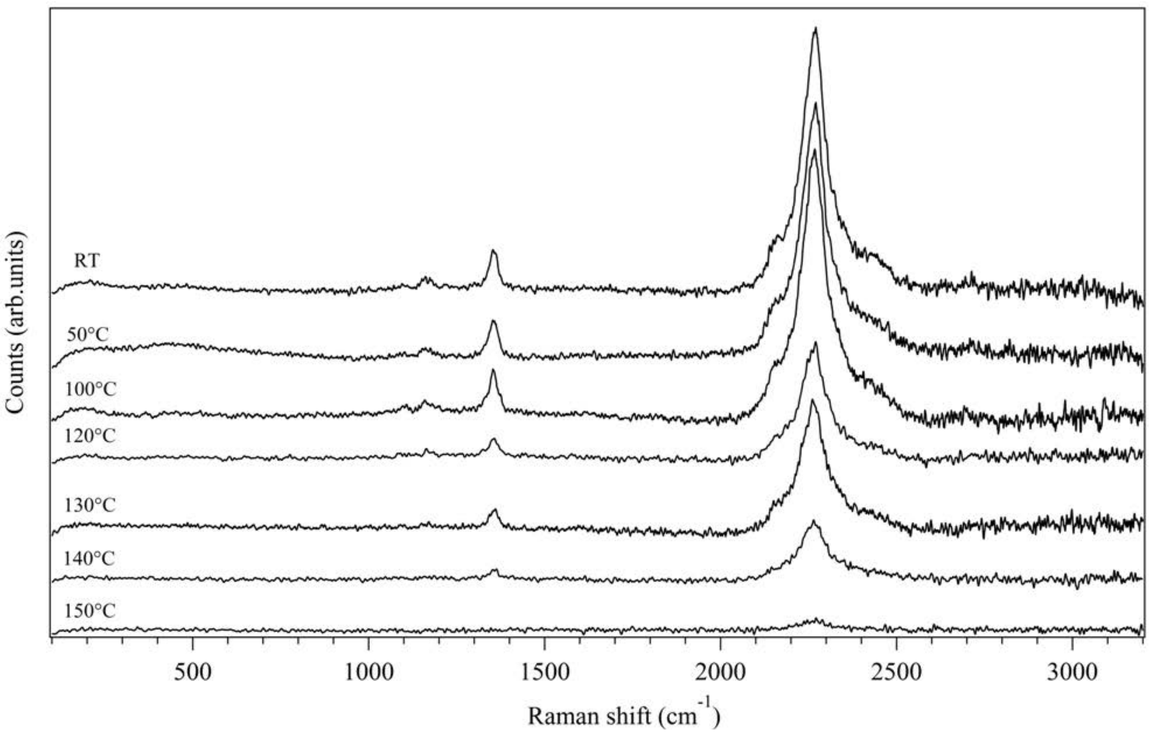

Figure 5.27 In-situ Raman spectra of $2LiBH_4$*-*$MnCl_2$ *sample milled for 360 minutes, heated at 2 °C/min in 1 bar Ar flowing at 100 ml/min*

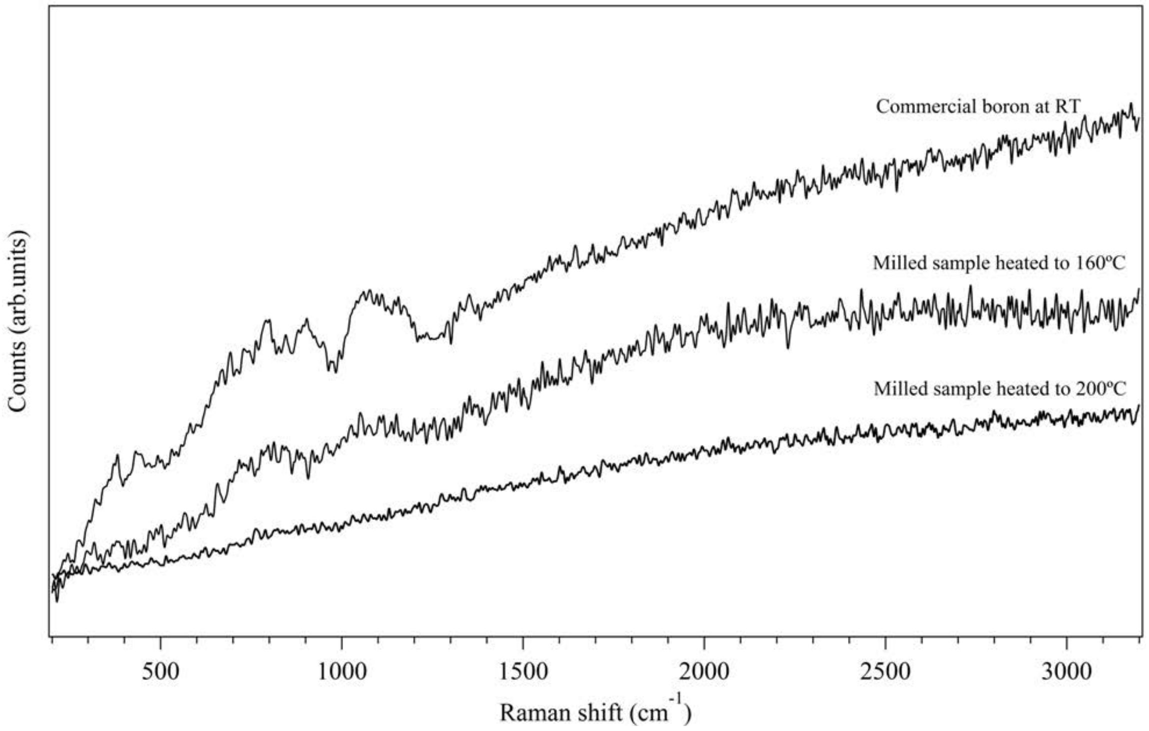

Figure 5.28 In-situ Raman spectra of $2LiBH_4$ *-*$MnCl_2$ *sample milled for 360 minutes, (heated to 160 °C and 200 ℃) and commercial amorphous boron (room temperature)*

Raman spectroscopic measurement was carried out on 360-minute milled $2LiBH_4$-$MnCl_2$ samples that had been heated to 200 and 500 °C, and then subsequently exposed to air for 5 minutes at room temperature. Figure 5.29 shows the Raman spectra of the decomposed products for the milled $2LiBH_4$-$MnCl_2$ sample and commercial manganese powder exposed to air as reference. A sharp band at 660 cm^{-1} is observed for all the samples, which is attributed to manganese oxide (Mn_3O_4) (Buciuman et al., 1999; Mironova-Ulmane et al., 2009). This result may indirectly indicate that manganese is formed as one of the decomposition products of the milled $2LiBH_4$-$MnCl_2$ sample.

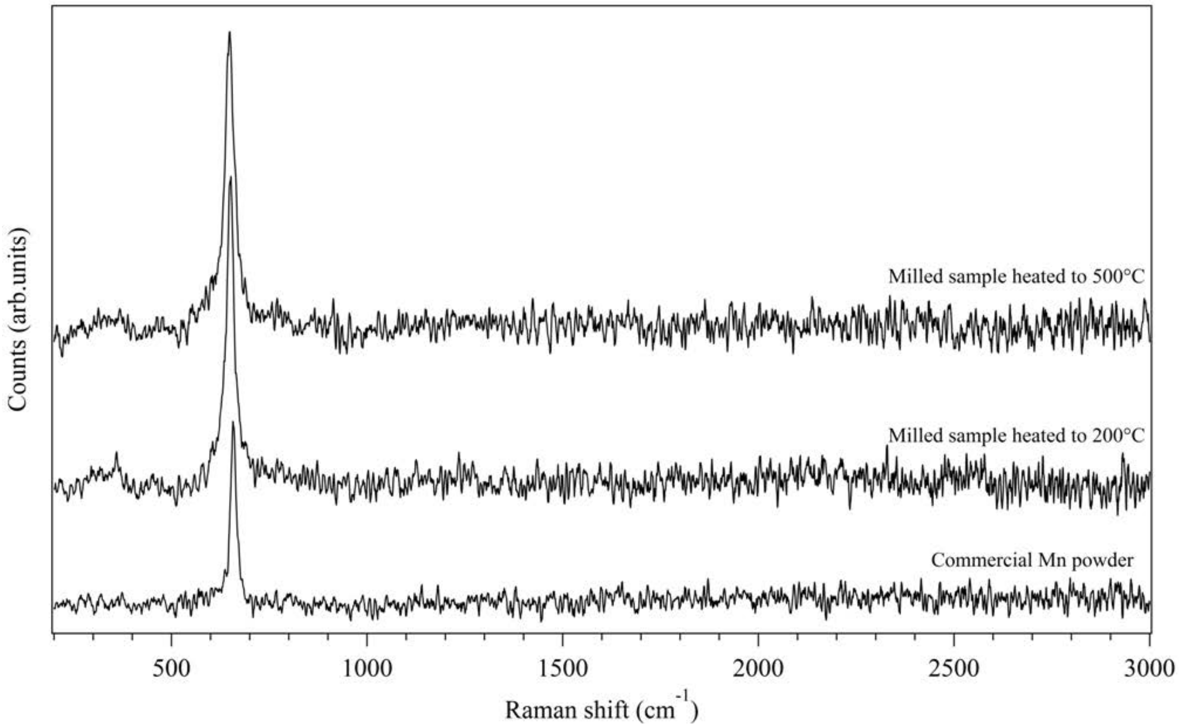

Figure 5.29 Raman spectra of $2LiBH_4$ -$MnCl_2$ milled for 360 minutes, heated to 200 and 500 ℃ and then exposed to air (commercial Mn powder, exposed to air, as a reference)

Figure 5.30 shows FTIR spectra of milled $2LiBH_4$-$MnCl_2$ sample after heating, with an as milled sample as a reference. The sample that had been heated to 200 °C shows no B-H vibration modes, as shown for the as milled sample, while bands at 943, 1039, 1245 and 1331

cm^{-1} may be associated with B-B vibrations attributed to amorphous boron. Upon further heating to 500 °C no new vibrations are observed.

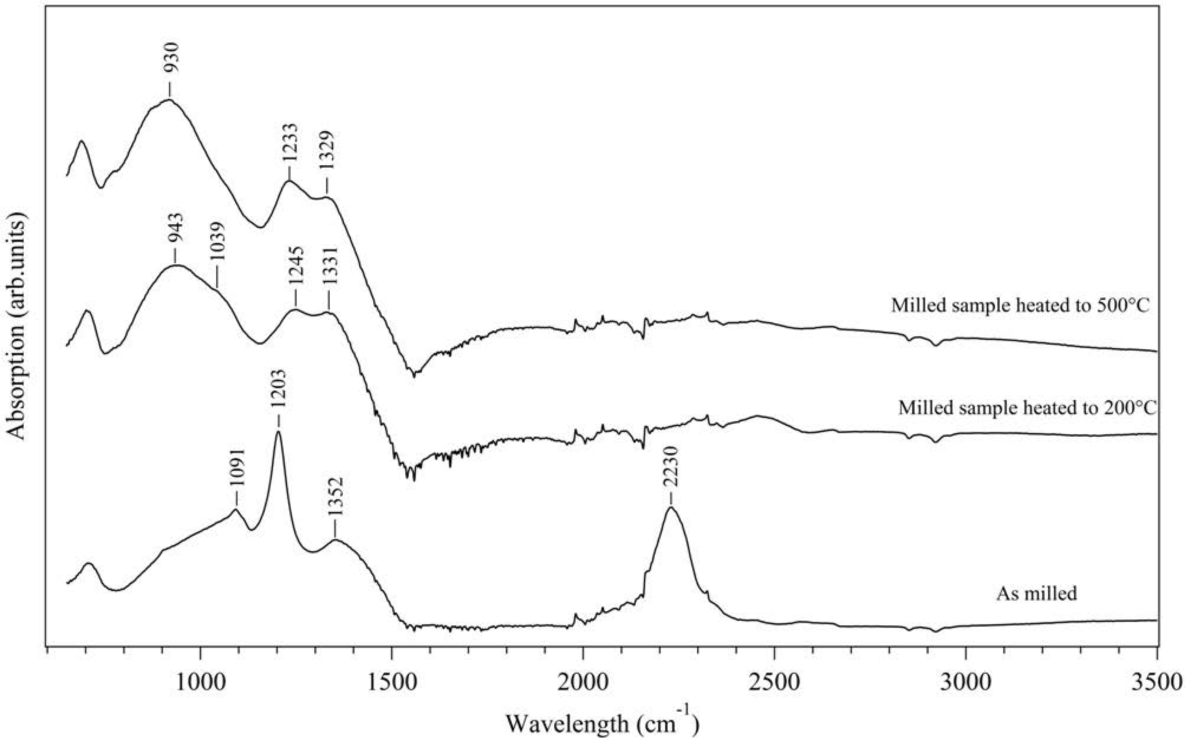

Figure 5.30 FTIR spectra of $2LiBH_4$-$MnCl_2$ *sample milled for 360 minutes, heated to 200 and 500 ℃ under Ar flowing (as milled sample as a reference)*

There are many thermal decomposition pathways possible for metal borohydrides (Choudhury et al., 2009a; Reed and Book, 2011). Many involve the evolution of hydrogen (and/or diborane) to leave the metal (equations (5.2) and (5.3)), boron (equations (5.2) and (5.5)), metal boride (equation (5.4)), metal hydride (equation (5.5) and (5.6)) or a borane(s) (e.g. dodecaborane $[B_{12}H_{12}]^{2-}$) as the solid decomposition products. The most probable decomposition reactions for $Mn(BH_4)_2$ (or a combination, thereof), were shown in equations (5.2) to (5.6) (Choudhury et al., 2009a). The expected mass loss for equations (5.2) and (5.4) would be 9.53 wt%. A mass loss of 35.08 wt% would be expected from equation (5.3), and 7.09 or 32.7 wt% respectively from equation (5.5) or (5.6). None of these values are consistent with the calibrated mass loss (16.9 wt%) based on the experimental data although the theoretical calculations have reported that equation (5.2) could be the most feasible based on the calculated standard-state enthalpy of reaction and Gibbs energy (Choudhury et al., 2009a). Therefore it is possible that a combination of the above reactions is needed in order to describe the overall decomposition pathway.

The act of mechanically milling lithium borohydride and manganese chloride results in the formation of manganese borohydride and lithium chloride, as expressed in equation (5.1). The thermal decomposition of manganese borohydride has occurred by a two-step mechanism resulting in the evolution of hydrogen and diborane (9:1 molar ratio; although as discussed in Section 5.2.1 the amount of diborane is probably underestimated) leaving residual manganese and boron. It therefore seems likely that the thermal decomposition reaction of $Mn(BH_4)_2$ proceeds via a combination of equations (5.2) and (5.3) with a 2:1 ratio as shown in equation (5.7):

$$3Mn(BH_4)_2 \rightarrow 3Mn + 4B + B_2H_6 + 9H_2 \tag{5.7}$$

where the theoretical mass loss is calculated as 8.9 wt.% in $Mn(BH_4)_2$-2LiCl mixture, which matches the experimental data (8.4 wt.%). It is not clear why Mn is not observed by XRD (Figures 5.25) in this study, unless it is possibly in the form of finely dispersed nanoscale grains. Alternatively, an amorphous Mn-B compound, such as MnB (Sun et al., 2010) would explain the absence of Mn X-ray peaks, while theoretically giving similar wt% changes. However, the absence of Mn-B vibrations in the Raman and FT-IR spectra (RIDB, 2009), as shown in Figures 5.28-5.30, suggests that this is probably unlikely.

5.3.2 Milled $3LiBH_4$-$MnCl_2$

In-situ XRD patterns of the 360-minute milled $3LiBH_4$-$MnCl_2$ sample heated to 400 °C are shown in Figure 5.31. The similarity to the milled $2LiBH_4$-$MnCl_2$ sample is observed at room temperature, showing all the reflections are attributed to LiCl and $Mn(BH_4)_2$. Upon heating the reflections due to the hexagonal phase of $LiBH_4$ are observed between 120 and 300 °C. The decomposition of $Mn(BH_4)_2$ occurs between 130 and 150 °C with only a slight trace observed at 140 °C, correlating with the TGA and DSC results (Figures 5.18 and 5.22). Above 320 °C a number of unknown phases are observed. These peaks are not consistent with MnH, LiH, $Li_2B_{12}H_{12}$, $Li_2B_{10}H_{10}$, or Li_2MnCl_4 (Fukai et al., 2002; Her et al., 2008; Lutz and Schneider, 1990). However, these peaks can be tentatively assigned as three separate phases. Unknown phase I is observed with reflections at 13.1, 19.3 and 26.4° 2θ and unknown phase II with reflections at 20.2, 27.4 and 27.9° 2θ. Unknown phase I is no longer present above 380 °C where as unknown phase II is stable to 400 °C. At 400 °C unknown phase III is observed as a single reflection at 14.4° 2θ. The temperature region from 320 to 400 °C is consistent with the decomposition temperature range of $LiBH_4$ shown in Figure 5.18 and 5.22, where a broad hydrogen release takes place together with two endothermic DSC peaks at 320-380 °C and 390-420 °C. Thus, these unknown phases are likely to be the decomposition products of $LiBH_4$ forming within, and/or reacting with, the mixture of decomposed $Mn(BH_4)_2$ phases (Orimo et al., 2006; Reed and Book, 2011).

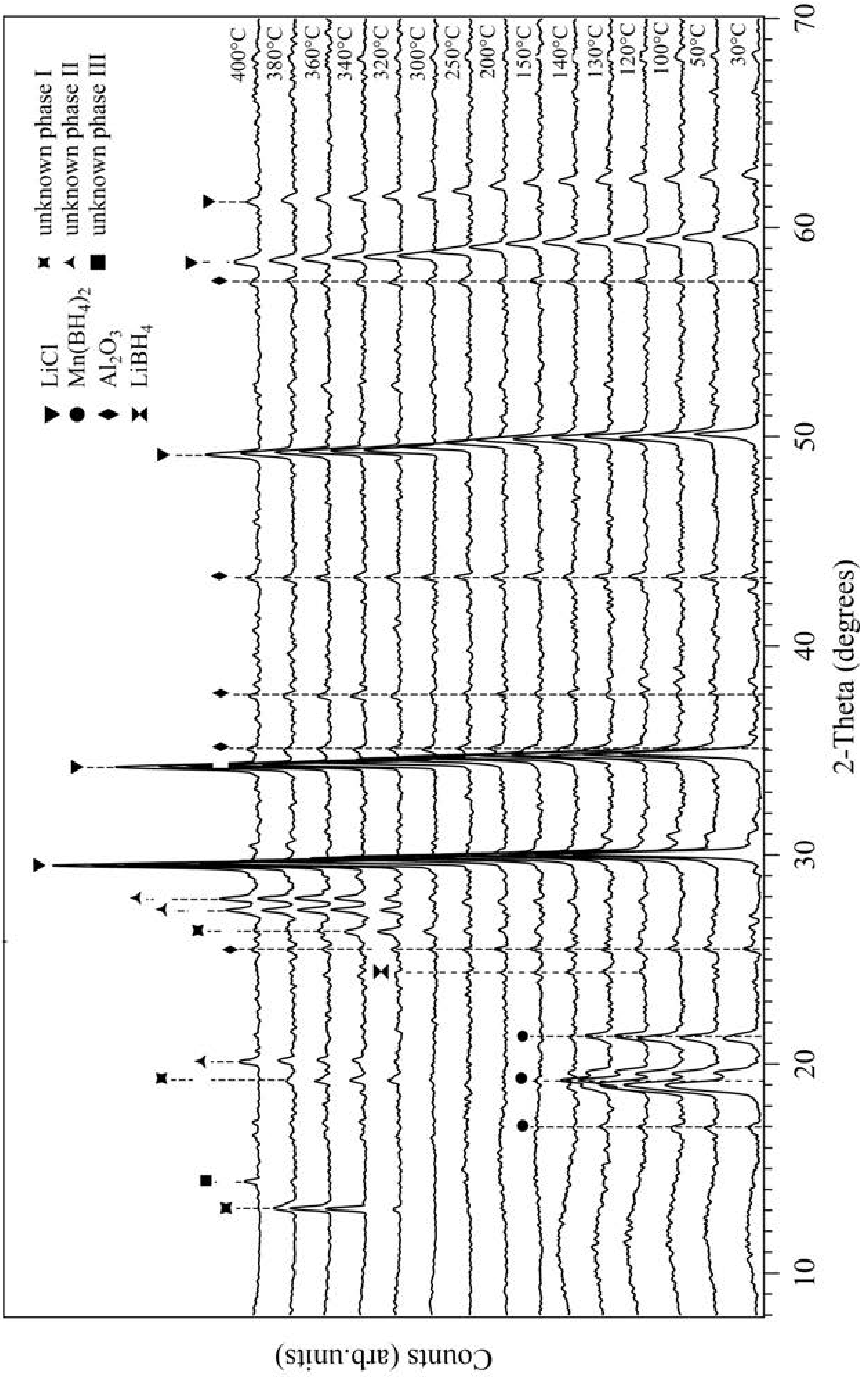

Figure 5.31 In-situ XRD patterns of $3LiBH_4$-$MnCl_2$ sample milled for 360 minutes, heated at 2 °C/min in 4 bar He flowing at 100 ml/min

In-situ Raman spectra of the milled $3LiBH_4$-$MnCl_2$ sample demonstrate the reduction in B-H stretching intensity, occurring at 100 °C with complete absence of B-H bonding above 130°C as $Mn(BH_4)_2$ decomposes (Figure 5.32). There are no bands observed for the remaining $LiBH_4$ after the decomposition of $Mn(BH_4)_2$. This is due to the small amount of $LiBH_4$ (approx 11.4 wt.%) in the mixture that consists of amorphous boron and manganese, decaying the Raman signal of $LiBH_4$. This decay effect has been investigated by physically mixing commercial amorphous boron with $LiBH_4$ in molar ratios between 1:10 and 2:1, as shown in Figure 5.33. The reduction in the intensity of the stretching modes of $LiBH_4$ is observed for the mixture of $LiBH_4$ and boron, and the B-H vibration modes completely disappear when the amount of boron in the mixture increases to a 2:1 molar ratio of boron to $LiBH_4$. After decomposition, very weak bands are formed around 700-900 and 1050-1150 cm^{-1} for the milled $3LiBH_4$-$MnCl_2$ (Figure 5.33), which is due to Raman vibrations of amorphous boron.

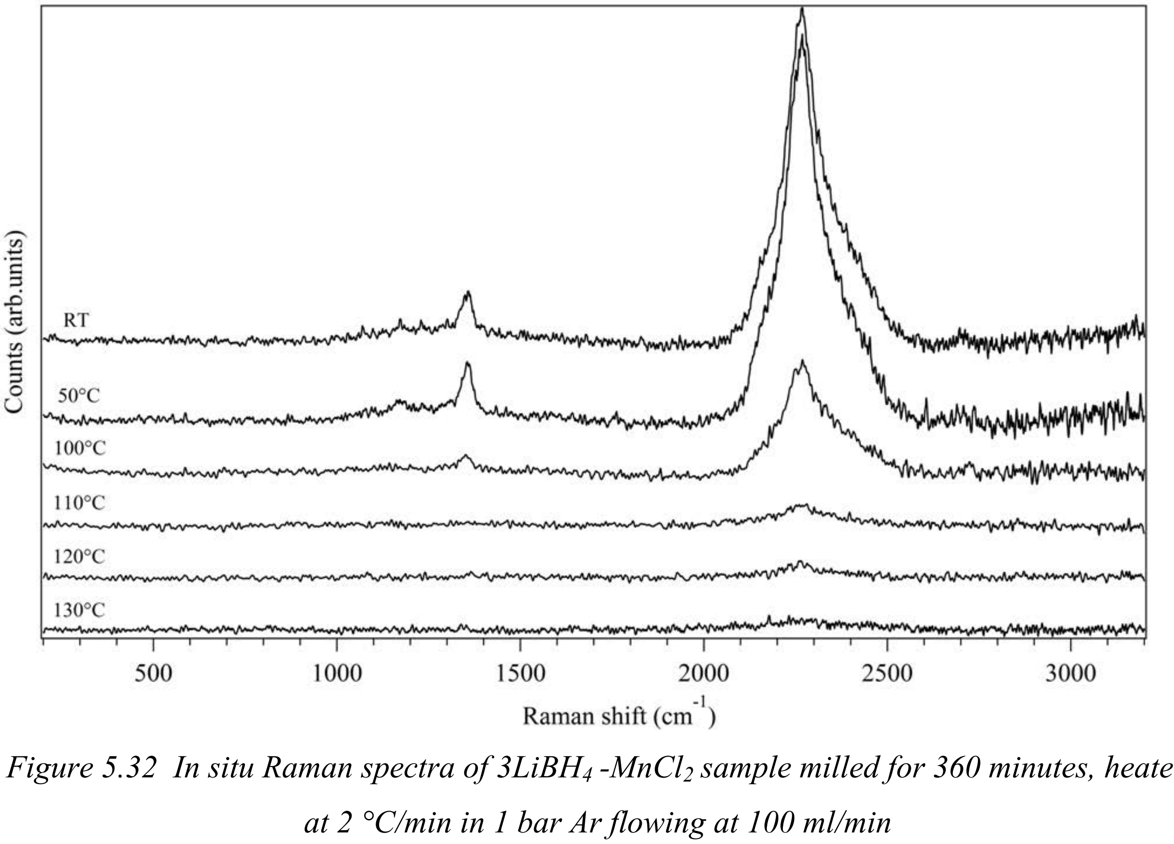

Figure 5.32 In situ Raman spectra of $3LiBH_4$ -$MnCl_2$ sample milled for 360 minutes, heated at 2 °C/min in 1 bar Ar flowing at 100 ml/min

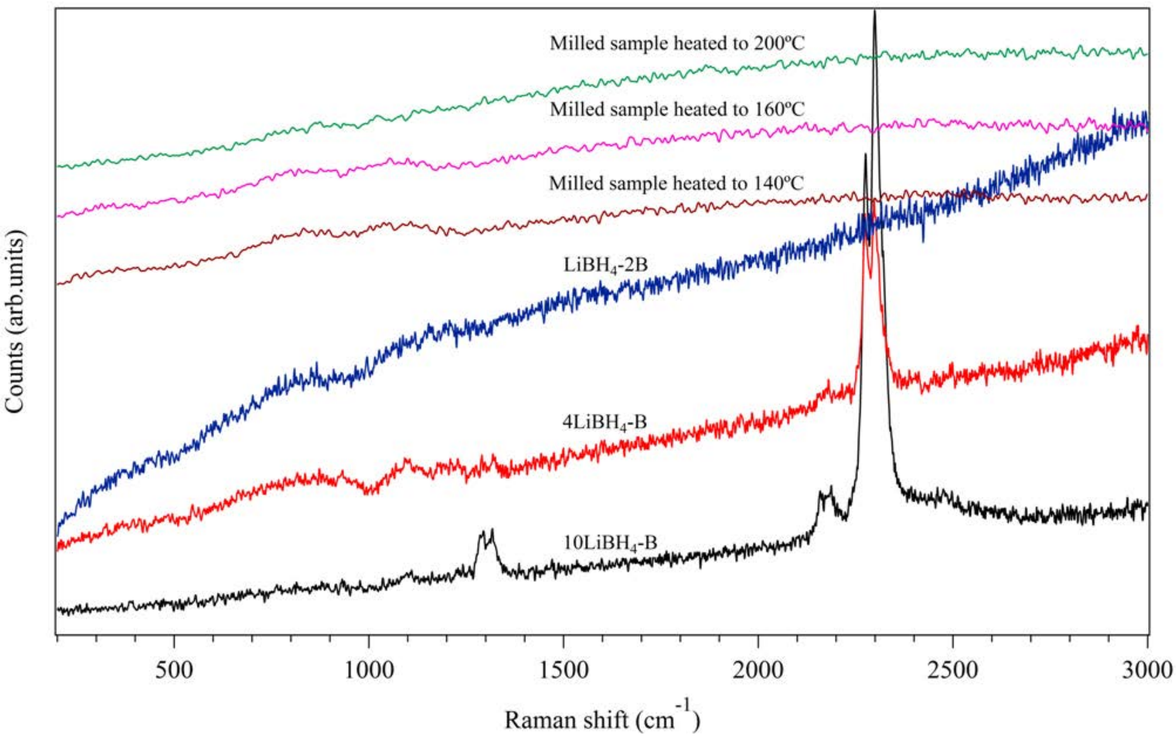

Figure 5.33 In-situ Raman spectra of milled $3LiBH_4$-$MnCl_2$ sample (heated to 140, 160 and 200 °C), and the mixture of $LiBH_4$ and boron with 10:1, 4:1 and 1:2 molar ratios(RT)

Raman spectra of the milled $3LiBH_4$-$MnCl_2$ decomposed at 200 and 500 °C show no peaks, however, when exposed to air for 2 minutes, the decomposed sample at 500 °C shows a sharp band at 648 cm^{-1}, which is similar to those of the milled $2LiBH_4$-$MnCl_2$ sample, attributed to Mn-O bonding vibration of manganese oxide (Figure 5.34) (Buciuman et al., 1999; Mironova-Ulmane et al., 2009). Moreover, there are additional Raman vibration modes occurring at 420, 480 and 598 cm^{-1} when the milled $3LiBH_4$-$MnCl_2$ sample decomposed at 200 °C was then exposed to air. These vibration modes are also believed to be associated with Mn-O bonding vibration of manganese oxide that transforms to different oxidation states, e.g. Mn_3O_4, Mn_2O_3, MnO_2, or interacts with the excess $LiBH_4$ in mixture (Buciuman et al., 1999; Julien et al., 2003; Mironova-Ulmane et al., 2009).

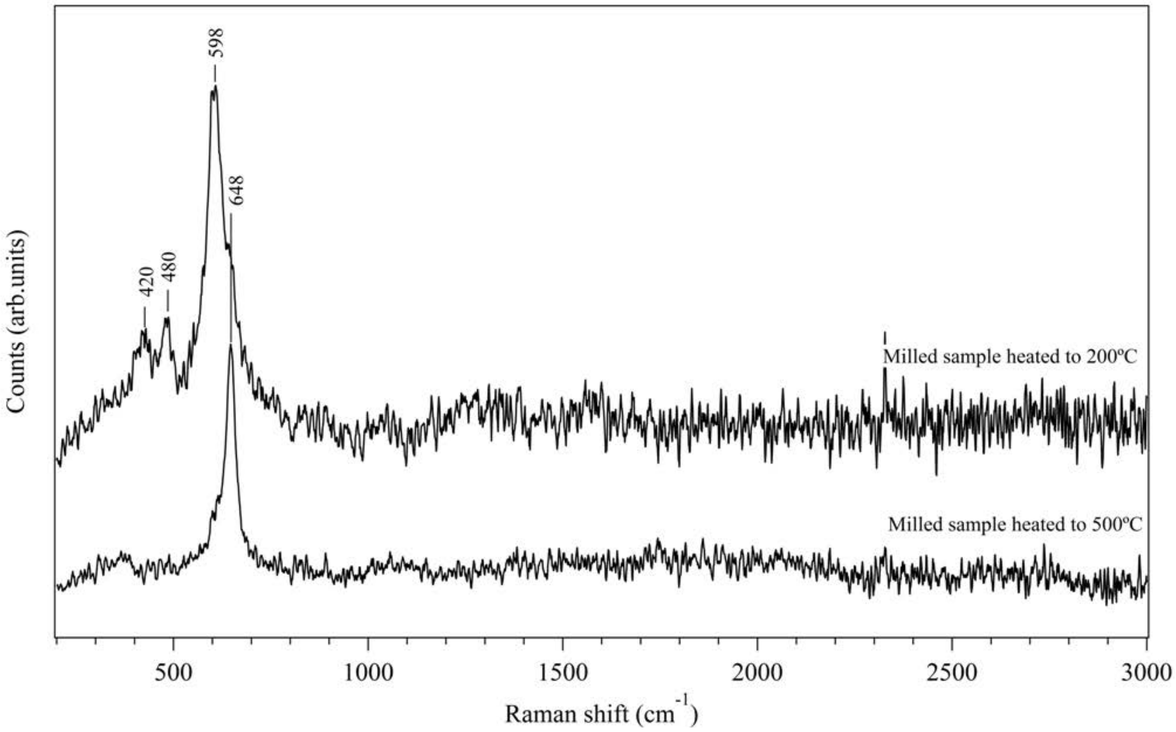

Figure 5.34 Raman spectra of 3$LiBH_4$-$MnCl_2$ sample milled for 360 minutes, heated to 200 and 500 ℃ under Ar flowing and then exposed to air

FTIR spectra of decomposed products for the milled 3$LiBH_4$-$MnCl_2$ sample are shown in Figure 5.35. Upon heating to 200 °C bands at 1093, 1237 and 2302 cm^{-1} are attributed to the bending and stretching modes respectively for $LiBH_4$, consistent with the presence of excess $LiBH_4$ that is not involved with the thermal decomposition of $Mn(BH_4)_2$. Bands at 946 and 1335 cm^{-1} for amorphous boron are consistent with the observations for the 2$LiBH_4$-$MnCl_2$ sample. Further heating to 500 °C the modes of $LiBH_4$ disappear and several new bands are observed at 684, 722, 868, 1079, 1142, 1362, 1395, 1604 and 2449 cm^{-1}. These bands have yet to be attributed to a specific compound(s) and may be related to the unknown phases observed during in situ XRD measurements.

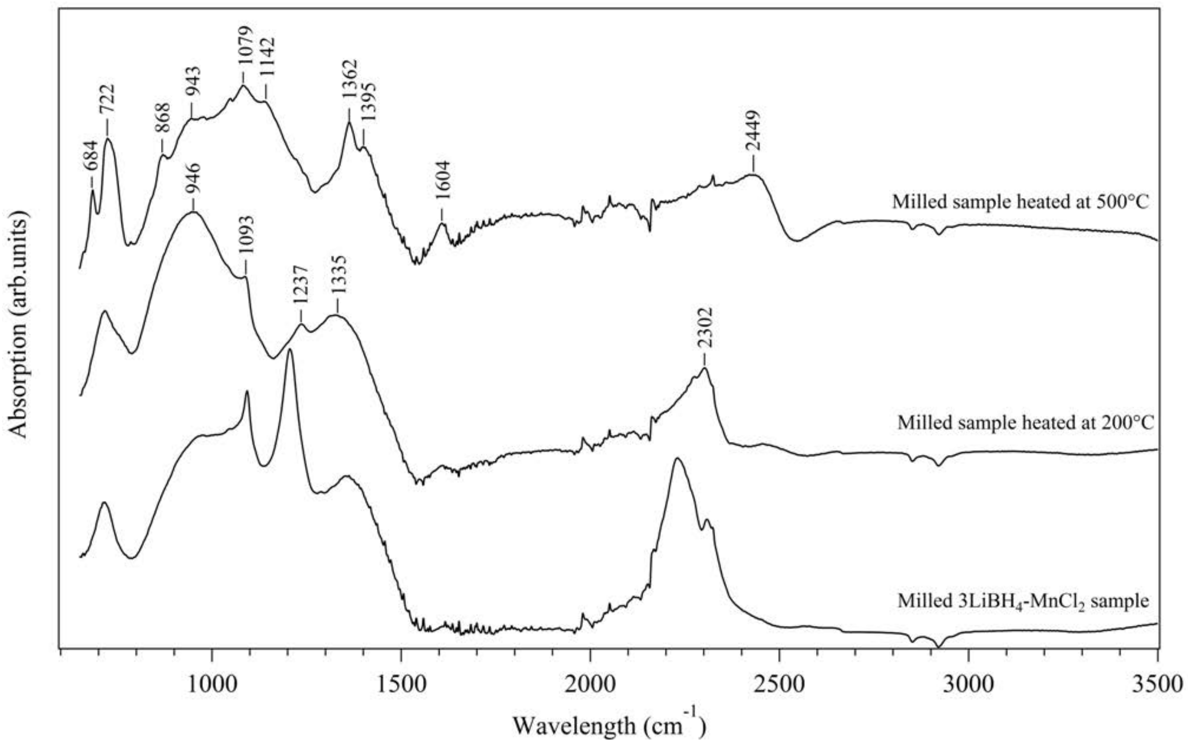

Figure 5.35 FTIR of 3LiBH$_4$*-MnCl*$_2$ *sample milled for 360 minutes, heated to 200 and 500 °C under Ar flowing (as milled sample as reference)*

5.4 Addition of 2mol% of additive

5.4.1 Effect of additives on synthesis

Many diverse species have been investigated as possible catalysts to modify adsorption and desorption properties of hydrogen in borohydrides. In this study, additives such as nickel (Ni), titanium (Ti), titanium chloride ($TiCl_3$) and niobium fluoride (NbF_5) were used to try to affect the decomposition behaviour of $Mn(BH_4)_2$, e.g. by changing the reaction temperature and/or reducing the amount of diborane evolved.

The XRD profiles of the $2LiBH_4$-$MnCl_2$-2 mol% A (A = Ni, Ti, $TiCl_3$ and NbF_5) samples milled for 360 minutes are shown in Figure 5.36. The diffraction peaks due to LiCl are present for all the milled samples and the reflections from $Mn(BH_4)_2$ are observed for the milled samples doped with Ni, Ti and $TiCl_3$ in spite of a reduction in the intensity of diffraction peak for the milled sample doped with $TiCl_3$. The most noticeable effect is for NbF_5, where no diffraction peaks for $Mn(BH_4)_2$ are observed.

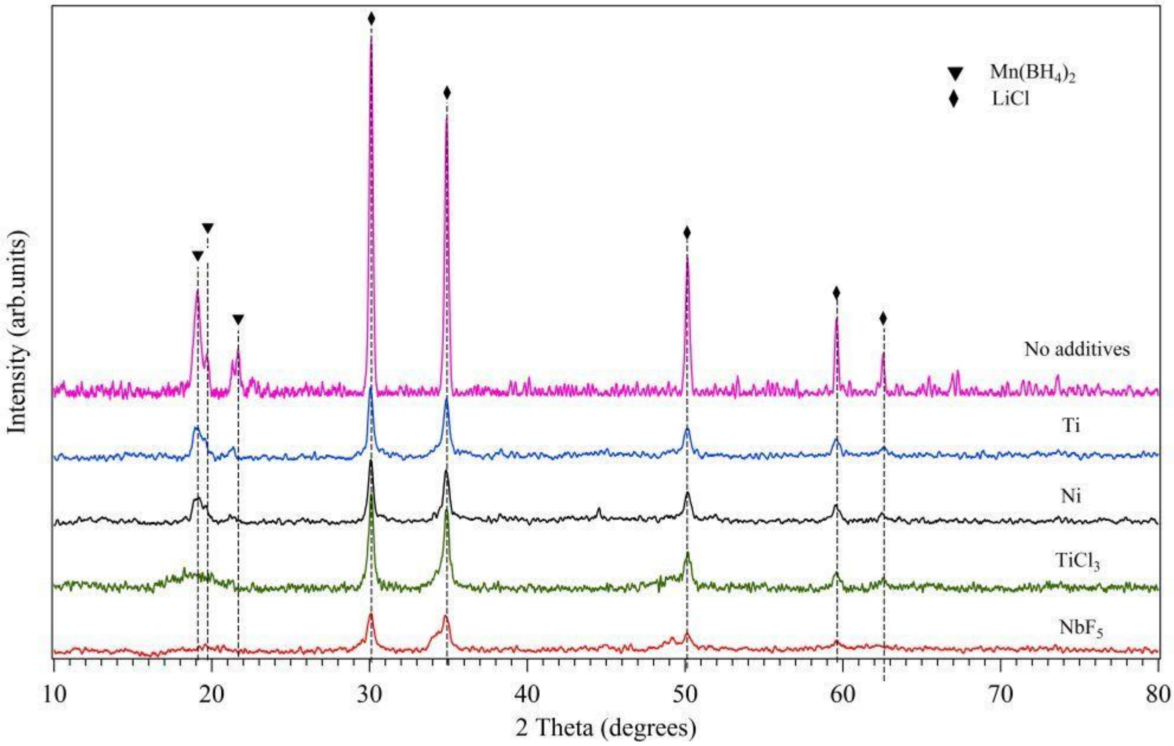

Figure 5.36 XRD patterns of $2LiBH_4$-$MnCl_2$-2 mol% A (A=Ni, Ti, $TiCl_3$ and NbF_5) samples milled for 360 minutes, undoped sample as reference

In the Raman spectra for the doped samples (Figure 5.37), Ni-, Ti- and $TiCl_3$-doped samples demonstrate the same vibration modes as the undoped sample with a reduction in Raman intensity for the $TiCl_3$ doped sample, showing B-H bending modes occurring at 1092, 1172 and 1353 cm^{-1} and B-H stretch at 2269 cm^{-1} with combination modes at 2155 and 2460 cm^{-1}. These bands confirm that there is no significant change in the bonding environment after adding dopants. While for the NbF_5 doped sample, no B-H Raman vibration modes are observed.

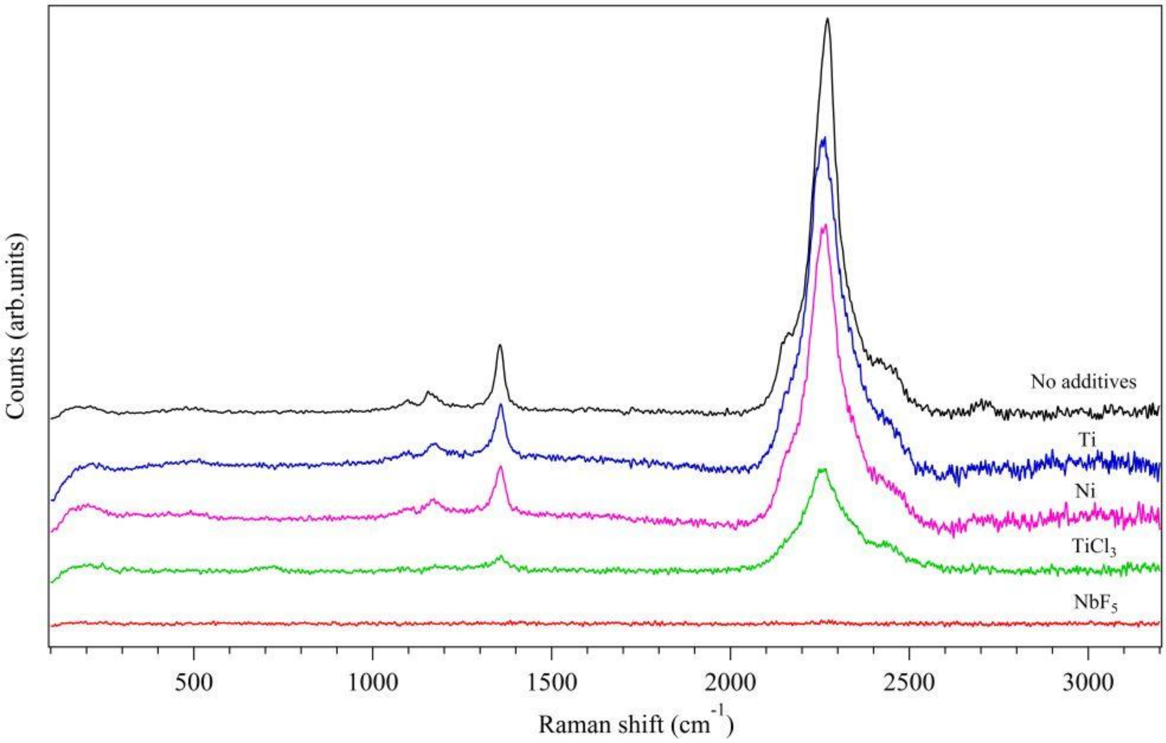

Figure 5.37 Raman spectra of $2LiBH_4$-$MnCl_2$-2 *mol% A (A=Ni, Ti,* $TiCl_3$ *and* NbF_5*) samples milled for 360 minutes, with undoped sample as reference*

5.4.2 Effect of additives on thermal decomposition

As shown earlier, $Mn(BH_4)_2$ that was produced after 360 minutes of ball-milling $2LiBH_4$-$MnCl_2$, starts to decompose at 130 °C, leading to a 8.4 wt% mass loss that is accompanied by the release of hydrogen and diborane. The TGA profiles of the doped samples (Figure 5.38) show that there is no significant change in decomposition temperature due to the addition of Ni, Ti and $TiCl_3$ but there are reductions in mass loss of 7.3 for Ni-, 7.1 for Ti- and 5.0 wt% for $TiCl_3$- doped samples after the calculation of added mass of the 2 mol% dopants, compared with the undoped sample (8.4 wt%). The mass losses are all accompanied by the release of hydrogen and diborane. For the NbF_5 doped sample, two mass loss regions are observed: 3.4 wt% from 98 to 142 ℃ , and 2.9 wt% from 310 to 440 ℃ .

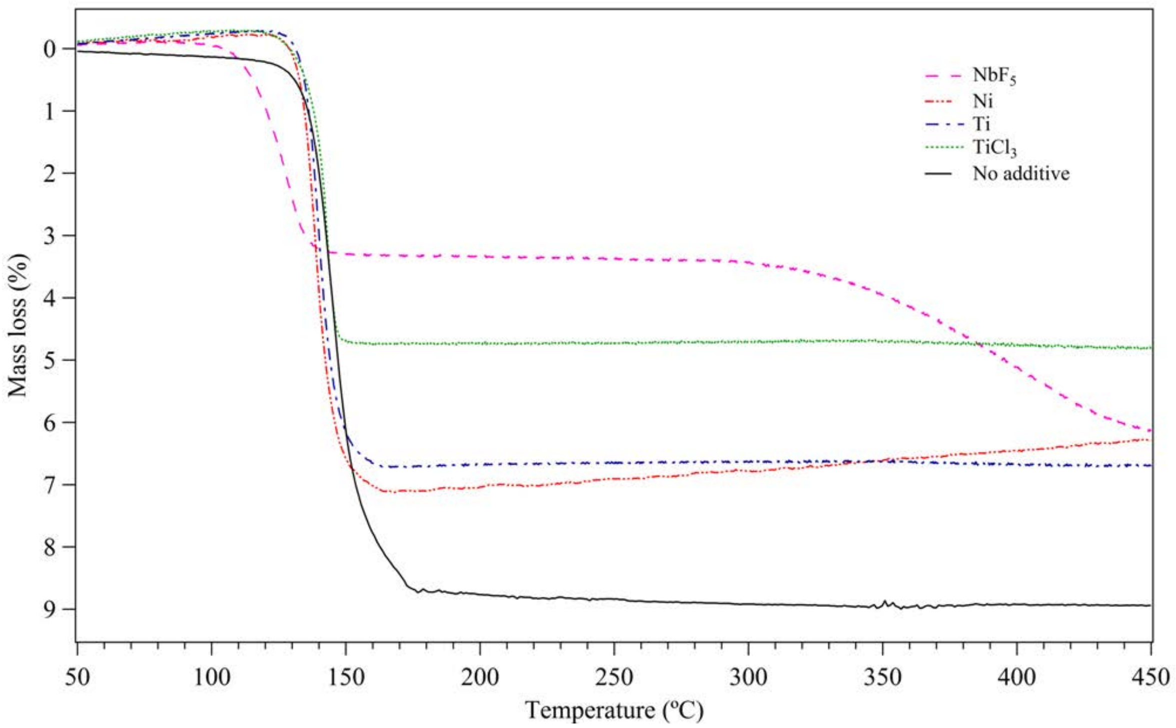

Figure 5.38 TGA profiles of 360-minute milled 2$LiBH_4$-$MnCl_2$-2 mol% A (A=Ni, Ti, $TiCl_3$ and NbF_5), undoped sample as reference, heated at 2 ℃ /min under 1.5 bar Ar flowing at 100 ml/min

TGA coupled with MS of the milled sample doped with NbF_5 indicates that the first mass loss region resultes from the evolution of hydrogen and diborane, while in the second region only hydrogen is released (Figure 5.39). A much lower onset decomposition temperature, reduced by 32 °C compared with the sample without additives, occurs at 98 °C.

Therefore, the slight reduction in mass loss observed for the Ti- and Ni- doped samples could be due to the alteration of the decomposition mechanism of $Mn(BH_4)_2$. The significant reduction in mass loss for the $TiCl_3$- doped sample may be associated with a partial decomposition during the milling, where an additional metathesis reaction between $TiCl_3$ and $LiBH_4$ occurs to form small amounts of Ti borohydride that then decomposes during milling (Hoekstra and Katz, 1949; Marks and Kolb, 1977). The alteration of the thermal decomposition behaviour for the NbF_5 doped sample is likely due to a change either in synthetic reaction mechanism such as the reaction of NbF_5 with $LiBH_4$ to form Nb borohydride which can partially decompose to yield Nb and LiF during the milling, or in the decomposition pathway of Mn-based borohydride. The formation of Nb and LiF was observed by Mao (2011) after ball-milling $2LiBH_4$-MgH_2-$0.1NbF_5$, giving a reduction in decomposition temperature for the milled sample. In this study, the Nb and LiF phases are not observed in XRD pattern of the milled $2LiBH_4$-$MnCl_2$-2 mol%NbF_5 sample, perhaps because only a small amount of NbF_5 (2 mol%) was added. To better understand the effect of dopants on the synthetic and decomposition of $Mn(BH_4)_2$, different amounts of dopants should be investigated, and FTIR and high resolution XRD measurement should be used to characterize the doped samples.

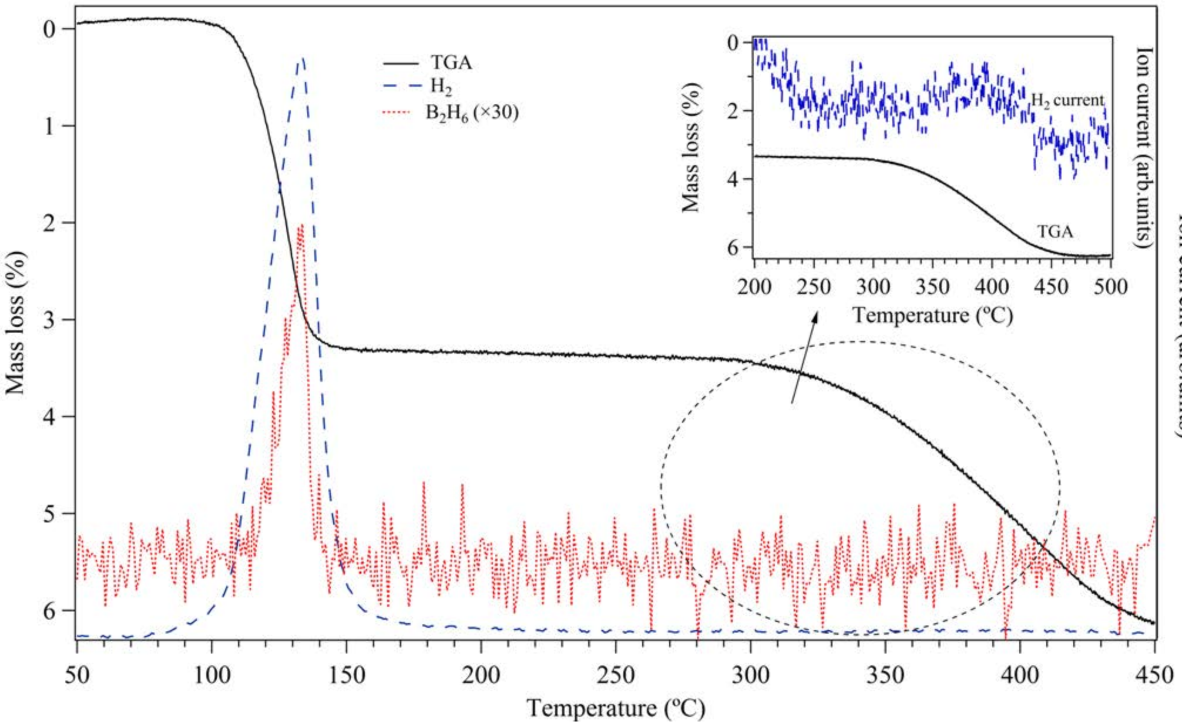

Figure 5.39 TGA profile coupled with MS of $2LiBH_4$-$MnCl_2$-2 mol% NbF_5 samples milled for 360 minutes, heated at 2 °C/min under 1.5 bar Ar flowing at 100 ml/min

5.5 Thermal decomposition under a hydrogen atmosphere

Thermal decomposition of the milled $2LiBH_4$-$MnCl_2$ sample was investigated using DSC under 3 bar hydrogen pressure, as shown in Figure 5.40. There is no significant difference in the decomposition reaction of $Mn(BH_4)_2$ under 3 bars argon and hydrogen pressure. The 3 bar hydrogen pressure may be too low to affect the decomposition reaction of borohydride compound.

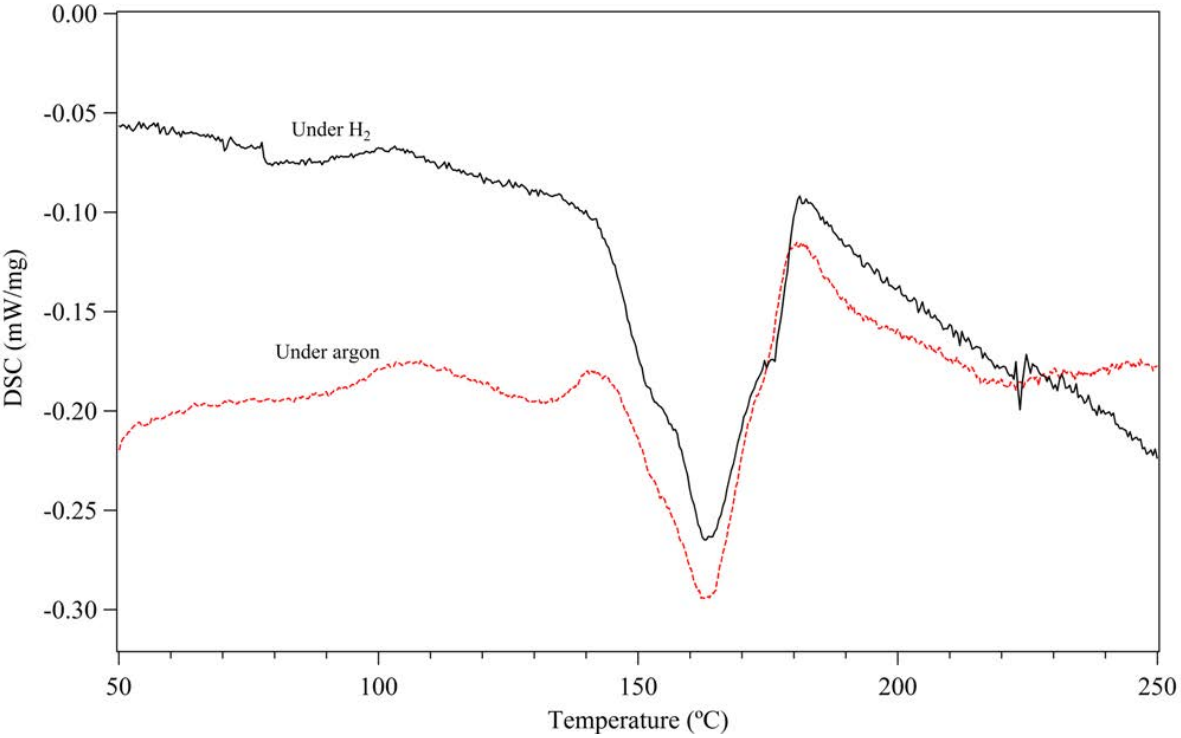

Figure 5.40 DSC profiles of $2LiBH_4$ -$MnCl_2$ sample milled for 360 minutes, heated at 2 °C/min under 3 bar flowing hydrogen, and under 3 bar flowing argon at 100 ml/min.

5.6 Possibility of rehydrogenation

Rehydrogenation was attempted on the 360-minute milled $2LiBH_4$-$MnCl_2$ sample decomposed by heating to 200 ºC under 1.5 bar Ar flowing at 40 ml/min. The decomposed sample was heated to 200 ºC in 100 bar H_2 flowing at 100 ml/min, without any isothermal dwell. However, no endo/exothermic DSC peaks were observed during heating in hydrogen, and subsequently, no mass loss or gas desorption was observed when the treated sample was heated in flowing argon on a TGA coupled to a mass spectrometer. This indicates that there is no reversibility within this system under these specific conditions.

Chapter 6 Results and Discussion: $NaBH_4$-$MnCl_2$ System

6.1 Synthesis and characterization

6.1.1 Crystallographic characterization

Powder XRD patterns of $2NaBH_4$-$MnCl_2$ samples mechanically milled under Ar for different durations, are shown in Figure 6.1. A broad band due to the Kapton dome sample holder at around 20° 2θ is present for all samples. The major diffraction peaks for the sample milled for 60 minutes are for the starting materials $NaBH_4$ and $MnCl_2$, and the resulting NaCl-type compound. There are no reflections associated with starting materials in the 240-minute milled sample, thereafter all remaining diffractions are attributed to an NaCl-type compound. It is noted that the diffraction peaks of the NaCl-type compound are very broad, gradually increase in intensity and shift slightly to low 2θ position with increasing milling time.

Similar behaviour is observed for the milled $3NaBH_4$-$MnCl_2$ samples (Figure 6.2), i.e. X-ray peaks for the starting materials $NaBH_4$ and $MnCl_2$, and the resulting NaCl-type compound are present after 60 minutes milling and with increasing milling time these diffraction peaks for the starting materials reduce and completely disappear to leave all the reflections owing to the NaCl-type compound with very broad diffraction peaks that shift to lower 2θ.

The disappearance of the starting materials might suggest the formation of a new complex borohydride, within the milled mixtures. The broad diffraction peaks from the NaCl-type compound and their shift in position could be possibly explained by the dissolution of a small amount of remaining $NaBH_4$ into NaCl during the ball milling, given the increase in lattice parameter of NaCl from 5.66 (1) to 5.74 (2) Å for the 60-360 minute milled $2NaBH_4$-$MnCl_2$, and from 5.68 (2) to 5.79 (1) Å for the 60-360 minute milled $3NaBH_4$-$MnCl_2$ samples.

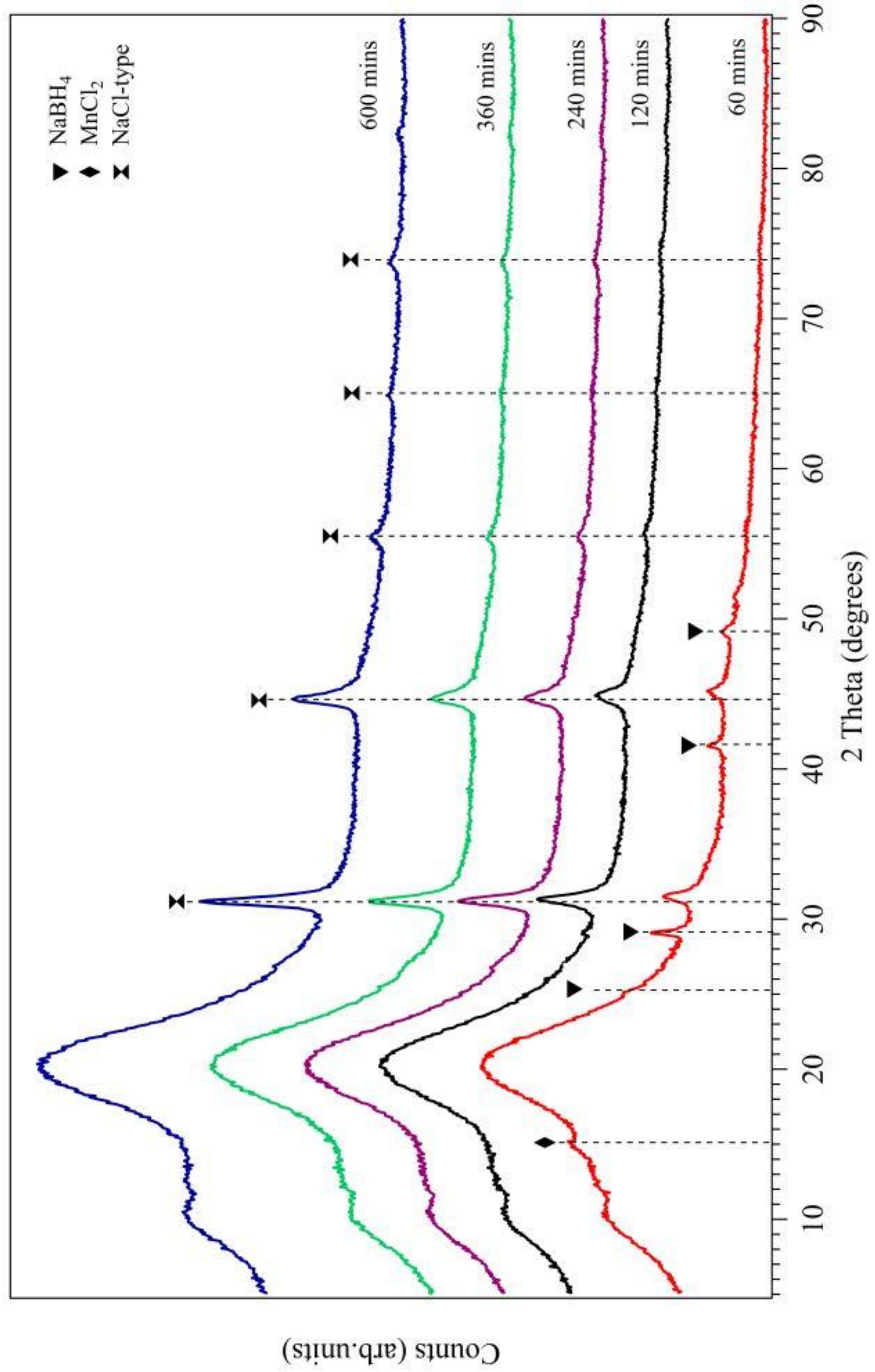

Figure 6.1 XRD patterns (Kapton dome) of $2NaBH_4$-$MnCl_2$ milled for different durations

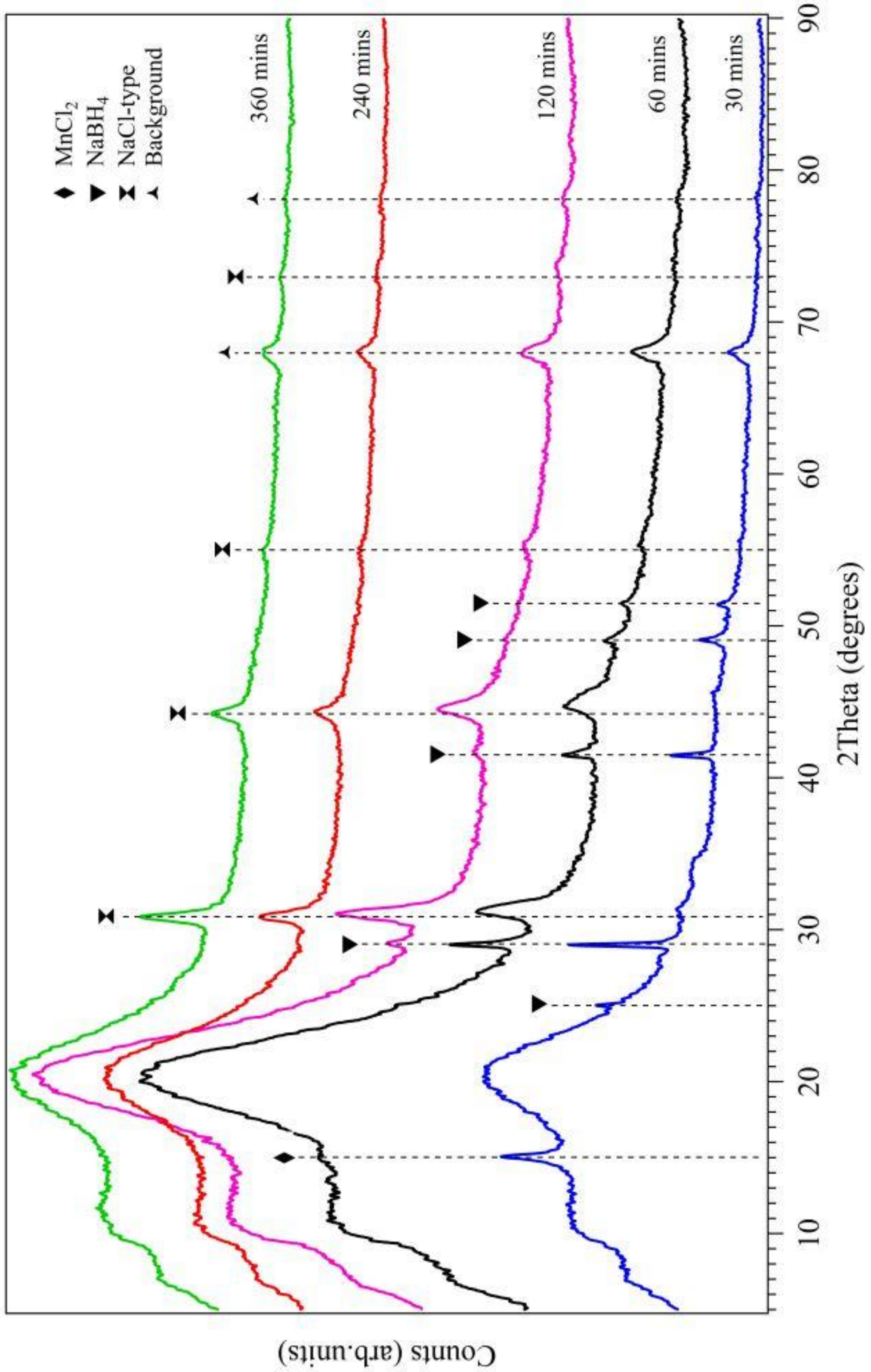

Figure 6.2 XRD patterns (Kapton dome) of $3NaBH_4$-$MnCl_2$ milled for different durations

To investigate the 10 to 25° 2θ region that is obscured due to the interactions of X-rays with the Kapton dome sample holder, XRD measurements were also performed using an Anton Parr XRK900 sample cell which has a Be window. Samples of 360-minute milled $2NaBH_4$-$MnCl_2$ and $3NaBH_4$-$MnCl_2$ were loaded into an aluminium oxide crucible, inside the sample cell (Figure 6.3). In the milled $2NaBH_4$-$MnCl_2$ sample, there are no distinct diffraction peaks attributed to the homoleptic $Mn(BH_4)_2$ phase in the trigonal crystal structure with the space group symmetry $P3_112$, as observed for milled $LiBH_4$-$MnCl_2$ (Černý et al., 2009). However, weak X-ray peaks for this $Mn(BH_4)_2$ phase are observed at around 20° 2θ for milled $3NaBH_4$-$MnCl_2$.

Significant reflections are associated with an NaCl-type compound in both the milled $2NaBH_4$-$MnCl_2$ and $3NaBH_4$-$MnCl_2$ samples, where the diffraction peaks shift slightly to lower 2θ for $3NaBH_4$-$MnCl_2$, compared with those for the $2NaBH_4$-$MnCl_2$ sample. Using TOPAS to refine the cell parameters, the lattice parameters (*a*) of NaCl-type compound are 5.74(2) Å and 5.791(2) Å for the milled $2NaBH_4$-$MnCl_2$ and $3NaBH_4$-$MnCl_2$ samples, respectively, which are higher than that of pure NaCl ($a = 5.64$ Å) (Swanson and Fuyat, 1953), possibly due to the substitution of BH_4^- ions for Cl^- ions (Lide, 2007). This indicates the formation of a solid solution in these systems with an approximate composition of $NaCl_{0.77}(BH_4)_{0.23}$ for the $2NaBH_4$-$MnCl_2$ sample and $NaCl_{0.68}(BH_4)_{0.32}$ for the $3NaBH_4$-$MnCl_2$ sample, according to Vegard's law (Denton and Ashcroft, 1991). The formation of a solid solution $NaCl_x(BH_4)_{1-x}$ has been reported through ball-milling or/and annealing of $NaBH_4$ and NaCl (Ravnsbaek et al., 2011). The absence of diffraction peaks from the initial reagents (i.e. $NaBH_4$ and $MnCl_2$), as well as remarkable diffraction signals from $NaCl_x(BH_4)_{1-x}$ confirms that $NaBH_4$ and $MnCl_2$ have reacted to potentially form an amorphous borohydride compound.

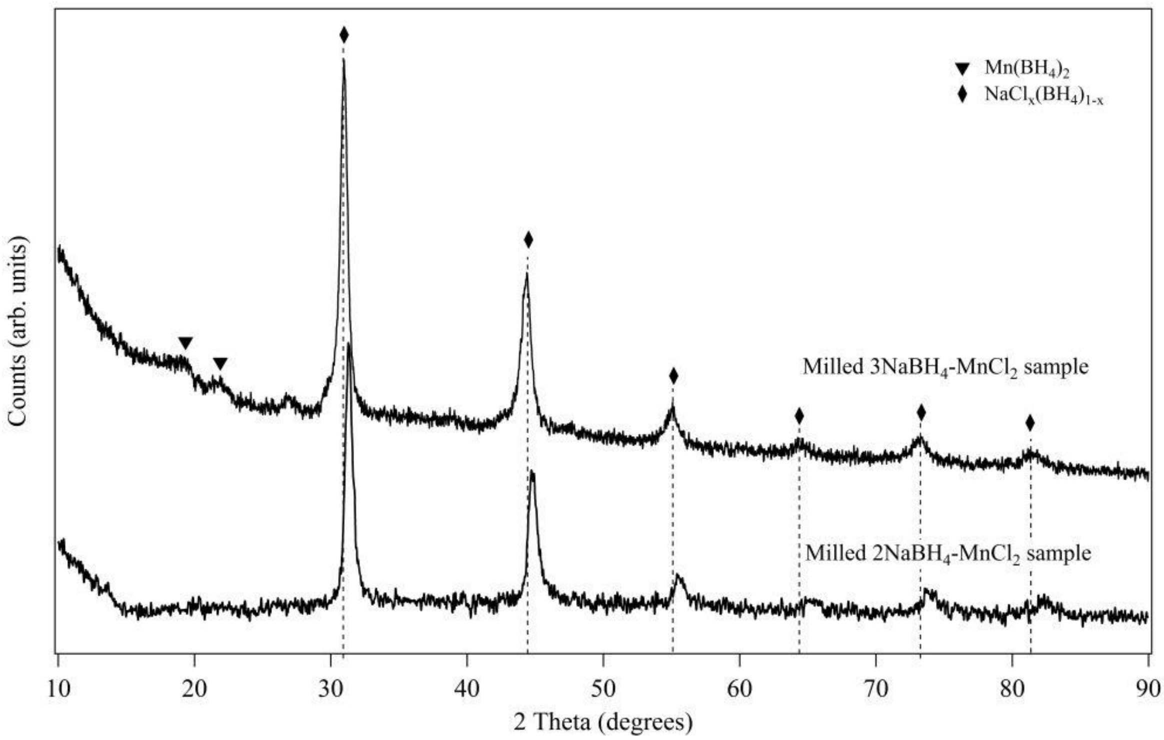

Figure 6.3 XRD patterns (Anton Parr cell) of x$NaBH_4$-$MnCl_2$ (x = 2 or 3) samples ball-milled for 360 minutes

To estimate the amorphous content, the 360-minute milled $2NaBH_4$-$MnCl_2$ and $3NaBH_4$-$MnCl_2$ samples were mixed with a known weight (10 wt%) of Si powder (Strem Chemicals, 99.999%). A full pattern pseudo-Rietveld refinement was carried out using TOPAS to perform quantitative phase analysis (Scarlett and Madsen, 2006). The amorphous content is estimated to be 65.7(8) and 65.4 (2) wt% for the milled $2NaBH_4$-$MnCl_2$ and $3NaBH_4$-$MnCl_2$ samples, respectively. This equals to the formation of 34.3(8) wt% $NaCl_{0.77}(BH_4)_{0.23}$ within the $2NaBH_4$-$MnCl_2$ sample and 34.6(2) wt% $NaCl_{0.68}(BH_4)_{0.32}$ in the $3NaBH_4$-$MnCl_2$ sample. This would mean that the overall ratio of ions within the amorphous component would be Mn-0.7Na-1.7(BH_4)-Cl in the $2NaBH_4$-$MnCl_2$ sample (although the exact nature of the compounds present is not known). In the $3NaBH_4$-$MnCl_2$ sample, it is not possible to estimate the amount of $Mn(BH_4)_2$ present as the intensities of X-ray diffraction peaks are too weak, however the ratio of the ions within the remaining components is Mn-1.4Na-2.5(BH_4)-0.9Cl.

Using mechanochemical synthesis, Jensen et al. (2007) reported that if sodium borohydride was used as a precursor, instead of forming $Mn(BH_4)_2$, a sodium manganese borohydride complex was formed. Further work confirmed that the formation of $Mn(BH_4)_2$ occurred when lithium borohydride was used as a reagent. However, when sodium borohydride was used, a distinctly different amorphous compound was formed, believed to be $Na_2Mn(BH_4)_4$, due to its amorphous and paramagnetic properties, precluding characterization by XRD and NMR (Severa et al., 2010a).

6.1.2 Spectroscopic characterization

To confirm the formation of the borohydride compound, the vibrational character of the milled samples was investigated by Raman and FTIR spectroscopy. Figures 6.4 and 6.5 show the Raman spectra of the $2NaBH_4$-$MnCl_2$ and $3NaBH_4$-$MnCl_2$ samples milled for different durations. There are three regions in the Raman spectra of interest for borohydrides – external vibrations (<300 cm^{-1}), internal bending modes (1000-1350 cm^{-1}), and internal stretching modes (2100-2460 cm^{-1}) of the BH_4 group. After mechanically milling $xNaBH_4$ with $MnCl_2$ ($x = 2$ or 3), the B-H bending modes are located at 1282(1283) and 1365(1367) cm^{-1} for the 60-minute milled sample, which then shift to 1304(1298) and 1359(1361) cm^{-1} for the 360-minute milled sample. New bending bands at 1100(1098) and 1172(1169) cm^{-1} are present after further milling. For the stretching vibrations, the intensity of the B-H symmetric mode at 2338(2330) cm^{-1} for the 60-minute milled sample dramatically reduces for the 120 minute sample, and then for the 360-minute milled sample a new band occurs at 2369(2357) cm^{-1}. Furthermore, an enhancement in band intensity for two stretching vibrations at 2245(2243) and 2272(2270) cm^{-1} is observed after increased milling. The internal bending and stretching modes for both samples as a function of milling time, are shown in Figures 6.6 and 6.7. External vibrations at 225(226) cm^{-1} are no longer present at 120 minutes and above. These changes in Raman shift and intensity indicate changes in the BH_4 surroundings. The Raman shift and the assignment for the $2NaBH_4$-$MnCl_2$ and $3NaBH_4$-$MnCl_2$ samples milled for different durations are summarized in the Table 6.1.

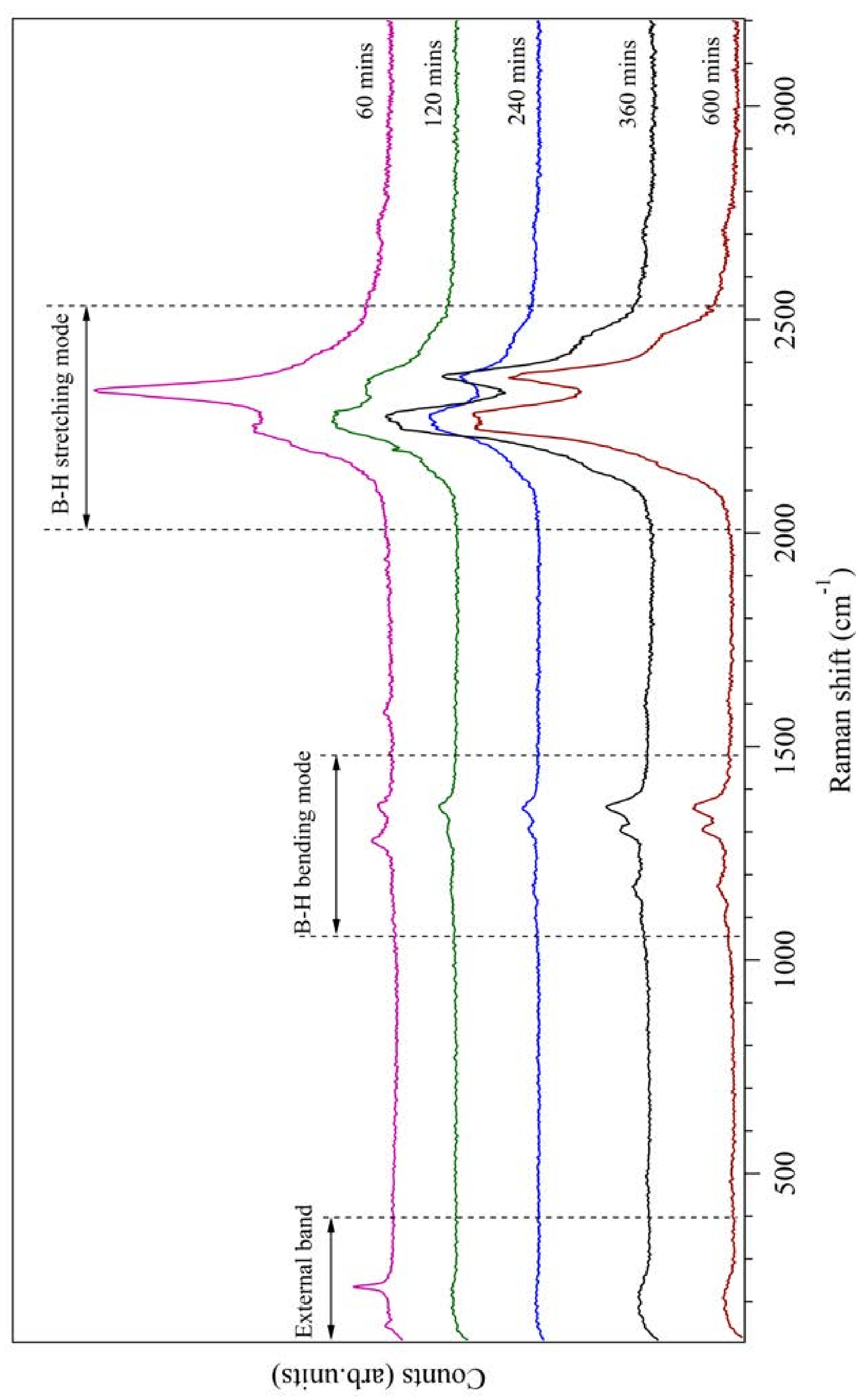

Figure 6.4 Raman spectra of $2NaBH_4$-$MnCl_2$ samples milled for different durations

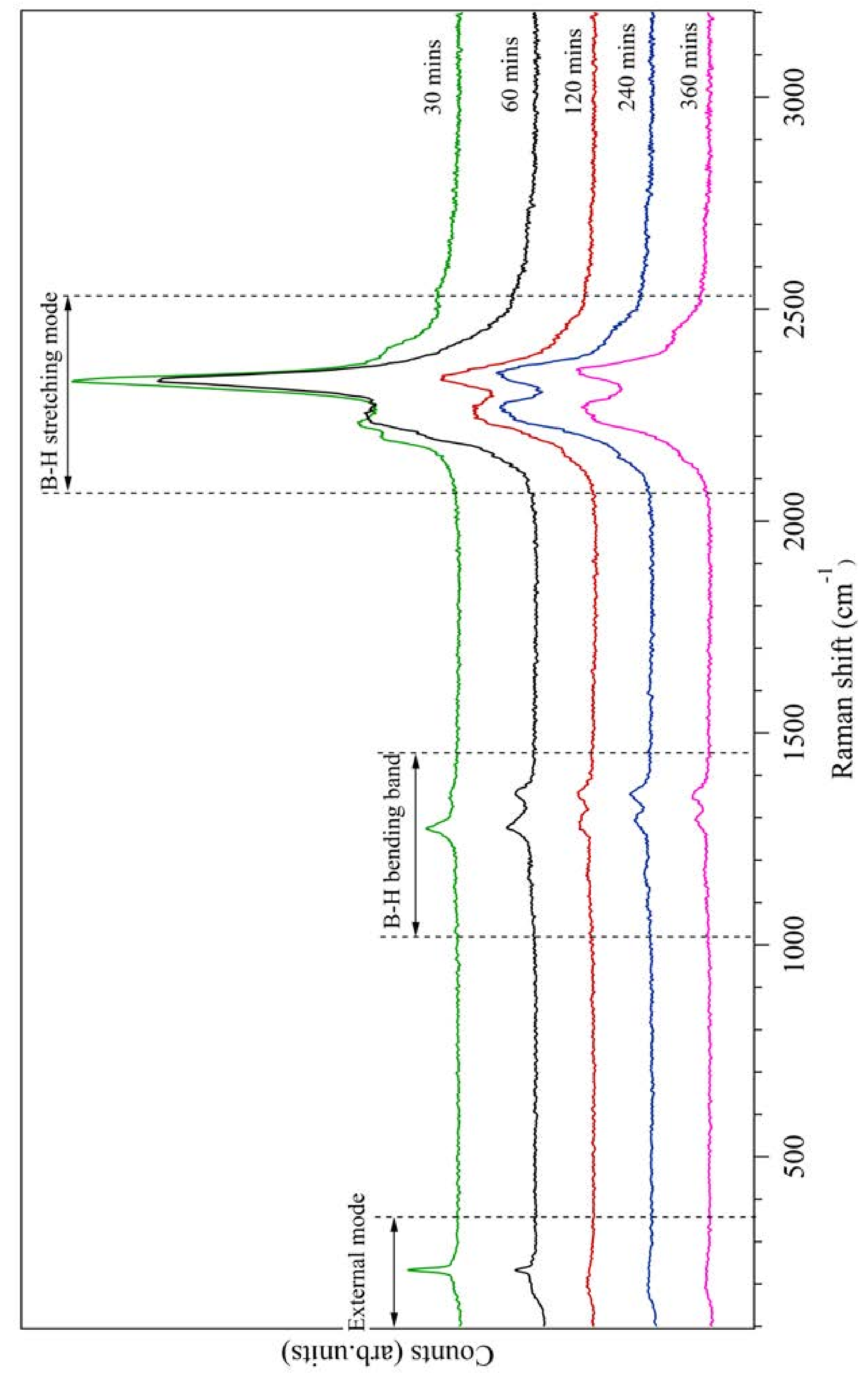

Figure 6.5 Raman spectra of $3NaBH_4$-$MnCl_2$ samples milled for different durations

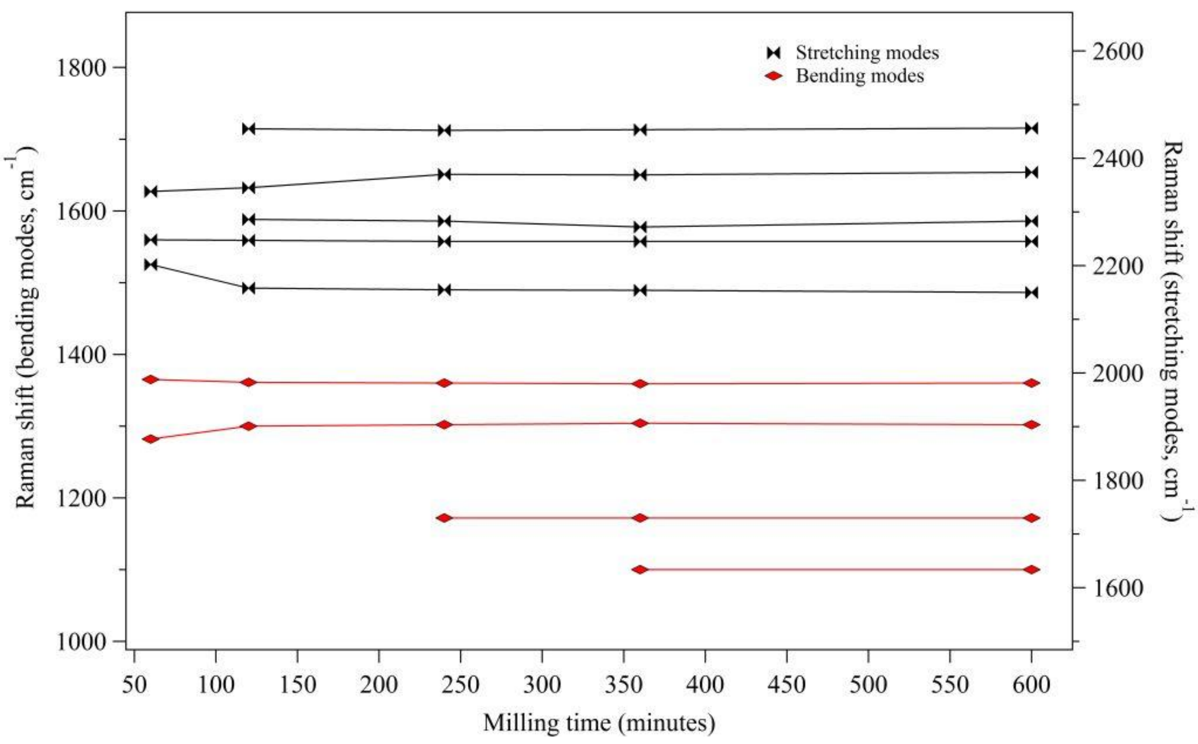

Figure 6.6 Bending and stretching vibration modes for $2NaBH_4$-$MnCl_2$ sample as a function of milling duration

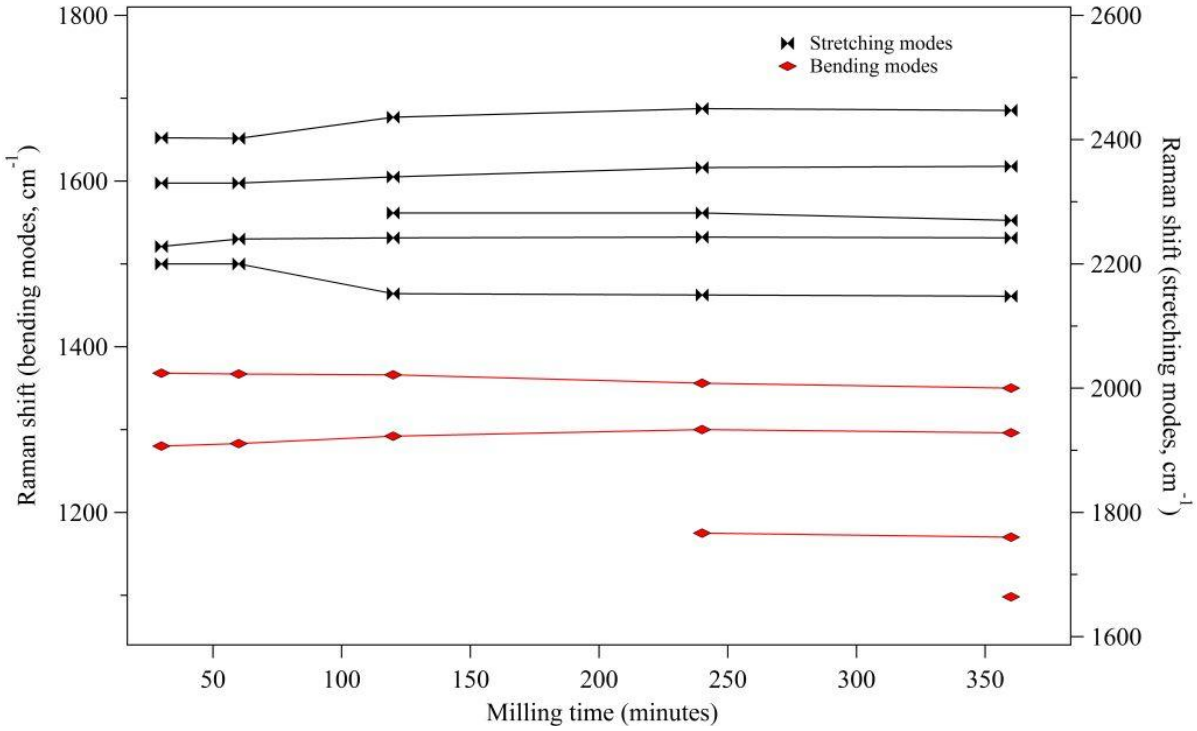

Figure 6.7 Bending and stretching vibration modes for $3NaBH_4$-$MnCl_2$ sample as a function of milling duration

Table 6.1 Raman shift (cm^{-1}) for x$NaBH_4$-$MnCl_2$ (x=2 or 3) milled for different durations

Raman shift (cm^{-1})							
$x$$NaBH_4$-$MnCl_2$ (x = 2 or 3) with different milling time (minute)							
30	60	120	240	360	600	Assignment	Comment*
-	225	<300	<300	<300	<300	External	*w*
(226)	(226)	(-)	(-)	(-)	(-)	modes	
-	-	-	-	1100	1100	B-H	*vw*
(-)	(-)	(-)	(-)	(1098)	(-)	bending	
-	-	-	1172	1172	1172	modes	*vw*
(-)	(-)	(-)	(1175)	(1169)	(-)		
-	1282	1300	1302	1304	1302		*w*
(1280)	(1283)	(1292)	(1300)	(1298)	(-)		
-	1365	1361	1360	1359	1360		*w*
(1368)	(1367)	(1366)	(1356)	(1361)	(-)		
-	2202	2158	2155	2154	2150	B-H	*w*
(2200)	(2200)	(2152)	(2150)	(2148)	(-)	stretching	
-	2248	2247	2245	2245	2245	modes	*s*
(2228)	(2240)	(2242)	(2243)	(2243)	(-)		
-	-	2286	2283	2272	2283		*s*
(-)	(-)	(2282)	(2282)	(2270)	(-)		
-	2338	2345	2370	2369	2374		*s*
(2330)	(2330)	(2340)	(2355)	(2357)	(-)		
-	-	2455	2452	2453	2465		*w*
(2403)	(2402)	(2436)	(2450)	(2455)	(-)		

** w-weak, vw-very weak, s-strong*

A comparison of the Raman spectra of the 360-minute milled $2NaBH_4$-$MnCl_2$ and $3NaBH_4$-$MnCl_2$ samples, as-received $NaBH_4$ and $Mn(BH_4)_2$ milled from $2LiBH_4$-$MnCl_2$ (Chapter 5) is shown in Figure 6.8. In both the milled samples there are ten Raman bands: one broad and weak external band, four bands from bending vibration modes and five from stretching modes. Raman shifts for as-received $NaBH_4$ are found in two regions, the two bending bands in the $[BH_4]^-$ anion at around 1118 and 1276 cm^{-1} and four B-H bond stretching modes, consisting of symmetric stretching at 2330 cm^{-1}, two overtones at 2191 and 2221 cm^{-1}, and a combination band at 2400 cm^{-1}. After milling $NaBH_4$ with $MnCl_2$, the two bending modes of BH_4 in $NaBH_4$ split into four vibration modes, located around 1100(1098), 1172(1169), 1304(1298) and 1359(1361) cm^{-1} for the milled $xNaBH_4$-$MnCl_2$ (x = 2 or 3) samples; while stretching region peaks are observed at 2245(2243), 2272(2270), 2369(2357) and 2453(2455) cm^{-1} for both the milled samples. A combination band is located at 2154(2148) cm^{-1}. The vibrations observed at 2272(2270), 1359(1361), 1172(1169) and 1100(1098) cm^{-1} in both the milled samples correspond to the vibrational modes observed for $Mn(BH_4)_2$ (Černý et al., 2009). This indicates that $Mn(BH_4)_2$ has been formed, however it is poorly crystalline and difficult to observe/characterize by lab-based XRD.

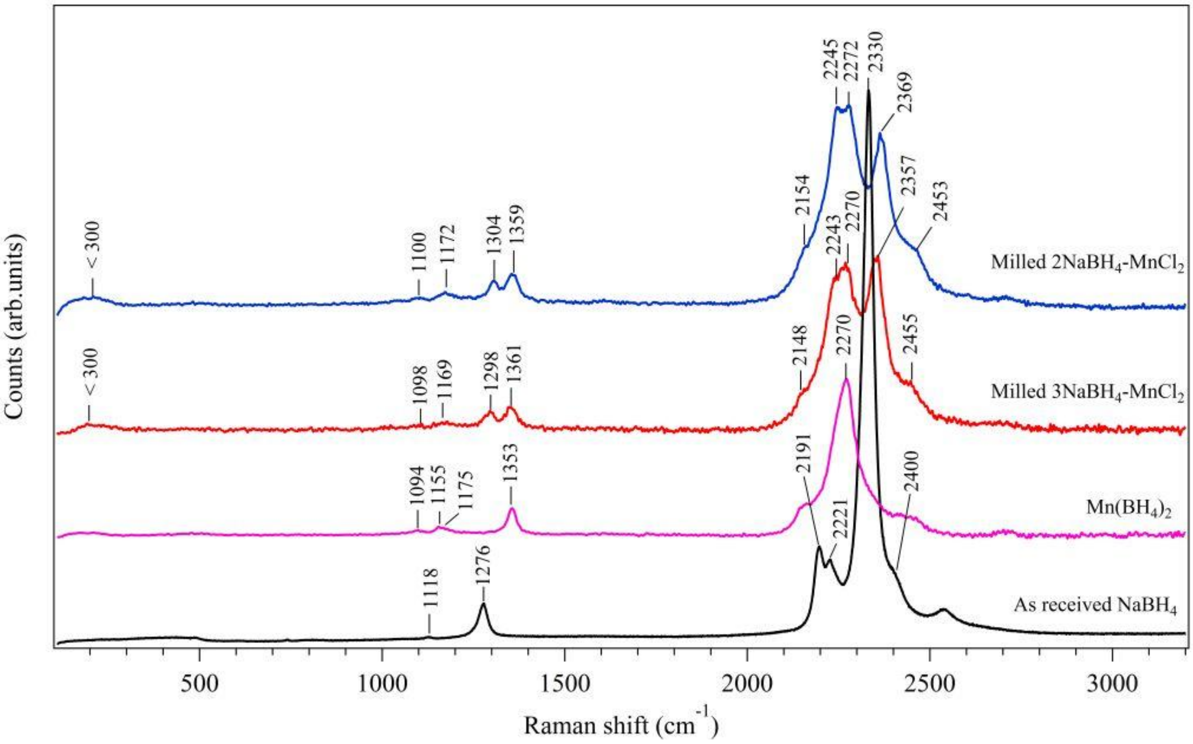

Figure 6.8 Raman spectra of $xNaBH_4$-$MnCl_2$ (x = 2 or 3) milled for 360 minutes, as-received $NaBH_4$ and $Mn(BH_4)_2$ milled from $2LiBH_4$-$MnCl_2$ (Chapter 5)

Therefore, the Raman spectra of both milled samples suggest that there are, at least, two separate ionic borohydride environments: an $NaCl_x(BH_4)_{1-x}$ solid solution and $Mn(BH_4)_2$. Apart from the vibrations of $Mn(BH_4)_2$, the peaks observed at 2369(2357) and 1304(1298) cm^{-1} for both the milled samples, are consistent with a borohydride with T_d symmetry (Renaudin et al., 2004). These vibrations are likely to be due to the $[BH_4]^-$ anions in the $NaCl_x(BH_4)_{1-x}$ solid solution.

All the Raman active modes (except for the 1361 cm^{-1} band) of the $3NaBH_4$-$MnCl_2$ sample, have slightly lower frequency values than those for the milled $2NaBH_4$-$MnCl_2$ sample. A relatively higher intensity in the Raman shifts of BH_4 with high symmetry around 2357-2360 cm^{-1} is observed in the milled $3NaBH_4$-$MnCl_2$ sample, than those for the milled $2NaBH_4$-$MnCl_2$ sample. These results indicate the formation of solid solution $NaCl_x(BH_4)_{1-x}$ phases with different compositions in the two milled samples, leading to different $[BH_4]^-$ environments.

On cooling the xNaBH$_4$-MnCl$_2$ (x =2 or 3) samples milled for 360 minutes to -190 °C, an increase in the intensities of all the vibration modes is observed for both the milled samples, as shown in Figures 6.9 and 6.10. For both the milled samples, the Raman active modes around 2243-2272 cm^{-1} observed at room temperature split into bands at 2250(2239) and 2280(2272) cm^{-1} at -193 °C. This similar refinement in Raman vibration modes to the milled $LiBH_4$-$MnCl_2$ sample (chapter 5) is due to a reduction in thermal vibrations between the molecules (Racu et al., 2008; Reed and Book, 2011).

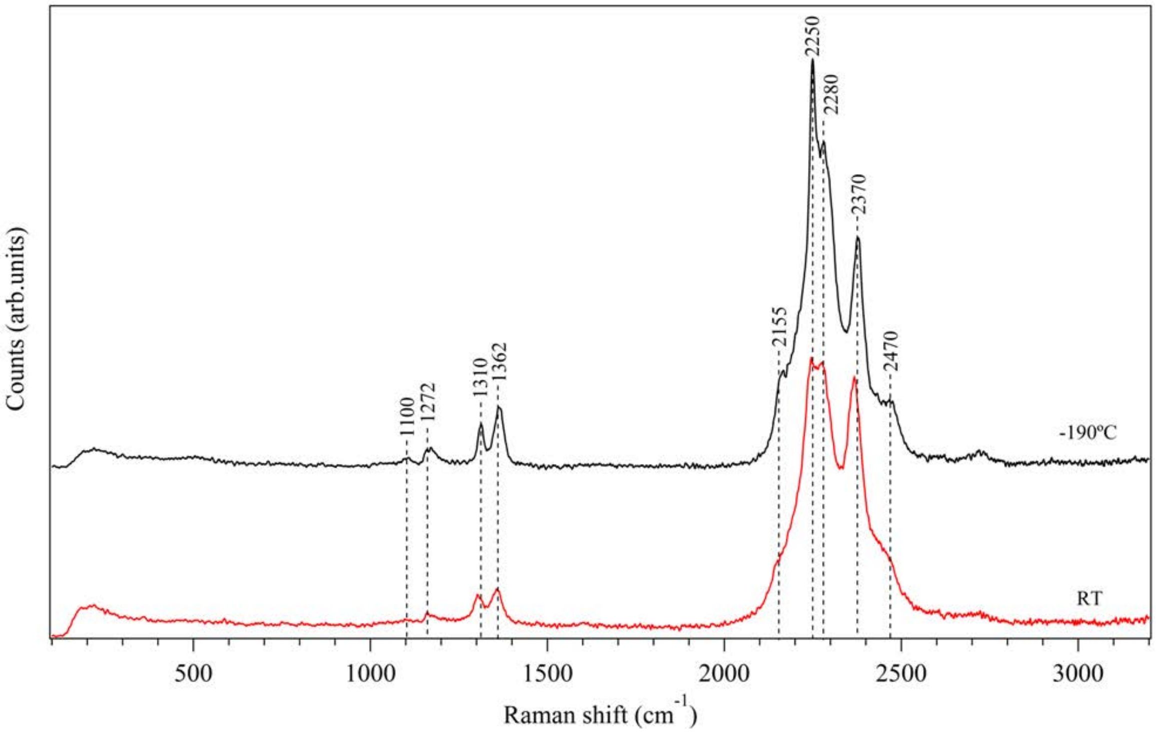

Figure 6.9 Raman spectra (RT and -190 ºC) of $2NaBH_4$-$MnCl_2$ milled for 360 minutes

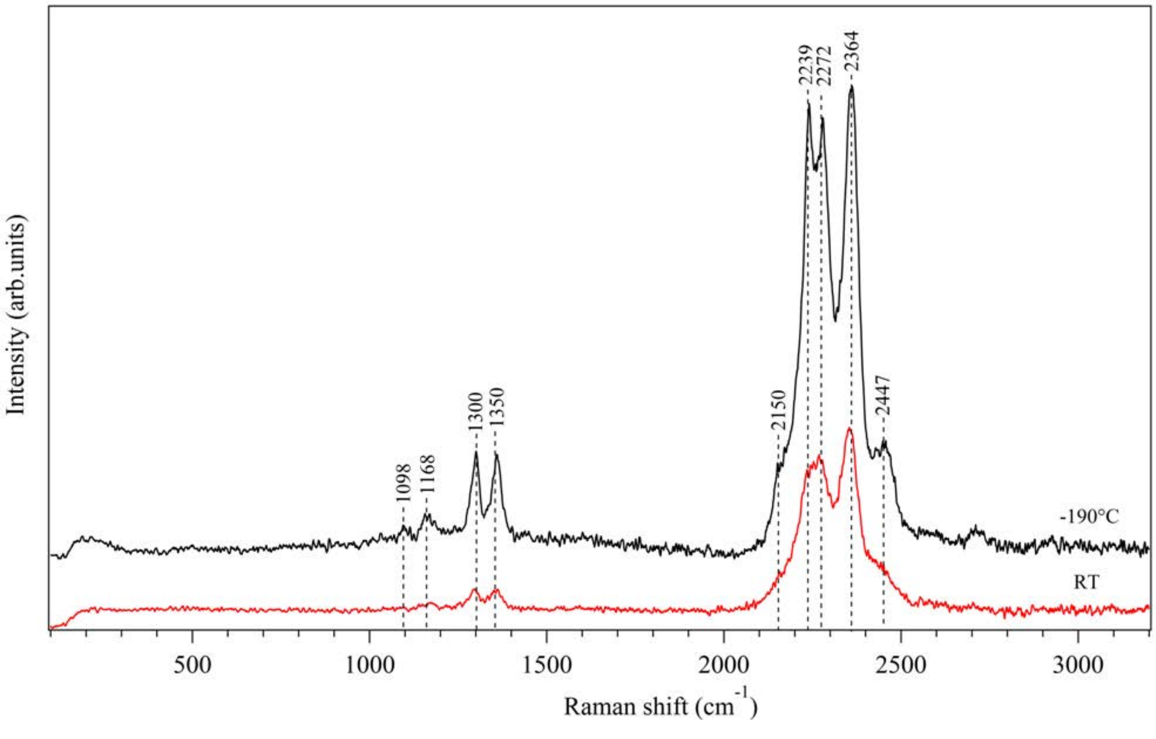

Figure 6.10 Raman spectra (RT and -190 ºC) of $3NaBH_4$-$MnCl_2$ milled for 360 minutes

The IR spectra of the milled $x$$NaBH_4$-$MnCl_2$ (x = 2 or 3) samples are shown in Figure 6.11. As received $NaBH_4$ has the corresponding strong characteristic bands at 2214 and 2285 cm^{-1}, originating from the stretching vibration, whereas three stretching bands at 2232(2230), 2283(2278) and 2364(2345) cm^{-1} are observed for the milled $x$$NaBH_4$-$MnCl_2$ samples. The strongest IR band at around 1109 cm^{-1} for $NaBH_4$, corresponds to the deformation modes of $[BH_4]^{-1}$, which split into three bands at around 1098(1098), 1158(1146) and 1219(1220) cm^{-1} for both the milled samples. The new bridging bending mode is observed at 1350(1352) cm^{-1} for the milled sample.

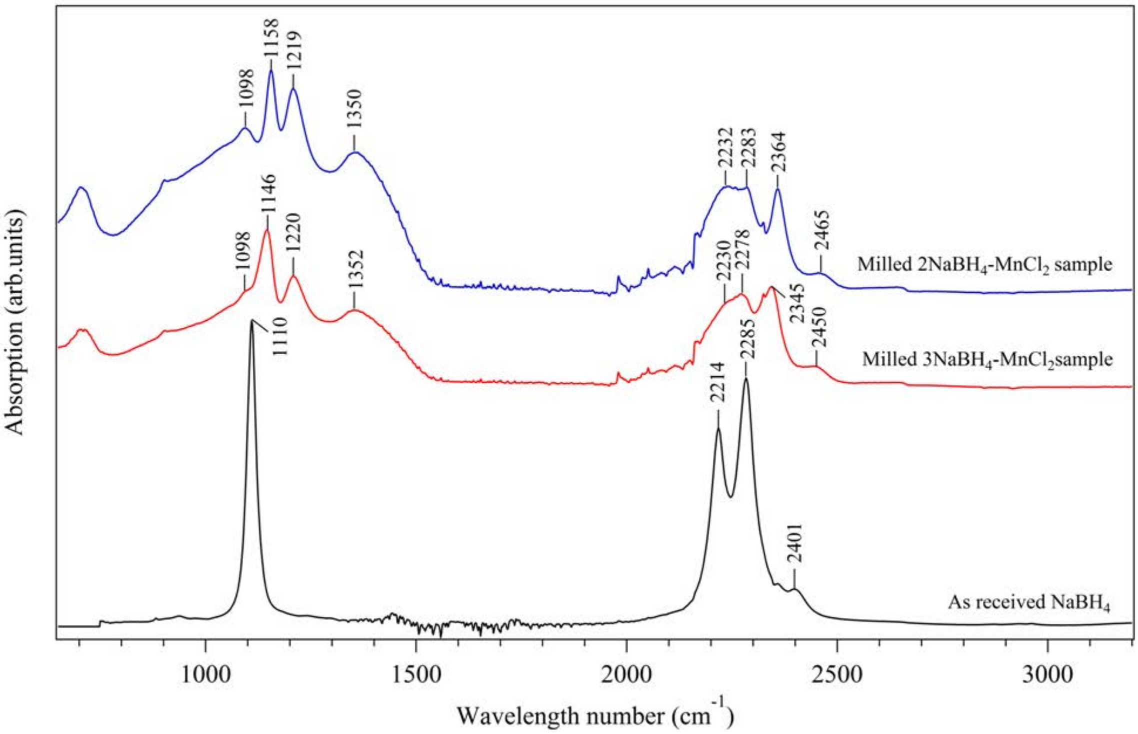

Figure 6.11 FTIR of x$NaBH_4$-$MnCl_2$ (x = 2 or 3) samples milled for 360 minutes, as-received $NaBH_4$ as a reference

Of these vibration modes, the bands at 2232(2230), 1350(1352), 1219(1220) and 1098(1098) cm^{-1} are believed to be associated with the $Mn(BH_4)_2$ compound, where the bands were observed at 2220, 1354, 1207 and 1093 cm^{-1} by Černý et al (2009) and at 2230, 1352, 1203 and 1091 cm^{-1} in this work (Chapter 5). The bands at 2283(2278), 2364(2345) and

1158(1146) cm^{-1} are likely to be related to the solid solution $Na(BH_4)_xCl_{1-x}$ or/and other Na-based borohydrides. The IR results are consistent with the vibrational spectra of bonds of solid solution $NaCl_x(BH_4)_{1-x}$ prepared by the ball-milling of $NaBH_4$ and transition metal (Ni, Ti) chloride (Llamas-Jansa et al., 2012).

Therefore, the reaction during ball milling for $x$$NaBH_4$-$MnCl_2$ (x = 2 or 3) samples can be expressed by equations (6.1) and (6.2) (where y and z values are unknown), though the exact composition and structure of the sodium manganese compound is not known.

$$MnCl_2 + 2NaBH_4 \rightarrow$$

$$1.3NaCl_{0.77}(BH_4)_{0.23} + y\mathrm{Mn(BH_4)_2} + \text{“}0.7\mathrm{Na}\text{-}(1\text{-}y)\mathrm{Mn}\text{-}(1.7\text{-}2y)(\mathrm{BH_4})\text{-}\mathrm{Cl}\text{”} \qquad (6.1)$$

$$MnCl_2 + 3NaBH_4 \rightarrow$$

$$1.6NaCl_{0.68}(BH_4)_{0.32} + z\mathrm{Mn(BH_4)_2} + \text{“}1.4\mathrm{Na}\text{-}(1\text{-}z)\mathrm{Mn}\text{-}(2.5\text{-}2z)(\mathrm{BH_4})\text{-}0.9\mathrm{Cl}\text{”} \qquad (6.2)$$

6.2 Thermal decomposition

6.2.1 Thermogravimetric analysis

The TGA profiles for $2NaBH_4$-$MnCl_2$ samples milled for different durations are shown in Figure 6.12; the mass losses and decomposition temperatures are summarized in Table 6.2. No significant differences in TGA profile are found for the samples milled from 60 to 600 minutes, between 50 and 180 °C. The thermal decomposition of the samples starts at around 118°C and completes at around 180 ℃ for the 60-minute milled sample, accompanied by a mass loss of 6.2 ± 0.2 wt%. With increasing milling duration, the end decomposition temperature slightly decreases, while the mass loss slightly increases to 6.3-6.5 wt%. But for the 60-minute milled sample, a larger difference (62 ℃) between onset and end decomposition temperatures is observed, compared to those of other milled samples, indicating a slower decomposition rate. The observed mass losses for all the milled samples are much higher than the theoretical hydrogen content in the mixture (3.97 wt%), suggesting that the evolution of H_2 is accompanied by other gases.

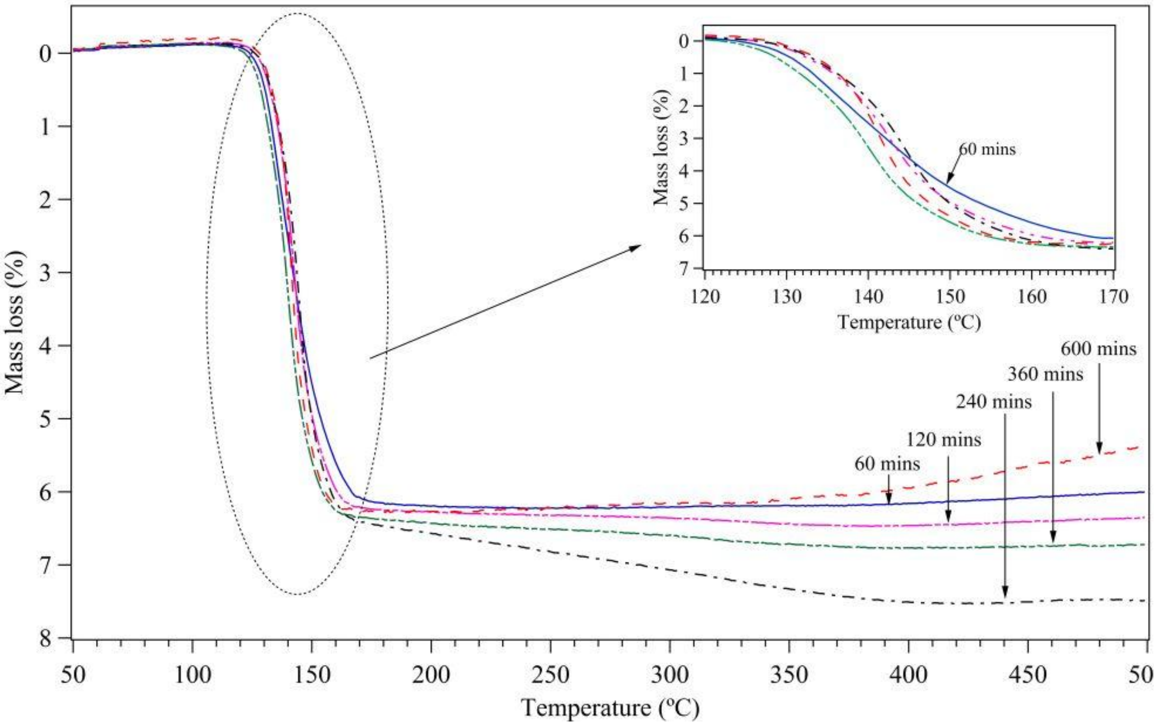

Figure 6.12 TGA profiles of $2NaBH_4$-$MnCl_2$ samples for different milling durations, heated at 2 °C/min under 1.5 bar Ar flowing at 40 ml/min

Table 6.2 Summary of TGA profiles for milled $2NaBH_4$-$MnCl_2$ samples

TGA properties	Milling time (minutes)				
	60	120	240	360	600
Onset decomposition temperature (°C)	118	118	118	118	118
End decomposition temperature (°C)	180	175	178	170	170
Total observed mass loss (wt%)	6.2±0.2	6.3±0.1	6.5±0.1	6.4±0.2	6.4±0.2
Theoretical H content in the mixture ($2NaBH_4$-$MnCl_2$) (wt%)			3.97		

TGA coupled with mass spectrometry for the 360-minute milled $2NaBH_4$-$MnCl_2$ sample shows that the main mass loss of 6.4 ± 0.2 wt% between 118 and 170 °C is accompanied by the evolution of a significant amount of hydrogen and diborane (Figure 6.13), which is attributed to the decomposition of manganese borohydride. According to equation (5.7), $Mn(BH_4)_2$ decomposes with the concurrent evolution of hydrogen and diborane in a ratio of 9:1. On this basis, a 6.4 ± 0.2 wt% mass loss would indicate that 35.7 wt% of the milled material is $Mn(BH_4)_2$, thus the y value in equation (6.1) can be expected to be 0.85. Following the main hydrogen desorption peaks a visible hydrogen evolution starts and peaks at ~ 310℃ . There is also a subtle change in the gradient of the TGA between 250 and 425 °C with a mass change of 0.35 ± 0.2 wt%, and no detectable diborane release. This is a slower process, corresponding to the decomposition of the $[BH_4]^-$ in the $NaCl_{0.77}(BH_4)_{0.23}$ solid solution.

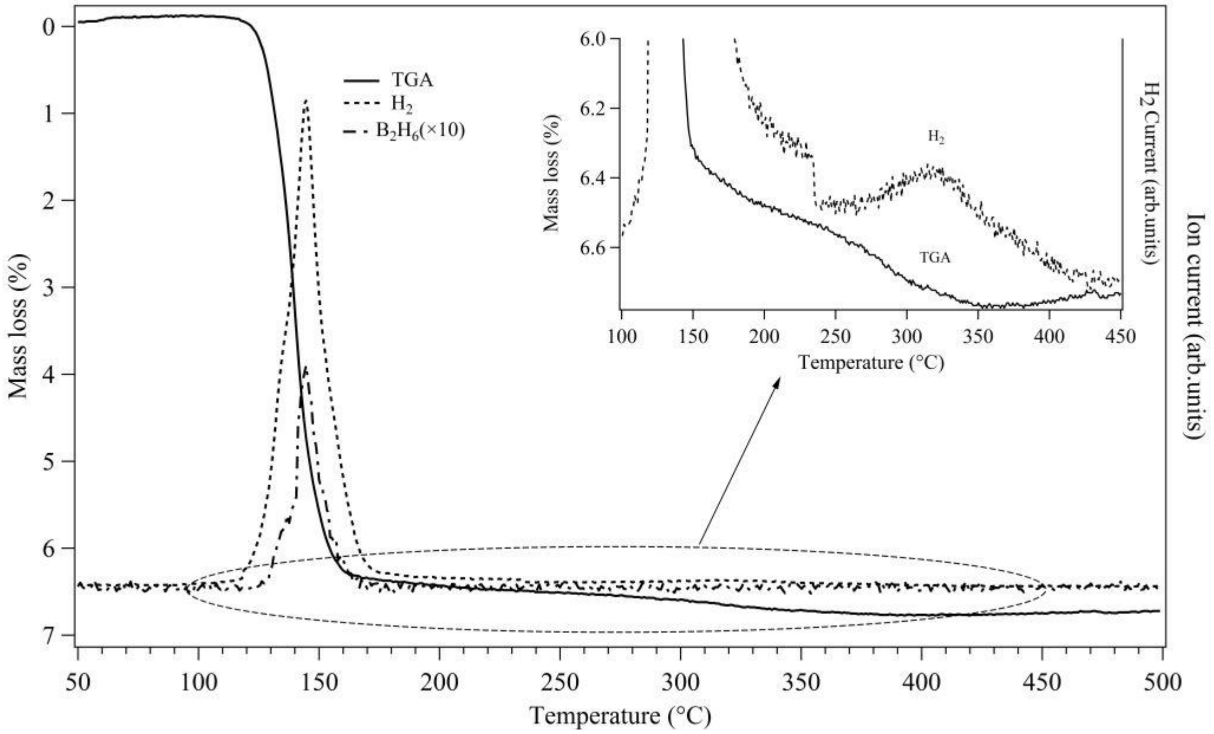

Figure 6.13 TGA profile coupled with MS for $2NaBH_4$-$MnCl_2$ sample milled for 360 minutes, heated at 2 °C/min under 1.5 bar Ar flowing at 40 ml/min

The $3NaBH_4$-$MnCl_2$ samples milled for different durations have two significant mass loss regions, as shown in Figure 6.14. In the first region, the onset decomposition temperature decreases from 120 to 110 ℃ for the samples milled from 30 to 360 minutes, and the decomposition is completed at around 160-170 ℃ . The first total mass losses are between 5.5 and 6.0 wt% with the lowest value for the sample milled for 30 minutes (as presented in Table 6.3), which is due to the decomposition of manganese borohydride. In the second region, the decomposition starts around 400 ℃ for the 30-minute milled sample, then decreases to 380 ℃ for the 360-minute milled sample, and it seems to be incomplete (for all samples) even after heating to 500 ℃ , indicating relatively slow thermal decomposition kinetics. This may be due to the partial dissociation of $[BH_4]^-$ within the $NaCl_x(BH_4)_{1-x}$ solid solution.

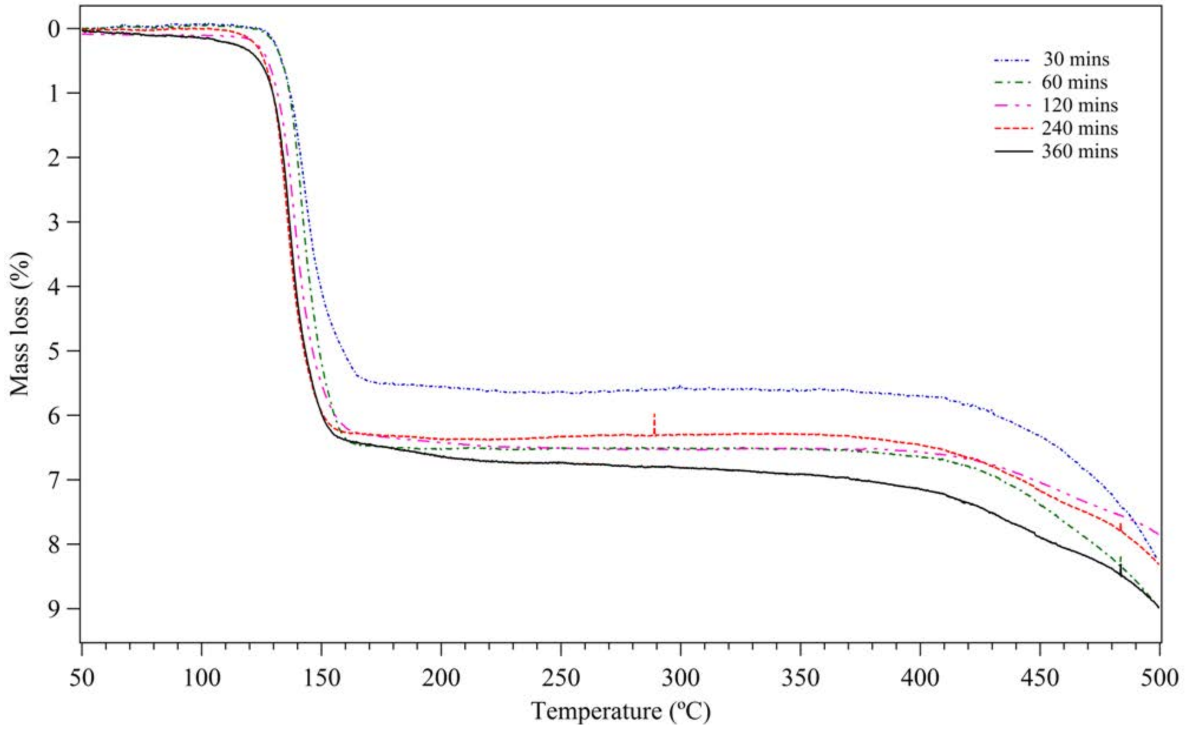

Figure 6.14 TGA profiles of $3NaBH_4$-$MnCl_2$ samples for different milling durations, heated at 2 °C/min under 1.5 bar Ar flowing at 40 ml/min

Table 6.3 Summary of TGA profiles for the milled $3NaBH_4$-$MnCl_2$ samples

TGA properties	Milling time (minutes)				
	30	60	120	240	360
First onset decomposition temperature (ºC)	120	120	120	120	110
First end decomposition temperature (ºC)	170	170	165	165	160
First total observed mass loss (wt%)	5.5±0.2	6.1±0.1	6.1±0.1	6.1±0.2	6.0±0.1
Second onset decomposition temperature (ºC)	400	380	380	380	380
Second end decomposition temperature (ºC)	up to 500				
Theoretical H content in the mixture ($3NaBH_4$-$MnCl_2$) (wt%)	5.01				

Mass spectroscopy of the 360-minute milled $3NaBH_4$-$MnCl_2$ sample shows the concurrent evolution of hydrogen and diborane accompanying the mass loss observed (6.0 ± 0.1 wt%) on the TGA between 110 and 160 ℃ (Figure 6.15), which is attributed to the thermal decomposition of $Mn(BH_4)_2$ with the concurrent evolution of hydrogen and diborane (9:1 ratio). This mass loss indicates that 31.9(8) wt% of the milled material is $Mn(BH_4)_2$, accordingly, the z value in equation (6.2) can be calculated to be 0.9. It should also be noted that there is a small amount of hydrogen release after the first major decomposition, showing a hydrogen peak at 210 ℃ . Unlike the milled $2NaBH_4$-$MnCl_2$ sample, the 360-minute milled $3NaBH_4$-$MnCl_2$ sample exhibits a third decomposition reaction involving the evolution of only hydrogen, starting at 380 ℃ (incomplete when the measurement ends at 500 °C) with a mass loss in excess of 1.7 wt%.

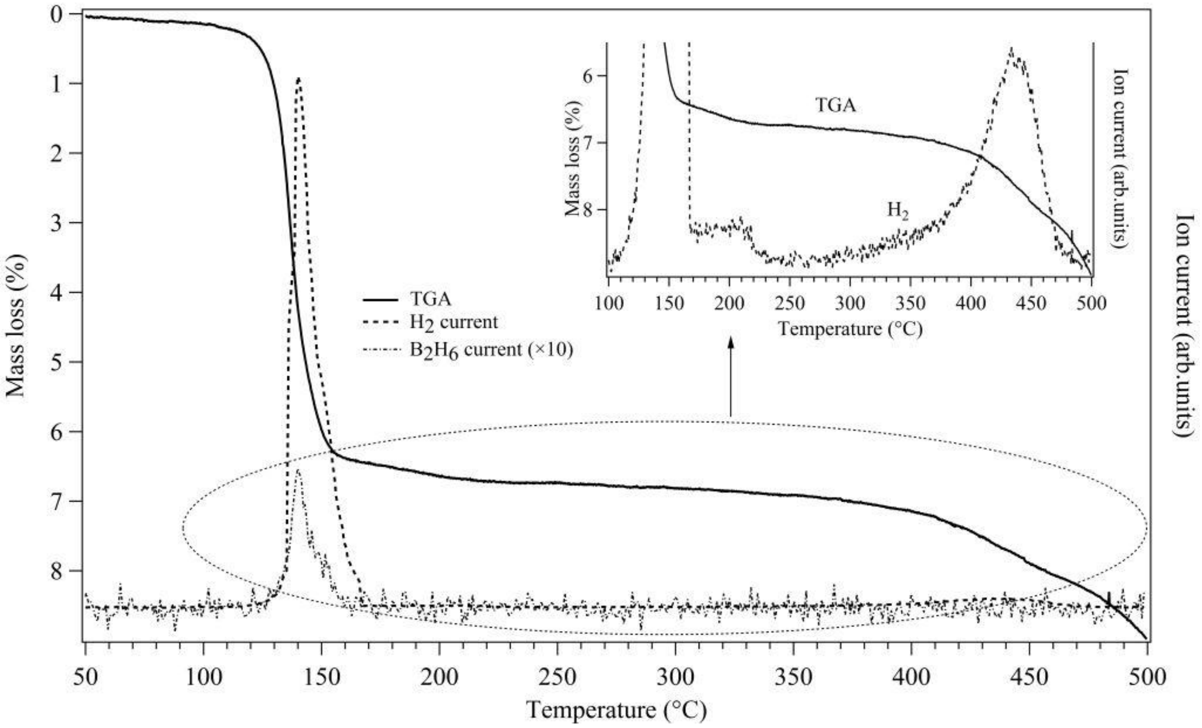

Figure 6.15 TGA profile coupled with MS for 3$NaBH_4$-$MnCl_2$ sample milled for 360 minutes, heated at 2 °C/min under 1.5 bar Ar flowing at 40 ml/min

A multi-step decomposition reaction has been observed for sodium tetrahydroboride ($NaBH_4$) in the solid state (Urgnani et al., 2008), indicating that the evolution of hydrogen starts at 240 ℃ and continues by several steps at different temperatures, with the most significant hydrogen emission starting at about 450 ℃ . Thus, the third release of hydrogen observed in this study is likely to be associated with the decomposition of $[BH_4]^-$ contained in $NaCl_x(BH_4)_{1-x}$ solid solution.

6.2.2 Differential scanning calorimetry

Figure 6.16 shows DSC curves of 2$NaBH_4$-$MnCl_2$ samples milled for different durations. A sharp endothermic peak occurs at around 140 °C for all the milled samples, attributed to the decomposition of $Mn(BH_4)_2$, which matches quite well with the first mass loss in the TGA curves. Prior to decomposition, a relatively weak and broad endothermic peak is present at around 50-70 °C in all the milled samples, followed by an exothermic peak between 80 and 125 °C. This exothermic peak also has a lower temperature shoulder that increases with milling, indicating two reactions. It seems that an endothermic reaction occurs in all the milled samples after the decomposition of manganese borohydride, showing a broad peak in the DSC at around 320-430 ℃ . In combination with mass spectrometry, a small hydrogen release can be observed in the temperature range 300-400 ℃ (see Figure 6.17).

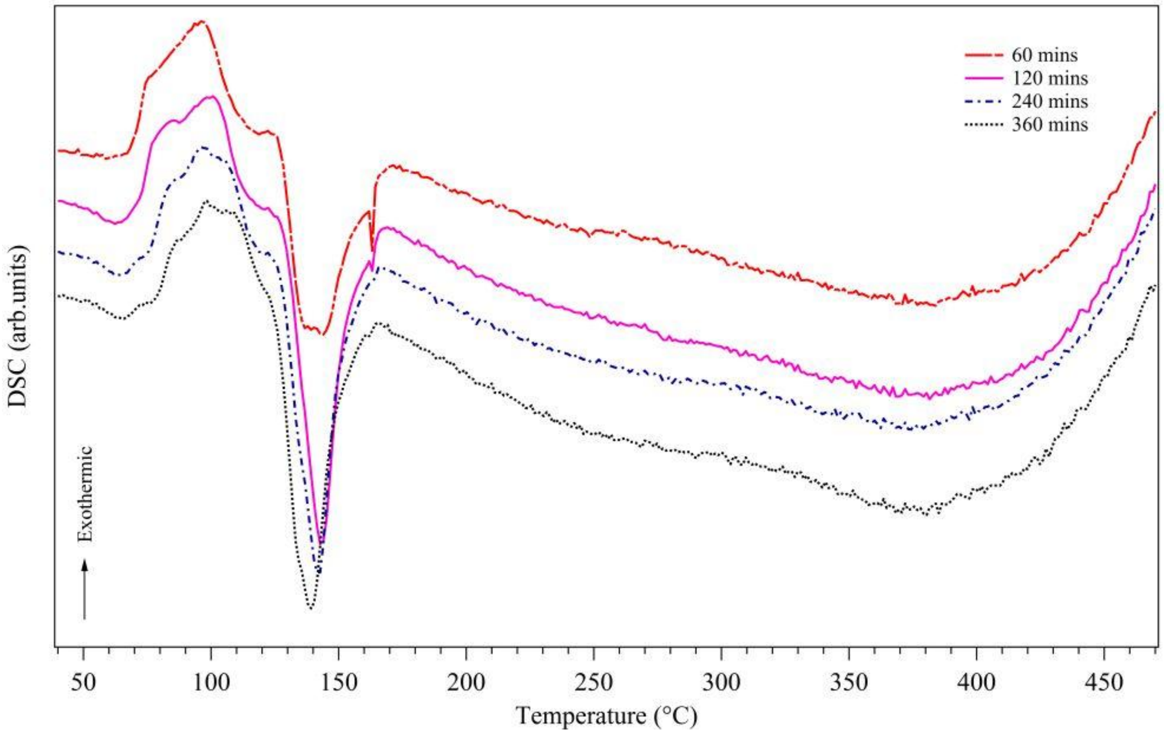

Figure 6.16 DSC curves of $2NaBH_4$-$MnCl_2$ samples milled for different durations, heated at 2 °C/min under 3 bar Ar flowing at 100 ml/min

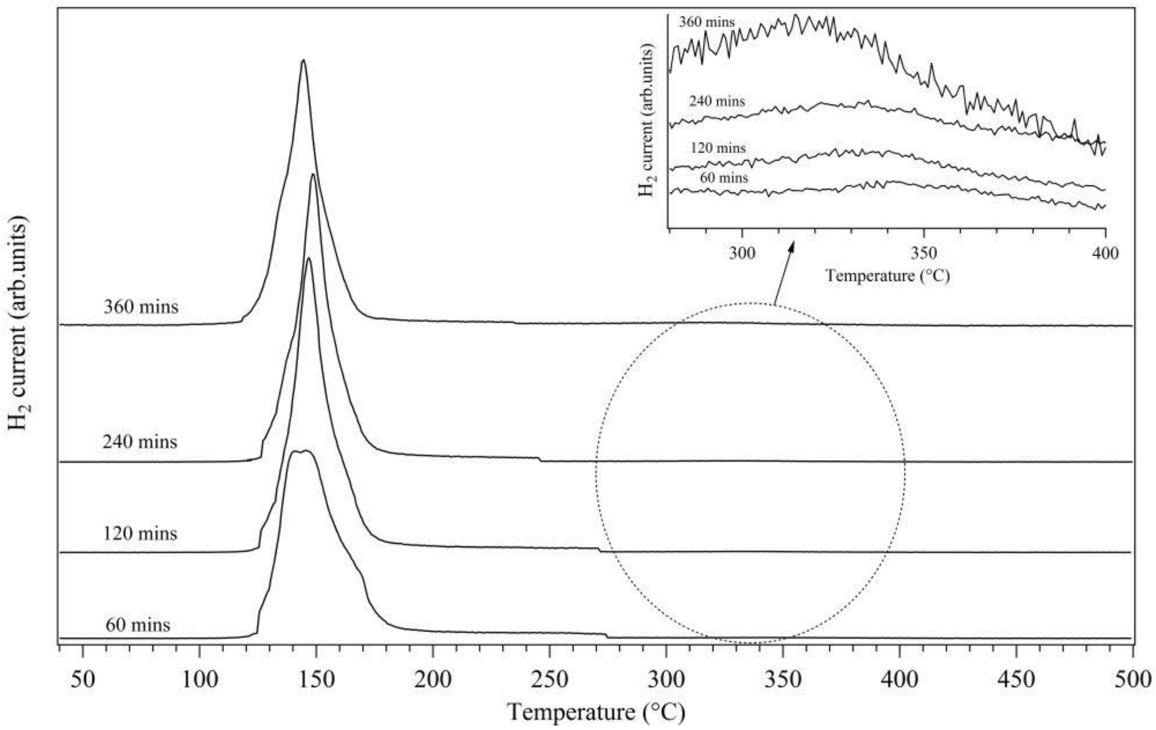

Figure 6.17 Mass spectrometry of $2NaBH_4$-$MnCl_2$ samples milled for different duration showing hydrogen ion current

It is noted that following the major endothermic decomposition peak for manganese borohydride, a small shoulder is observed at 163 °C for the 60 or 120-minute milled samples which gradually disappears after increased milling (Figure 6.16). This endothermic shoulder peak involves hydrogen and diborane evolution, as shown in Figure 6.18. In addition, the overlap of the DSC and mass spectrometry peaks at around 140 ℃ confirms the multiple release process of hydrogen and diborane for the 60-minute milled sample, as opposed to the single peak observed for the 360-minute milled sample (Figure 6.19). These observations imply that the formation of the borohydride compound depends on the milling conditions, with multi-step decomposition behaviour observed after shorter milling durations which is possibly due to mixtures of $Mn(BH_4)_2$ and Mn-based borohydride compounds. It could be interesting to investigate this further by in situ synchrotron XRD and FTIR. After decomposition of the milled samples at 500 °C, no thermal events can be found in DSC profiles for all milled samples during cooling.

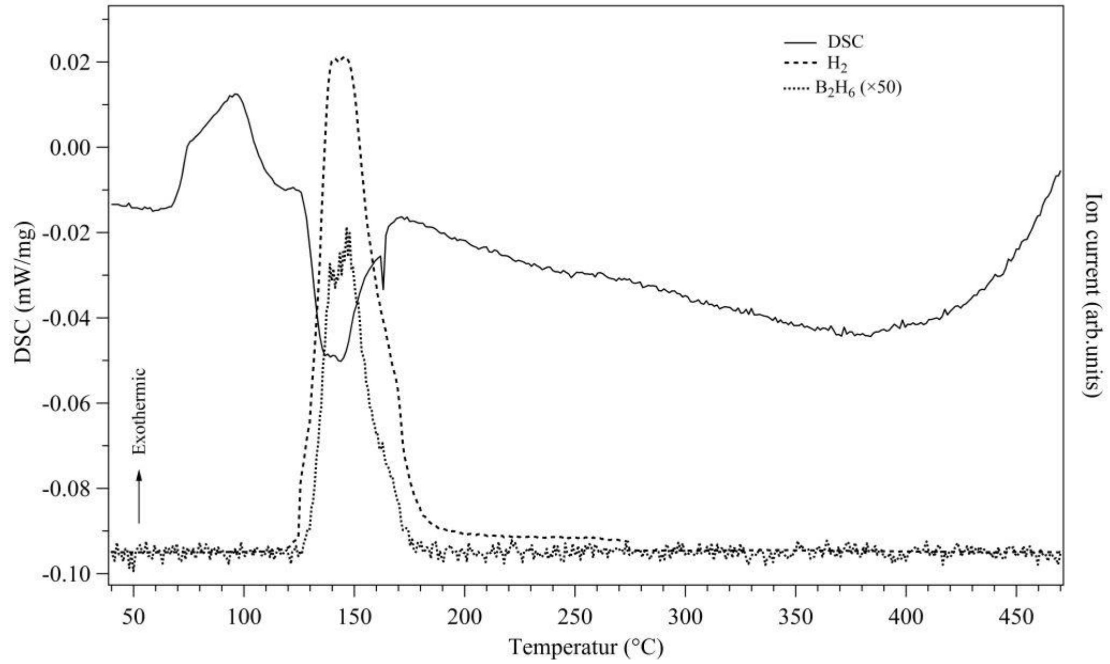

Figure 6.18 DSC profile coupled with MS of $2NaBH_4$-$MnCl_2$ sample milled for 60 minutes

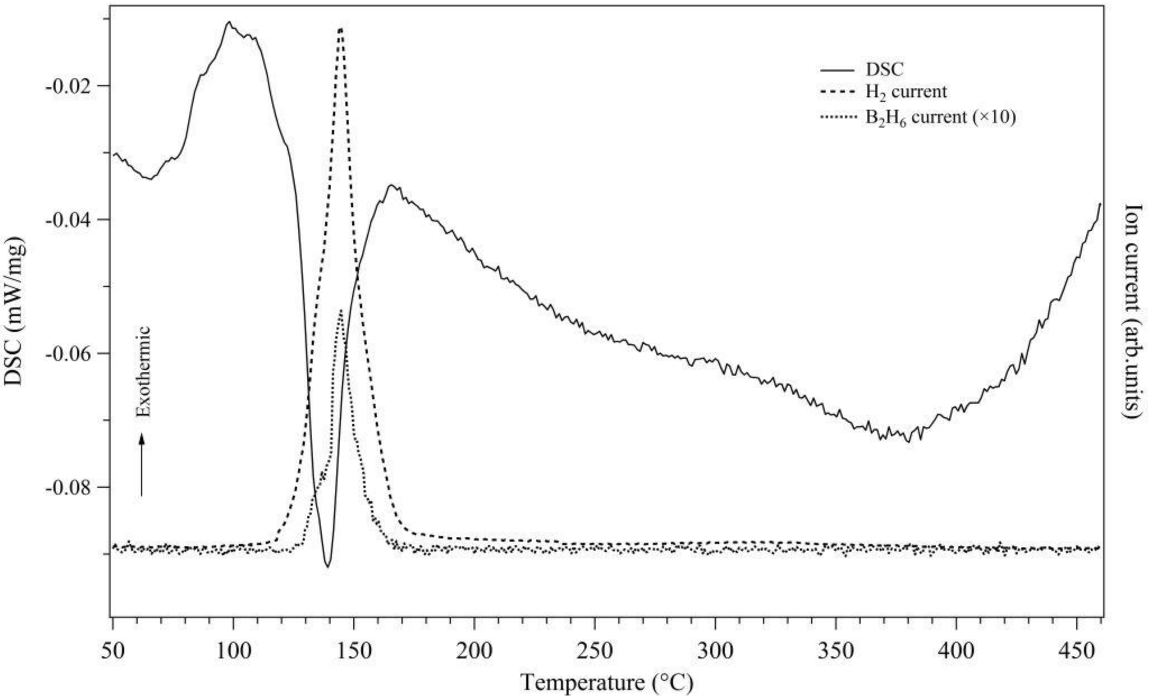

Figure 6.19 DSC profile coupled with MS of $2NaBH_4$-$MnCl_2$ sample milled for 360 minutes

In the case of milled $3NaBH_4$-$MnCl_2$ samples, the endothermic peak associated with the decomposition of $Mn(BH_4)_2$ occurs at 138 ℃ for the 30-minute milled sample, and shifts to a slightly lower temperature (132 ℃) for the 360-minute milled sample, as shown in Figure 6.20. This indicates accelerated decomposition kinetics with increasing milling duration. As observed for the milled $2NaBH_4$-$MnCl_2$ samples, the major decomposition is followed by small shoulders at around 162 ℃ for the 30- or 60-minute milled $3NaBH_4$-$MnCl_2$ sample, with a small amount of hydrogen released (see Figure 6.21). The weak and broad endothermic peak observed at around 50-70 ℃ is possibly due to the ordering of the milled samples, and the broad exothermic peak at around 80-125 ℃ might be derived from the crystallization of phases from the amorphous material observed by *in-situ* XRD (discussed in the next section 6.3). Interestingly, an exothermic peak at 78 ℃ in the DSC curves of the 60-360 minute milled samples increases in intensity with increasing milling duration.

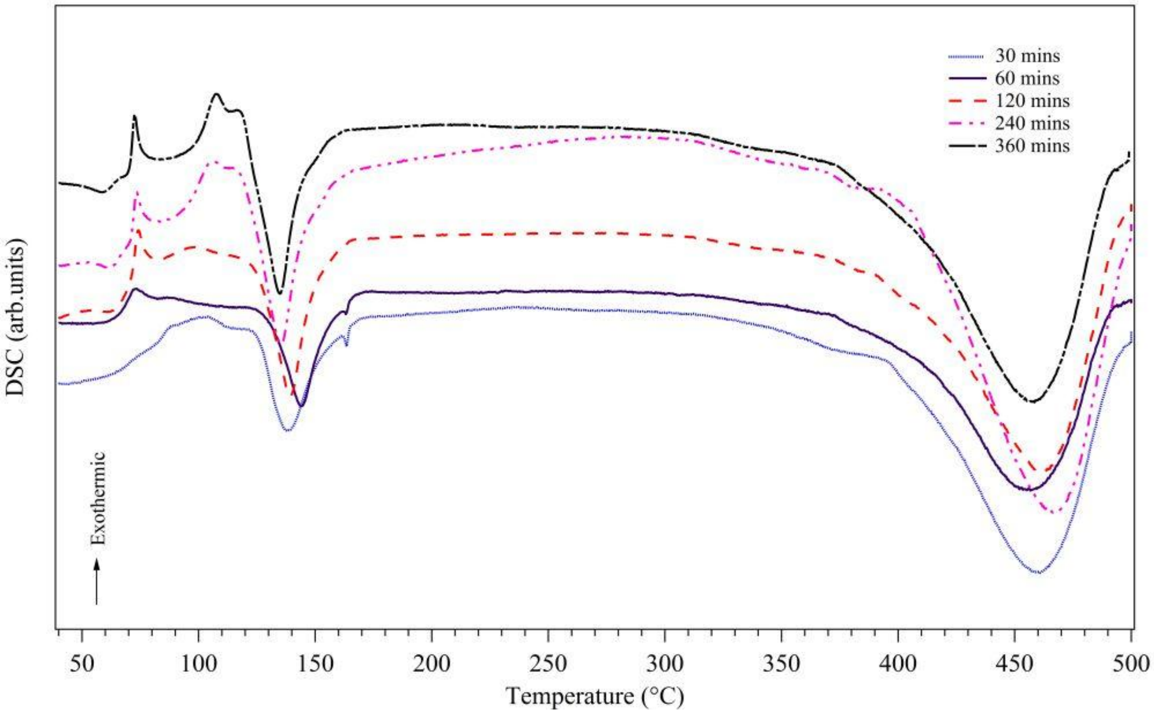

Figure 6.20 DSC profiles of $3NaBH_4$-$MnCl_2$ samples milled for different durations, heated at 2 °C/min under 3 bar Ar flowing at 100 ml/min

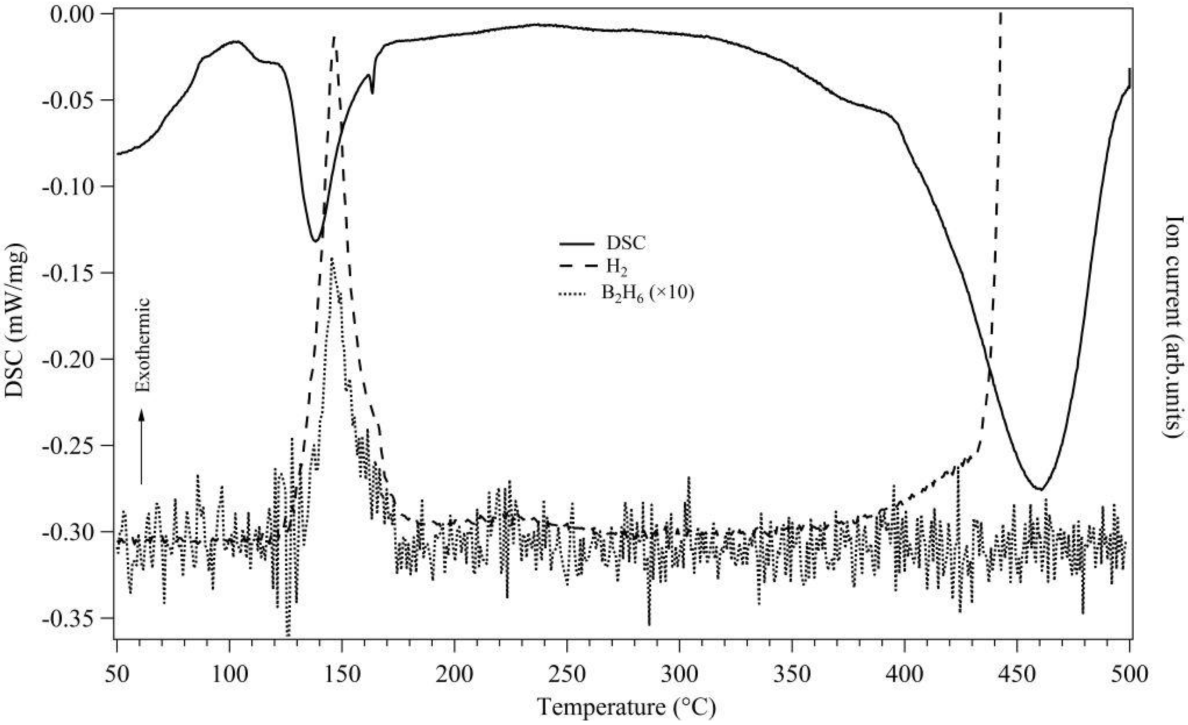

Figure 6.21 DSC profiles coupled with MS for 30-minute milled $3NaBH_4$-$MnCl_2$

There are two main differences between the DSC profiles of the 360-minute milled $2NaBH_4$-$MnCl_2$ (Figure 6.19) and $3NaBH_4$-$MnCl_2$ (Figure 6.22) samples. Firstly, a sharp exothermic peak is observed at 78 ℃ in the $3NaBH_4$-$MnCl_2$ sample. After heating to 100 ℃ , no reversible reaction was observed when the sample was then cooled (Figure 6.23). Also the MS data shows that no hydrogen evolution is observed at 78 ℃ . This suggests that the exothermic peak may be attributed to the formation and/or crystallisation of phases from the amorphous material. Secondly, a large and broad endothermic peak is observed in the $3NaBH_4$-$MnCl_2$ sample from 350 ℃ , which has an associated hydrogen evolution (as shown in a higher magnification of the H_2 MS plot, in the inset of Figure 6.22). This endothermic reaction is potentially associated with hydrogen evolution from $NaBH_4$ contained in the $NaCl_x(BH_4)_{1-x}$ solid solution, which is similar to the decomposition behaviour of $NaBH_4$ alone and in solid solution $NaCl_x(BH_4)_{1-x}$, reported in recent studies (Ravnsbaek et al., 2011; Urgnani et al., 2008).

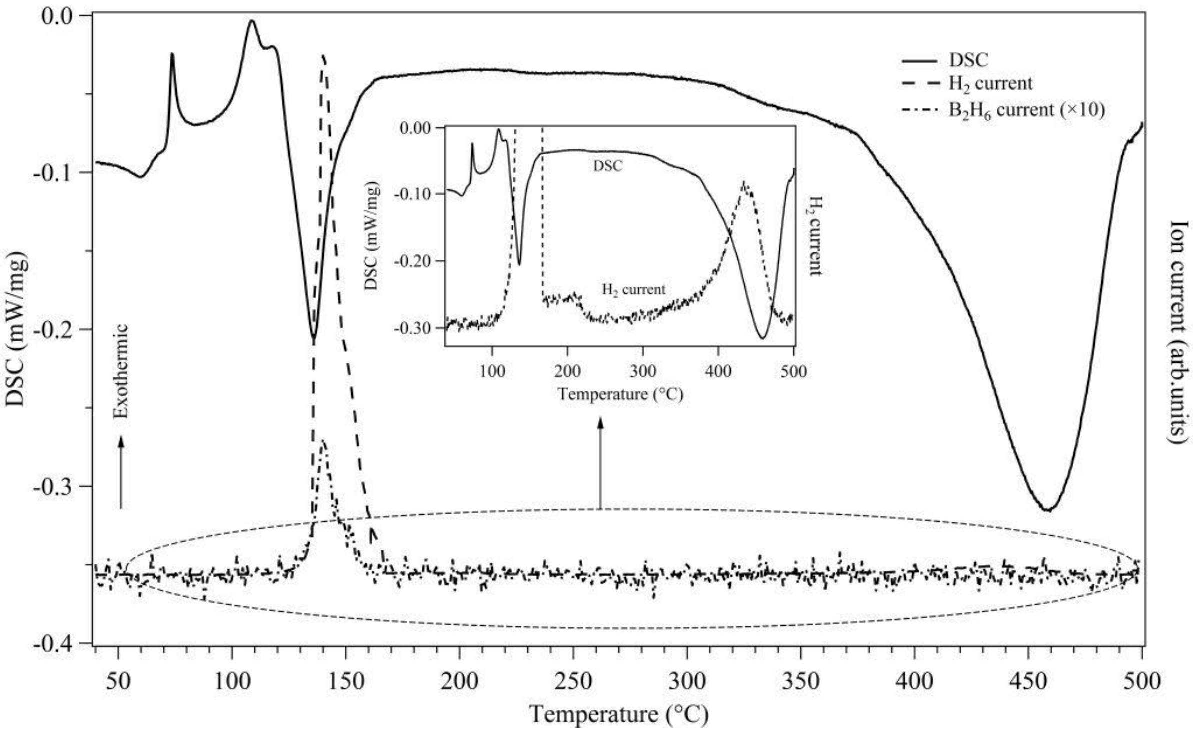

Figure 6.22 DSC profile coupled with MS data for 360-minute milled $3NaBH_4$-$MnCl_2$

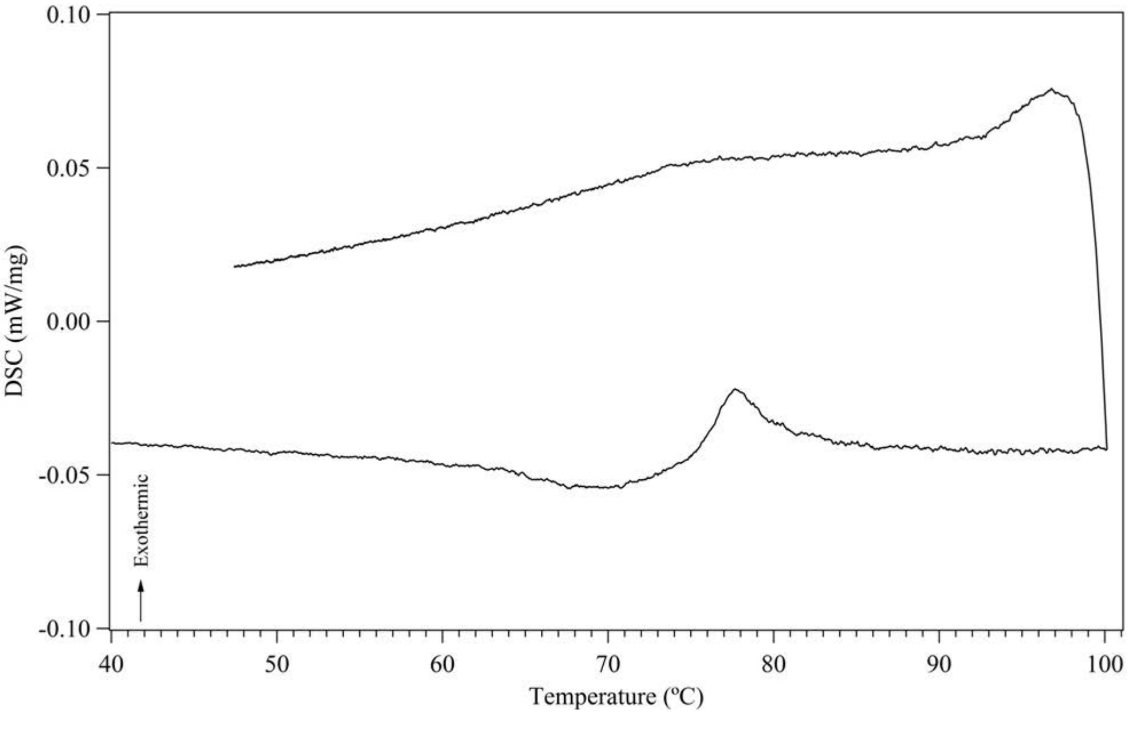

Figure 6.23 DSC profile of 360-minute milled $3NaBH_4$-$MnCl_2$ sample, heated to 100 ℃ at 2 °C/min under 3 bar Ar flowing at 100 ml/min, then cooled to RT

6.3 Decomposition behaviour

6.3.1 Milled $2NaBH_4$-$MnCl_2$

To characterize the decomposition mechanism of the milled $2NaBH_4$-$MnCl_2$ and $3NaBH_4$-$MnCl_2$ samples, *in-situ* XRD and Raman spectroscopy heating from room temperature to 500°C in an inert atmosphere, as well as *ex-situ* Raman and FTIR spectroscopy were used to monitor decomposition reactions, phase changes and any other temperature-dependent transformations.

Figure 6.24 shows *in-situ* XRD patterns of the 360-minute milled $2NaiBH_4$-$MnCl_2$ sample. At room temperature the diffraction peaks of a solid solution $NaCl_x(BH_4)_{1-x}$ and Al_2O_3 are observed. The Al_2O_3 phase is due to the sample crucible. As previously discussed, the milled sample contains approximately 65.7 wt% amorphous Mn-0.7Na-1.7(BH_4)-Cl with the only crystalline phase being a solid solution $NaCl_{0.77}(BH_4)_{0.23}$.

Upon heating to 80 °C the reflections of $Mn(BH_4)_2$ and Na_6MnCl_8 are observed. The formation of $Mn(BH_4)_2$ phase is derived from the crystallization of as milled amorphous material. The reflections due to $Mn(BH_4)_2$ increase in intensity between 100 and 110 °C, and the crystallization of $Mn(BH_4)_2$ and formation of Na_6MnCl_8 correspond to the exothermic DSC peak observed between 75 and 120 °C. Decomposition between 118 and 170 ℃ observed by TGA, is accompanied by a reduction in intensity for $Mn(BH_4)_2$, which is not observed above 150 °C, confirming that the main desorption is due to the thermal decomposition of $Mn(BH_4)_2$. Between 150 and 300 ℃ , no new reflections are present. As with $Mn(BH_4)_2$ formed from the metathesis reaction between $LiBH_4$ and $MnCl_2$ no metallic manganese is observed as a decomposition product.

The ternary chloride, Na_6MnCl_8 forms at the same time as $Mn(BH_4)_2$ crystallizes, indicating that these phases are formed through crystallization from the amorphous component of the as milled material with the maximum intensity on XRD pattern at 130 ℃ . This could be due to a reaction between xNaCl and $(1-x)MnCl_2$ within the as milled mixture, resulting in the formation of Na_6MnCl_8. The reaction of Na_6MnCl_8 between 140 and 350 ℃ is observed, due to the interaction between Na_6MnCl_8 and the $NaCl_x(BH_4)_{1-x}$ solid solution phase(s) to form NaCl, accompanied by the release of hydrogen. A similar reaction of ternary chloride Na_2ZnCl_4 with an alkali-metal borohydride compound to form metallic Zn and NaCl was suggested by Ravnsbaek et al (2009).

Figure 6.25 shows the unit cell volume of $NaCl_x(BH_4)_{1-x}$ as a function of temperature. Initially, the unit cell volume of $NaCl_{0.77}(BH_4)_{0.23}$ increases during heating to 100 °C (at a rate of 5.21×10^{-2} Å^3/°C). Between 100 and 250 °C there is a slight contraction in the cell volume (-2.7×10^{-3} Å^3/°C), apart from an expansion and contraction between 120 and 160°C corresponding to the decomposition of $Mn(BH_4)_2$. This slight contraction is due to annealing of the $NaCl_x(BH_4)_{1-x}$ solution within the ternary $NaBH_4$-$MnCl_2$-NaCl system. Between 250 and 370 °C there is a contraction in the lattice which corresponds to a second evolution of hydrogen. This is due to further substitution of $[BH_4]^-$ ions by Cl^- within the lattice. This lattice contraction also coincides with the reaction of Na_6MnCl_8, leading to excess Cl^- entering into the $NaCl_x(BH_4)_{1-x}$ solution. Above 380 °C, the lattice expansion corresponds to that of pure NaCl . Subsequent cooling from 500 to 30 °C results in a cell volume of 179.82 (2) Å^3 for the rocksalt phase, which agrees with that for NaCl (179.4 Å^3) at 30 °C (Swanson and Fuyat, 1953).

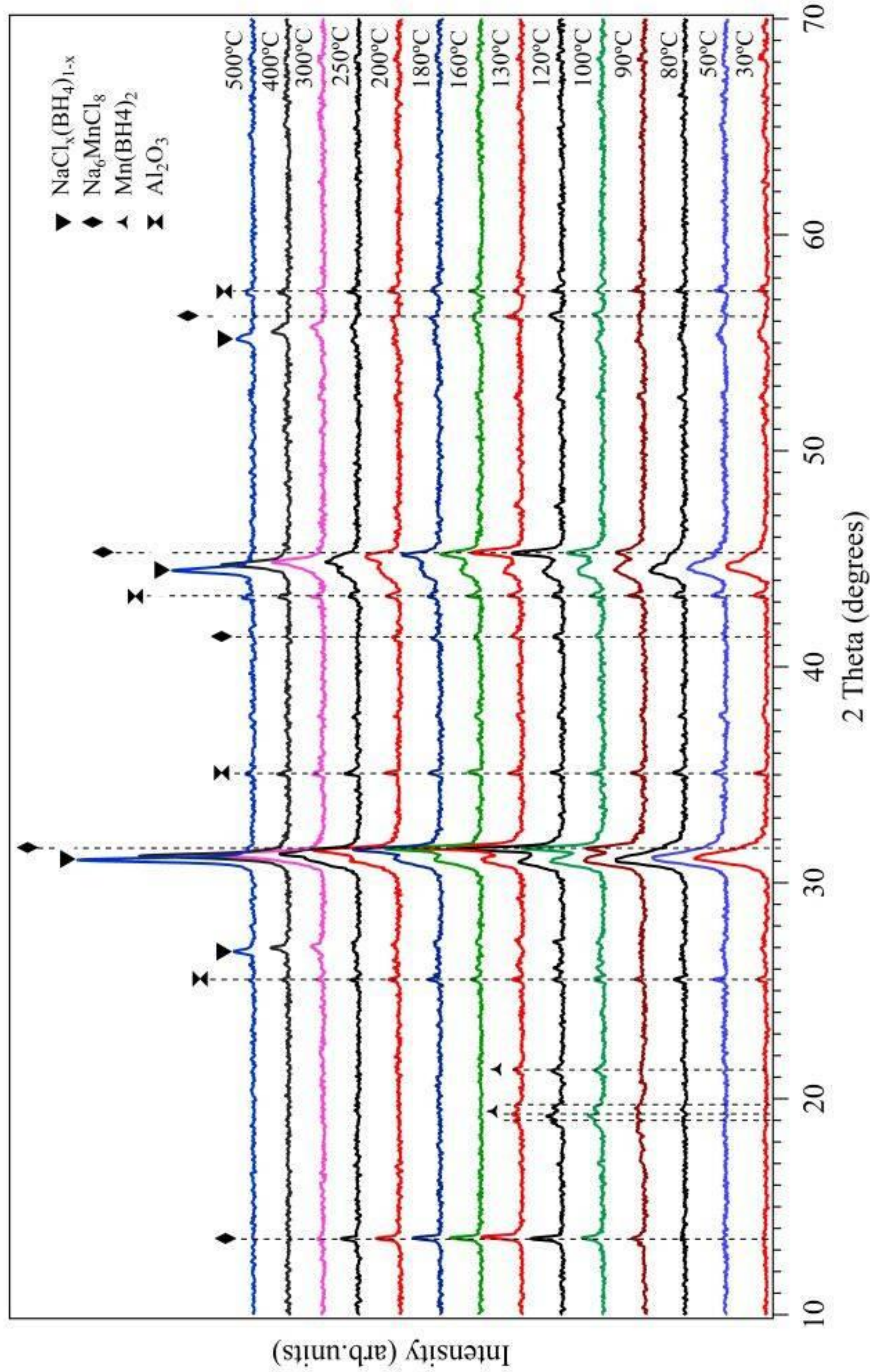

Figure 6.24 In-situ XRD patterns of the 360-minute milled $2NaBH_4$-$MnCl_2$ sample, heated from 30 to 500°C in 3 bar He flowing at 100 ml/min

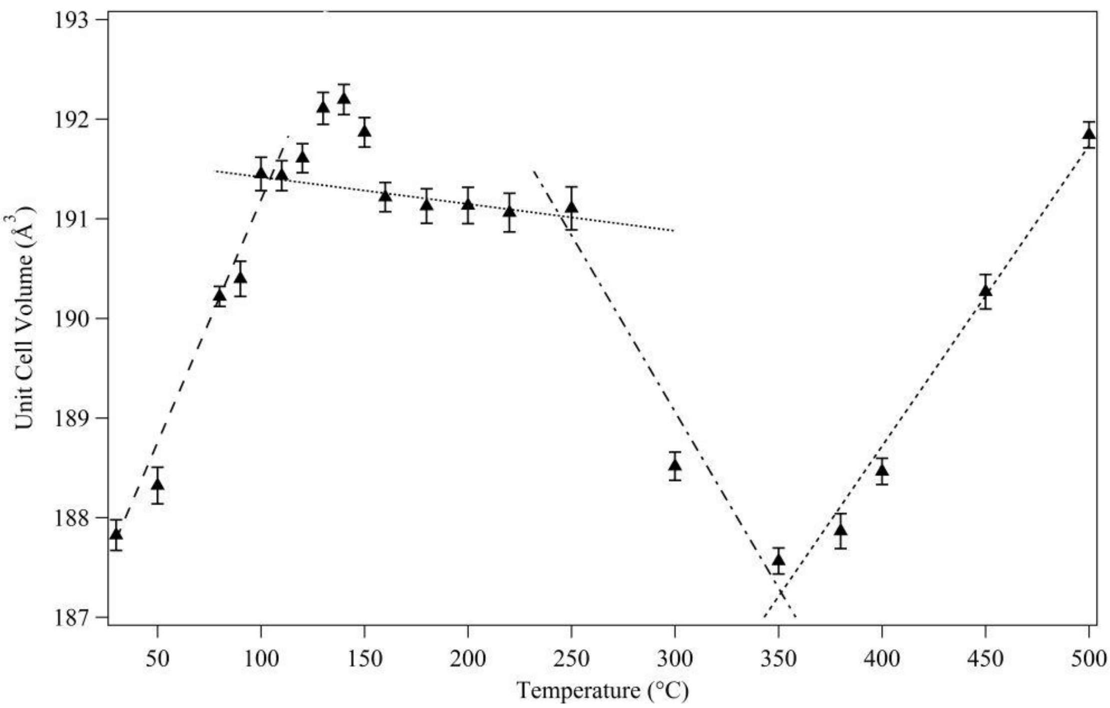

Figure 6.25 Unit cell volume for $NaCl_x(BH_4)_{1-x}$ *formed from milled* $2NaBH_4$-$MnCl_2$ *sample between 30 and 500 °C, calculated from Figure 6.24; error bars show 3ESDs*

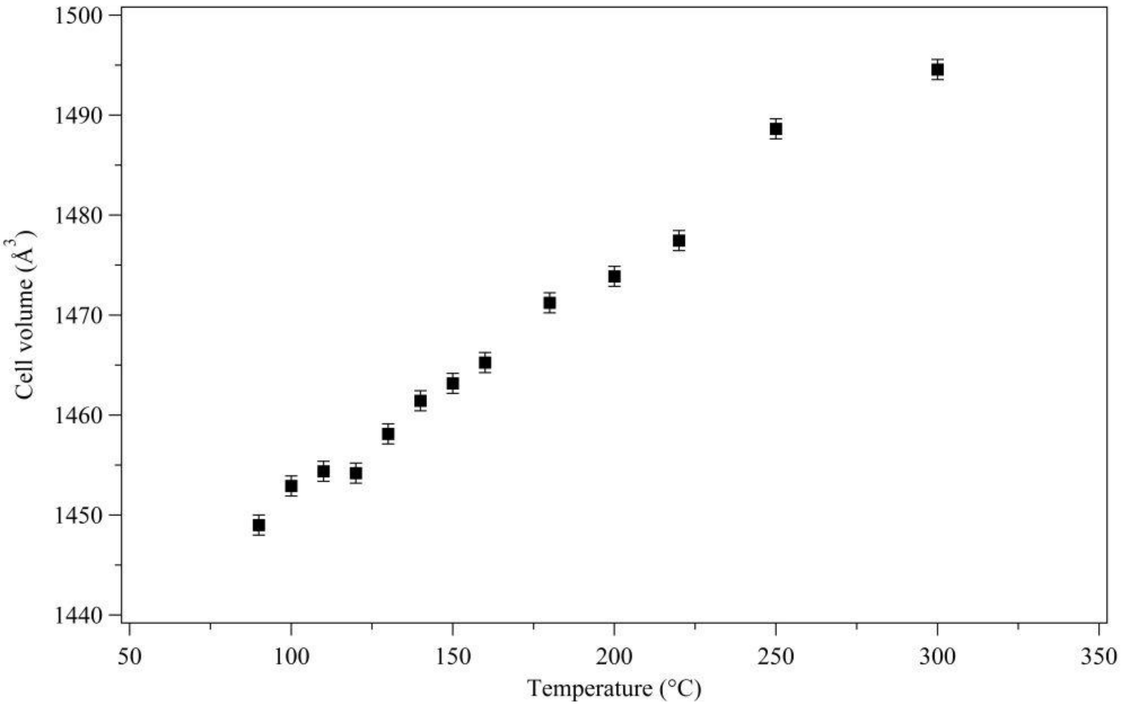

Figure 6.26 Unit cell volume for Na_6MnCl_8 *between 90 and 300 °C in flowing He (3 bar 100 ml/min), calculated from Figure 6.24; error bars show 3ESDs*

The unit cell volume for Na_6MnCl_8 shows a linear expansion between 90 and 300 °C of 5.76 $\times 10^{-2}$ Å^3/°C (Figure 6.26). This indicates that there is no substitution of $[BH_4]^-$ for Cl^- within this compound, which suggests that all the remnant $[BH_4]^-$ in the sample after the decomposition of $Mn(BH_4)_2$ must reside within the $NaCl_x(BH_4)_{1-x}$ solution.

In-situ Raman spectroscopy of the 360-minute milled $2NaBH_4$-$MnCl_2$ sample is shown in Figure 6.27. The intensity of the bending of the $[BH_4]^-$ bands between 1100 and 1400 cm^{-1}, and of the B-H bond stretching modes between 2240 and 2360 cm^{-1}, decrease with increasing temperature. Above 130 °C no vibrations are observed for any BH_4 compound, corresponding to the thermal decomposition of $Mn(BH_4)_2$. There is a small trace of B-B bonding consistent with amorphous boron with weak bands at around 350-450, 700-900 and 1050-1150 cm^{-1}, at 130, 150 and 200 °C, respectively (Figure 6.28). The absence of Mn-B or B-H bonding in the Raman spectra suggests that either no manganese boride or borane compounds form during the decomposition of $Mn(BH_4)_2$, or that any such Raman peaks are hidden by fluorescence effects.

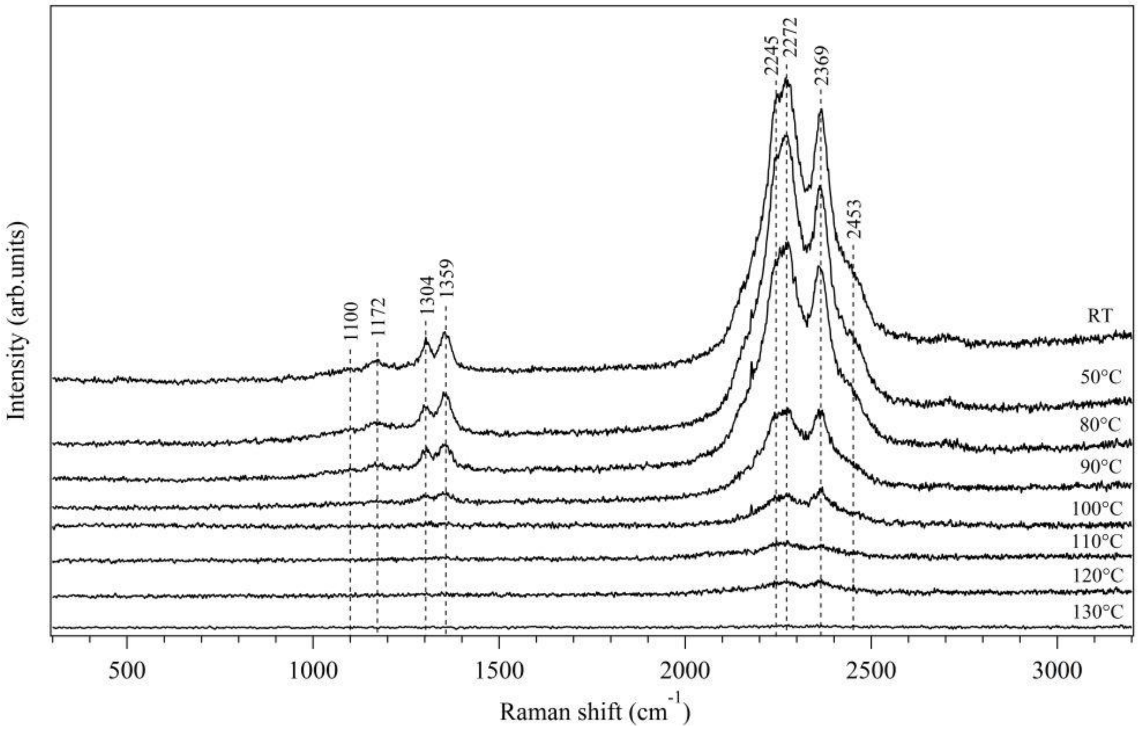

Figure 6.27 In-situ Raman spectroscopy of 360-minute milled $2NaBH_4$-$MnCl_2$ sample heated from RT to 130°C in 1 bar Ar flowing at 100 ml/min

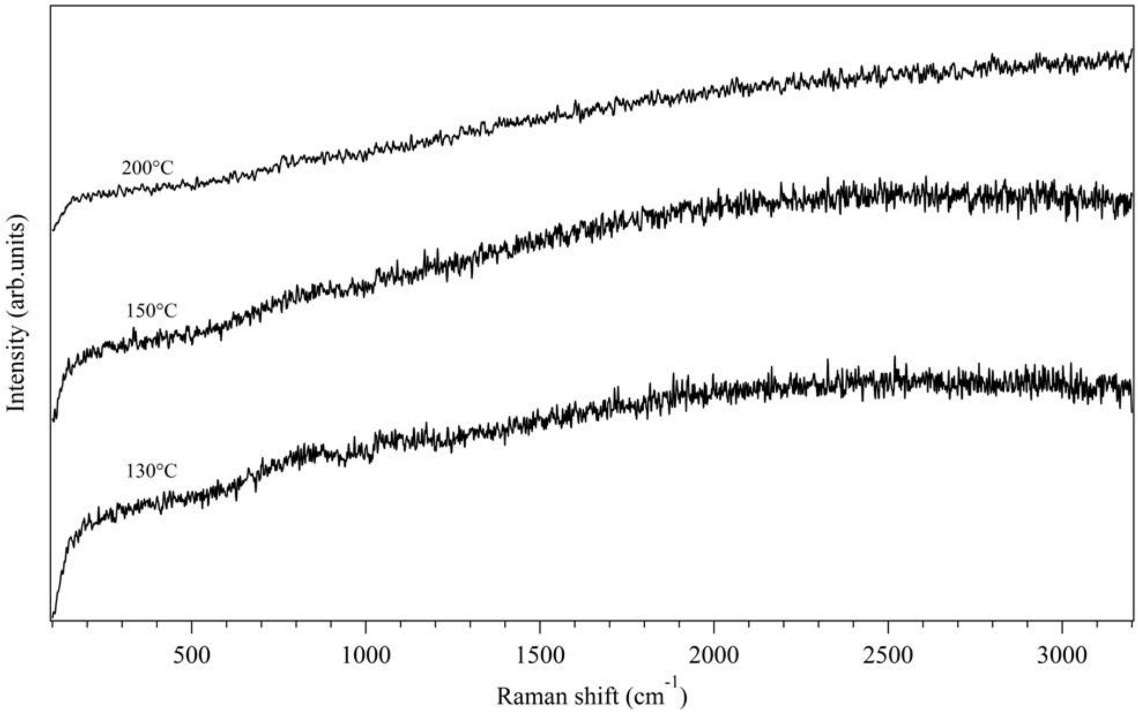

Figure 6.28 In-situ Raman spectroscopy of 360-minute milled $2NaBH_4$-$MnCl_2$ sample heated to 130, 150 and 200°C in 1 bar Ar flowing at 100 ml/min

Raman measurements were carried out on the 360-minute milled $2NaBH_4$-$MnCl_2$ sample that had been heated to 200 °C and then cooled to room temperature: no vibration modes are observed. However, a sharp band at 641 cm^{-1} is present after the decomposed sample was exposed to air for 5 minutes (Figure 6.29), which may be attributed to the formation of manganese oxide (Mn_3O_4) (Buciuman et al., 1999; Mironova-Ulmane et al., 2009). This result indirectly indicates that finely dispersed manganese may be formed as one of the decomposition products, for the milled $2NaBH_4$-$MnCl_2$ sample.

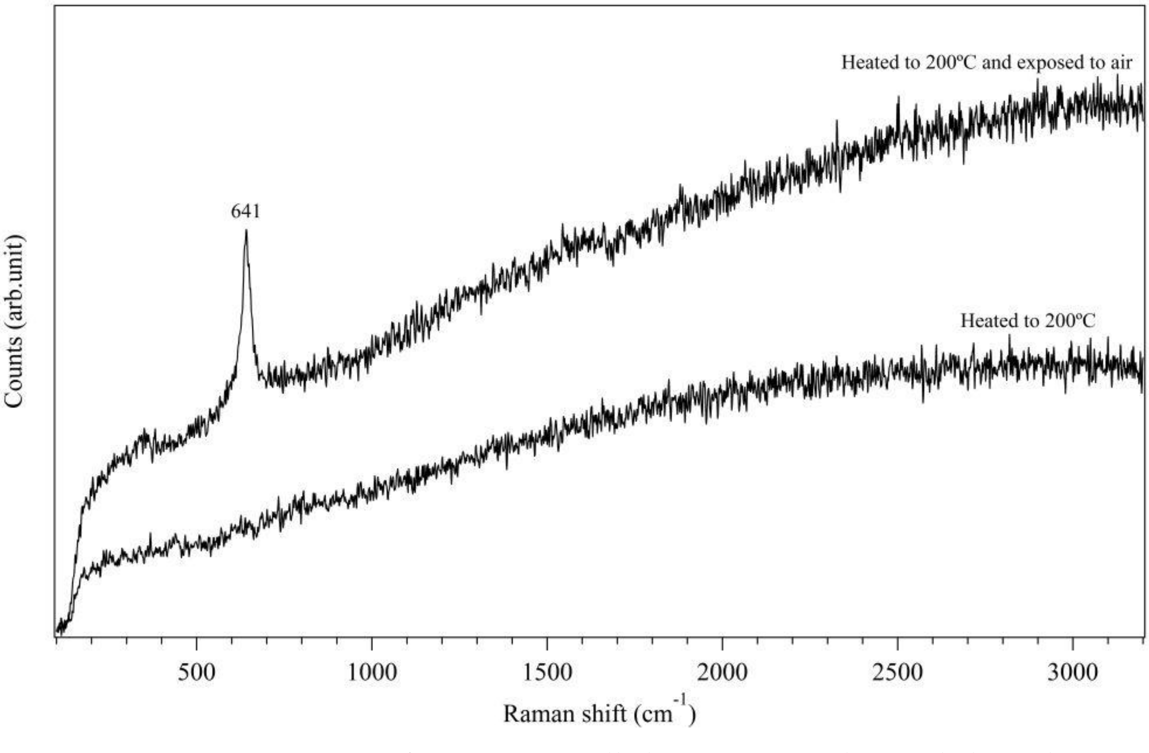

Figure 6.29 Raman spectra of 360-minute milled $2NaBH_4$-$MnCl_2$ sample heated to 200 °C then exposed to the air for 5 minutes

Figure 6.30 shows FTIR spectra of the 360-minute milled $2NaBH_4$-$MnCl_2$ sample. The decomposed sample at 200 °C shows that bands at 2360, 2290 and 1150 cm^{-1} are still present; these are the ionic $[BH_4]^-$ tetrahedra within the $NaCl_x(BH_4)_{1-x}$ solid solution. The reduction in intensity of the B-H modes and the absence of any vibrations due to $Mn(BH_4)_2$ supports previous measurements that show the complete decomposition of $Mn(BH_4)_2$. The bands at

1258 and 1338 cm^{-1} are associated with B-B vibrations due to amorphous boron. Upon further heating to 500 °C, no B-H vibrations remain, indicating the decomposition of the solid solution within the mixture, yielding NaCl. Although less well defined due to an elevated background, amorphous boron is still present.

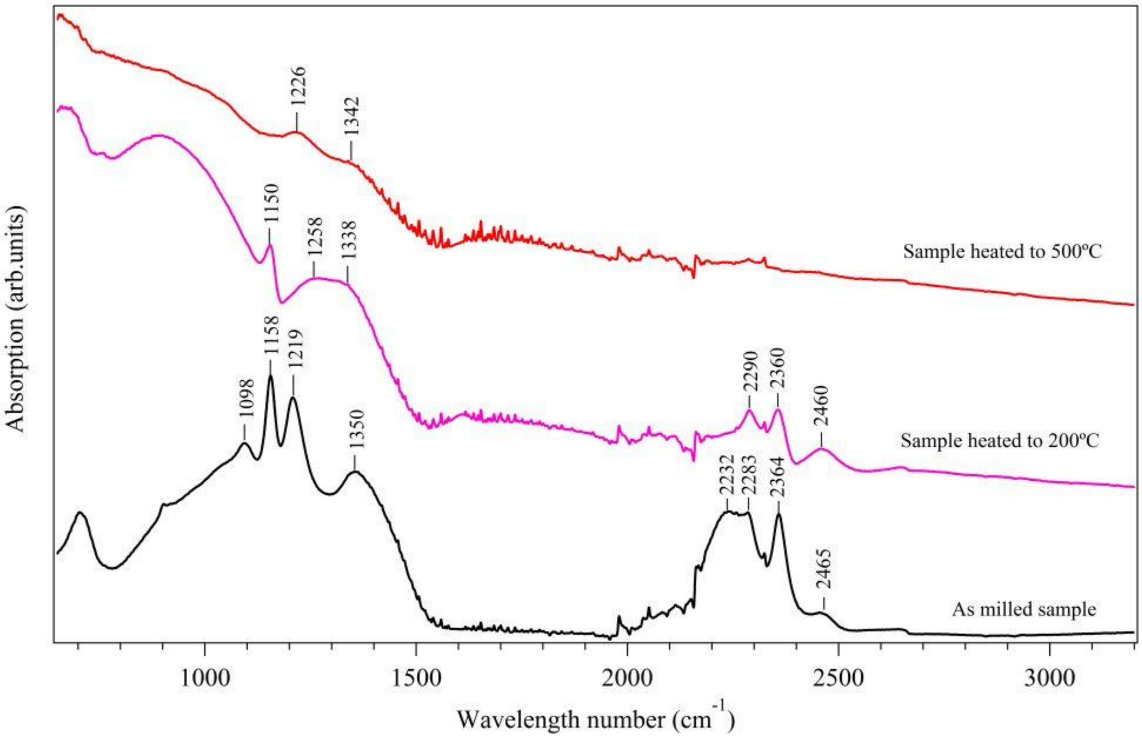

Figure 6.30 FTIR spectra of 360-minute milled $2NaBH_4$-$MnCl_2$ *sample heated to 200 and 500 °C in 3 bar Ar flowing at 100 ml/min*

Through the combination of thermal analysis and *in-situ* measurements, the thermal decomposition process for the 360-minute milled $2NaBH_4$-$MnCl_2$ sample can be expressed in equation (6.3). This total reaction involves several steps. The first exothermic step between 80 and 115 °C corresponds to the crystallization of $Mn(BH_4)_2$ and Na_6MnCl_8 (equation (6.4)). From 120 to 170 °C there is an endothermic reaction corresponding to the decomposition of $Mn(BH_4)_2$ with the evolution of hydrogen and diborane according to equation (5.7). It is not clear why Mn is not observed by XRD in this study, or in a previous study using $LiBH_4$ as the reagent (Chapter 5). It may be because the Mn takes the form of finely dispersed nanoscale grains. Alternatively, it may take the form of an amorphous Mn-B compound, e.g. MnB, MnB_2 or MnB_4 , however, the absence of Mn-B vibrations in the Raman and FTIR spectra would then need to be explained. From 250 to 425 °C a reaction between $NaCl_x(BH_4)_{1-x}$ phase(s) and Na_6MnCl_8 occurs with the evolution of hydrogen (equation (6.5)).

$$1.29NaCl_{0.77}(BH_4)_{0.23} + 0.85Mn(BH_4)_2 + \text{“}0.7Na\text{-}0.15Mn\text{-}Cl\text{”} \rightarrow$$

$$2NaCl + Mn + 1.44B + 3.16H_2 + 0.28B_2H_6 \qquad (6.3)$$

$$1.29NaCl_{0.77}(BH_4)_{0.23} + 0.85Mn(BH_4)_2 + \text{“}0.7Na\text{-}0.15Mn\text{-}Cl\text{”} \rightarrow$$

$$0.85Mn(BH_4)_2 + 0.15Na_6MnCl_8 + 1.1NaCl_{0.72}(BH_4)_{0.28} \qquad (6.4)$$

$$0.15Na_6MnCl_8 + 1.1NaCl_{0.72}(BH_4)_{0.28} \rightarrow$$

$$2NaCl + 0.15Mn + 0.31B + 0.61H_2 \qquad (6.5)$$

6.3.2 Milled $3NaBH_4$-$MnCl_2$

Figure 6.31 shows the *in-situ* XRD patterns of the 360-minute milled $3NaBH_4$-$MnCl_2$ sample. As previously discussed, the as milled material shows reflections due to $NaCl_{0.68}(BH_4)_{0.32}$ and very weak reflections due to $Mn(BH_4)_2$, with an amorphous content of about 64 wt%. Upon heating to 80 °C the reflections attributed to $Mn(BH_4)_2$ become significantly stronger, indicative of improved crystallinity. At 100 °C, as with the 360-minute milled $2NaBH_4$-$MnCl_2$ sample, reflections due to Na_6MnCl_8 are observed, indicating that this reaction process is likely to correspond to the two exothermic DSC peaks observed between 80 and 125 ℃ .

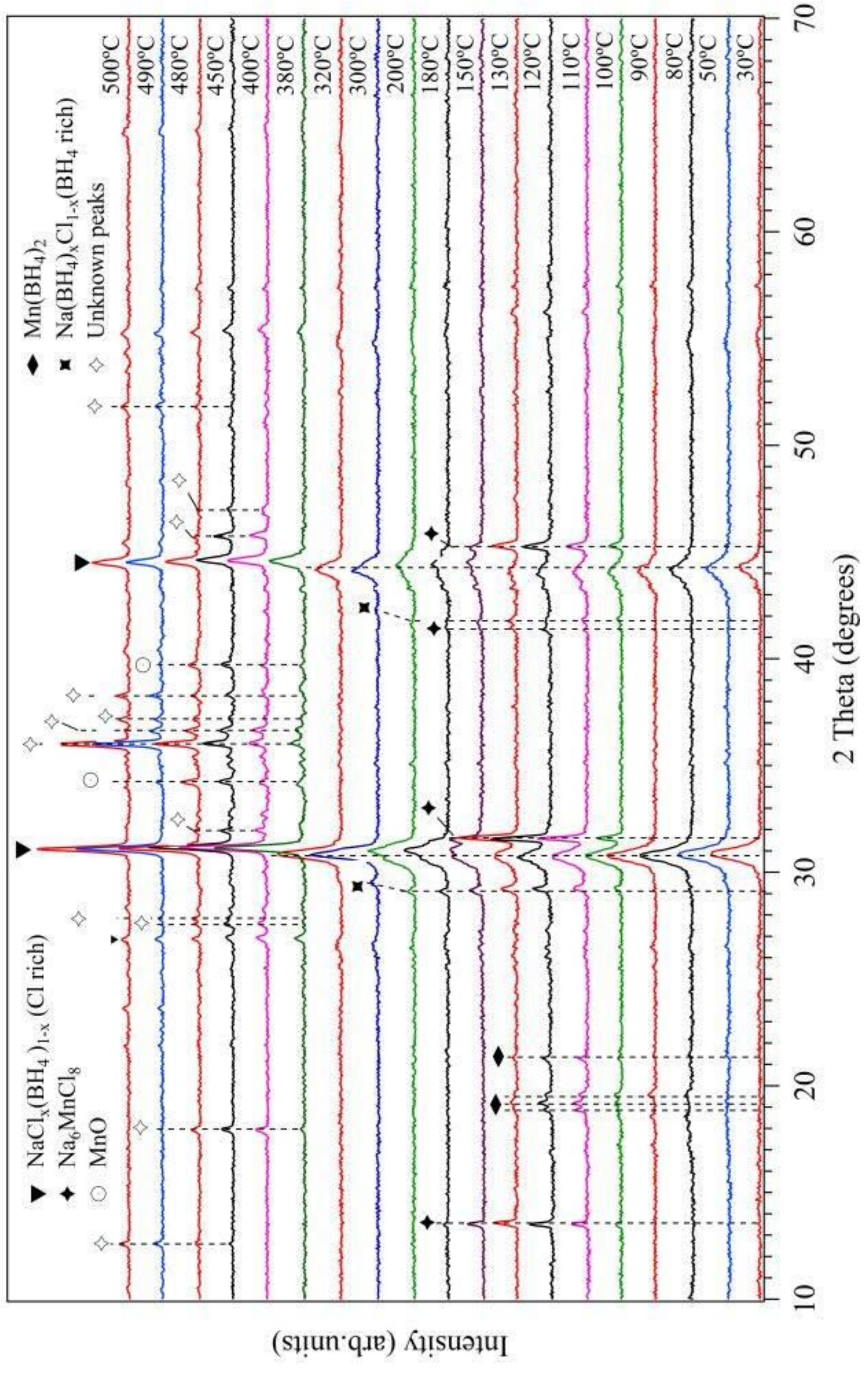

Figure 6.31 In-situ XRD patterns of 360-minute milled $3NaBH_4$-$MnCl_2$ sample, heated from 30 to 500 °C in 3 bar He flowing at 100 ml/min

Between 100 and 320 °C, a $NaBH_4$-type phase is observed. Through refinement of XRD patterns using TOPAS, the lattice parameters of this phase at 100 °C are estimated to be 6.097(2) Å (*a*) and 226.7(3) $Å^3$ (cell volume), which are lower than those for $NaBH_4$ (a = 6.139 Å, v = 231.4 $Å^3$) even at room temperature (Soldate, 1947). The reduction in lattice parameters is due to the substitution of Cl^- for BH_4^- in $NaBH_4$ to form BH_4^--rich solid solution phase(s) $Na(BH_4)_xCl_{1-x}$. The BH_4^--rich solid solution phase forms at the time as the ternary chloride Na_6MnCl_8 appears, indicating that these phases are produced through crystallization from the amorphous component of the as-milled material. The formation of the ternary chloride phase causes a decrease in Cl^- content of the remaining material, and so resulting in the formation of a BH_4^--rich solid solution phase.

Reflections due to $Mn(BH)_4$ are no longer present at 150 °C, indicating that decomposition is complete, as suggested in Figure 6.31, which is consistent with the decomposition of $Mn(BH_4)_2$ between 110 and 160 °C shown in the TGA profile (Figure 6.15). The ternary chloride Na_6MnCl_8 is no longer observed above 200 °C, where it reacts with $NaCl_x(BH_4)_{1-x}$ to form NaCl, as with the 360-minute milled $2NaBH_4$-$MnCl_2$ sample, with the release of hydrogen.

Above 370 °C, two small X-ray peaks corresponding to MnO are observed at 34.1 and 39.6° 2θ, together with several unknown peaks in the XRD pattern. The peaks are believed to originate from the decomposition of the $NaCl_x(BH_4)_{1-x}$ solid solution phase(s). These decomposition products do not have X-ray peaks consistent with Mn_xB_y, $NaBO_2$, NaH, Na, $Na_2B_{12}H_{12}$, $Na_2B_{10}H_{10}$, $Na_xMn_yO_z$, Na_2O or NaOH. However, with the limitations of lab-based diffraction, accurate determination of the number and nature of these phase(s) has not been possible. At 380 °C the reflections at 17.9, 27.8, 28.4, 31.8, 35.9, 36.6, 37.1 and 38.5°

2θ are observed. Of these peaks, the reflections at 17.9, 27.8, 28.4, 31.8° 2θ are present until 490 °C, and the reflections at 35.9, 36.6, 37.1 and 38.5° 2θ are present to 500°C. Another series of reflection are observed at around 450-480 °C at 12.6, 22.0, 23.6, 40.3, 48.2, 51.8 and 54.3° 2θ, and remain after heating to 500 °C and after subsequent cooling to room temperature.

To understand the transformations that occur between the solid solutions better, the lattice parameters of the two different solid solutions are plotted against temperature (Figure 6.32). Initially, the broad reflections give a $NaCl_x(BH_4)_{1-x}$(Cl-rich) phase(s) of average composition $NaCl_{0.68}(BH_4)_{0.32}$. Upon heating the expected thermal expansion is not observed between 50 and 80 ℃ , indicating that either a new phase is formed that cannot be distinguished as a discrete phase or the formation of a more chloride-rich composition occurs within the solid solution.

Linear thermal expansion is observed between 80 and 130 °C (7.1 x 10^{-2} Å^3/ °C), this is accompanied by a reduction in peak width at 100 °C and the observation of the other solid solution $Na(BH_4)_xCl_{1-x}$(BH_4-rich). Between 200 and 250 °C, the cell volume of $NaCl_x(BH_4)_{1-x}$(Cl-rich) decreases, suggesting higher Cl^- substitution in the solid solution which corresponds to small amounts of hydrogen evolution, and then remains consistent until 320 °C.

For the $Na(BH_4)_xCl_{1-x}$(BH_4-rich) phase, the expected thermal expansion in the lattice is observed between 100 and 170°C. From 170 to 320 °C there is a reduction in cell volume, suggesting more Cl^- ions in the lattice which is possibly due to the interaction between the two solid solutions.

Above 320 °C, the two solid solutions consolidate to form a single $NaCl_x(BH_4)_{1-x}$ solid solution. Between 320 and 440 °C there is a contraction in the lattice, this corresponds to the third evolution of hydrogen observed in TGA (Figure 6.15), with more Cl^- substitution into the lattice. Above 440 °C the increase in cell volume is due to the thermal expansion of the NaCl-type phase.

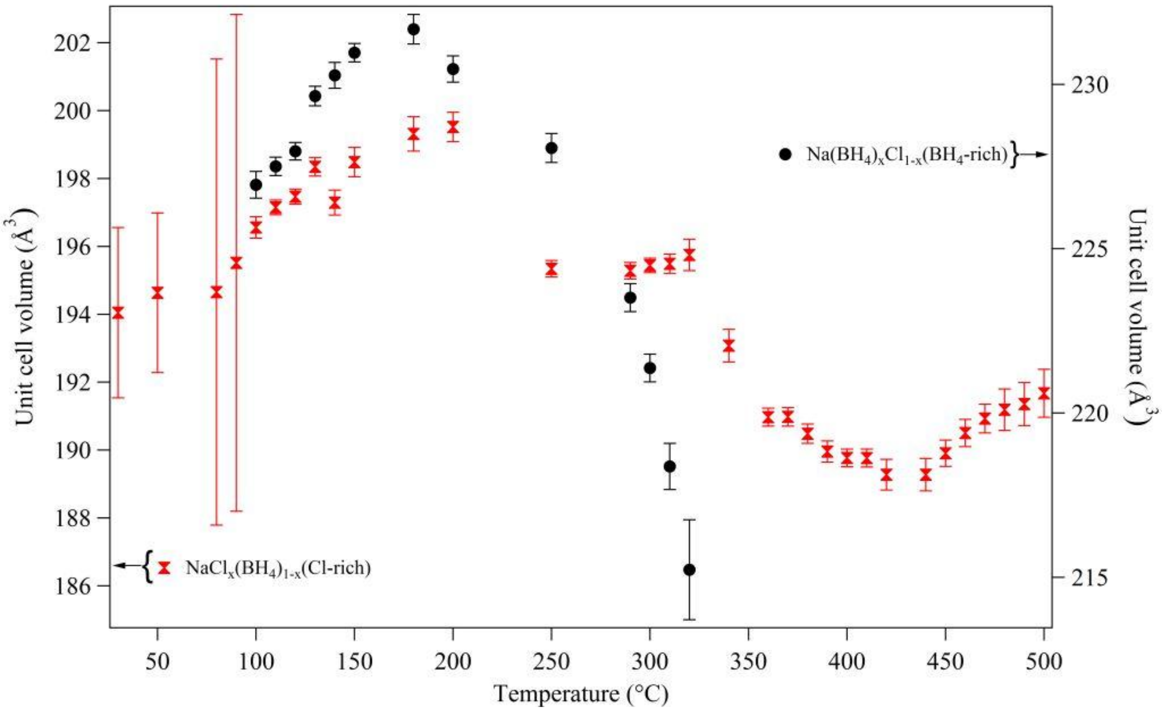

Figure 6.32 Unit cell volume for $NaCl_x(BH_4)_{1-x}$ formed from the 360-minute milled $3NaBH_4$-$MnCl_2$ sample between 30 and 500 °C, calculated from Figure 6.31; error bars show 3ESDs

In-situ Raman spectroscopy of the 360-minute milled $3NaBH_4$-$MnCl_2$ is shown in Figure Figure 6.33. The intensity of the B-H bending bands at around 1100-1400 cm^{-1}, and the B-H stretching mode at around 2240-2360 cm^{-1}, both decrease with increasing temperature. B-H stretching or bending modes are no longer observed after 130 ℃ , which corresponds to the decomposition of $Mn(BH_4)_2$. Above 130 °C, although *in-situ* XRD shows that the $NaCl_x(BH_4)_{1-x}$ solid solutions are present, their vibrational modes are not observed. The weak bands around 350-450, 700-900 and 1050-1150 cm^{-1} at 130, 160 and 200 ℃ are present as shown Figure 6.34, which are associated with B-B bands.

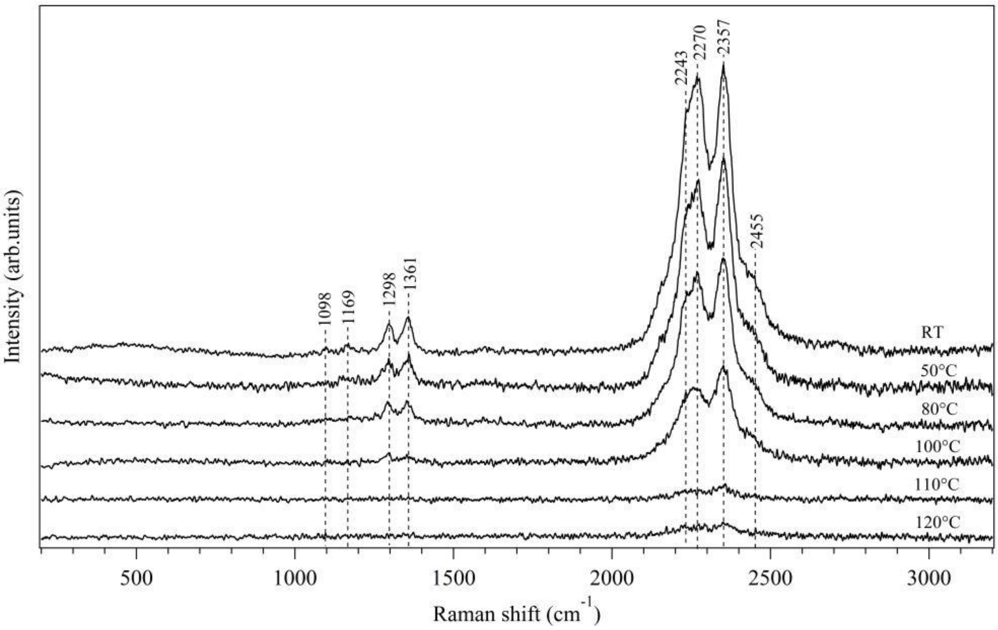

Figure 6.33 In-situ Raman spectroscopy of 360-minute milled 3$NaBH_4$-$MnCl_2$ sample, heated from RT to 120℃ in 1 bar Ar flowing at 100 ml/min

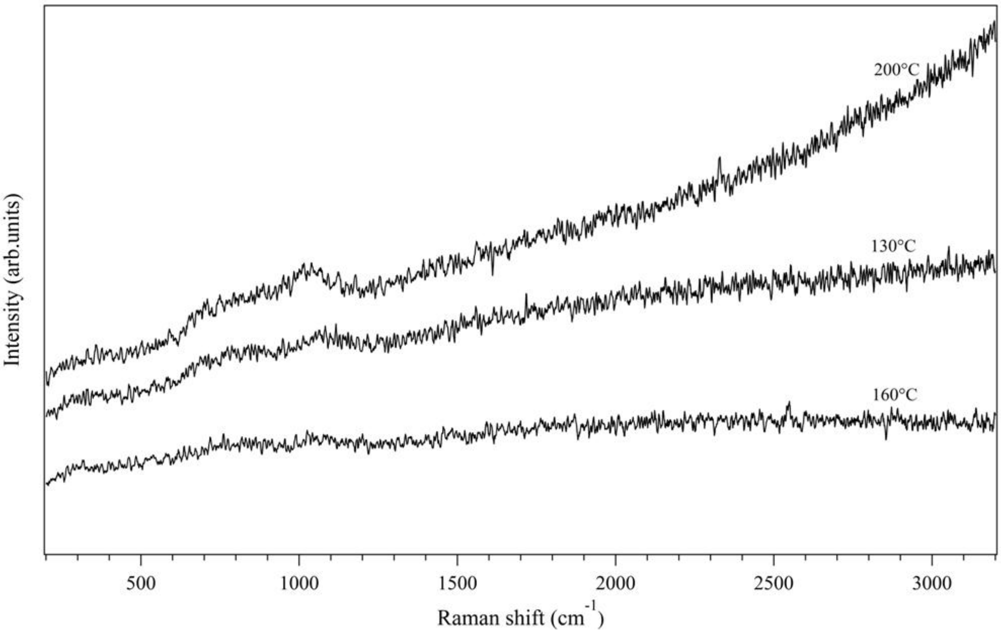

Figure 6.34 In-situ Raman spectroscopy of 360-minute milled 3$NaBH_4$-$MnCl_2$ sample heated to 130, 160 and 200℃ in 1 bar Ar flowing at 100 ml/min

However, IR measurements (Figure 6.35) shows that on heating to 200 °C significant B-H vibration modes are observed at 1120, 2292 and 2332 cm^{-1} due to $NaCl_x(BH_4)_{1-x}$ solid solutions which are not observed by Raman spectroscopy. The observed vibration bands at 900, 1253 and 1332 cm^{-1} are associated with B-B vibrations due to amorphous boron.

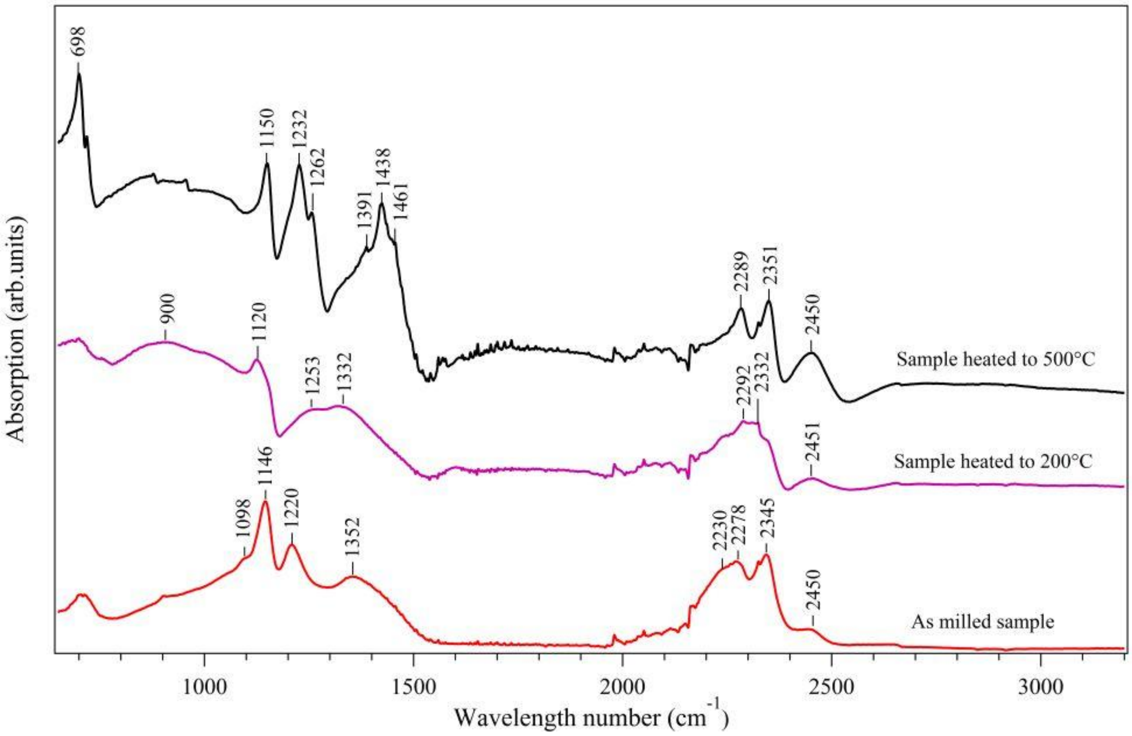

Figure 6.35 FTIR spectra of 360-minute milled $3NaBH_4$-$MnCl_2$ sample heated to 200 and 500 °C in 3bar Ar flowing at 100 ml/min

On further heating to 500 °C, B-H bands which vibration modes remain at 1150 and 2351 cm^{-1} are close to those reported for $NaBH_4$, indicating that there is still some remnant $NaCl_x(BH_4)_{1-x}$ solid solution (Renaudin et al., 2004). Peaks at 1232 and 2289 cm^{-1} are also consistent with ionic tetrahedral $[BH_4]^-$ with a B-H distance shorter than that for $NaBH_4$ (Renaudin et al., 2004). The peak at 1262 cm^{-1} is due to B-B vibrations within amorphous boron. The peak observed at 698 cm^{-1} is in the region of several Mn_xO_y and Mn_xB_y compounds; full identification is not possible due to limitations in measured spectral range

(Buciuman et al., 1999). The band at 2450 cm^{-1} is in the region of a B-H stretch for a borane compound (e.g. $Na_2B_{12}H_{12}$) (Muetterties et al., 1962), however, the peaks at 1070 and 720 cm^{-1}, which would be expected for $Na_2B_{12}H_{12}$, are not observed. It has not been possible to identify the peaks observed at 1438, 1391, 1461 and 2450 cm^{-1}, although the sample temperature suggests that they may correspond to the unknown phase(s) observed during *in-situ* XRD.

Raman measurements were carried out on the 360-minute milled $3NaBH_4$-$MnCl_2$ sample that was heated to 200 or 500 °C then exposed to air for 5 minutes. As shown in Figure 6.36, there is a sharp band observed at around 640 cm^{-1} for the decomposed samples, attributed to the Mn-O vibrational mode of manganese oxides (MnO_x) (Buciuman et al., 1999). This indirectly indicates that amorphous or nano-manganese is formed.

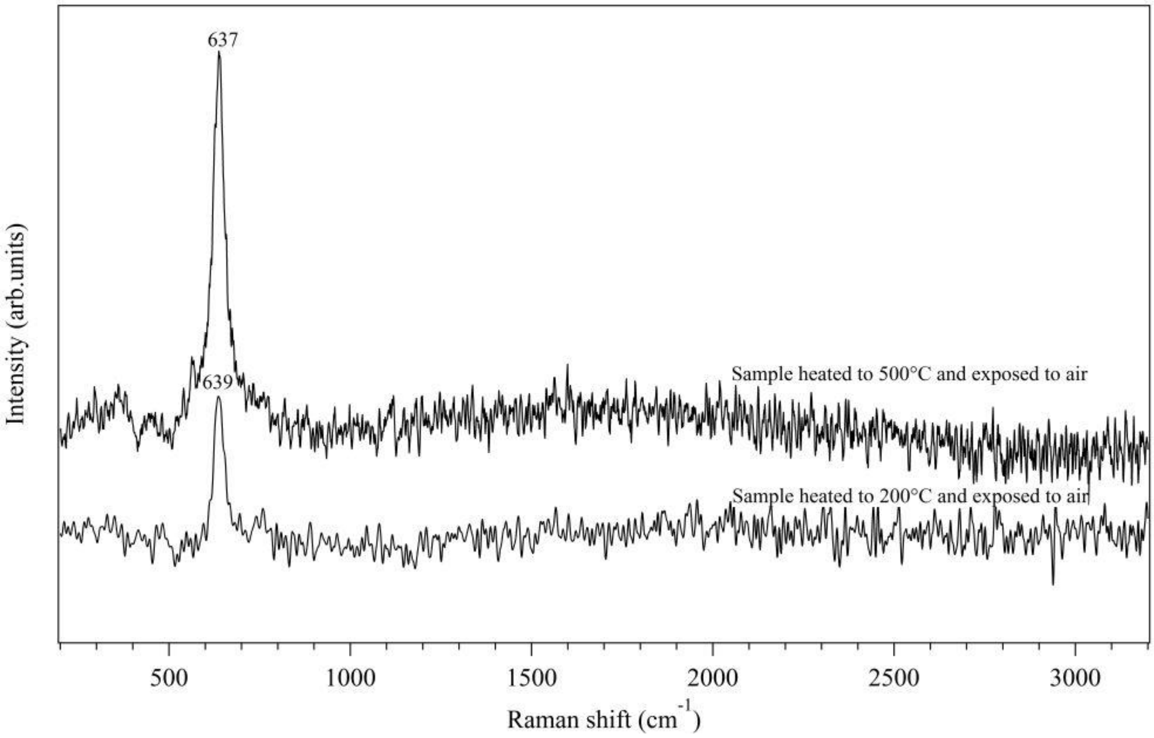

Figure 6.36 Raman spectra of 360-minute milled $3NaBH_4$-$MnCl_2$ sample heated to 200 and 500 ℃ then exposed to the air for 5 minutes

In summary, the overall decomposition reaction for the 360-minute milled $3NaBH_4$-$MnCl_2$ sample is shown in equation (6.6), which consists of several steps. Firstly, poorly crystalline $Mn(BH_4)_2$, and amorphous 1.4Na-0.1Mn-0.7(BH_4)-0.9Cl components react to form crystalline $Mn(BH_4)_2$, Na_6MnCl_8 and a BH_4-rich $Na(BH_4)_xCl_{1-x}$ phase(s) between room temperature and 100 °C (equation (6.7)). Simultaneously, $Mn(BH_4)_2$ decomposes to form amorphous B, Mn (as discussed for the milled $2NaBH_4$-$MnCl_2$) and releases H_2 and B_2H_6 (equation (5.7)). An interaction between the two solid solutions (BH_4-rich $Na(BH_4)_xCl_{1-x}$ and Cl-rich $NaCl_x(BH_4)_{1-x}$) and Na_6MnCl_8 occurs, leading to the formation of a single solid solution and the release of hydrogen (equation (6.8)) at higher temperature. The single solid solution phase then possibly decomposes to form unknown phases, accompanied by the evolution of hydrogen (equation (6.9)).

$$1.6\,NaCl_{0.68}(BH_4)_{0.32} + 0.9Mn(BH_4)_2 + \text{“1.4Na-0.1Mn-0.7(BH}_4\text{)-0.9Cl”} \rightarrow$$

$$xNaCl_{0.95}(BH_4)_{0.05} + Mn + 1.4B + 4.6H_2 + 0.3B_2H_6 + \text{“unknown phases”} \qquad (6.6)$$

$$0.9Mn(BH_4)_2 + 1.4Na\text{-}0.1Mn\text{-}0.7(BH_4)\text{-}0.9Cl \rightarrow$$

$$0.9Mn(BH_4)_2 + 0.1Na_6MnCl_8 + 0.8NaCl_{0.15}(BH_4)_{0.85} \qquad (6.7)$$

$$1.6\,NaCl_{0.68}(BH_4)_{0.32} + 0.1Na_6MnCl_8 + 0.8NaCl_{0.15}(BH_4)_{0.85} \rightarrow$$

$$3NaCl_{0.67}(BH_4)_{0.33} + 0.4H_2 + 0.1Mn + 0.2B \qquad (6.8)$$

$$3NaCl_{0.67}(BH_4)_{0.33} \rightarrow xNaCl_{0.95}(BH_4)_{0.05} + 1.5H_2 + \text{“unknown phases”} \qquad (6.9)$$

Chapter 7 Results and Discussion: KBH_4-$MnCl_2$ System

7.1 Synthesis and characterization

7.1.1 Crystallographic characterization

Potassium borohydride (KBH_4) and manganese chloride ($MnCl_2$) with the molar ratio of 2 to 1, as starting materials, were ball-milled for different durations from 30 to 360 minutes. The powder XRD patterns are shown in Figure 7.1. The background diffraction at 68 and 78° 2θ, and the two broad peaks at ~ 10-15° and 15-25° 2θ, due to the Kapton dome of the silica sample holder, are observed for all the milled samples. No diffraction peaks for $MnCl_2$ are found in any of the milled samples, indicating that reactions have occurred between KBH_4 and $MnCl_2$ during ball milling. In the case of the sample milled for 30 minutes, the X-ray diffraction peaks are identified as cubic KBH_4 and KCl phases, orthorhombic $KMnCl_3$(o) phase, and a small amount of tetragonal $KMnCl_3$(t) phase (Horowitz et al., 1982). With increasing the milling duration, the intensities of the diffraction peaks of KBH_4 and $KMnCl_3$ (t) decrease, but are still observed in the 360-minute milled sample. The diffraction peaks associated with the KCl phase disappear after 240 minutes. There is no significant change in the intensities for the orthorhombic $KMnCl_3$(o) phase from 30 to 360 minutes although a small amount of the $KMnCl_3$ phase transforms from a tetragonal to an orthorhombic structure with increasing milling time. This agrees with previous studies (Gurewitz et al., 1982; Horowitz et al., 1982), where $KMnCl_3$ was reported to form tetragonal, perovskite-like orthorhombic and non-perovskite-like orthorhombic phases. The perovskite-like orthorhombic phase was not stable, and depending on the preparation method, tended to slowly transform into the non-perovskite-like orthorhombic phase.

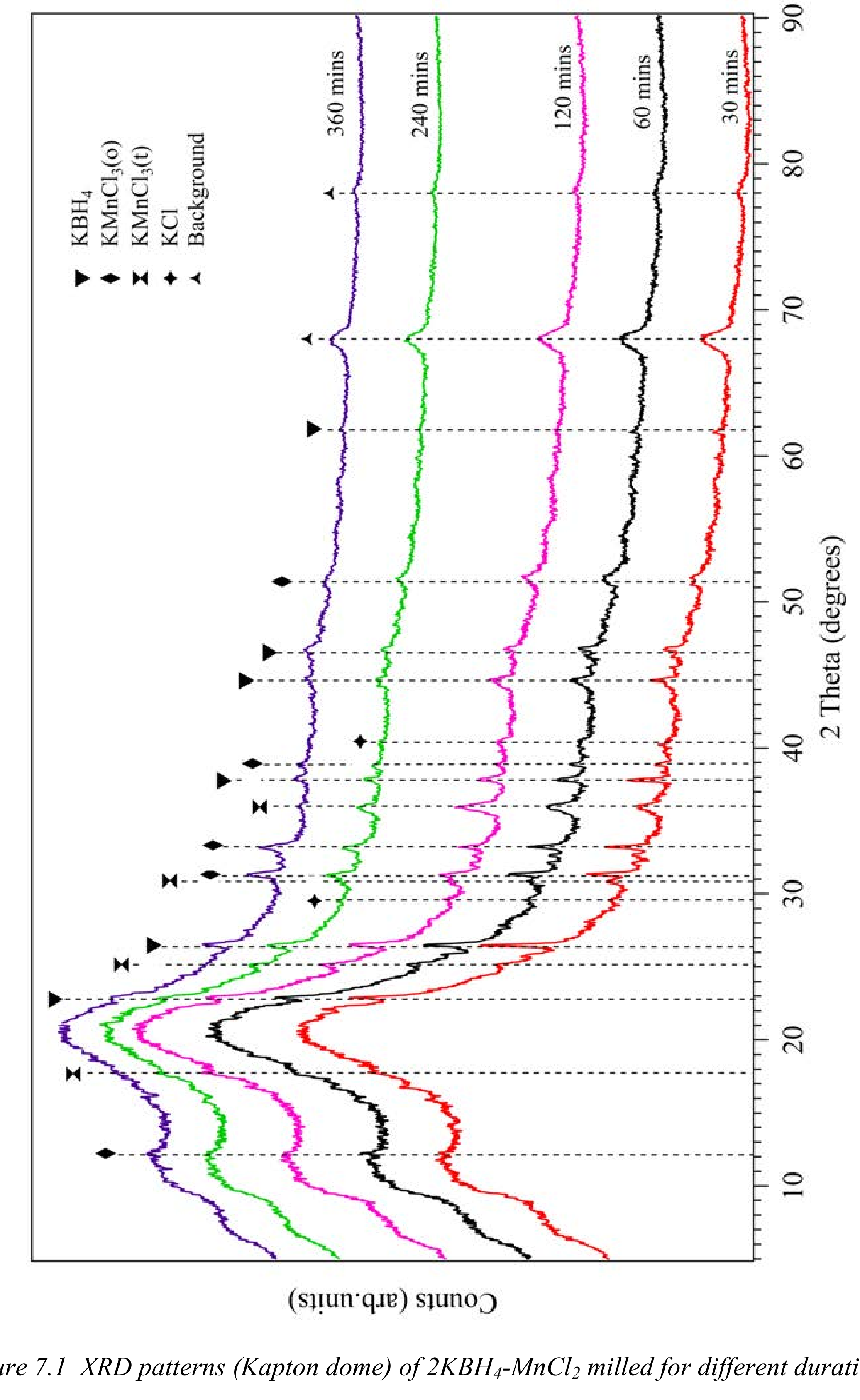

Figure 7.1 XRD patterns (Kapton dome) of $2KBH_4$-$MnCl_2$ milled for different durations

In order to investigate the nature of the broad peak from 10 to 25° 2θ, powder XRD was also performed on the 360-minute milled $2KBH_4$-$MnCl_2$ sample using an Anton Parr XRK900 cell, which has a Be window (instead of Kapton) with an aluminium oxide crucible, as shown in Figure 7.2. There are three major phases, identified as $KMnCl_3$(o) (a = 8.79 (4) Å, b = 3.88 (5) Å, c = 14.42 (2) Å) (Gurewitz et al., 1982), KBH_4 (a = 6.715 (6) Å) and $K_2Mn(BH_4)_4$ with a space group of $P2_1/n$ (a = 8.1347 (5) Å, b = 9.860 (6) Å, c = 12.768 (8) Å, β = 100.530(6)°) (Schouwink et al., 2012). Owing to the effect of the strong broad peak at 10-25° 2θ from the Kapton sample holder, the $K_2Mn(BH_4)_4$ phase (with the weak diffraction peaks at ~ 16.8 and 22° 2θ in Figure 7.2) was not observed in Figure 7.1. The insignificant $KMnCl_3$ (t) phase observed in Figure 7.1 is not present in Figure 7.2. This is believed to be due to a phase transformation from $KMnCl_3$(t) to $KMnCl_3$(o), which will even occur at room temperature (Gurewitz et al., 1982; Horowitz et al., 1982).

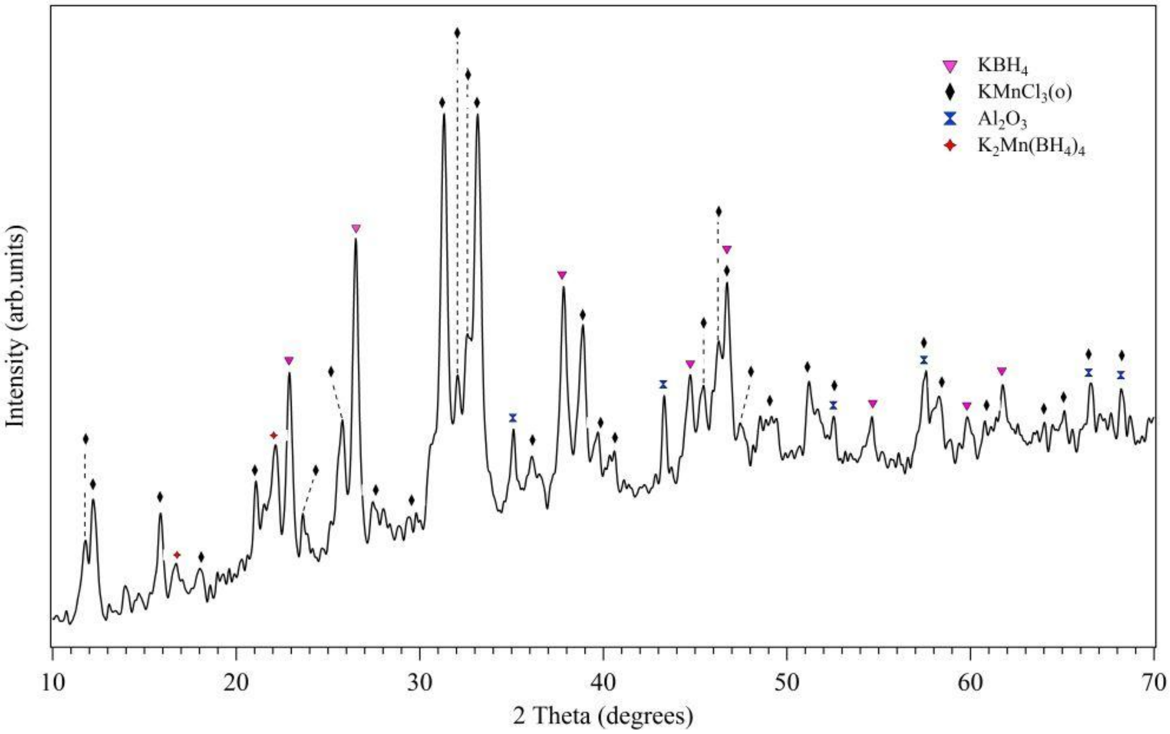

Figure 7.2 XRD pattern (Anton Parr cell) of $2KBH_4$-$MnCl_2$ milled for 360 minutes

The structure of the $K_2Mn(BH_4)_4$ compound was recently reported by Schouwink et al. (2012), who prepared it by ball milling of KBH_4-$MnCl_2$ or KBH_4-$Mn(BH_4)_2$ and identified its structure by SR-PXD. A mixed-cation borohydride $KSc(BH_4)_4$ and mixed-anion and -cation borohydride compound $KZn(BH_4)Cl_2$ have also been prepared through ball milling of KBH_4 with $ScCl_3$, and KBH_4 with $ZnCl_2$ respectively (Černý et al., 2010b; Ravnsbaek et al., 2010b). Accordingly, the synthetic process of ball milling the KBH_4-$MnCl_2$ sample with 2:1 molar ratio can be proposed via equation (7.1), giving excess KBH_4 in the milled sample:

$$6KBH_4 + 3MnCl_2 \rightarrow 2KMnCl_3\ (o) + K_2Mn(BH_4)_4 + 2KBH_4 \qquad (7.1)$$

7.1.2 Spectroscopic characterization

Raman spectroscopy was used to investigate the molecular bonding of the formed borohydride compound in the milled $2KBH_4$-$MnCl_2$ samples. As shown in Figure 7.3, there are three vibration mode regions in the Raman spectra of all the milled samples: external vibrations at low frequency <400 cm^{-1}, internal bending band around 1000-1330 cm^{-1} and stretching mode bands between 2100 and 2400 cm^{-1} from the $[BH_4]^-$ group. A band of bending modes located at 1200 cm^{-1} no longer exists in the sample milled for longer duration, indicating that the environment of $[BH_4]^-$ within formed borohydride by ball milling from 30 to 360 minutes has slightly altered.

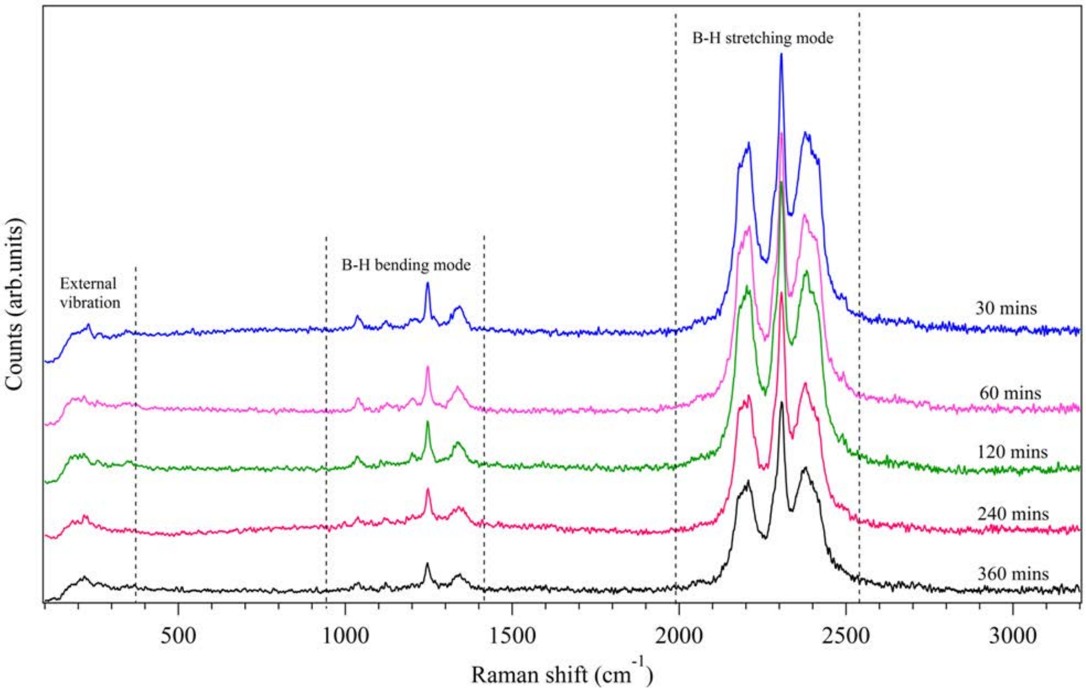

Figure 7.3 Raman spectra of $2KBH_4$-$MnCl_2$ samples milled for different durations

Raman spectra of samples of $2KBH_4$-$MnCl_2$ and KBH_4 milled for 360 minutes are shown in Figure 7.4. In the B-H stretching region, the spectrum of KBH_4 consists of strong band at 2305 cm^{-1}, overtones located at 2183, 2210 and 2495 cm^{-1}, and a combination band at 2380 cm^{-1} (Harvey and McQuaker, 1971). After ball milling KBH_4 with $MnCl_2$, the intensity of the strongest band at 2305 cm^{-1} for KBH_4 decreases dramatically with no change in Raman shift. The superposition of two overtones at 2183 and 2210 cm^{-1} from KBH_4 is observed for the milled $2KBH_4$-$MnCl_2$ sample around at 2175 and 2206 cm^{-1}. The doublet bands with an increasing intensity around the combination band (2380 cm^{-1}) of KBH_4 compound appear to be present in the milled $2KBH_4$-$MnCl_2$ sample at 2380 and 2408 cm^{-1}. An overtone for KBH_4 at 2495 cm^{-1} is not present in the milled $2KBH_4$-$MnCl_2$ sample. In addition to the bending modes at 1248 and 1118 cm^{-1} in both milled KBH_4 and $2KBH_4$-$MnCl_2$ samples, there are two new vibration modes observed only for the milled $2KBH_4$-$MnCl_2$ sample at 1342 and 1035 cm^{-1}. This indicates that the Raman spectrum of the milled $2KBH_4$-$MnCl_2$ sample is consistent with two separate borohydride environments: one from excess KBH_4 and the other from the newly formed $K_2Mn(BH_4)_4$ with three additional Raman frequencies at 1035, 1342 and 2408 cm^{-1}, compared with those of KBH_4. This is consistent with the results reported by Schouwink et al., (2012). The vibration assignments for the milled KBH_4 and $2KBH_4$-$MnCl_2$ samples are presented in Table 7.1.

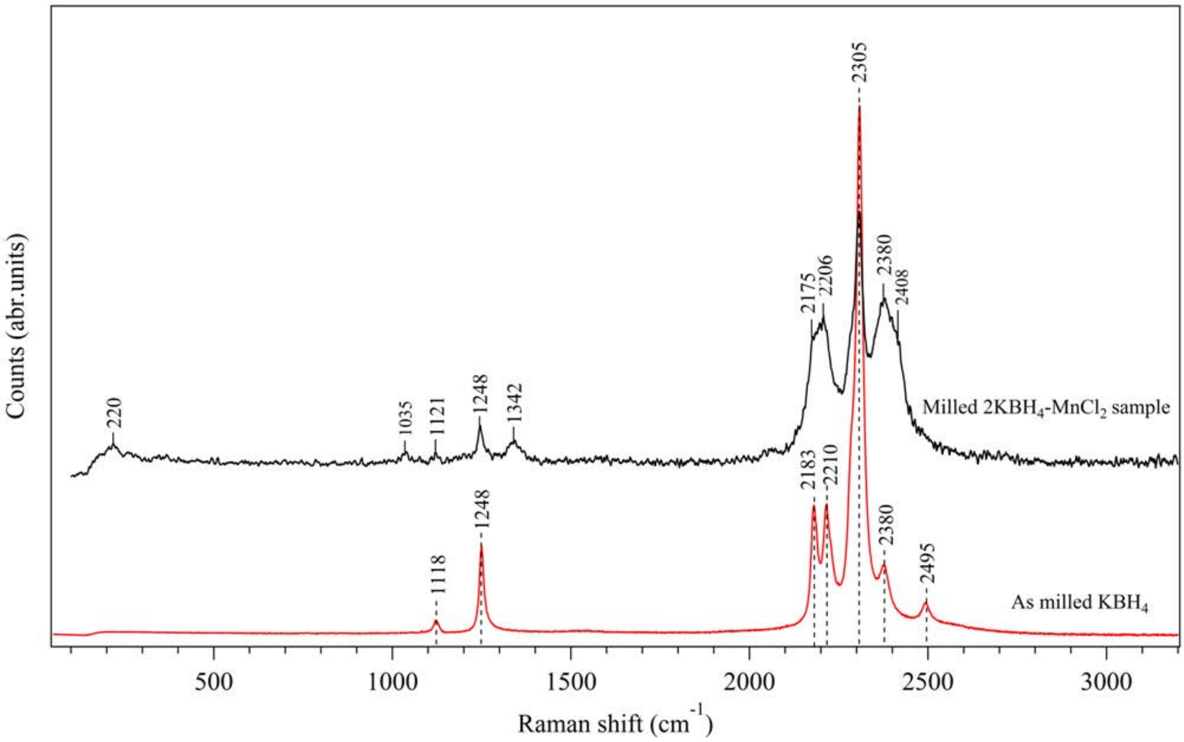

Figure 7.4 Raman spectra of $2KBH_4$-$MnCl_2$ and KBH_4 samples milled for 360 minutes

Upon cooling the 360-minute milled $2KBH_4$-$MnCl_2$ sample to -190 °C, a significant modification to the Raman vibration modes is observed, showing an increase in the intensities of the vibration peaks and a decrease in the peak widths, as shown in Figure 7.5. In addition, the splitting of B-H stretching vibration bands for the milled $2KBH_4$-$MnCl_2$ sample at -190 °C produces three more vibration modes (at 2235, 2288 and 2500 cm^{-1}) than those at room temperature. Compared to the milled KBH_4, the three additional bands and the band splitting are due to the presence of excess KBH_4, where seven vibration modes at room temperature split to nine Raman modes. Two more vibrations are located at 2240 and 2293 cm^{-1}. The Raman frequency shift and the peak splitting at low temperature are due to the reduction of the thermal expansion and fluctuation within a lattice. The thermal vibration causes uniform displacement of molecules and coupling between vibrations within the molecules (Racu et al., 2008; Reed and Book, 2011).

Table 7.1 Raman shift (cm^{-1}) at RT and -190℃ for 360-minute milled $2KBH_4$-$MnCl_2$ and KBH_4 samples.

Raman shift (cm^{-1})*					Assignment
KBH_4 (Harvey and McQuaker, 1971)	KBH_4 (RT, this work)	$2KBH_4$-$MnCl_2$ (RT)	KBH_4 (-190 °C, this work)	$2KBH_4$-$MnCl_2$ (-190°C)	
-	-	150-400*w*	-	-	External modes
-	-	1035*vw*	-	1034*vw*	Internal bending modes
1118 (v_4)	1118*vw*	1121*vw*	1132*vw*	1122*vw*	
-	-	-	-	1201*vw*	
1248.5(v_2)	1248*w*	1248*w*	1258*ms*	1250*ms*	
-	-	1342w	-	1342*vw*	
2181($2v_4$)	2183*ms*	2175*ms*	2183*s*	2180*s*	Internal stretching modes
2217($2v_4$)	2210*ms*	2206*ms*	2218*ms*	2212*ms*	
-	-	-	2240*w*	2235*w*	
-	-	-	2293*ms*	2288*ms*	
2310(v_1)	2305*vs*	2305*s*	2311*s*	2305*s*	
2380(v_2+v_4)	2380*w*	2380*ms*	2390*w*	2383*w*	
-	-	2408*ms*	-	2412*w*	
2495($2v_2$)	2495*w*	-	2502*w*	2500*w*	

**vw-very weak, w-weak, ms-medium strong, s-strong*

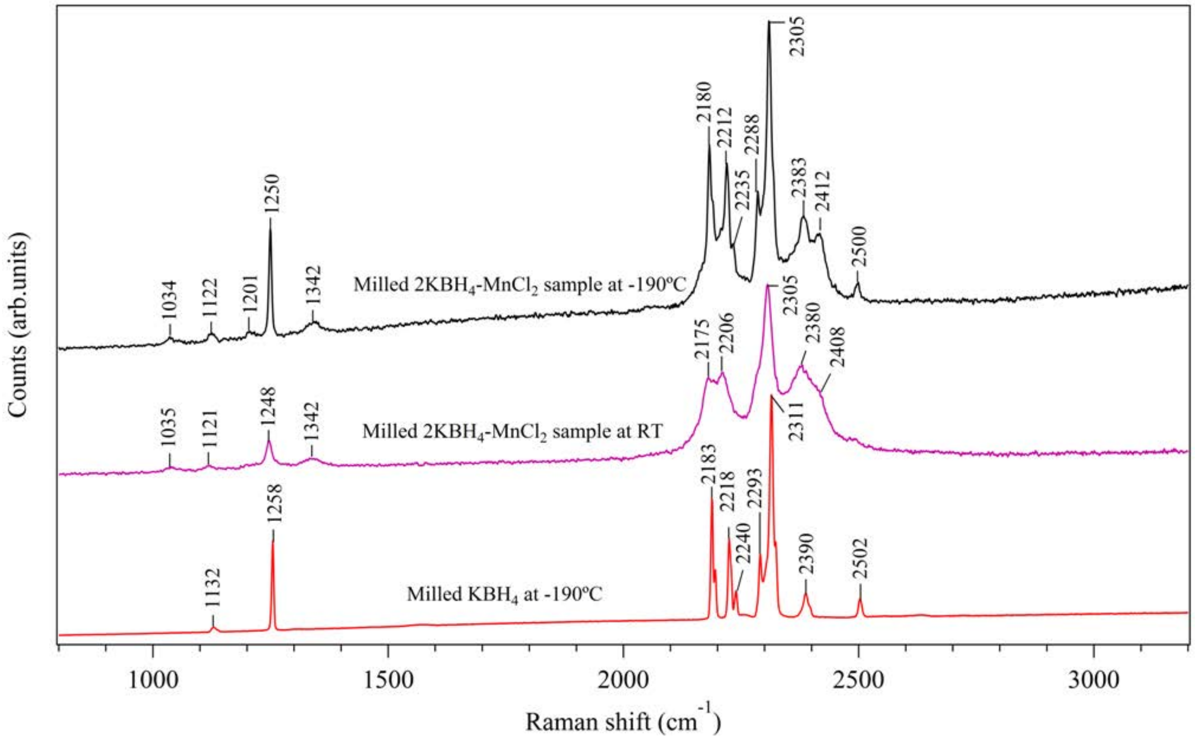

Figure 7.5 Raman spectra of 360-minute milled $2KBH_4$-$MnCl_2$, measured at RT and -190 ºC (with 360-minute milled KBH_4 at -190 ºC, as a reference)

Figure 7.6 show FTIR spectra of the 360-minute milled $2KBH_4$-$MnCl_2$ and KBH_4 samples. There are nine vibration bands displayed in the IR spectrum of milled $2KBH_4$-$MnCl_2$ sample, four of which, at 1118, 2210, 2282 and 2273 cm^{-1}, are related to excess KBH_4 in spite of a slight shifting in peak position compared to the pure KBH_4. The other five vibration modes, located at 1038, 1204, 1342, 2174 and 2428 cm^{-1}, are associated with $K_2Mn(BH_4)_4$. These are consistent with Raman results.

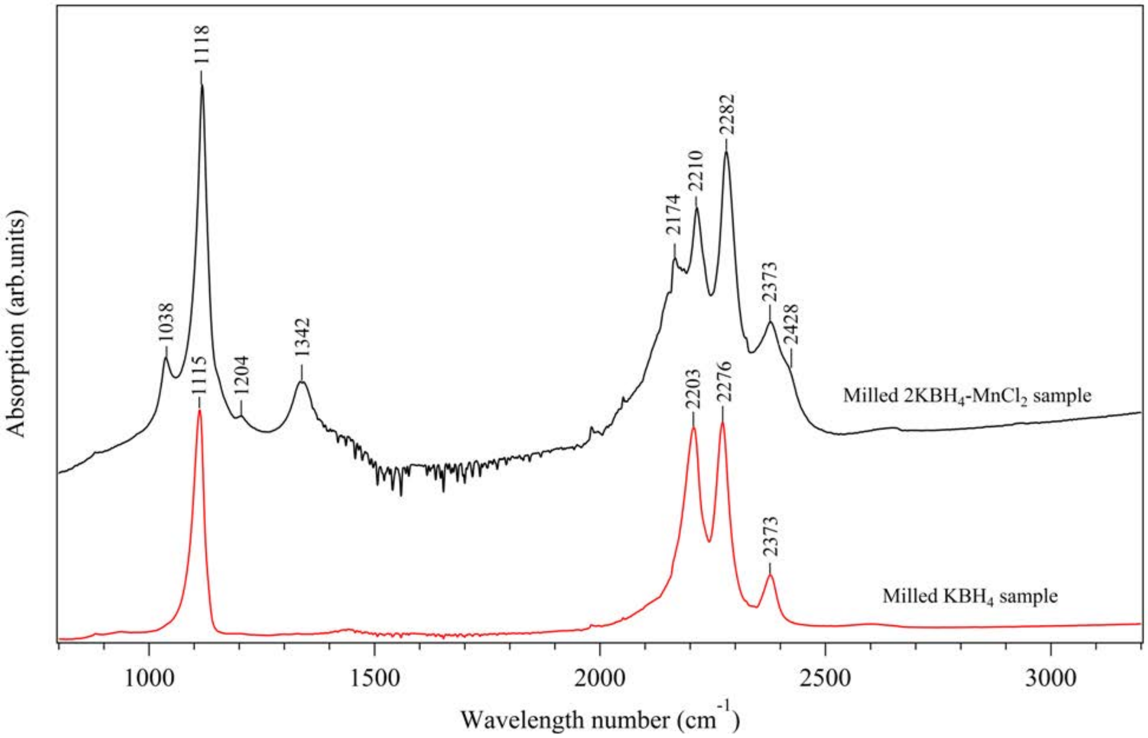

Figure 7.6 FTIR spectra of 360-minute milled $2KBH_4$-$MnCl_2$ and KBH_4 samples

The combination of vibration spectroscopy and XRD results confirm that the $K_2Mn(BH_4)_4$ borohydride complex is formed through ball milling of $2KBH_4$-$MnCl_2$, with excess KBH_4 according to equation (7.1).

7.2 Thermal decomposition

7.2.1. Thermogravimetric analysis

Figure 7.7 shows TGA profiles of $2KBH_4$-$MnCl_2$ samples milled for different durations. Two main mass loss regions are observed for all the milled samples: 100 to 170 ℃ with a mass loss of 1.6-1.9 wt%, which is associated with the decomposition of the formed $K_2Mn(BH_4)_4$ compound; and 165 to 270 ℃ with a mass loss of 1.9-2.3 wt%, which is possibly due to the decomposition of KBH_4 within the mixture. The results are summarized in Table 7. 2.

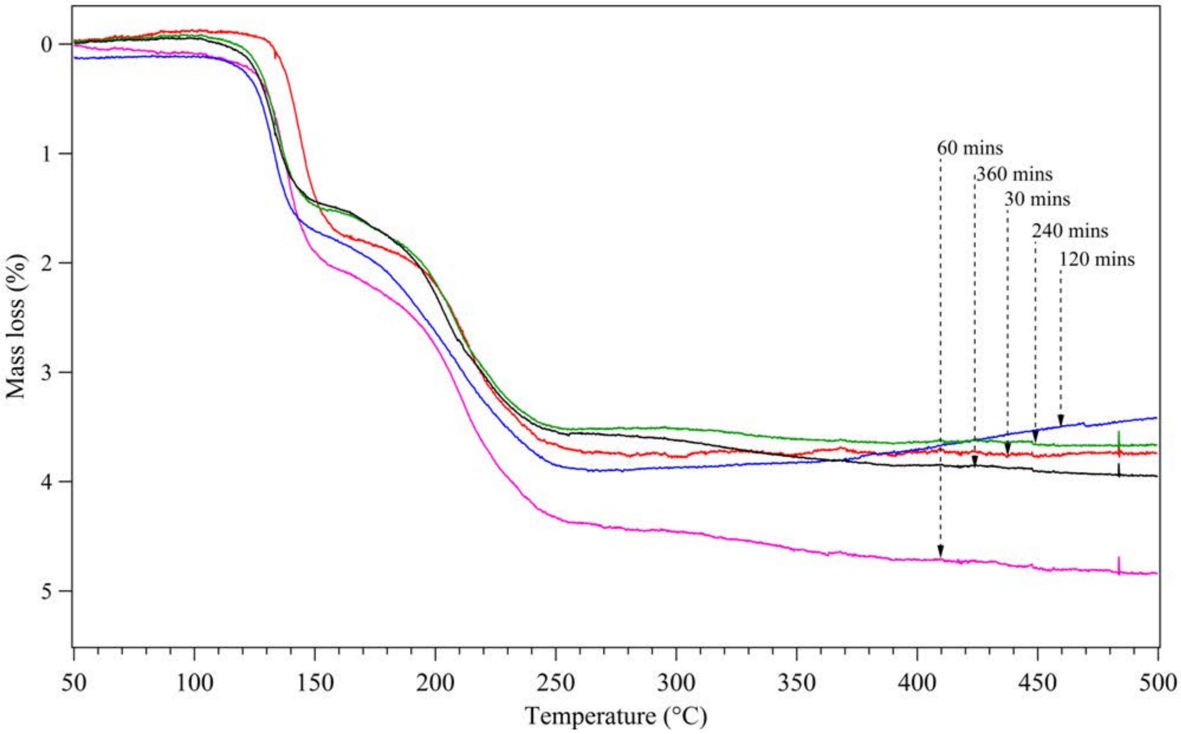

Figure 7.7 TGA profiles of $2KBH_4$-$MnCl_2$ samples milled for different durations, heated at 2 °C/min under 1.5 bar Ar flowing at 40 ml/min

When the ball milling duration was increased from 30 to 360 minutes, the decomposition temperature reduced by 20 ℃ for the onset temperature at the first step and 10 ℃ for the end temperature of the first step with observed decreasing mass loss from 1.9 to 1.6 %, indicating that the extension of milling period results in the complete formation of potassium manganese borohydride that partially decomposes as a result of the heat transformation derived from friction during the milling process. Additionally, there is no disparity in the second observed mass loss for all of the milled samples but the onset or end decomposition temperatures decrease with an increasing milling time.

Table 7.2 Summary of TGA profiles for $2KBH_4$-$MnCl_2$ samples milled for different durations

Milling time (minutes)	30	60	120	240	360
First mass loss region					
Onset decomposition temperature (℃)	120	110	100	100	100
End decomposition temperature (℃)	170	165	160	160	160
Mass loss observed (wt%)	1.9±0.1	1.9±0.2	1.7±0.1	1.6±0.2	1.6±0.1
Second mass loss region					
Onset decomposition temperature (℃)	175	170	165	165	165
End decomposition temperature (℃)	270	270	270	260	260
Mass loss observed (wt%)	1.9±0.1	2.3±0.1	2.1±0.1	1.9±0.1	1.9±0.2

Mass spectra coupled with TGA profiles of the 30 or 360-minute milled $2KBH_4$-$MnCl_2$ samples (Figure 7.8) show that the mass losses in the two regions are accompanied by the release of hydrogen. A trace amount of diborane is detected by MS during the first decomposition process of the milled $2KBH_4$-$MnCl_2$ samples. The first hydrogen evolution is observed at 146 ℃ for the 30-minute milled $2KBH_4$-$MnCl_2$, and shifts to lower temperature (135 ℃) for the 360-minute milled $2KBH_4$-$MnCl_2$. In the second mass loss region, a hydrogen release around 170-260 ℃ seems to have large doublets at 220 and 240 ℃ for the 30-minute milled sample, and at 210 and 230 ℃ for the 360-minute milled sample, suggesting that a multi-step decomposition process occurs.

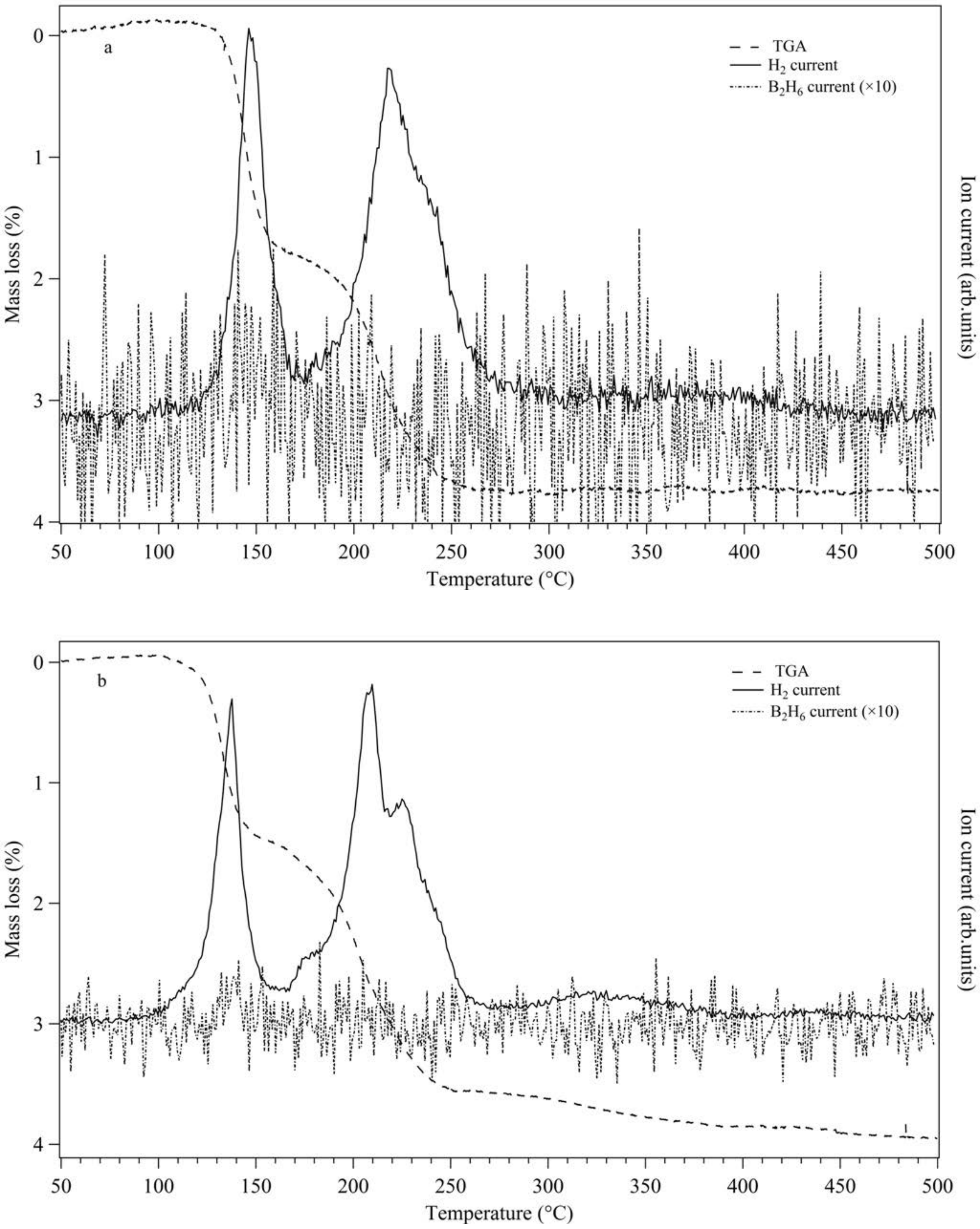

Figure 7.8 TGA coupled with mass spectrometry of $2KBH_4$-$MnCl_2$ samples milled for (a) 30 and (b) 360 minutes.

After major hydrogen evolution, a small amount of hydrogen is released at 320 ℃, reaching a peak at 370℃ for the 30-minute milled sample; this reaction takes place at lower temperature for the 360-minute milled sample, starting at 290 ℃ and reaching a peak at 320 ℃. This might be related to the subsequent decomposition of the intermediates derived from decomposed KBH_4.

7.2.2 Differential scanning calorimetry

DSC profiles of the $2KBH_4$-$MnCl_2$ samples milled for different durations, show that on heating from room temperature to 500 ℃, there are several major endothermic and exothermic reactions, as shown in Figure 7.9. The 30-minute milled sample exhibits exothermic peaks at 93 and 125 ℃, and endothermic peaks at 138, 214, 225 and 240 ℃. With increased milling period, the exothermic peak at 93 ℃ gradually disappears and the other thermal reaction peaks shift to 115, 129, 203, 214 and 231 ℃ for the 360-minute milled sample, indicating improved reaction kinetics, which may partially be due to a reduction in particle size (Varin et al., 2006). The temperature of the endothermic peak at 451 ℃ appears to be the same for all the milled samples.

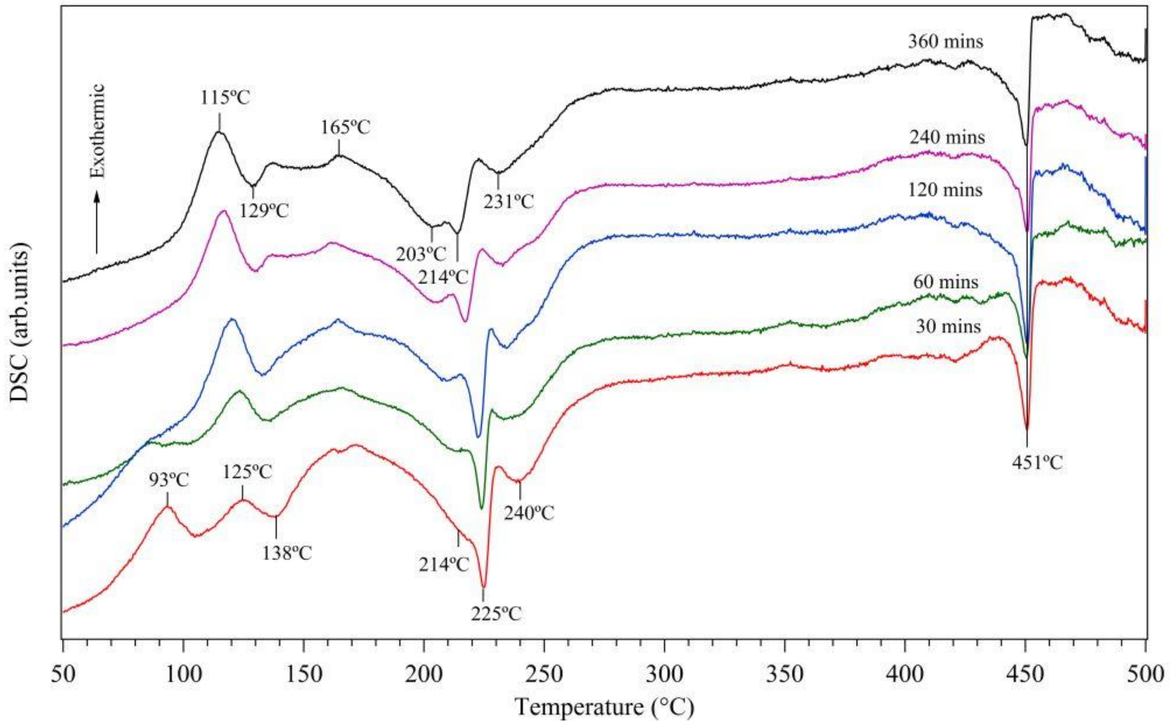

Figure 7.9 DSC profiles of $2KBH_4$-$MnCl_2$ samples milled for different durations

To understand the DSC peak assignments better, the DSC profiles in conjunction with mass spectrometry are shown in Figure 7.10. It can be suggested that the endothermic DSC peak at 138 ℃ for the 30-minute milled sample and at 129 ℃ for the 360-minute milled sample is due to the decomposition of the $K_2Mn(BH_4)_4$ compound, accompanied by hydrogen evolution with a trace amount of diborane. The peaks at 214, 225 and 240 ℃ for the 30-minute milled sample and at 203, 214 and 231 ℃ for the 360-minute milled sample are associated with the second multi-step decomposition reaction within the mixture by desorbing hydrogen, which is consistent with TGA results. The tetragonal $KMnCl_3$ phase has been identified by XRD for the $2KBH_4$-$MnCl_2$ samples milled for shorter time periods, i.e. less than 120 minutes for the conditions used in this study (see Figure 7.1). However, this phase slowly transforms into an orthorhombic-nonperovskite phase (Gurewitz et al., 1982; Horowitz et al., 1982). Therefore, the exothermic reaction at 93 ℃ for shorter milling time samples is possibly due to a phase change in the $KMnCl_3$ compound from a tetragonal to an orthorhombic non-perovskite structure. The exothermic peaks before the decomposition at 125 ℃ for the 30-minute milled sample or at 115 ℃ for the 360-minute milled sample are not accompanied by the release of hydrogen, possibly due to the dissociation of $K_2Mn(BH_4)_4$ to form new phases. The sharp endothermic peak at 451 ℃ can be related to a phase change in one of the final decomposition products. This will be discussed further in the next section.

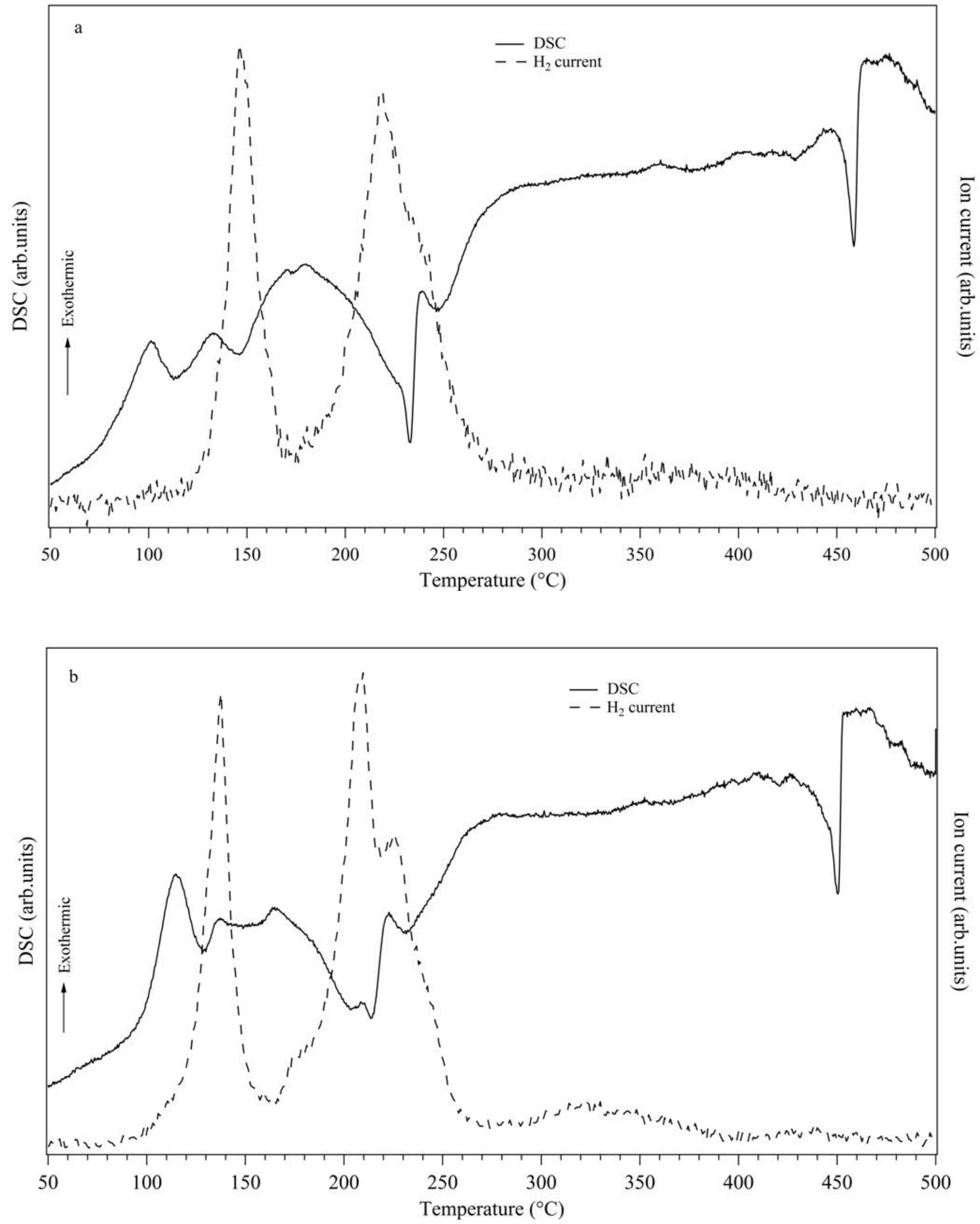

Figure 7.10 DSC and mass spectrometry of $2KBH_4$-$MnCl_2$ *samples milled for (a) 30 and (b) 360 minutes*

7.3 Decomposition behaviour

Figure 7.11 shows *in-situ* XRD patterns of the 360-minute milled $2KBH_4$-$MnCl_2$ sample in the temperature range of 30 to 500 ℃ . At room temperature, the XRD pattern indicates the presence of $KMnCl_3$, $K_2Mn(BH_4)_4$ and KBH_4. Upon heating, the very weak diffraction peaks corresponding to $K_2Mn(BH_4)_4$ at 16.7 and 22.1° 2θ disappear above 120 ℃ , due to decomposition of the $K_2Mn(BH_4)_4$ complex. This corresponds to the endothermic DSC peaks at around 129 ℃ , and with TGA mass losses between 100 and 158 ℃ with hydrogen and diborane evolution. Simultaneously, an increase in the intensity of the diffraction peaks for KBH_4 occurs between 100 and 160 ℃ . The content of KBH_4 in the mixture was estimated using TOPAS software and the weight percent of KBH_4 in the mixture increases from 23.3% at 100℃ to 29.8 % at 170 ℃ (Figure 7.12). This suggests that the $K_2Mn(BH_4)_4$ compound decomposes to form KBH_4. Schouwink et al. (2012) also found that the decomposition of the $K_2Mn(BH_4)_4$ compound resulted in the formation of KBH_4 with strong XRD peaks, and a further new phase with weak XRD reflections which has been identified as $KMn(BH_4)_3$ (however, the XRD data was not clear enough to allow the accurate crystal structure to be solved). Although the KBH_4 phase is formed during the decomposition of $K_2Mn(BH_4)_4$ in this study, peaks for $KMn(BH_4)_3$ are not observed in the *in-situ* XRD pattern (Figure 7.11). However, an exothermic peak at 115 ℃ in the DSC profile may be related to the decomposition of $K_2Mn(BH_4)_4$ to form KBH_4 and $KMn(BH_4)_3$.

On the other hand, the lattice parameter (*a*) of KBH_4 linearly increases from room temperature to 150 ℃ , due to thermal expansion, then tends to stay constant between 150 and 170 ℃ , after which it contracts (Figure 7.12). This result indicates that a proportion of the BH_4^- ions within KBH_4 are substituted by Cl^- ions to form a $K(BH_4)_{1-x}Cl_x$ solid solution; this corresponds to the exothermic DSC peak at 165 ℃. The formation of the KBH_4 phase has also been observed during the decomposition of $KSc(BH_4)_4$ by Černý et al (2010b), which had been formed by the ball-milling of $4KBH_4$-$ScCl_3$. They reported that from room temperature to 220 ℃, no Cl^- ions substitution in KBH_4 was observed, although a significant substitution occurred at 220-320 ℃.

On further heating, diffraction peaks of KBH_4 gradually broaden, decrease in their intensities and shift towards a higher 2θ above 180 °C. Simultaneously, the reflections of $KMnCl_3$ reduce and new diffraction peaks at 14.6, 25.3, 31.2, 33.0 and 34.8 ° 2θ, possibly due to K_4MnCl_6, are observed. With continued heating, the X-ray reflections of $K(BH_4)_{1-x}Cl_x$ slowly approach the diffraction positions of KCl-type, suggesting more Cl^- substituting for BH_4^-. All the diffraction peaks disappear completely other than those of KCl above 450 °C. These results suggest that between 165 and 260 ℃, three processes occur: the ternary chloride $KMnCl_3$ reacts with KBH_4 to produce KCl and possible finely dispersed manganese, boron or borane species (accompanied by hydrogen evolution in multiple steps); some of the produced KCl dissolves into KBH_4 to form a $K(BH_4)_xCl_{1-x}$ and some reacts with $KMnCl_3$ to form a K_4MnCl_6 phase. This is reasonably consistent with the second mass loss step in the TGA profile coupled with mass spectrometry and several DSC peaks between 170 and 250 °C.

Above 450 ℃, apart from the reflections of KCl, the diffraction peaks due to the K_4MnCl_6 phase are absent, most likely due to its decomposition and melting at this temperature (CRCT, 2009), which corresponds to a significant endothermic DSC peak at 451 ℃.

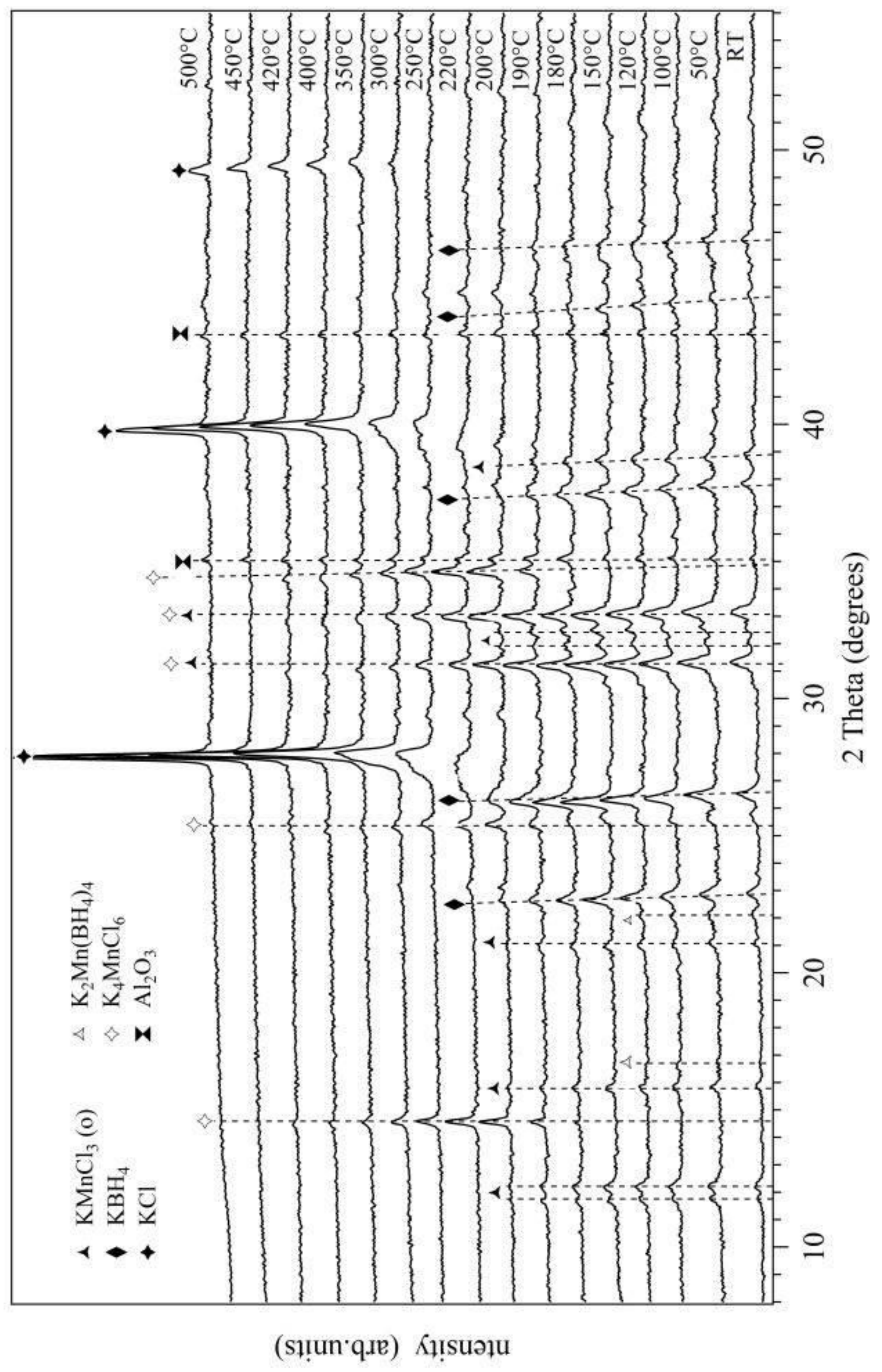

Figure 7.11 In-situ XRD of $2KBH_4$-$MnCl_2$ milled for 360 minutes, heated at 2 °C/min in 4 bar He flowing at 100 ml/min

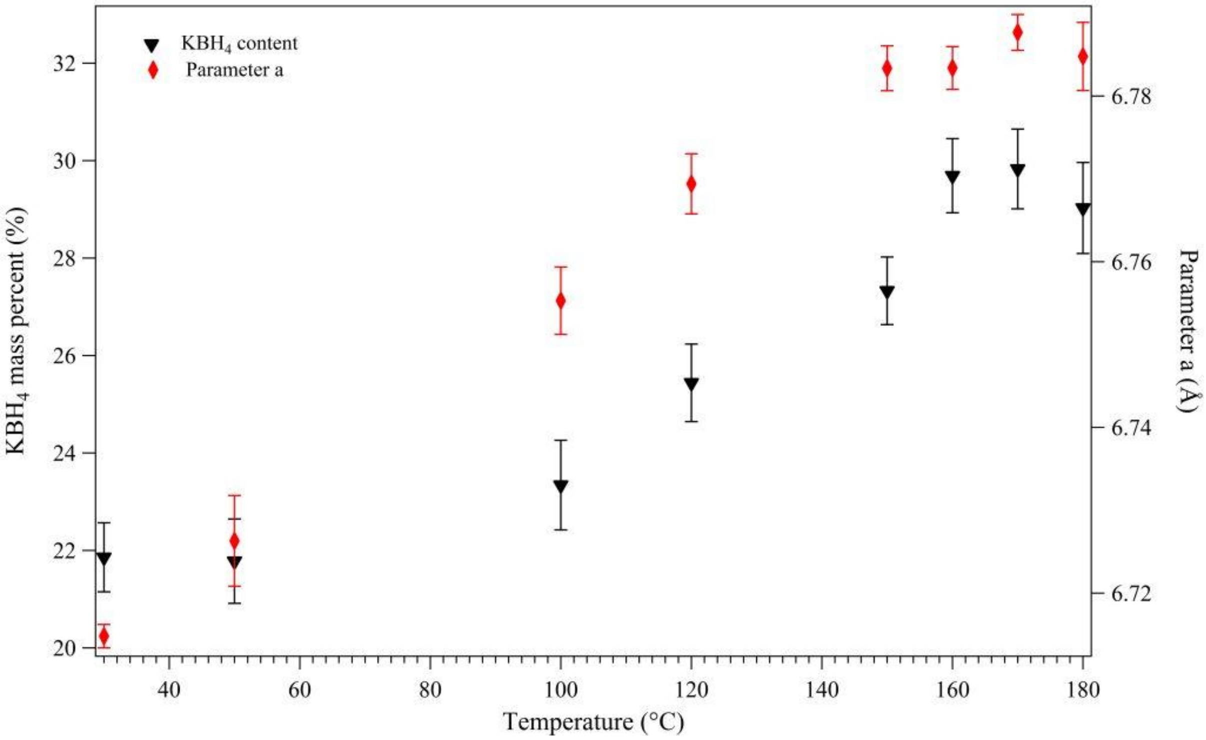

*Figure 7.12 The lattice parameter(**a**) for KBH_4 and an estimate of KBH_4 content (within the milled $2KBH_4$-$MnCl_2$ mixture) versus temperature (from Fig 7.11); error bars show 3ESDs*

The thermal decomposition of $K_2Mn(BH_4)_4$ in this study is very similar to that of $KSc(BH_4)_4$ prepared by ball milling of KBH_4 and $Sc(BH_4)$ (Černý et al., 2010b). In both cases, KBH_4 is formed during the first decomposition of the complex borohydrides with the concurrent release of hydrogen. The KBH_4 then reacts with K-Mn(Sc)-Cl resulting in a second hydrogen evolution and the formation of KCl. This KCl is then subsequently dissolved into the remaining KBH_4 to give a $K(BH_4)_{1-x}Cl_x$ solid solution.

In-situ Raman spectrometry was performed on the 360-minute milled $2KBH_4$-$MnCl_2$ sample to investigate the change of the B-H vibrations during heating (Figures 7.13 and 7.14). A decrease in intensity for each B-H vibration mode is observed with increasing temperature. When heated to 120 °C the external vibrations, the stretching mode at 2408 cm^{-1}, and the bending bands at 1342 and 1035 cm^{-1} disappear, corresponding to the decomposition of the formed mixed-ions compound $K_2Mn(BH_4)_4$. At 120 °C, there are still B-H stretching bands at 2175, 2205, 2306 and 2380 cm^{-1}, and a bending band at 1248 cm^{-1}, which are all associated with the unreacted KBH_4 compound. These vibration modes exist until 220 ℃ , when KBH_4 reacts with ternary chlorides (e.g. $KMnCl_3$) to release hydrogen and consequently to the disappearance of the B-H bands in the borohydride compound. These observations agree with the *in-situ* XRD results (Figure 7.11).

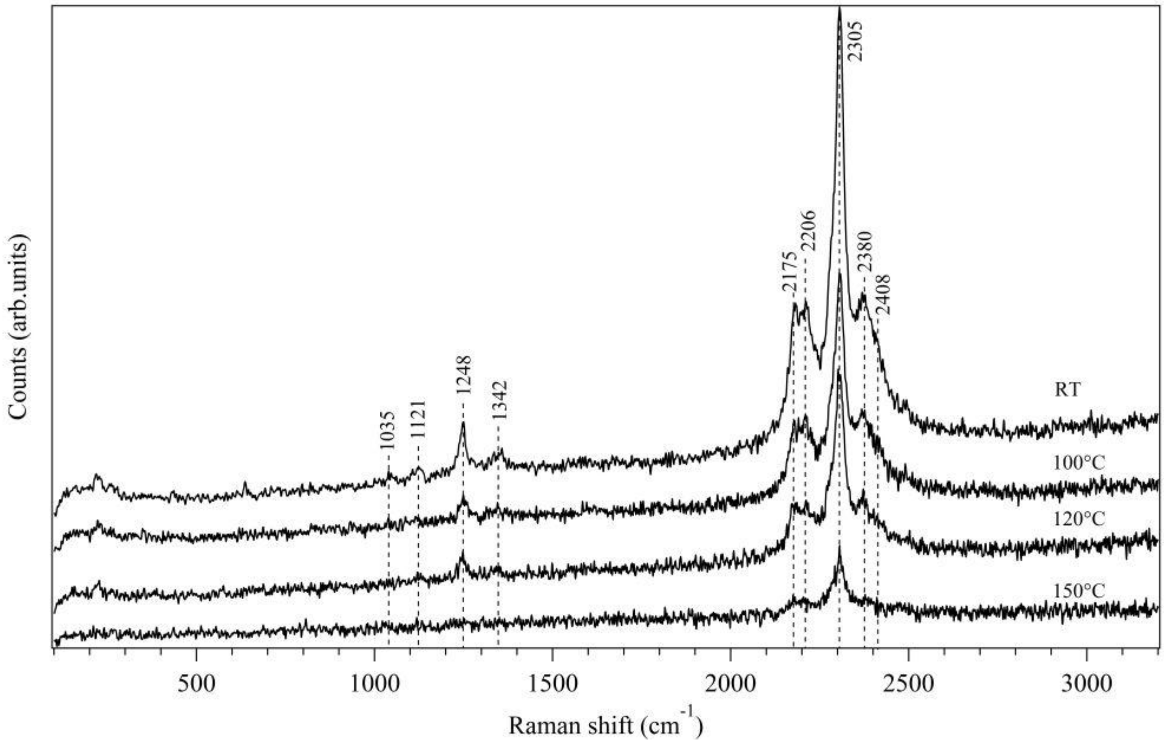

Figure 7.13 In-situ Raman spectra of 2KBH$_4$-MnCl$_2$ milled for 360 minute, heated from RT to 150 ℃ at 2 ℃ /min in 1 bar Ar flowing at 100 ml/min

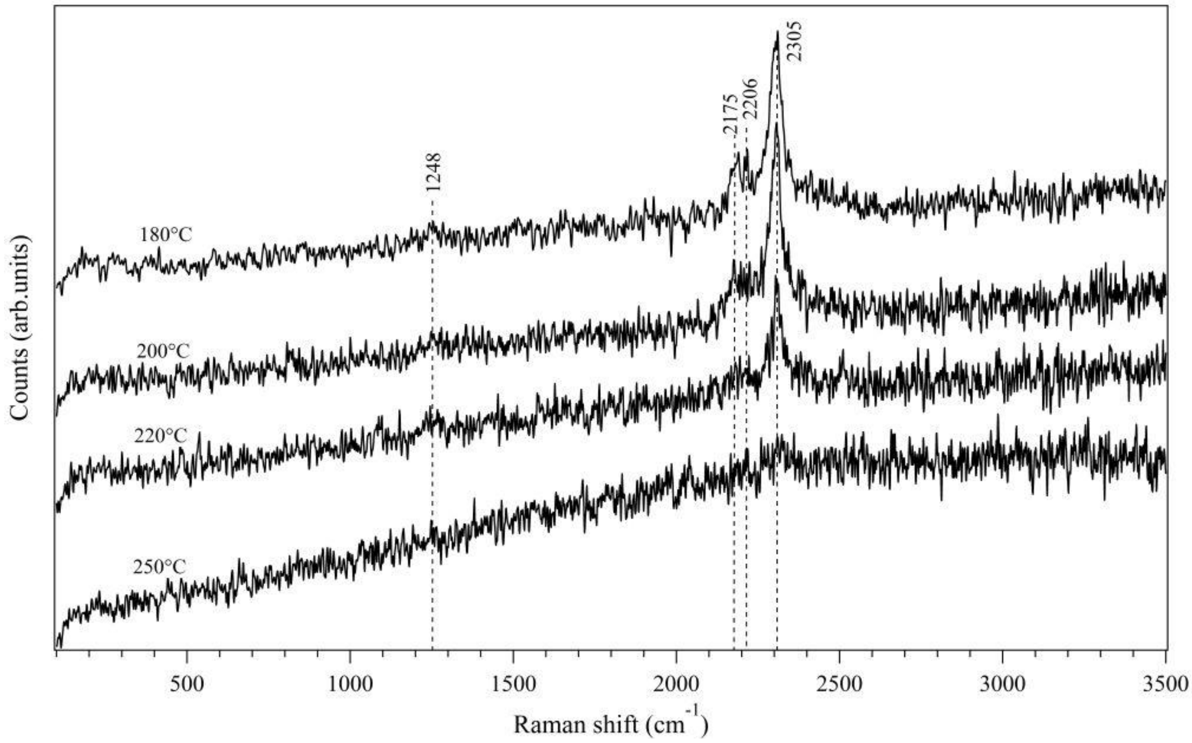

Figure 7.14 In-situ Raman spectra of $2KBH_4$-$MnCl_2$ milled for 360 minutes, heated from 180 to 250 ℃ at 2 ℃ /min in 1 bar Ar flowing at 100 ml/min

FTIR spectrometry was carried out on the 360-minute milled $2KBH_4$-$MnCl_2$ sample heated to 150, 250 and 450 °C then cooled to room temperature, as shown in Figure 7.15. The milled sample heated to 150 °C shows that five modes at 1038, 1204, 1342, 2174 and 2428 cm^{-1} disappear, due to the decomposition of $K_2Mn(BH_4)_3$. Four B-H bands at 1118, 2210, 2282 and 2373 cm^{-1} corresponding to KBH_4, and vibration modes at 1246 and 1365cm^{-1} due to B-B bonding are observed. On further heating to 250 °C, a significant shifting of the four B-H bands (1135, 2245, 2303, and 2408 cm^{-1}) due to KBH_4 are observed, which corresponds to the dissolution of KBH_4 into KCl to form a $K(BH_4)_{1-x}Cl_x$ solid solution. This observation is consistent with the *in-situ* XRD patterns, where the reflections for KBH_4 slowly approach those for KCl. Apart from the B-H bands due to $K(BH_4)_{1-x}Cl_x$ solid solution and the B-B bands exhibited at 928, 1263 and 1346 cm^{-1} in the decomposed sample at 250 °C, there is a very weak vibration mode at 2478 cm^{-1}, which is due to the reaction of KBH_4 contained in the solid solution with ternary chloride to possibly form a borane species ($K_2B_{12}H_{12}$), however, the peaks at 1070 and 720 cm^{-1}, which would be expected for $K_2B_{12}H_{12}$ (Muetterties et al., 1962), are not observed.

A borane compound is not observed in the *in-situ* XRD pattern (perhaps due to a small relative proportion and/or lack of crystallinity), however between 170 and 260 °C there are several endothermic DSC peaks and multi-step hydrogen release is shown by mass spectrometry, which suggests that intermediate compounds may form during the thermal decomposition process. The decomposed sample at 450 °C shows no B-H bands owing to KBH_4, very weak vibration modes at 1075 and 2470 cm^{-1} corresponding to borane species, and broad bands at 925, 1239 and 1351 cm^{-1} associated with B-B bonding.

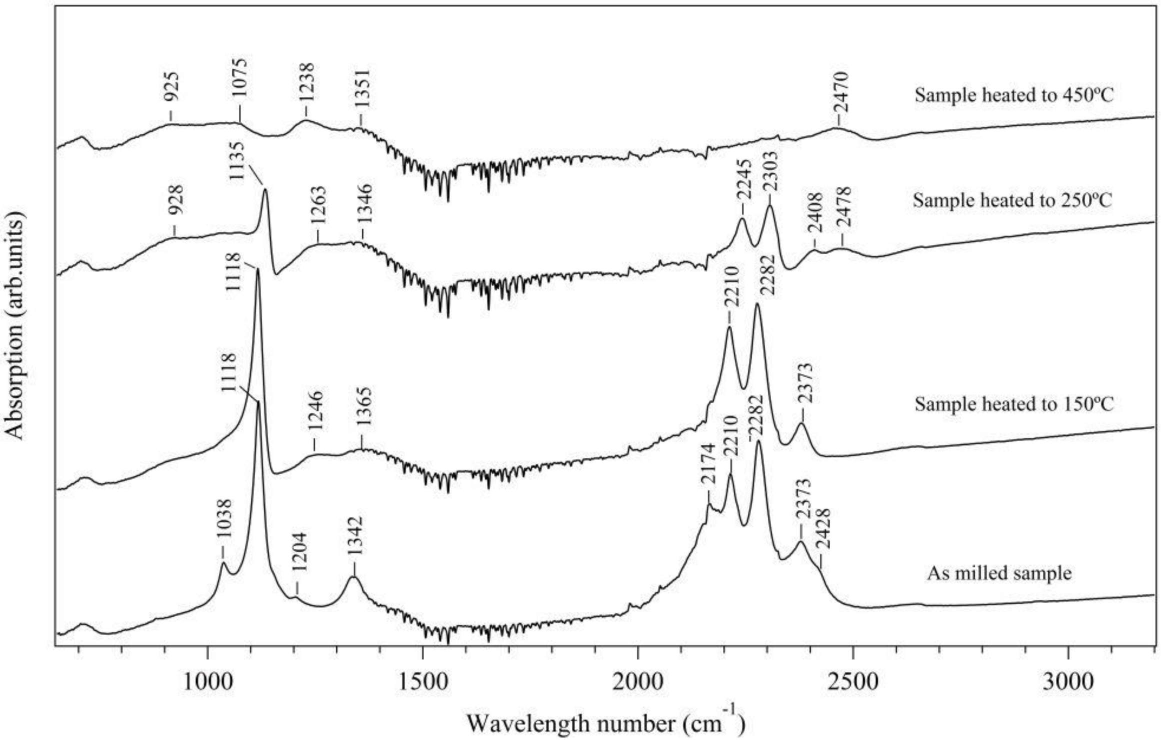

Figure 7.15 FTIR spectra of $2KBH_4$-$MnCl_2$ milled for 360 minutes after heating to 150, 250 and 450 ºC under Ar flowing (as-milled sample as a reference)

Raman spectra of the 360-minute milled $2KBH_4$-$MnCl_2$ sample indicate no vibration modes observed for three samples decomposed at 150, 250 and 450 ℃ , respectively. However, after being exposed to air at room temperature, these samples exhibit a shark peak at 641 cm^{-1} (Figure 7.16), which is believed to be due to the vibrational mode for a manganese oxide (Buciuman et al., 1999), which indirectly implies that finely dispersed manganese is formed during the decomposition of milled $2KBH_4$-$MnCl_2$ sample.

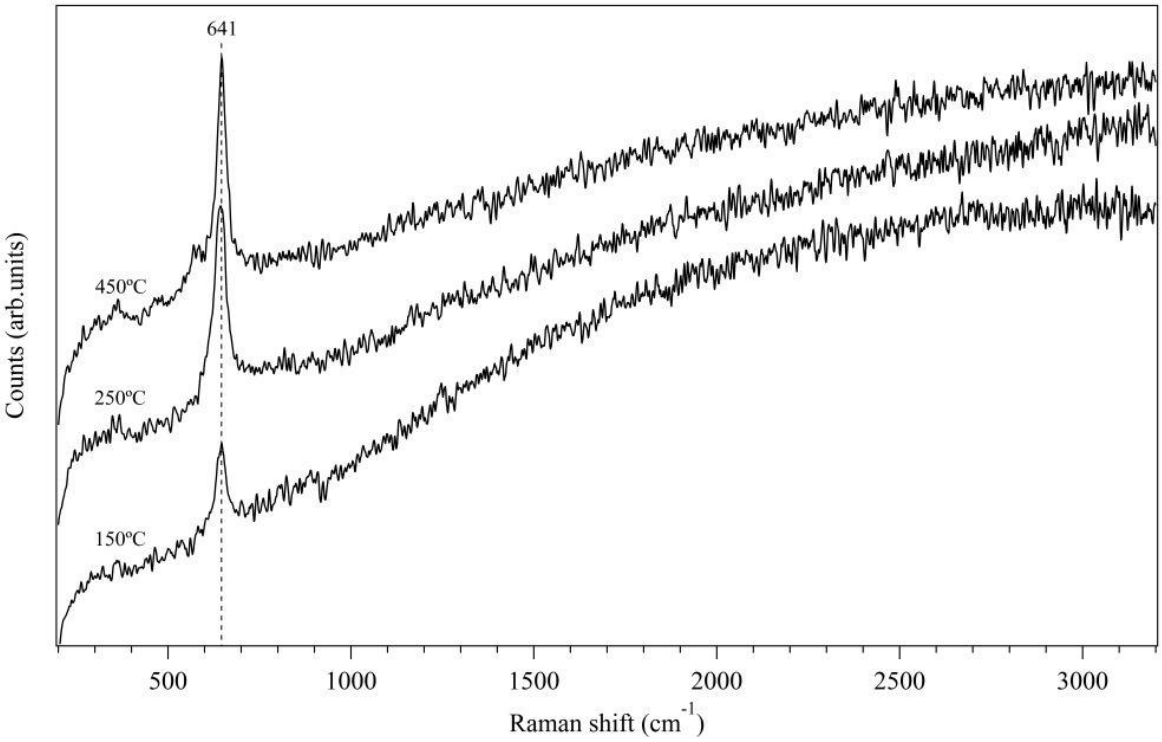

Figure 7.16 Raman spectra of 360-minute milled $2KBH_4$-$MnCl_2$ sample heated to 150, 250 and 450 °C under Ar flowing then exposed to air at RT for 2 minutes.

Therefore, by considering the combination of *in-situ* XRD and Raman spectrometry, *ex-situ* IR, TGA and DSC results, the first thermal decomposition of the 360-minute milled $2KBH_4$-$MnCl_2$ sample between 100 and 160 ℃ can be described in equation (7.2):

$2KMnCl_3$ (o) + $K_2Mn(BH_4)_4$ + $2KBH_4$

$$\rightarrow 4KBH_4 + 2KMnCl_3 + Mn + 12/7B + 1/7B_2H_6 + 25/7H_2 \tag{7.2}$$

where the theoretical mass loss is calculated as 1.58 wt% in the mixture, which is consistent with the experimental data (1.6 wt%).

In the second thermal decomposition between 170 and 260 ℃ , there are several reactions taking place simultaneously: the reaction of KBH_4 with ternary chloride to release hydrogen and form KCl, boron, finely dispersed manganese and possibly small amounts of higher borane species, as shown in equation (7.3), where the theoretical mass loss is calculated as 1.96 wt% in the mixture, which is consistent with the experimental data (1.9 wt%); the dissolution of KBH_4 into KCl phase to form the solid solution as expressed in equation (7.4); and the transformation of ternary chloride as shown in equation (7.5).

$$2KMnCl_3 + 4KBH_4$$

$$\rightarrow 6KCl + 2Mn + (4\text{-}2y/z)B + 7H_2 + 2/z[B_yH_z] \tag{7.3}$$

$$xKCl + (1\text{-}x)KBH_4 \rightarrow K(BH_4)_{1\text{-}x}Cl_x \tag{7.4}$$

$$KMnCl_3 + 3KCl \rightarrow K_4MnCl_6 \tag{7.5}$$

7.4 Possibility of rehydrogenation

After decomposition of the 360-minute milled $2KBH_4$-$MnCl_2$ sample by heating to 250 ℃ under 1.5 bar flowing Ar (40 ml/min), preliminary attempts to reform the borohydride complex by heating to 225 ℃ in 150 bar H_2 flowing at 100 ml/min for two days were performed. However, no mass loss and hydrogen evolution can be observed when the sample was heated in flowing argon on a TGA coupled to a mass spectrometer and also the Raman spectra have not shown any B-H band vibration modes. Therefore, this type of borohydride is irreversible under the experimental conditions investigated in this study.

Chapter 8 Summary and Conclusions

8.1 Formation of manganese-based borohydrides

Manganese-based borohydrides with different compositions were successfully synthesized by mechanochemical milling of ABH_4-$MnCl_2$ (A = Li, Na, K) mixtures, in 2:1 and 3:1 molar ratios. A comparison of the resulting products after 360 minutes of milling is shown in Table 8.1.

Analysis of the milled $x$$LiBH_4$-$MnCl_2$ (x = 2 or 3) materials showed the presence of crystalline LiCl and $Mn(BH_4)_2$ in both samples, plus excess $LiBH_4$ in the $3LiBH_4$-$MnCl_2$ sample. The $Mn(BH_4)_2$ phase had XRD reflections consistent with the $P3_112$ structure proposed by Černý et al (2009), and Raman spectroscopy indicted that the $[BH_4]^-$ units were in an ionic tetrahedral configuration.

$Mn(BH_4)_2$ was also formed for $x$$NaBH_4$-$MnCl_2$ (x = 2 or 3). However, when $NaBH_4$ was used as the reagent, the resulting material (under comparable milling conditions) was poorly crystalline. Analysis of the milled material revealed that a solid solution of $NaCl_x(BH_4)_{1-x}$ and an amorphous Na-Mn-(BH_4)-Cl composition were formed. It was estimated that amorphous phases accounted for 66 ± 1 and 65 ± 1 wt% for the as-milled $2NaBH_4$-$MnCl_2$ and $3NaBH_4$-$MnCl_2$ samples, respectively. The $[BH_4]^-$ environment was consistent with $Mn(BH_4)_2$ and a high symmetry ionic $[BH_4]^-$ unit (consistent with a solid solution phase).

In the milled $2KBH_4$-$MnCl_2$ sample, there were no distinct X-ray reflections associated with the $Mn(BH_4)_2$ phase. Characterization of the milled materials shows mixed-ion borohydride $K_2Mn(BH_4)_4$, ternary chloride $KMnCl_3$ and unreacted KBH_4 phases. The $K_2Mn(BH_4)_4$ phase had XRD reflections consistent with the *$P2_1/n$* structure recently proposed by Schouwink et al. (2012).

This result shows that the ball-milling metathesis route with Na- or K- borohydrides as starting materials had resulted in a complex multiphase system, rather than just the target borohydride and a salt.

Table 8. 1 Composition of 360-minute milled samples and resulting products

Reactants	Molar ratios	Ball-milling products
$LiBH_4$-$MnCl_2$	2:1	$Mn(BH_4)_2$, LiCl
	3:1	$Mn(BH_4)_2$, LiCl, unreacted $LiBH_4$
$NaBH_4$-$MnCl_2$	2:1	$Mn(BH_4)_2$(amorphous), $NaCl_{0.77}(BH_4)_{0.23}$, 0.7Na- 0.15Mn-Cl (amorphous)
	3:1	$Mn(BH_4)_2$(poorly crystalline), $NaCl_{0.68}(BH_4)_{0.32}$, 1.4Na-0.1Mn-0.7(BH_4)-0.9Cl (amorphous)
KBH_4-$MnCl_2$	2:1	$K_2Mn(BH_4)_4$, $KMnCl_3$, unreacted KBH_4

8.2 Thermal decomposition

The thermal decomposition properties of manganese-based borohydrides are summarized in Table 8.2. Thermal decomposition of $Mn(BH_4)_2$ occurred between 130 and 181 °C for the milled $2LiBH_4$-$MnCl_2$ sample and from 105 to 145 °C for $3LiBH_4$-$MnCl_2$ resulting in the concurrent evolution of hydrogen and diborane with the mass loss of 8.4 ± 0.2 and 8.1 ± 0.1 wt%. A second TGA decomposition step between 320 and 410 °C for the milled $3LiBH_4$-$MnCl_2$ sample might possibly indicate a two-step process for decomposition, involving the formation of an intermediate phase.

For the milled $NaBH_4$-$MnCl_2$ samples, $Mn(BH_4)_2$ decomposed between 110 and 170 °C, with mass changes of 6.4 ± 0.2 and 6.0 ± 0.1 wt.% for the $2NaBH_4$-$MnCl_2$ and $3NaBH_4$-$MnCl_2$ samples, respectively. This was accompanied by the concurrent evolution of hydrogen and diborane. These decomposition behaviours were consistent with those observed for $Mn(BH_4)_2$ synthesized from $LiBH_4$. The second mass loss had an onset of 390 °C and was incomplete at 500°C releasing only hydrogen and a mass loss in excess of 1.7 ± 0.2 wt%.

This result showed that an increased cation concentration reduced the decomposition temperature: 118-170 °C for the $2NaBH_4$-$MnCl_2$ sample, and 110-160 °C for the $3NaBH_4$-$MnCl_2$ sample. This phenomenon was also observed for the $LiBH_4$-synthesized samples: 130-181 °C for $2LiBH_4$-$MnCl_2$ sample, and 105-145 °C for $3LiBH_4$-$MnCl_2$ sample.

Mixed-cation borohydride ($K_2Mn(BH_4)_4$) formed as a result of ball milling of $2KBH_4$-$MnCl_2$ decomposed to release hydrogen and trace diborane from 100 to 160 °C with a mass loss of 1.6 ± 0.1 wt%. Between 117 to 260 °C the reaction of KBH_4 (or $KCl_x(BH_4)_{1-x}$ solid solution) with $KMnCl_3$ ternary chloride led to only hydrogen release with a mass loss of 1.9 ± 0.1 wt%.

*Table 8.2 Summary of decomposition temperatures and mass losses**

Samples	MR	T_o (ºC)	T_e (ºC)	*ML* (%)	*GE*	*Eq*	T_o (ºC)	T_e (ºC)	*ML* (%)	*GE*	*Eq*
		First mass loss (TGA)					Second mass loss (TGA)				
$LiBH_4$-$MnCl_2$	2:1	130	181	8.4±0.2	H_2, B_2H_6	(5.7)					
	3:1	105	145	8.1±0.1	H_2, B_2H_6	(5.7)	320	410	0.9±0.2	H_2	
$NaBH_4$-$MnCl_2$	2:1	118	170	6.4±0.2	H_2, B_2H_6	(5.7)					
	3:1	110	160	6.1±0.1	H_2, B_2H_6	(5.7)	380	500	1.7±0.2	H_2	(6.9)
KBH_4-$MnCl_2$	2:1	100	160	1.6±0.1	H_2, B_2H_6	(7.2)	165	260	1.9±0.1	H_2	(7.3)

**MR: molar ratio*; *T_o: onset decomposition temperature; Te: end decomposition temperature; ML: mass loss; Eq: equation; GE: gas evolution*

These results indicated that the decomposition temperature of Mn-based borohydrides highly depended on their composition and nature: the formed $Mn(BH_4)_2$ compound with excess alkali metal borohydrides from the milled $3ABH_4$-$MnCl_2$ (A = Li, Na) samples, and the formation of mixed-ion borohydride ($K_2Mn(BH_4)_4$) from the milled $2KBH_4$-$MnCl_2$ sample reduced the decomposition temperature.

8.3 Analysis of decomposition behaviour

Decomposition for all the milled $xABH_4$-$MnCl_2$ ($x = 2, 3$; A= Li, Na, K) samples suggested the formation of amorphous boron, due to the absence of Mn-B vibrations in Raman and FTIR measurements. In addition, Raman peaks showed the formation of manganese oxide in decomposed samples that had been deliberately exposed to air, indirectly supporting the probable formation of manganese.

The $Mn(BH_4)_2$ compound formed from the milled $xLiBH_4$-$MnCl_2$ (x = 2 or 3) sample decomposed most likely through the overall reaction: $Mn(BH_4)_2 \rightarrow Mn + {}^4/_3B + {}^1/_3B_2H_6 + 3H_2$. The $3LiBH_4$-$MnCl_2$ sample had excess $LiBH_4$ which went through the orthorhombic to hexagonal phase change at 100 °C (lower than that of as received $LiBH_4$), indicating partial substitution of Cl^- for $[BH_4]^-$ within the lattice. Melting occurred at 285 °C followed by a series of reactions as $LiBH_4$ interacted with the decomposition products of $Mn(BH_4)_2$ with the evolution of H_2 and the formation of three as yet unidentified phases (320-400 °C).

For the milled $xNaBH_4$-$MnCl_2$ samples (where $x = 2, 3$), a series of reactions took place during heating. From 50 to 70 °C, $Mn(BH_4)_2$ and Na_6MnCl_8 crystallized from the amorphous milled material. $Mn(BH_4)_2$ decomposed between 110 and 170 °C following the same decomposition behaviour as for $Mn(BH_4)_2$ synthesized from $LiBH_4$. The ternary chloride reacted with the solid solutions, resulting in the release of hydrogen in both samples. For the 3$NaBH_4$-$MnCl_2$ sample, two types of solid solution phases were observed between 100 and 350 °C, which decomposed to form unknown phases above 380 °C.

The milled 2KBH_4-$MnCl_2$ sample showed a two-step decomposition behaviour. The first between 100 and 160 °C was associated with the decomposition of $K_2Mn(BH_4)_4$ to form KBH_4, boron, finely dispersed manganese, as well as the release of hydrogen and trace diborane. The second between 165 and 260 °C, showed several reactions taking place simultaneously: the reaction of KBH_4 with ternary chloride to release hydrogen and to form KCl, boron, finely dispersed manganese and possibly small amounts of higher borane species; the dissolution of KCl into the KBH_4 phase to form a $KCl_x(BH_4)_{1-x}$ solid solution phase; and the transformation of ternary chloride from $KMnCl_3$ to K_4MnCl_6. The phase compositions before and after decomposition of milled ABH_4-$MnCl_2$ samples are shown in Table 8.3.

*Table 8.3 Products of 360-minute milled samples before and after decomposition**

Samples	Molar ratios	Products-B	Products-A$_1$	Products-A$_2$
$LiBH_4$-$MnCl_2$	2:1	$Mn(BH_4)_2$, LiCl	Mn, B, LiCl	
	3:1	$Mn(BH_4)_2$, LiCl, unreacted $LiBH_4$	Mn, B, LiCl	Mn, B, LiCl, unknown phases
$NaBH_4$-$MnCl_2$	2:1	$Mn(BH_4)_2$, Na_6MnCl_8, $NaCl_{0.72}(BH_4)_{0.28}$,	Mn, B, Na_6MnCl_8 $NaCl_{0.72}(BH_4)_{0.28}$,	
	3:1	$Mn(BH_4)_2$, Na_6MnCl_8 , $NaCl_{0.68}(BH_4)_{0.32}$, $NaCl_{0.15}(BH_4)_{0.85}$	Mn, B, Na_6MnCl_8 $NaCl_{0.68}(BH_4)_{0.32}$ $NaCl_{0.15}(BH_4)_{0.85}$	Mn, B, $NaCl_{0.95}(BH_4)_{0.05}$, unknown phases
KBH_4-$MnCl_2$	2:1	$K_2Mn(BH_4)_4$, $KMnCl_3$, unreacted KBH_4	Mn, B, KBH_4, $KMnCl_3$,	Mn, B, KCl, unknown [B_xH_y]

**Product-B: product compositions before the first decomposition; Product-A$_1$: products after the first decomposition; Products-A$_2$: products after the second decomposition*

8.4 Rehydrogenation

Good reversibility is one of the requirements for an efficient hydrogen storage material. Alkali and alkaline earth metal borohydrides e. g. $LiBH_4$, $Mg(BH_4)_2$ and $Ca(BH_4)_2$ have been reported to be partially or fully reversible at certain temperatures under high pressure hydrogen (100-500 bar) (Kim et al., 2008b; Soloveichik et al., 2009b; Züttel et al., 2007). However, the dehydrogenation of the transition metal borohydrides formed so far was found to be irreversible, owing to the release of diborane apart from hydrogen during their decomposition (Černý et al., 2010c; Gennari et al., 2009; Reed, 2009).

In this work, the milled $2ABH_4$-$MnCl_2$ (A = Li, K) samples were preheated to 200-225 ºC under 1.5 bar Ar flowing at 40 ml/min, then attempts were made to reform the borohydride complex in 100-150 bar(g) H_2 flowing at 100 ml/min for two days. However, no mass loss and hydrogen evolution can be observed when the recombined samples were heated in flowing argon on a TGA coupled to a mass spectrometer and also Raman spectra did not show any B-H band vibration information. Therefore, it appears that the dehydrogenation of this type of borohydride was irreversible, under the conditions investigated. The poor rehydrogenation properties of Mn-based borohydrides were derived not only from the release of diborane, but also from the presence of salts, which prevented the reformation of Mn-based borohydrides. Thus, the removal of salts and prevention of diborane evolution can be said to be prerequisites to allow the possibility of recombination.

Alternatively, the reactive hydride composite such as borohydrides mixed with metal hydrides could be used to improve rehydrogenation properties by the alteration of the decomposition pathway(s). In this approach, the overall reaction enthalpy is lowered by the exothermic formation of a new compound during the endothermic decomposition of two hydrides

(Pinkerton and Meyer, 2008; Vajo et al., 2005). The utilization of catalytically active nanoparticles and nanostructured materials has also been proposed for improving the rehydrogenation properties of metal borohydride, where active nanoparticles have high catalytic activity to accelerate rehydrogenation reactions and nanomaterials are expected to form a net-like structure after being milled together with host metal borohydrides, thus creating a microconfined environment for the decomposition/rehydriding (Gosalawit-Utke et al., 2011; Vajo et al., 2005).

8.5 Metathesis reaction

The solvent-free synthesis of Mn-based borohydrides through ball-milling appears to be a very simple and efficient approach. As for the other transition metal borohydrides, this preparation involves a complete or incomplete ion exchange reaction between alkali borohydrides and manganese chloride. The ball-milling metathesis route in this work resulted in a complex multiphase system, rather than just the target borohydride and a salt. The series of decomposition and inter-phase reaction makes it more difficult to use as a means to study the hydrogen storage properties of the $Mn(BH_4)_2$ compound. The salts are byproducts from ball-milling metathesis reaction and the removal of salts to produce pure Mn borohydride compound may improve hydrogen storage properties, for example, by increasing hydrogen capacity and modifying the decomposition/rehydrogenation mechanism, although the strategies of removing salt from milled ABH_4-$MnCl_2$ have not been reported. Having said that, the hydrogen sorption properties of the solid solution phases themselves may also be of interest for further study in terms of both fundamental scientific research and an application in hydrogen storage and batteries.

Chapter 9 Future Work

Metal borohydrides have the potential to be used as onboard storage media for hydrogen in mobile applications, if the hydrogen sorption kinetics can be accelerated and reversibility introduced. Fundamental studies on a range of borohydride compounds, covering topics such as preparation technique, structural characteristics and thermal behaviour have increased greatly over last few years. However, much more research is still needed to further improve their hydrogen storage properties.

- This study has demonstrated that different compositions of manganese-based borohydrides can be prepared by partial and complete metathesis reactions, which depend on the starting materials and their molar ratios. The correct molar ratio of starting materials e.g. ABH_4-$MnCl_2$ with molar ratio of 1:1, 2:1, 3:1, 4:1, is needed to optimise the type of Mn-based borohydride with optimal hydrogen storage properties. Additionally, a distinct structure and composition of Mn-based borohydride from $Mn(BH_4)_2$ – synthesized from the 360-minute milled $LiBH_4$-$MnCl_2$ samples, was probably formed from the $LiBH_4$-$MnCl_2$ samples milled for shorter durations (e.g. 10 minutes), thus the structure and composition of the Mn-based borohydride should be identified by high resolution XRD.
- Powder XRD patterns showed that the mixed-cation borohydride $K_2Mn(BH_4)_4$, ternary $KMnCl_3$ and unreacted KBH_4 were formed for the milled $2KBH_4$-$MnCl_2$ sample. Various molar ratios between KBH_4 and $MnCl_2$ should be selected to form different composites after milling, then characterisation of the crystal structure(s) and decomposition products through synchrotron-XRD or neutron diffraction to obtain higher intensity reflections.

- The decomposition of the milled $3LiBH_4$-$MnCl_2$ and $3NaBH_4$-$MnCl_2$ samples has indicated that there were a number of unknown phases. *In-situ* synchrotron radiation XRD could help to identify any intermediate decomposition products.
- The decomposition for all the milled $xABH_4$-$MnCl_2$ ($x = 2, 3$; A= Li, Na, K) samples suggested the formation of amorphous B and Mn that was indirectly supported by exposing the decomposed sample to air to form manganese oxide. It is not yet clear why Mn was not observed by XRD in this study, unless it is possibly in the form of finely dispersed nanoscale grains. Alternatively, an amorphous Mn-B compound would explain the absence of Mn X-ray peaks. However, the Mn–B vibrations in the Raman and FT-IR spectra were absent. Therefore, according to the magnetic properties of Mn-B, thermal magnetic analysis could be used to try to identify whether B or a Mn-B compound (strong ferromagnetic Tc = 300 ºC) has formed after the decomposition.
- Further investigations into the reversibility for this type of borohydride are needed to ascertain whether recombination is possible under optimized conditions, including the design of novel composites e.g. Mg-hydride composites (Li et al., 2011b; Vajo et al., 2005), catalytically active metal nanoparticles (Li et al., 2011b) and carbon nanostructured materials (Gosalawit-Utke et al., 2011; Sartori et al., 2009) ball-milled with host Mn-based borohydride to avoid the release of diborane during the decomposition. The temperature and hydrogen pressure should also be optimized for the rehydrogenation.
- In this study NbF_5 has exhibited a significant impact on the decomposition behaviour of the materials. Detailed work is needed on the effect of additives at different

concentration, in particular, on improving dehydriding/rehydriding kinetics, thermodynamic modification and reduction or elimination of diborane release.

- This work has shown that the ball milling $x\text{ABH}_4\text{-MnCl}_2$ resulted in the formation of the target compounds and byproducts e.g. binary chlorides or ternary chlorides. The byproducts lead to a decreased gravimetric hydrogen storage capacity. Therefore, a new synthetic route(s) needs to be developed. For instance a direct reaction between Mn boride and boranes under high pressure of hydrogen needs to be investigated although this route has not been reported on the formation of Mn-based borohydride. Another possible method is to remove chloride compounds from the milled mixture by solvent extraction. However, the removal of the salt byproduct is very difficult because of the decomposition of this type of borohydride. The removal of the solvent occurs at nearly the same temperature as decomposition (see Chapter 3). Therefore various types of solvents and extraction parameters should be selected and investigated in detail to optimise the operational conditions for preventing the decomposition during the extraction and evaporation of solvent.

Reference List

Agresti, F. and Khandelwal, A. (2009) Evidence of formation of $LiBH_4$ by high-energy ball milling of LiH and B in a hydrogen atmosphere. **Scripta Materialia**, 60: 753-755.

Aguey-Zinsou, K. F., Nicolaisen, T., Fernandez, J. R. A. et al. (2007) Effect of nanosized oxides on MgH_2 (de)hydriding kinetics. **Journal of Alloys and Compounds**, 434: 738-742.

Amankwah, A. K. G., Noh, J. S. and Schwarz, A. J. (1989) Hydrogen storage on superactivated carbon at refrigeration temperatures. **International Journal of Hydrogen Energy**, 14(7): 437-447.

Amendola, S. C., Sharp-Goldman, S. L., Janjua, M. S. et al. (2000) An ultrasafe hydrogen generator: aqueous, alkaline borohydride solutions and Ru catalyst. **Journal of Power Sources**, 85: 186-189.

Andreasen, A. (2008) Hydrogenation properties of Mg-Al alloys. **International Journal of Hydrogen Energy**, 33(24): 7489-7497.

Anson, A., Lafuente, E., Urriolabeitia, E. et al. (2006) Hydrogen capacity of palladium-loaded carbon materials. **Journal of Physical Chemistry B**, 110(13): 6643-6648.

Ares, J. R., Aguey-Zinsou, K. F., Leardini, F. et al. (2009) Hydrogen absorption/desorption mechanism in potassium alanate ($KAlH_4$) and enhancement by $TiCl_3$ doping. **Journal of Physical Chemistry C**, 113(16): 6845-6851.

Ares, J. R., Aguey-Zinsou, K. F., Porcu, M. et al. (2008) Thermal and mechanically activated decomposition of $LiAlH_4$. **Materials Research Bulletin**, 43(5): 1263-1275.

Arnbjerg, L. M., Ravnsbæk, D. B., Filinchuk, Y. et al. (2009) Structure and dynamics for $LiBH_4$-LiCl solid solutions. **Chemistry of Materials**, 21(24): 5772-5782.

Ashby, E. C. and Kobetz, P. (1966) The direct synthesis of Na_3AlH_6. **Inorganic Chemistry**, 5: 1615-1617.

Au, M. and Jurgensen, A. (2006) Modified lithium borohydrides for reversible hydrogen storage. **Journal of Physical Chemistry B**, 110: 7062-7067.

Au, M., Jurgensen, A. R., Spencer, W. A. et al. (2008a) Stability and reversibility of lithium borohydrides doped by metal halides and hydrides. **Journal of Physical Chemistry C**, 112(47): 18661-18671.

Au, M., Spencer, W., Jurgensen, A. et al. (2008b) Hydrogen storage properties of modified lithium borohydrides. **Journal of Alloys and Compounds**, 462: 303-309.

Banus, M. D. and Bragdon, R. W. (1955). US patent 2,720,444.

Barbir, F. (2005) PEM electrolysis for production of hydrogen from renewable energy sources. **Solar Energy**, 78(5): 661-669.

Bardaji, E. G., ZhaoKarger, Z., Boucharat, N. et al. (2011) $LiBH_4$-$Mg(BH_4)_2$: A physical mixture of metal borohydrides as hydrogen storage material. **Journal of Physical Chemistry C**, 115(13): 6095-6101.

Barkhordarian, G., Jensen, T. R., Doppiu, S. et al. (2008) Formation of $Ca(BH_4)_2$ from hydrogenation of CaH_2+MgB_2 composite. **Journal of Physical Chemistry C**, 112(7): 2743-2749.

Barkhordarian, G., Klassen, T. and Bormann, R. (2004) Effect of Nb_2O_5 content on hydrogen reaction kinetics of Mg. **Journal of Alloys and Compounds**, 364(1-2): 242-246.

Barrer, R. M. (1978) **Zeolites and Clay Minerals as Sorbents and Molecular Sieves**. London: Academic Press.

Bird, P. B. and Churchill, M. R. (1967) The crystal structure of zirconium(IV) borohydride (at -160°C). **Chemical Comunications,**(8): 403-403.

Bogdanović, B., Bohmhamme, K., Christ, B. et al. (1999) Thermodynamic investigation of the magnesium-hydrogen system. **Journal of Alloys and Compounds**, 282: 84-92.

Bogdanović, B., Felderhoff, M., Pommerin, A. et al. (2006) Advanced hydrogen-storage materials based on Sc-, Ce-, and Pr-doped $NaAlH_4$. **Advanced Materials**, 18(9): 1198-1199.

Bogdanović, B. and Schwickardi, M. (1997) Ti-doped alkali metal aluminium hydrides as potential novel reversible hydrogen storage materials. **Journal of Alloys and Compounds**, 253: 1-9.

Bowman, R. C. and Fultz, B. (2002) Metallic hydrides I: Hydrogen storage and other gas-phase applications. **MRS Bulletin**, 27(9): 688-693.

Broach, R. W., Chuang, S. I., Marks, T. J. et al. (1983) Metrical characterization of tridentate tetrahydroborate ligation to a transition-metal ion. Structure and bonding in $Hf(BH_4)_4$ by single-crystal neutron diffraction. **Inorganic Chemistry**, 22: 1081-1084.

Brown, H. C., Choi, Y. M. and Narasimhan, S. (1981) Convenient procedure for the conversion of sodium borohydride into lithium borohydride in simple ether solvents. **Inorganic Chemistry**, 20: 4454-4456.

Buciuman, F., Patcas, F., Craciun, R. et al. (1999) Vibrational spectroscopy of bulk and supported manganese oxides. **Physical Chemistry Chemical Physics**, 1: 185-190.

Cakanyildirim, C. and Guru, M. (2008) Processing of $LiBH_4$ from its elements by ball milling method. **Renewable Energy**, 33(11): 2388-2392.

Callear, S. K., Nickels, E. A., Jones, M. O. et al. (2011) Order and disorder in lithium tetrahydroborate. **Journal of Materials Science**, 46(2): 566-569.

Carpetis, C. and Peschka, W. (1980) A study on hydrogen storage by use of cryoadsorbents. **International Journal of Hydrogen Energy**, 5(5): 539-554.

CDS (2009) **Chemical Crystal Database** [online]. Available from: http://cds.dl.ac.uk [Accessed 10 Augest 2009].

Černý, R., Filinchuk, Y., Hagemann, H. et al. (2007) Magnesium borohydride: Synthesis and crystal structure. **Angewandte Chemie-International Edition**, 46(30): 5765-5767.

Černý, R., Kim, K. C., Penin, N. et al. (2010a) $AZn_2(BH_4)_5$ (A = Li, Na) and $NaZn(BH_4)_3$: structural studies. **Journal of Physical Chemistry C**, 114(44): 19127-19133.

Černý, R., Penin, N., Hagemann, H. et al. (2009) The first crystallographic and spectroscopic characterization of a 3d-metal borohydride: $Mn(BH_4)_2$. **Journal of Physical Chemistry C**, 113(20): 9003-9007.

Černý, R., Ravnsbaek, D. B., Severa, G. et al. (2010b) Structure and characterization of $KSc(BH_4)_4$. **Journal of Physical Chemistry C**, 114(45): 19540-19549.

Černý, R., Severa, G., Ravnsbaek, D. B. et al. (2010c) $NaSc(BH_4)_4$: A novel scandium-based borohydride. **Journal of Physical Chemistry C**, 114(2): 1357-1364.

Chater, P. A., Anderson, P. A., Prendergast, J. W. et al. (2007a) Synthesis and characterization of amide-borohydrides: New complex light hydrides for potential hydrogen storage. **Journal of Alloys and Compounds**, 446: 350-354.

Chater, P. A., David, W. I. F. and Anderson, P. A. (2007b) Synthesis and structure of the new complex hydride $Li_2BH_4NH_2$. **Chemical Communications**, 45: 4770-4772.

Chater, P. A., David, W. I. F., Johnson, S. R. et al. (2006) Synthesis and crystal structure of $Li_4BH_4(NH_2)_3$. **Chemical Communications**, 23: 2439-2441.

Chen, P., Wu, X., Lin, L. et al. (1999a) High H_2 uptake by alkali-doped carbon nanotubes under ambient pressure and moderate temperatures. **Science**, 285(5424): 91-93.

Chen, P., Xiong, Z. T., Luo, J. Z. et al. (2002) Interaction of hydrogen with metal nitrides and imides. **Nature**, 420(6913): 302-304.

Chen, P. and Zhu, M. (2008) Recent progress in hydrogen storage. **Materials Today**, 11(12): 36-43.

Chen, Y., Fitz Gerald, J. D., Chadderton, L. T. et al. (1999b) Nanoporous carbon produced by ball milling. **Applied Physics Letters**, 74(19): 2782-2784.

Chlopek, K., Frommen, C., Leon, A. et al. (2007) Synthesis and properties of magnesium tetrahydroborate, $Mg(BH_4)_2$. **Journal of Materials Chemistry**, 17(33): 3496-3503.

Chong, M., Karkamkar, A., Autrey, T. et al. (2011) Reversible dehydrogenation of magnesium borohydride to magnesium triborane in the solid state under moderate conditions. **Chemical Communications**, 47(4): 1330-1332.

Choudhury, P., Bhethanabotla, V. R. and Stefanakos, E. K. (2009a) Manganese borohydride as a hydrogen-storage candidate: first-principles crystal structure and thermodynamic properties. **Journal of Physical Chemistry C**, 113(30): 13416-13424.

Choudhury, P., Srinivasan, S. S., Bhethanabotla, V. R. et al. (2009b) Nano-Ni doped Li-Mn-B-H system as a new hydrogen storage candidate. **International Journal of Hydrogen Energy**, 34(15): 6325-6334.

Chua, Y. S., Wu, G. T., Xiong, Z. T. et al. (2010) Investigations on the solid state interaction between $LiAlH_4$ and $NaNH_2$. **Journal of Solid State Chemistry**, 183(9): 2040-2044.

Coelho, A. A. (2004) **TOPAS, General Profile and Structure Analysis Software for Powder Diffraction Data, version 3.0**. Bruker AXS: Karlsruhe, Germany.

CRCT (2009) **FactSage FTsalt salt database: List of systems and phases** [online]. Available from: http://www.crct.polymtl.ca/fact/documentation/FTsalt/FTsalt_list.htm [Accessed 08 September 2009].

Crivello, J. C., Nobuki, T. and Kuji, T. (2009) Improvement of Mg-Al alloys for hydrogen storage applications. **International Journal of Hydrogen Energy**, 34(4): 1937-1943.

Czujko, T., Varin, R. A., Wronski, Z. et al. (2007) Synthesis and hydrogen desorption properties of nanocomposite magnesium hydride with sodium borohydride (MgH_2 + $NaBH_4$). **Journal of Alloys and Compounds**, 427(1-2): 291-299.

Dai, B., Sholl, D. S. and Johnson, J. K. (2008a) First-principles study of experimental and hypothetical $Mg(BH_4)_2$ crystal structures. **Journal of Physical Chemistry C**, 112(11): 4391-4395.

Dai, H., Zhang, H. M., Luo, Q. T. et al. (2008b) Properties and fuel cell performance of proton exchange membranes prepared from disulfonated poly(sulfide sulfone). **Journal of Power Sources**, 185(1): 19-25.

Dai, H. B., Liang, Y. and Wang, P. (2011) Effect of trapped hydrogen on the induction period of cobalt-tungsten-boron/nickel foam catalyst in catalytic hydrolysis reaction of sodium borohydride. **Catalysis Today**, 170(1): 27-32.

Dalach, P., Frost, H., Snurr, R. Q. et al. (2008) Enhanced hydrogen uptake and the electronic structure of lithium-doped metal-organic frameworks. **Journal of Physical Chemistry C**, 112(25): 9278-9284.

Delogu, F. and Mulas, G. (2009) Hydrogen absorption processes in Mg_2Ni-based systems: Thermal and mechanochemical kinetics. **International Journal of Hydrogen Energy**, 34(7): 3026-3031.

Denton, A. R. and Ashcroft, N. W. (1991) Vegard's law. **Physical Review A**, 43: 3161-3164.

Dillon, A. C., Jones, K. M., Bekkedahl, T. A. et al. (1997) Storage of hydrogen in single-walled carbon nanotubes. **Nature**, 386(6623): 377-379.

Dixon, R. K. (2007) Advancing towards a hydrogen energy economy: Status, opportunities and barriers. **Mitigation and Adaptation Strategies for Global Change**, 12: 325-341.

U.S Department of Energy (2009) "Hydrogen Storage". In **2009 Annual Merit Review Proceedings: Hydrogen program & Vehical Technologies Program**, Arlington, Virginia: 18-22th May 2009.

Dolotko, O., Paulson, N. and Pecharsky, V. K. (2010) Thermochemical transformations in $2MNH_2$-$3MgH_2$ systems (M = Li or Na). **International Journal of Hydrogen Energy**, 35(10): 4562-4568.

Dolotko, O., Zhang, H. Q., Ugurlu, O. et al. (2007) Mechanochemical transformations in Li(Na)AlH_4-Li(Na)NH_2 systems. **Acta Materialia**, 55(9): 3121-3130.

Du, X. M. and Wu, E. D. (2006) Physisorption of hydrogen in A, X and ZSM-5 types of zeolites at moderately high pressures. **Chinese Journal of Chemical Physics**, 19(5): 457-462.

Dufour, J. and Huot, J. (2007) Rapid activation, enhanced hydrogen sorption kinetics and air resistance in laminated Mg-Pd 2.5 wt.%. **Journal of Alloys and Compounds**, 439(1-2): L5-L7.

Epp, V. and Wilkening, M. (2010) Fast Li diffusion in crystalline $LiBH_4$ due to reduced dimensionality: Frequency-dependent NMR spectroscopy. **Physical Review B**, 82(2): 020301-020305.

Evans, J. S. O. (2009) **TOPAS accademic** [online]. Available from: http://www.dur.ac.uk/john.evans/topas_academic/topas_main.htm [Accessed 07 Augest 2009].

Fang, Z. Z., Kang, X. D., Luo, J. H. et al. (2010a) Formation and hydrogen storage properties of dual-cation (Li, Ca) borohydride. **Journal of Physical Chemistry C**, 114(51): 22736-22741.

Fang, Z. Z., Kang, X. D., Wang, P. et al. (2010b) Unexpected dehydrogenation behavior of $LiBH_4/Mg(BH_4)_2$ mixture associated with the in situ formation of dual-cation borohydride. **Journal of Alloys and Compounds**, 491(1-2): L1-L4.

Farha, O. K., Mulfort, K. L. and Hupp, J. T. (2008) An example of node-based postassembly elaboration of a hydrogen-sorbing, metal-organic framework material. **Inorganic Chemistry**, 47(22): 10223-10225.

Feankcombe, T. J., Kroes, G. J. and Züttel, A. (2005) Theoretical calculation of the energy of formation of $LiBH_4$. **Chemical Physics Letters**, 405: 73-78.

Fichtner, M. (2005) Nanotechnological aspects in materials for hydrogen storage. **Advanced Engineering Materials**, 7(6): 443-455.

Filinchuk, Y., Cerny, R. and Hagemann, H. (2009a) Insight into $Mg(BH_4)_2$ with synchrotron X-ray diffraction: structure revision, crystal chemistry, and anomalous thermal expansion. **Chemistry of Materials**, 21(5): 925-933.

Filinchuk, Y., Ronnebro, E. and Chandra, D. (2009b) Crystal structures and phase transformations in $Ca(BH_4)_2$. **Acta Materialia**, 57(3): 732-738.

Fillinchuk, Y., Chernyshov, D. and Černý, R. (2008) Lightest borohydride probed by sysnchrotron X-ray diffraction: experiment call for a new theoretical revision. **Journal of Physical Chemistry C**, 112: 10579-10584.

Friedrichs, O., Borgschulte, A., Kato, S. et al. (2009a) Low-temperature synthesis of $LiBH_4$ by gas-solid reaction. **Chemistry-a European Journal**, 15(22): 5531-5534.

Friedrichs, O., Buchter, F., Borgschulte, A. et al. (2008) Direct synthesis of $LiBH_4$ and $LiBD_4$ from the elements. **Acta Materialia**, 56: 949-954.

Friedrichs, O., Kim, J. W., Remhof, A. et al. (2009b) The effect of Al on the hydrogen sorption mechanism of $LiBH_4$. **Physical Chemistry Chemical Physics**, 11(10): 1515-1520.

Friedrichs, O., Kim, J. W., Remhof, A. et al. (2010a) Core shell structure for solid gas synthesis of $LiBD_4$. **Physical Chemistry Chemical Physics**, 12(18): 4600-4603.

Friedrichs, O., Remhof, A., Borgschulte, A. et al. (2010b) Breaking the passivation-the road to a solvent free borohydride synthesis. **Physical Chemistry Chemical Physics**, 12(36): 10919-10922.

Friedrichs, O., Remhof, A., Hwang, S. J. et al. (2010c) Role of $Li_2B_{12}H_{12}$ for the formation and decomposition of $LiBH_4$. **Chemistry of Materials**, 22: 3265–3268.

Frommen, C., Aliouane, N., Deledda, S. et al. (2010) Crystal structure, polymorphism, and thermal properties of yttrium borohydride $Y(BH_4)_3$. **Journal of Alloys and Compounds**, 496(1-2): 710-716.

Fukai, Y., Haraguchi, T., Shinomiya, H. et al. (2002) Constitution of the Mn-H system at high hydrogen pressures. **Scripta Materialia**, 46: 679-684.

Furukawa, H., Millerb, M. A. and Yaghi, O. M. (2007) Independent verification of the saturation hydrogen uptake in MOF-177 and establishment of a benchmark for hydrogen adsorption in metal-organic frameworks. **Journal of Materials and Chemistry**, 17: 3197-3204.

Gennari, F. C., Albanesi, L. F., Puszkiel, J. A. et al. (2011) Reversible hydrogen storage from $6LiBH_4$ MCl_3 (M = Ce, Gd) composites by in-situ formation of MH_2. **International Journal of Hydrogen Energy**, 36(1): 563-570.

Gennari, F. C., Albanesi, L. F. and Rios, I. J. (2009) Synthesis and thermal stability of $Zr(BH_4)_4$ and $Zr(BD_4)_4$ produced by mechanochemical processing. **Inorganica Chimica Acta**, 362(10): 3731-3737.

Gerbec, M., Jovan, V. and Petrovcic, J. (2008) Operational and safety analyses of a commercial PEMFC system. **International Journal of Hydrogen Energy**, 33(15): 4147-4160.

Goerrig, D. (1958). Synthesis of $LiBH_4$ from the elements. German Patent. **1077644**.

Gomes, S., Hagemann, H. and Yvon, K. (2002) Lithium borohydride $LiBH_4$: II. Raman spectroscopy. **Journal of Alloys and Compounds**, 346: 206-210.

Gosalawit-Utke, R., Nielsen, T. K., Saldan, I. et al. (2011) Nanoconfined $2LiBH_4$-MgH_2 prepared by direct melt infiltration into nanoporous materials. **Journal of Physical Chemistry C**, 115(21): 10903-10910.

Gremaud, R., Borgschulte, A., Friedrichs, O. et al. (2011) Synthesis mechanism of alkali borohydrides by heterolytic diborane splitting. **Journal of Physical Chemistry C**, 115(5): 2489-2496.

Guo, S. H., Wang, G. Q., Zhao, D. L. et al. (2011) Effect of doping RE catalysts on dehydriding properties and phase structures of complex hydride $LiAlH_4$. **Rare Metal Materials and Engineering**, 40(3): 547-550.

Gurewitz, E., Melamud, M. and Horowitz, A. (1982) Polytypism in $KMnCl_3$, neutron-difraction study of the distored-perovskite-structure compound. **Physical Review B**, 25(8): 5220-5229.

Hagemann, H., Filinchuk, Y., Chernyshov, D. et al. (2009) Lattice anharmonicity and structural evolution of $LiBH_4$: an insight from Raman and X-ray diffraction experiments. **Phase Transitions**, 82(4): 344-355.

Hagemann, H., Longhini, M., Kaminski, J. W. et al. (2008) LiSc(BH4)4: A novel salt of Li^+ and discrete $Sc(BH_4)_4^-$ complex anions. **Journal of Physical Chemistry A**, 112(33): 7551-7555.

Harris, P. M. and Meibohm, E. P. (1947) The crystal structure of lithium borohydride $LiBH_4$. **Journal of the American Chemical Society**, 69(5): 1231-1232.

Harvey, K. B. and McQuaker, N. R. (1971) Infrared and Raman spectra of potassium and sodium borohydride. **Canadian Journal of Chemistry**, 49: 3272-3281.

Her, J. H., Stephens, P. W., Gao, Y. et al. (2007) Structure of unsolvated magnesium borohydride $Mg(BH_4)_2$. **Acta Crystallographica Section B-Structural Science**, 63: 561-568.

Her, J. H., Yousufuddin, M., Zhou, W. et al. (2008) Crystal structure of $Li_2B_{12}H_{12}$: a possible intermediate species in the decomposition of $LiBH_4$. **Inorganic Chemistry**, 47: 9757-9759.

Hoekstra, H. R. and Katz, J. J. (1949) The preparation and properties of the group IV-B metal borohydrodes. **Journal of the American Chemical Society**, 71(7): 2488-2492.

Horowitz, A., Amit, M. and Makovsky, J. (1982) Structure types of phase transformation in $KMnCl_3$ and $TlMnCl_3$. **Journal of Solid State Chemistry**, 43: 107-125.

Hou, P. X., Yang, Q. H., Bai, S. et al. (2002) Bulk storage capacity of hydrogen in purified multiwalled carbon nanotubes. **Journal of Physical Chemistry B**, 106(5): 963-966.

Hu, Y. Q., Yan, C., Zhang, H. F. et al. (2004) Preparation and hydrogenation characteristics of Mg-30wt.% $Ti_{37.5}V_{25}Cr_{37.5}$ composite. **Journal of Alloys and Compounds**, 375: 265-269.

Hwang, S. J., Bowman, R. C., Reiter, J. W. et al. (2008) NMR confirmation for formation of $[B_{12}H_{12}]^{2-}$ complexes during hydrogen desorption from metal borohydrides **Journal of Physical Chemistry C**, 112(9): 3164-3169.

International Energy Agency (2011) **2011 World Energy Outlook: Executive Summary** [online]. Available from: http://www.worldenergyoutlook.org [accessed 16th April 2012].

ILPI (2012) **Ball milling** [online]. Available from: http://www.ilpi.com/inorganic/glassware/ballmill.html [Accessed 10 May 2012].

International Planet on Climate Change (2007) **The IPCC Fourth Assessment Report: Climate Change 2007** [online]. Available from: http://www.ipcc.ch/publications_and_data/publications_and_data_reports.shtml [Accessed 17th April 2012].

Ismail, M., Zhao, Y., Yu, X. B. et al. (2011) Improved hydrogen desorption in lithium alanate by addition of SWCNT-metallic catalyst composite. **International Journal of Hydrogen Energy**, 36(5): 3593-3599.

Jain, I. P., Lal, C. and Jain, A. (2010) Hydrogen storage in Mg: A most promising material. **International Journal of Hydrogen Energy**, 35(10): 5133-5144.

James, B. D., Nanda, R. K. and Wallbridge, M. G. H. (1966) Spectroscopic studies of borohydride derivatives of zirconium and hafnium. **Journal of the Chemical Society A: Inorganic, Physical, Theoretical**: 182-184.

James, B. D. and Wallbridge, M. G. H. (1970) Metal tetrahydroborates. **Progress in Inorganic Chemistry**, 11: 99-231.

Janon, A. and Andrews, J. (2008) "Direct coupling of a fixed-pitch variable-speed aerogenerator to PEM electrolysers in a wind-hydrogen sysstem for remote area power supply". In **17th World Hydrogen Energy Conference**, Queensland, Australia: 15-19th June 2008. pp 111-114.

Janot, R., Eymery, J. B. and Tarascon, J. M. (2007) Investigation of the processes for reversible hydrogen storage in the Li-Mg-N-H system. **Journal of Power Sources**, 164: 496–502.

Jaron, T. and Grochala, W. (2010) $Y(BH_4)_3$-an old-new ternary hydrogen store aka learning from a multitude of failures. **Dalton Transactions**, 39(1): 160-166.

Jensen, C. M., Sulic, M., Kuba, M. et al. (2007) "Fundamental studies of advanced high-capacity, reversible metal hydides". In **Proceedings of the U.S. Department of Energy Hydrogen Program Annual Merit Review**. pp 386-389.

Jensen, J. O. (2003a) Calculation of the vibrational frequencies and structure of zirconium tetrahydroborate. **Vibrational spectroscopy**, 31: 227-250.

Jensen, J. O. (2003b) Vibrational frequencies and structural determination of hafnium tetrahydroborate. **Spectrochimica Acta Part A-Molecular Biomolecular Spectroscopy**, 59: 379-392.

Jeon, E. and Cho, Y. (2006) Mechanochemical synthesis and thermal decomposition of zinc borohydride. **Journal of Alloys and Compounds**, 422(1-2): 273-275.

Jin, H. G. and Ishida, M. (2000) A novel gas turbine cycle with hydrogen-fueled chemical-looping combustion. **International Journal of Hydrogen Energy**, 25(12): 1209-1215.

Johnson, S. R., Anderson, P. A., Edwards, P. P. et al. (2005) Chemical activation of MgH_2: a new route to superior hydrogen storage materials. **Chemical Communications**, 22: 2823-2825.

Julien, C., Massotb, M., Baddour-Hadjeanc, R. et al. (2003) Raman spectra of birnessite manganese dioxides. **Solid State Ionics**, 159: 345-356.

Kayacan, I., Dogan, O. M. and Uysal, B. Z. (2011) Effect of magnesium on sodium borohydride synthesis from anhydrous borax. **International Journal of Hydrogen Energy**, 36(13): 7410-7415.

Kidnay, A. J. and Hiza, M. J. (1967) High pressure adsorption isotherms of neon, hydrogen and helium at 76 K. **Advances in Cryogenic Engineering**, 12: 730-740.

Kim, C., Hwang, S. J., Bowman, R. C. et al. (2009a) $LiSc(BH_4)_4$ as a hydrogen storage material: Multinuclear high-resolution solid-state NMR and first-principles density functional theory studies. **Journal of Physical Chemistry C**, 113(22): 9956-9968.

Kim, J. H., Jin, S. A., Shim, J. H. et al. (2008a) Reversible hydrogen storage in calcium borohydride $Ca(BH_4)_2$. **Scripta Materialia**, 58: 481-483.

Kim, J. H., Jin, S. A., Shima, J. H. et al. (2008b) Thermal decomposition behavior of calcium borohydride $Ca(BH_4)_2$. **Journal of Alloys and Compounds**, 461: L20-L22.

Kim, J. H., Shim, J. H. and Cho, Y. W. (2008c) On the reversibility of hydrogen storage in Ti- and Nb-catalyzed $Ca(BH_4)_2$. **Journal of Power Sources**, 181: 140-143.

Kim, K. S., Lee, H., Han, K. S. et al. (2005) Hydrogen storage in Ni nanoparticle-dispersed multiwalled carbon nanotubes. **Journal of Physical Chemistry B**, 109(18): 8983-8986.

Kim, Y., Reed, D., Lee, Y. S. et al. (2009b) Identification of the dehydrogenated product of $Ca(BH_4)_2$. **Journal of Physical Chemistry C**, 113(14): 5865-5871.

Ko, J., Newell, K., Geving, B. et al. (2005) "Low cost, high efficiency, high pressure hydrogen storage". In **FY 2005 Progress Report on DOE Hydrogen Program**, Arlington, Virginia: 23-26th May 2005. pp 653-656.

Kodera, Y., Yamasaki, N., Yamamoto, T. et al. (2007) Hydrogen storage Mg_2Ni alloy produced by induction field activated combustion synthesis. **Journal of Alloys and Compounds**, 446: 138-141.

Kojima, Y. and Haga, T. (2003) Recycling process of sodium metaborate to sodium borohydride. **International Journal of Hydrogen Energy**, 28: 989-993.

Kostka, J., Lohstroh, W., Fichtner, M. et al. (2007) Diborane release from $LiBH_4$/silica-gel mixture and the effect of additives. **Journal of Physical Chemistry C**, 111: 14026-14029.

Kou, H. Q., Xiao, X. Z., Chen, L. X. et al. (2011) Formation mechanism of MgB_2 in $2LiBH_4 + MgH_2$ system for reversible hydrogen storage. **Transactions of Nonferrous Metals Society of China**, 21(5): 1040-1046.

Kumar, R. S. and Cornelius, A. L. (2005) Structural transitions in $NaBH_4$ under pressure. **Applied Physics Letters**, 87: 2619161-2619163.

Laberty, C., Zhao, F., Swider-Lyons, K. E. et al. (2007) High-performance solid oxide fuel cell cathodes with lanthanum-nickelate-based composites. **Electrochemical and Solid State Letters**, 10(10): B170-B174.

Langmi, H. W., Book, D., Walton, A. et al. (2005) Hydrogen storage in ion-exchanged zeolites. **Journal of Alloys and Compounds**, 404: 637-642.

Langmi, H. W., Walton, A., Al-Mamouri, M. M. et al. (2003) Hydrogen adsorption in zeolites A, X, Y and RHO. **Journal of Alloys and Compounds**, 356: 710-715.

Larminie, J. and Dicks, A. (2000) **Fuel cell systems explained**. Chichester, England: John Wiley and Sons.

Lee, G., Lee, J. Y. and Kim, J. S. (2006) Ab initio P-T phase diagram of $NaBH_4$. **Solid State Communication**, 139(10): 516-521.

Lee, G. J., Shim, G. H., Cho, Y. W. et al. (2007) Reversible hydrogen storage in $NaAlH_4$ catalyzed with lanthanide oxides. **International Journal of Hydrogen Energy**, 32(12): 1911-1915.

Lee, H., Kang, Y. S., Kim, S. H. et al. (2002) Hydrogen desorption properties of multiwall carbon nanotubes with closed and open structures. **Applied Physics Letters**, 80(4): 577-579.

Lee, J. Y., Ravnsbaek, D. B., Lee, Y. S. et al. (2009) Decomposition reactions and reversibility of the $LiBH_4$-$Ca(BH_4)_2$ composite. **Journal of Physical Chemistry C**, 113(33): 15080-15086.

Leng, H. Y., Ichikawa, T., Hino, S. et al. (2004) New metal−N−H system composed of $Mg(NH_2)_2$ and LiH for hydrogen storage. **Journal of Physical Chemistry B**, 108(26): 8763–8765.

Li, H. W., Kikuchi, K., Nakamori, Y. et al. (2007a) Effects of ball milling and additives on dehydriding behaviors of well-crystallized $Mg(BH_4)_2$. **Scripta Materialia**, 57(8): 679-682.

Li, H. W., Kikuchi, K., Nakamori, Y. et al. (2008) Dehydriding and rehydriding processes of well-crystallized $Mg(BH_4)_2$ accompanying with formation of intermediate compounds. **Acta Materialia**, 56(6): 1342-1347.

Li, H. W., Miwa, K., Ohba, N. et al. (2009) Formation of an intermediate compound with a $B_{12}H_{12}$ cluster: experimental and theoretical studies on magnesium borohydride $Mg(BH_4)_2$. **Nanotechnology**, 20(20): 2040131-2040137.

Li, H. W., Orimo, S., Nakamori, Y. et al. (2007b) Materials designing of metal borohydrides: Viewpoints from thermodynamical stabilities. **Journal of Alloys and Compounds**, 446: 315-318.

Li, H. W., Yan, Y. G., Orimo, S. et al. (2011a) Recent progress in metal borohydrides for hydrogen storage. **Energies**, 4(1): 185-214.

Li, W. Y., Li, C. S., Ma, H. et al. (2007c) Magnesium nanowires: Enhanced kinetics for hydrogen absorption and desorption. **Journal of the American Chemical Society**, 129(21): 6710-6711.

Li, X. S., Zhu, H. W., Ci, L. J. et al. (2001) Hydrogen uptake by graphitized multi-walled carbon nanotubes under moderate pressure and at room temperature. **Carbon**, 39(13): 2077-2079.

Li, Y., Izuhara, T. and Takeshita, H. T. (2011b) Promotional effect of aluminum on MgH_2+LiBH_4 hydrogen storage materials. **Materials Transactions**, 52(4): 641-646.

Li, Z. P., Liu, B. H., Zhu, J. H. et al. (2007d) NaBH4 formation mechanism by reaction of sodium borate with Mg and H_2. **Journal of Alloys and Compounds**, 437(1-2): 311-316.

Li, Z. P., Liu, B. H., Zhu, J. K. et al. (2003a) Preparation of potassium borohydride by a mechano-chemical reaction of saline hydrides with dehydrated borate through ball milling. **Journal of Alloys and Compounds**, 354(1-2): 243-247.

Li, Z. P., Morigazaki, N., Liu, B. H. et al. (2003b) Preparation of sodium borohydride by the reaction of MgH_2 with dehydrated borax through ball milling at room temperature. **Journal of Alloys and Compounds**, 349(1-2): 232-236.

Liang, C., Liu, Y. F., Fu, H. L. et al. (2011) Li-Mg-N-H-based combination systems for hydrogen storage. **Journal of Alloys and Compounds**, 509(30): 7844-7853.

Liao, B., Lei, Y. Q., Chen, L. X. et al. (2006) The structural and electrochemical properties of $La2Mg(Ni0.8\text{-}xCo0.2Al_x)_9$ (x=0-0.03) hydrogen storage electrode alloys. **Journal of Alloys and Compounds**, 415(1-2): 239-243.

Lide, D. R. (2007) **CRC handbook of chemistry and physics,** . 88th ed.: CRC, Boca Raton.

Lin, S. Y., Harada, M., Suzuki, Y. et al. (2002) Hydrogen production from coal by separating carbon dioxide during gasification. **Fuel**, 81(16): 2079-2085.

Liu, B. H., Li, Z. P., Morigasaki, N. et al. (2008) Kinetic characteristics of sodium borohydride formation when sodium meta-borate reacts with magnesium and hydrogen. **International Journal of Hydrogen Energy**, 33(4): 1323-1328.

Liu, C., Fan, Y. Y., Liu, M. et al. (1999) Hydrogen storage in single-walled carbon nanotubes at room temperature. **Science**, 286(5442): 1127-1129.

Llamas-Jansa, I., Aliouane, N., Deledda, S. et al. (2012) Chloride substitution induced by mechano-chemical reactions between $NaBH_4$ and transition metal chlorides. **Journal of Alloys and Compounds**, 530: 186-192.

Lochan, R. C. and Head-Gordon, M. (2006) Computational studies of molecular hydrogen binding affinities: The role of dispersion forces, electrostatics, and orbital interactions. **Physical Chemistry Chemical Physics**, 8(12): 1357-1370.

Łodziana, Z. and Vegge, T. (2004) Structural stability of complex hydrides: $LiBH_4$ revisited. **Physical Review Letters**, 93(14): 1455011-1455014.

Luck, R. L. and Schelter, E. J. (1999) Potassium borohydride. **Acta Crystallographica Section C**, 55(11): IUC9900151-IUC9900157.

Lueking, A. D. and Yang, R. T. (2004) Hydrogen spillover to enhance hydrogen storage—study of the effect of carbon physicochemical properties. **Applied Catalysis A: General**, 265: 259-268.

Luo, K., Liu, Y., Wang, F. et al. (2009) Hydrogen storage in a Li–Al–N ternary system. **International Journal of Hydrogen Energy**, 34: 8101-8107.

Luo, W. (2004) $LiNH_2$–MgH_2: A viable hydrogen storage system. **Journal of Alloys and Compounds**, 381: 284–287.

Luo, W. and Ronnebro, E. (2005) Towards a viable hydrogen storage system for transportation application. **Journal of Alloys and Compounds**, 404: 392-395.

Lupu, D., Ardelean, O., Blanita, G. et al. (2011) Synthesis and hydrogen adsorption properties of a new iron based porous metal-organic framework. **International Journal of Hydrogen Energy**, 36(5): 3586-3592.

Lutz, H. D. and Schneider, M. (1990) The crystal structure of Li_2MnCl_4. **Zeitschrift für Naturforschung B**, 45: 1543-1547.

Makhaev, V. D., Borisov, A. P., Gnilomedova, T. P. et al. (1987) Production of manganese borohydride complexes of manganese solvated with THF, and the structure of $Mn(BH_4)_2(THF)_3$. **Izvestiya Akademii Nauk SSSR, Seriya Khimicheskaya**, 8: 1712-1716.

Makhaev, V. D., Borisov, A. P. and Lobkovskii, E. B. (1984) **Russian Journal of Inorganic Chemistry**, 29(5): 666-669.

Maltseva, N. N., Myakishev, K. G., Saidov, B. I. et al. (1989) Synthesis of zinc borohydride and its derivatives by mechanoactivation of mixtures of alkali-metal borohydrides with zinc-chloride. **Zhurnal Neorganicheskoi Khimii**, 34(6): 6659-6663.

Mao, J. F. (2011) **Light metal hydrides for reversible hydrogen storage applications**. PhD thesis, University of Wollongong.

Mao, J. F., Guo, Z. P., Yu, X. B. et al. (2011) Enhanced hydrogen storage performance of $LiAlH_4$-MgH_2-TiF_3 composite. **International Journal of Hydrogen Energy**, 36(9): 5369-5374.

Mao, J. F., Yu, X. B., Guo, Z. P. et al. (2009) Enhanced hydrogen storage performances of $NaBH_4$-MgH_2 system. **Journal of Alloys and Compounds**, 479(1-2): 619-623.

Marks, T. J. and Kolb, J. R. (1977) Covalent transition-metal. Lanthanide, and actinide tetrahydroborate complexes. **Chemical Reviews**, 77(2): 263-293.

Matsunaga, T., Buchter, F., Miwa, K. et al. (2008) Magnesium borohydride: A new hydrogen storage materal. **Renewable Energy**, 33: 193-196.

Mauron, P., Buchter, F., Friedrichs, O. et al. (2008) Stability and reversibility of $LiBH_4$. **Journal of Physical Chemistry B**, 112(3): 906-910.

Mikheeva, V. I. and Arkhipev, S. M. (1966) Rubidium and caesium tetrahydroborates. **Russian Journal of Inorganic Chemistry**, 11(7): 805-810.

Mikheeva, V. I., Selivokhina, M. S. and Kryukova, O. N. (1962) Fusion diagram in the potassium hydroborate-potassium hydroxide system. **Russian Journal of Inorganic Chemistry**, 7(7): 838-841.

Mironova-Ulmane, N., Kuzmin, A. and Grube, M. (2009) Raman and infrared spectromicroscopy of manganese oxides. **Journal of Alloys and Compounds**, 480: 97-99.

Miwa, K., Aoki, M., Noritake, T. et al. (2006) Thermodynamical stability of calcium borohydride $Ca(BH_4)_2$. **Physical Review B**, 74(15): 1551221-1551225.

Miwa, K., Ohba, N. and Towata, S. (2004) First-principes study on lithium borohydride $LiBH_4$. **Physical Review B**, 69: 245120-245125.

Monnier, G. (1957) **Annales de Chimie (Cachan, France)**, 13: 14-57.

Morioka, H., Kakizaki, K., Cheong, C. S. et al. (2003) Reversible hydrogen decomposition of $KAlH_4$. **Journal of Alloys and Compounds**, 353(1-2): 310-314.

Mosegaard, L., Møller, B., Jørgensen, J. E. et al. (2008) Reactivity of $LiBH_4$: In situ synchrotron radiation powder X-ray diffraction study. **Journal of Physical Chemistry C**, 112(4): 1299-1303.

Moysés Araújo, C., Ahuja, R., Talyzin, A. V. et al. (2005) Pressure-induced structural phase transition in $NaBH_4$. **Physical Review B**, 72(5): 0541251-0541255.

Mass Spectrometry Resource (MSR) (2012) **Quadruple & Triple Quadrupole (QQQ) Mass Analysis** [online]. Available from: http://www.chm.bris.ac.uk/ms/theory/quad-massspec.html [Accessed 20 May 2012].

Muetterties, E. L., Merrifield, R. E., Knoth, W. H. et al. (1962) Chemistry of boranes: 3. Infrared and Raman spectra of $B_{12}H_{12}$ and related anions. **Journal of the American Chemical Society**, 84: 2506-2511.

Nakamori, Y., Li, H. W., Kikuchi, K. et al. (2007) Thermodynamical stabilities of metal-borohydrides. **Journal of Alloys and Compounds**, 446: 296-300.

Nakamori, Y., Miwa, K., Ninomiya, A. et al. (2006) Correlation between thermodynamical stabilities of metal borohydrides and cation electronegativites: First-principles calculations and experiments. **Physical Review B**, 74(4): 0451261-0451269.

Nakamori, Y. and Orimo, S. (2008) "Borohydrides as hydrogen storage materials, ". In Walker, G. (Ed.) **Solid-State Hydrogen Storage**. Cambridge, UK: Woodhead Publishing Limited, pp.420-449.

Nakamoto, K. (1997) **Infrared and Raman Spectra of Inorganic and Coordination Compounds, Part A: Theory and Applications in Inorganic Chemistry**. 5th Edition. New York: John Wiley & Sons, Ltd.

NETZSCH (2012) **DSC 204 HP Phoenix® - Technical Specifications (subject to change)** [online]. Available from: http://www.netzsch-thermal-analysis.com/en/products/detail/pid,3,t,2.html [Accessed 19 May 2012].

Newhouse, R. J., Stavila, V., Hwang, S. J. et al. (2010) Reversibility and improved hydrogen release of magnesium borohydride. **Journal of Physical Chemistry C**, 114(11): 5224-5232.

Nickels, E. A., Jones, M. O., David, W. F. et al. (2008) Tuning the decomposition temperature in complex hydrides: Synthesis of a mixed alkali metal borohydride. **Angewandte Chemie-International Edition**, 47(15): 2817-2819.

Nielsen, T. K., Polanski, M., Zasada, D. et al. (2011) Improved hydrogen storage kinetics of nanoconfined $NaAlH_4$ catalyzed with $TiCl_3$ nanoparticles. **Acs Nano**, 5(5): 4056-4064.

Niemann, M. U., Srinivasan, S. S., Kumar, A. et al. (2009) Processing analysis of the ternary $LiNH_2$–MgH_2–$LiBH_4$ system for hydrogen storage. **International Journal of Hydrogen Energy**, 34: 8086-8093.

Nishimiya, N., Kishi, T., Mizushima, T. et al. (2001) Hyperstoichiometric hydrogen occlusion by palladium nanoparticles included in NaY zeolite. **Journal of Alloys and Compounds**, 319(1-2): 312-321.

Oguchi, H., Matsuo, M., Hummelshoj, J. S. et al. (2009) Experimental and computational studies on structural transitions in the $LiBH_4$-LiI pseudobinary system. **Applied Physics Letters**, 94: 1419121-1419123.

Ohba, N., Miwa, K., Aoki, M. et al. (2006) First-principles study on the stability of intermediate compounds of $LiBH_4$ **Physical Review B**, 74(7): 075110-075117.

Orimo, S., Majer, G., Fukunaga, T. et al. (1999) Hydrogen in the mechanically prepared nanostructured graphite. **Applied Physics Letters**, 75(20): 3093-3095.

Orimo, S., Nakamori, I. Y. and Züttel, A. (2004) Material properties of MBH_4 (M = Li, Na, and K). **Materials Science and Engineering B**, 108: 51-53.

Orimo, S., Nakamori, Y., Kitahara, G. et al. (2005) Dehydriding and rehydriding reactions of $LiBH_4$. **Journal of Alloys and Compounds**, 404-406: 427-430.

Orimo, S., Nakamori, Y., Ohba, N. et al. (2006) Experimental studies on intermediate compound of $LiBH_4$. **Applied Physics Letters**, 89: 0219201-0219203.

Orimo, S. I., Nakamori, Y., Eliseo, J. R. et al. (2007) Complex hydrides for hydrogen storage. **Chemical Reviews**, 107(10): 4111-4132.

Outeiro, M. T., Chibante, R., Carvalho, A. S. et al. (2008) A parameter optimized model of a proton exchange membrane fuel cell including temperature effects. **Journal of Power Sources**, 185(2): 952-960.

Ozolins, V., Majzoub, E. H. and Wolverton, C. (2009) First-principles prediction of thermodynamically reversible hydrogen storage reactions in the Li-Mg-Ca-B-H system. **Journal of the American Chemical Society**, 131(1): 230-237.

Palade, P., Lungu, G. A. and Husanu, A. M. (2010) Thermodynamic destabilization of Li-N-H system by Si addition. **Journal of Alloys and Compounds**, 505(1): 343-347.

Panella, B., Hirscher, M., Putter, H. et al. (2006) Hydrogen adsorption in metal-organic frameworks: Cu-MOFs and Zn-MOFs compared. **Advanced Functional Materials**, 16(4): 520-524.

Patah, A., Takasaki, A. and Szmyd, J. S. (2009) Influence of multiple oxide (Cr_2O_3/Nb_2O_5) addition on the sorption kinetics of MgH_2. **International Journal of Hydrogen Energy**, 34(7): 3032-3037.

Pendolino, F., Mauron, P., Borgschulte, A. et al. (2009) Effect of boron on the activation energy of the decomposition of $LiBH_4$. **The Journal of Physical Chemistry C**, 113: 17231-17234.

Pinkerton, F. E. and Meyer, M. S. (2008) Reversible hydrogen storage in the lithium borohydride-calcium hydride coupled system. **Journal of Alloys and Compounds**, 464(1-2): L1-L4.

Pistidda, C., Garroni, S., Dolci, F. et al. (2010) Synthesis of amorphous $Mg(BH_4)_2$ from MgB_2 and H_2 at room temperature. **Journal of Alloys and Compounds**, 508(1): 212-215.

Prasanth, K. P., Pillai, R. S., Bajaj, H. C. et al. (2008) Adsorption of hydrogen in nickel and rhodium exchanged zeolite X. **International Journal of Hydrogen Energy**, 33(2): 735-745.

Puszkiel, J. A. and Gennari, F. C. (2009) Reversible hydrogen storage in metal-doped Mg-$LiBH_4$ composites. **Scripta Materialia**, 60(8): 667-670.

Quakernaat, J. (1995) Hydrogen in a global long-term perspective. **International Journal of Hydrogen Energy**, 20(6): 485-492.

Racu, A. M., Schoenes, J., Lodziana, Z. et al. (2008) High-resolution Raman spectroscopy study of phonon modes in $LiBH_4$ and $LiBD_4$. **Journal of Physical Chemistry A**, 112(40): 9716-9722.

Rafi-ud-din, Qu, X., Li, P. et al. (2011) Hydrogen sorption improvement of $LiAlH_4$ catalyzed by Nb_2O_5 and Cr_2O_3 nanoparticles. **The Journal of Physical Chemistry C**, 115: 13088–13099.

Ravnsbaek, D., Filinchuk, Y., Cerenius, Y. et al. (2009) A series of mixed-metal borohydrides. **Angewandte Chemie-International Edition**, 48(36): 6659-6663.

Ravnsbaek, D. B., Filinchuk, Y., Cerny, R. et al. (2010a) Thermal polymorphism and decomposition of $Y(BH_4)_3$. **Inorganic Chemistry**, 49(8): 3801-3809.

Ravnsbaek, D. B., Rude, L. H. and Jensen, T. R. (2011) Chloride substitution in sodium borohydride. **Journal of Solid State Chemistry**, 184: 1858-1866.

Ravnsbaek, D. B., Sorensen, L. H., Filinchuk, Y. et al. (2010b) Mixed-anion and mixed-cation borohydride $KZn(BH_4)Cl_2$: synthesis, structure and thermal decomposition. **European Journal of Inorganic Chemistry**(11): 1608-1612.

Reed, D. (2009) **An investigation into the synthesis and characterisation of metal borohydrides for hydrogen storage**. PhD thesis, University of Birmingham.

Reed, D. and Book, D. (2011) Recent applications of Raman spectroscopy to the study of complex hydrides for hydrogen storage. **Current Opinion in Solid State & Materials Science**, 15: 62-72.

Reguera, L., Balmaseda, J., del Castillo, L. F. et al. (2008) Hydrogen storage in porous cyanometalates: role of the exchangeable alkali metal. **The Journal of Physical Chemistry C: Nanomaterials and Interfaces**, 112(14): 5589-5597.

Reid, W. E., Bish, J. M. and Brenner, A. (1957) Electrodeposition of metal from organic solution. 3. Preparation and electrolysis of titanium and zirconium compounds in noaqueous media. **Journal of the Electrochemical Society**, 104(1): 21-29.

Renaudin, G., Gomesa, S., Hagemann, H. et al. (2004) Structural and spectroscopic studies on the alkali borohydrides MBH_4 (M = Na, K, Rb, Cs). **Journal of Alloys and Compounds**, 375: 98-106.

RIDB (2009) **Raman Spectra Database of Minerals and Inorganic Materials (RASMIN)** [online]. Available from: http://riodb.ibase.aist.go.jp/db092/cgi-bin/inorganic_search.pl?lang=E&name=&Atom_B=ON&Atom_Mn=ON [Accessed 20 September 2009].

Riktor, M. D., Sorby, M. H., Chlopek, K. et al. (2007) In situ synchrotron diffraction studies of phase transitions and thermal decomposition of $Mg(BH_4)_2$ and $Ca(BH_4)_2$. **Journal of Materials Chemistry**, 17(47): 4939-4942.

Rongeat, C., D'Anna, V., Hagemann, H. et al. (2010) Effect of additives on the synthesis and reversibility of $Ca(BH_4)_2$. **Journal of Alloys and Compounds**, 493(1-2): 281-287.

Rongeat, C., Lindemann, I., Borgschulte, A. et al. (2011) Effect of the presence of chlorides on the synthesis and decomposition of $Ca(BH_4)_2$. **International Journal of Hydrogen Energy**, 36(1): 247-253.

Ronnebro, E. and Majzoub, E. H. (2007) Calcium borohydride for hydrogen storage: Catalysis and reversibility. **Journal of Physical Chemistry B**, 111(42): 12045-12047.

Ronnebro, E. and Majzoub, E. H. (2008) "Discovery and development of metal hydride for reversible on-board storage, ". In **DOE hydrogen program and annual peer review meeting proceedings. Project ID ST 36**. pp

Rosi, N. L., Eckert, J., Eddaoudi, M. et al. (2003) Hydrogen storage in microporous metal-organic frameworks. **Science**, 300(5622): 1127-1129.

Rostrup-Nielsen, J. R. (1984) "Catalytic steam reforming". In Anderson, J. R. and Boudart, M. (Eds.) **Catalysis: Science and technology**. New York: Springer.

Sartori, S., Knudsen, K. D., Zhao-Karger, Z. et al. (2009) Small-angle scattering investigations of Mg-borohydride infiltrated in activated carbon. **Nanotechnology**, 20(50): 5057021-5057027.

Sato, T., Miwa, K., Nakamori, Y. et al. (2008) Experimental and computational studies on solvent-free rare-earth metal borohydrides $R(BH_4)_3$ (R = Y, Dy, and Gd). **Physical Review B**, 77(10): 104114-104122.

Satyapal, S., Petrovic, J., Read, C. et al. (2007) The US Department of Energy's National Hydrogen Storage Project: Progress towards meeting hydrogen-powered vehicle requirements. **Catalysis Today**, 120(3-4): 246-256.

Sayers, R., Liu, J., Rustumji, B. et al. (2008) Novel K_2NiF_4-type materials for solid oxide fuel cells: Compatibility with electrolytes in the intermediate temperature range. **Fuel Cells**, 8(5): 338-343.

Scarlett, N. V. Y. and Madsen, I. C. (2006) Quantification of phases with partial or no known crystal structures. **Powder Diffraction**, 21: 278-284.

Schlapbach, L. (2002) Hydrogen as a fuel and its storage for mobility and transport. **MRS Bulletin**, 27: 675-679.

Schlapbach, L. and Züttel, A. (2001) Hydrogen-storage materials for mobile applications. **Nature**, 414(6861): 353-358.

Schlesinger, H. I. and Brown, H. C. (1940) Mettlo borohydrides III. Lithium borohydride. **Journal of the American Chemical Society**, 62: 3429-3435.

Schlesinger, H. I., Brown, H. C., Abraham, B. et al. (1953a) New developments in the chemistry of diborane and the borohydrides. I. general summary. **Journal of the American Chemical Society**, 75(1): 186-190.

Schlesinger, H. I., Brown, H. C. and Finholt, A. E. (1953b) The preparation of sodium borohydride by the high temperature reactionof sodium hydride with borate esters. **Journal of American Chemical Society**, 75(1): 205-209.

Schlesinger, H. I., Brown, H. C., Finholt, A. E. et al. (1953c) New developments in the chemistry of diborane and of the borohydrides .9. Sodium borohydride, Its hydrolysis and its use as a reducing agent and in the generation of hydrogen. **Journal of the American Chemical Society**, 75(1): 215-219.

Schlesinger, H. I., Brown, H. C., Hoekstra, H. R. et al. (1953d) Reactions of diborane with alkali metal hydrides and their addition compounds: new sysnthesis of borohydrides. sodium and potassium borohydrides. **Journal of American Chemical Society**, 75(1): 199-204.

Schouwink, P., D'Anna, V., Ley, M. B. et al. (2012) Bimetallic Borohydrides in the System $M(BH_4)_2$–KBH_4 (M = Mg, Mn): On the Structural Diversity. **Journal of Physical Chemistry C**, 116: 10829-10840.

Seballos, L., Zhang, J. Z., Ronnebro, E. et al. (2009) Metastability and crystal structure of the bialkali complex metal borohydride $NaK(BH_4)_2$. **Journal of Alloys and Compounds**, 476(1-2): 446-450.

Service, R. F. (2004) Toward a hydrogen economy: The carbon conundrum. **Sciences**, 305: 962-963.

Severa, G., Hagemann, H., Longhini, M. et al. (2010a) Thermal desorption, vibrational spectroscopic, and DFT computational studies of the complex manganese borohydrides $Mn(BH_4)_2$ and $Mn(BH_4)_4^{2-}$. **Journal of Physical Chemistry C**, 114(36): 15516-15521.

Severa, G., Ronnebro, E. and Jensen, C. M. (2010b) Direct hydrogenation of magnesium boride to magnesium borohydride: demonstration of > 11 weight percent reversible hydrogen storage. **Chemical Communications**, 46(3): 421-423.

Sheppard, D. A., Paskevicius, M. and Buckley, C. E. (2011) Hydrogen desorption from the $NaNH_2$-MgH_2 system. **Journal of Physical Chemistry C**, 115(16): 8407-8413.

Shim, J. H., Lim, J. H., Rather, S. U. et al. (2010) Effect of hydrogen back pressure on dehydrogenation behavior of $LiBH_4$-based reactive hydride composites. **Journal of Physical Chemistry Letters**, 1(1): 59-63.

Shimko, M. A. (2005) "Combined reverse-brayton Joule Thompson hydrogen liquefaction cycle". In **FY 2005 Progress Report on DOE Hydrogen Program**, Arlington, Virginia: 23-26th May 2005. pp 437-439.

Shin, W. H., Yang, S. H., Goddard, W. A. et al. (2006) Ni-dispersed fullerenes: Hydrogen storage and desorption properties. **Applied Physics Letters**, 88(5): 0531111-0531113.

Smith, M. R., Bittner, E. W., Shi, W. et al. (2003) Chemical activation of single-walled carbon nanotubes for hydrogen adsorption. **Journal of Physical Chemistry B**, 107(16): 3752-3760.

Soldate, A. M. (1947) Crystal structure of sodium borohydride. **Journal of the American Chemical Society**, 69: 987-988.

Soloveichik, G. L., Andrus, M., Gao, Y. et al. (2009a) Magnesium borohydride as a hydrogen storage material: Synthesis of unsolvated $Mg(BH_4)_2$. **International Journal of Hydrogen Energy**, 34(5): 2144-2152.

Soloveichik, G. L., Gao, Y., Rijssenbeek, J. et al. (2009b) Magnesium borohydride as a hydrogen storage material: Properties and dehydrogenation pathway of unsolvated $Mg(BH_4)_2$. **International Journal of Hydrogen Energy**, 34(2): 916-928.

Somer, M., Acar, S., Koz, C. et al. (2010) alpha- and beta-Na-2BH_4 NH_2 : Two modifications of a complex hydride in the system $NaNH_2$-$NaBH_4$; syntheses, crystal structures, thermal analyses, mass and vibrational spectra. **Journal of Alloys and Compounds**, 491(1-2): 98-105.

Soulié, J. P., Renaudin, G., Černý, R. et al. (2002) Lithium boro-hydride $LiBH_4$: I. Crystal structure. **Journal of Alloys and Compounds**, 346: 200-205.

Sperling, D. and Cannon, J. S. (2004) **The Hydrogen Energy Transition: Moving Toward the Post Petroleum Age in Transportation**. London: Elsevier Academic Press.

Srepusharawoot, P., Blomqvist, A., Araujo, C. M. et al. (2011) Hydrogen binding in alkali-decorated iso-reticular metal organic framework-16 based on Zn, Mg, and Ca. **International Journal of Hydrogen Energy**, 36(1): 555-562.

Srinivasan, S., Escobar, D., Jurczyk, M. et al. (2008) Nanocatalyst doping of $Zn(BH_4)_2$ for on-board hydrogen storage. **Journal of Alloys and Compounds**, 462(1-2): 294-302.

Steryladkina, Z. K., Kryukova, O. N. and Mikheeva, V. I. (1965) **Russian Journal of Inorganic Chemistry**, 10(3): 316-318.

Sumida, K., Brown, C. M., Herm, Z. R. et al. (2011) Hydrogen storage properties and neutron scattering studies of Mg-2(dobdc)-a metal-organic framework with open Mg^{2+} adsorption sites. **Chemical Communications**, 47(4): 1157-1159.

Sun, T., Huang, C. K., Wang, H. et al. (2008) The effect of doping $NiCl_2$ on the dehydrogenation properties of $LiAlH_4$. **International Journal of Hydrogen Energy**, 33(21): 6216-6221.

Sun, W., Du, Y., Liu, S. et al. (2010) Thermodynamic assessment of the Mn-B system. **Journal of Phase Equilibria and Diffusion**, 31(4): 357-364.

Sundqvist, B. and Andersson, O. (2006) Low-temperature phase transformation in $NaBH_4$ under pressure. **Physics Review B**, 73(9): 1092102-1092105.

Swanson, H. E. and Fuyat, R. K. (1953) Standard X-ray diffraction patterns. Sodium chloride, Na Cl (cubic). **National Bureau of Standards**, 539: 41-43.

Takahashi, S., Morita, H., Kurata, O. et al. (2003) Hydrogen internal combustion stirling engine (1st report, combustion experiment on prototype engine). **JSME International Journal Series B**, 46(4): 633-642.

Teng, Y. L., Ichikawa, T. and Kojima, Y. (2011) Catalytic effect of Ti-Li-N compounds in the Li-N-H system on hydrogen desorption properties. **Journal of Physical Chemistry C**, 115(2): 589-593.

Thomas, K. M. (2009) Adsorption and desorption of hydrogen on metal–organic framework materials for storage applications: comparison with other nanoporous materials. **The Royal Society of Chemistry: Dalton Transactions**: 1487-1505.

Titov, L. V. (1964) Synthesis of calcium borohydride. **IZD-VO Akademii Nauk SSSR**, 154(3): 654-656.

Torres, F. J., Vitillo, J. G., Civalleri, B. et al. (2007) Interaction of H_2 with alkali-metal-exchanged zeolites: a quantum mechanical study. **Journal of Physical Chemistry C**, 111: 2505-2513.

Tsivadze, A. Y., Tarasevich, M. R., Bogdanovskaya, V. A. et al. (2008) Nanosized cobalt-containing electrocatalysts for alkaline fuel cells. **Doklady Physical Chemistry**, 420: 154-157.

Urgnani, J., Torres, F. J., Palumbo, M. et al. (2008) Hydrogen release from solid state $NaBH_4$. **International Journal of Hydrogen Energy**, 33(12): 3111-3115.

Vajo, J. J., Skeith, S. L. and Mertens, F. (2005) Reversible storage of hydrogen in destabilized $LiBH_4$. **Journal of Physical Chemistry B**, 109: 3719-3722.

Varin, R. A., Chiu, C. and Wronski, Z. S. (2008) Mechano-chemical activation synthesis (MCAS) of disordered $Mg(BH_4)_2$ using $NaBH_4$. **Journal of Alloys and Compounds**, 462: 201-208.

Varin, R. A., Czujko, T. and Wronski, Z. (2006) Particle size, grain size and γ -MgH_2 effects on the desorption properties of nanocrystalline commercial magnesium hydride processed by controlled mechanical milling. **Nanotechnology**, 17: 3856-3865.

Varin, R. A. and Zbroniec, L. (2010) The effects of ball milling and nanometric nickel additive on the hydrogen desorption from lithium borohydride and manganese chloride ($3LiBH_4$ + $MnCl_2$) mixture. **International Journal of Hydrogen Energy**, 35(8): 3588-3597.

Vittetoe, A. W., Niemann, M. U., Srinivasan, S. S. et al. (2009) Destabilization of $LiAlH_4$ by nanocrystalline MgH_2. **International Journal of Hydrogen Energy**, 34(5): 2333-2339.

Volkov, V. V. and Myakishev, K. G. (1992) On mechanochemical reaction of synthesis of titanium(III) tetrahydroborate. **Sibirskii Khimicheskii Zhurnal**(5): 105-108.

Volkov, V. V. and Myakishev, K. G. (1999) Mechanochemical reactions in the chemistry of boranes. **Inorganica Chimica Acta**, 289(1-2): 51-57.

von Ardenne, M., Musiol, G. and Reball, S. (1990) **Effekte der Physik**. Frankfurt am Main: Verlag Harry Deutsch.

Wan, Y., Peppley, B., Creber, K. A. M. et al. (2008) Quaternized-chitosan membranes for possible applications in alkaline fuel cells. **Journal of Power Sources**, 185(1): 183-187.

Wanet, E. C., Suman, B. and Schmidt, L. D. (2005) Partial oxidation of alcohols to produce hydrogen and chemicals in millisecond-contact time reactors. **Journal of Catalysis**, 235(1): 18-27

Wang, L. F. and Yang, R. T. (2008) Hydrogen storage properties of carbons doped with ruthenium, platinum, and nickel nanoparticles. **Journal of Physical Chemistry C**, 112(32): 12486-12494.

Wang, L. H., Yang, F. H., Yang, R. T. et al. (2009) Effect of surface oxygen groups in carbons on hydrogen storage by spillover. **Industrial & Engineering Chemistry Research**, 48(6): 2920-2926.

Wang, P., Kang, X. D. and Cheng, H. M. (2005) Improved hydrogen storage of TiF_3-doped $NaAlH_4$. **Chemphyschem**, 6(12): 2488-2491.

Wiberg, E. and Bauer, R. (1950) Zur kenntnis eines magnesium-bor-wasserstoffs $Mg(BH_4)_2$. **Zeitschrift Fur Naturforschung Section B-a Journal of Chemical Sciences**, 5(7): 397-397.

Wiberg, E. and Henle, W. (1952) Zur kenntnis eines atherloslichen zink-bor-wasserstoffs $Zn(BH_4)_2$. **Zeitschrift fuer Naturforschung Section B-a Journal of Chemical Sciences**, 7(9-10): 579-580.

Winter, C. J. and Nitsch, J. (1988) **Hydrogen as an energy carrier: technoloies, system, econmy**. Berlin: Spriner.

Wong-Foy, A. G., Matzger, A. J. and Yaghi, O. M. (2006) Exceptional H_2 saturation uptake in microporous metal-organic frameworks. **Journal of the American Chemical Society**, 128: 3494-3495.

Xiong, Z. T., Wu, G. T., Hu, H. J. et al. (2004) Ternary imides for hydrogen storage. **Advanced Materials**, 16(17): 1522-1523.

Xiong, Z. T., Wu, G. T., Hu, H. J. et al. (2006) Investigations on hydrogen storage over Li-Mg-N-H complex - the effect of compositional changes. **Journal of Alloys and Compounds**, 417(1-2): 190-194.

Yan, Y. G., Li, H. W., Sato, T. et al. (2009) Dehydriding and rehydriding properties of yttrium borohydride $Y(BH_4)_3$ prepared by liquid-phase synthesis. **International Journal of Hydrogen Energy**, 34(14): 5732-5736.

Yang, H. W., Orefuwa, S. and Goudy, A. (2011) Study of mechanochemical synthesis in the formation of the metal-organic framework $Cu\text{-}3(BTC)_2$ for hydrogen storage. **Microporous and Mesoporous Materials**, 143(1): 37-45.

Yang, J., Sudik, A. and Wolverton, C. (2007) Destabilizing LiBH4 with a metal (M = Mg, Al, Ti, V, Cr, or Sc) or metal hydride (MH_2 = MgH_2, TiH_2, or CaH_2). **Journal of Physical Chemistry C**, 111: 19134-19140.

Yang, S., Lin, X., Blake, A. J. et al. (2008) Enhancement of H_2 adsorption in Li^+-exchanged co-ordination framework materials. **Chemical Communications**(46): 6108-6110.

Yaremov, P. S. and Il'in, V. G. (2008) Features of the adsorption of hydrogen by various types of microporous materials. **Theoretical and Experimental Chemistry**, 44: 67-74.

Ye, Y., Ahn, C. C., Witham, C. et al. (1999) High pressure saturation of hydrogen stored by single-wall carbon nanotubes. **Applied Physics Letters**, 74: 2307-2309

Yoo, J. H., Shim, G., Yoon, J. S. et al. (2009) Effects of substituting Al for Cr in the $Ti_{0.32}Cr_{0.43}V_{0.25}$ alloy on its microstructure and hydrogen storage properties. **International Journal of Hydrogen Energy**, 34(3): 1463-1467.

Yu, L. and Matthews, M. A. (2011) Hydrolysis of sodium borohydride in concentrated aqueous solution. **International Journal of Hydrogen Energy**, 36(13): 7416-7422.

Yu, X. B., Grant, D. M. and Walker, G. S. (2009) Dehydrogenation of $LiBH_4$ destabilized with various oxides. **Journal of Physical Chemistry C**, 113: 17945-17949.

Yuan, P. P., Liu, B. H., Zhang, B. J. et al. (2011) Reversible hydrogen storage composite based on $6LiBH_4 + CaF_2$. **Journal of Physical Chemistry C**, 115(14): 7067-7075.

Zervas, P. L., Tatsis, A., Sarimveis, H. et al. (2008) Development of a novel computational tool for optimizing the operation of fuel cells systems: Application for phosphoric acid fuel cells. **Journal of Power Sources**, 185(1): 345-355.

Zhang, Q. J., Li, X. H., Fujimoto, K. et al. (2005) Hydrogen production from partial oxidation and reforming of DME. **Catalysis Letters**, 102(3-4): 197-200.

Zhang, Y., Tian, Q. F., Chu, H. L. et al. (2009a) Hydrogen de/resorption properties of the $LiBH_4\text{-}MgH_2\text{-}Al$ system. **Journal of Physical Chemistry C**, 113(52): 21964-21969.

Zhang, Y., Tian, Q. F., Zhang, J. et al. (2009b) The dehydrogenation reactions and kinetics of $2LiBH_4\text{-}Al$ composite. **Journal of Physical Chemistry C**, 113(42): 18424-18430.

Zhang, Z. G., Zhang, S. F., Wang, H. et al. (2010) Feasibility study of the direct synthesis of $Mg(BH_4)_2$ complex hydrides by mechanical milling. **Journal of Alloys and Compounds**, 505(2): 717-721.

Zhao, X. Y., Ma, L. Q., Yao, Y. et al. (2010) Ti2Ni alloy: a potential candidate for hydrogen storage in nickel/metal hydride secondary batteries. **Energy & Environmental Science**, 3(9): 1316-1321.

Zheng, X. P., Feng, X. and Liu, S. L. (2011) Microstructure and desorption properties study of catalyzed $NaAlH_4$. **Journal of Alloys and Compounds**, 509(19): 5873-5876.

Zheng, X. P., Ping, L., Humail, I. S. et al. (2007) Effect of catalyst $LaCl_3$ on hydrogen storage properties of lithium alanate ($LiAlH_4$). **International Journal of Hydrogen Energy**, 32(18): 4957-4960.

Zhou, W., Wu, H. and Yildirim, T. (2008) Enhanced H_2 adsorption in isostructural metal-organic frameworks with open metal sites: strong dependence of the binding strength on metal ions. **Journal of the American Chemical Society**, 130(46): 15268-15269.

Züttel, A. (2003) Materials for hydrogen storage. **Materials Today**, 6(9): 24-33.

Züttel, A., Borgschulte, A. and Orimo, S. I. (2007) Tetrahydroborates as new hydrogen storage materials. **Scripta Materialia**, 56(10): 823-828.

Züttel, A., Rentsch, S., Fischer, P. et al. (2003a) Hydrogen storage properties of $LiBH_4$. **Journal of Alloys and Compounds**, 356-357: 515-520.

Züttel, A., Sudan, P., Mauron, P. et al. (2002) Hydrogen storage in carbon nanostructures. **International Journal of Hydrogen Energy**, 27(2): 203-212.

Züttel, A., Wenger, P., Rentsch, S. et al. (2003b) $LiBH_4$ a new hydrogen storage material. **Journal of Power Sources**, 118: 1-7.

Publications:

Peer-reviewed Journal papers:

- **Ruixia Liu,** Daniel Reed, David Book, Decomposition behaviour of $Mn(BH_4)_2$ formed by ball-milling $LiBH_4$ and $MnCl_2$, *Journal of Alloys and Compounds*, 2012, 515: 32-38.
- **Ruixia Liu**, Daniel Reed, David Book, Decomposition behaviour of $Mn(BH_4)_2$ synthesised by ball-milling $NaBH_4$ and $MnCl_2$, *Journal of Alloys and Compounds*, Submitted and revised.

Conference presentations:

- **Ruixia Liu**, Daniel Reed, David Book, Mn-based Borohydride Compounds for Hydrogen Storage, *1st International Conference on Clean Energy*, 10 - 13 April 2011, Dalian, China. (poster).
- **Ruixia Liu**, Daniel Reed, David Book, Hydrogen Storage Properties of Mn-based Borohydride Compounds, *Hydrogen Storage Materials: Faraday Discussion 151*, 18 - 20 April 2011, Didcot, Oxon, UK. (poster).
- Daniel Reed, **Ruixia Liu**, David Book, Synthesis and Decomposition of Manganese-based Borohydrides, *International Symposium on Metal-Hydrogen Systems*, 21-26th, Oct. 2012, Kyoto, Japan. (oral).
- D. Reed, D. Brampton, **R. Liu**, A. Walton, A. Bevan, and D. Book, Metal and Complex Hydrides for Hydrogen Storage. Building the Hydrogen and Fuel Cells Future, *5th Annual International Conference & Exhibition*, 25th March 2009, Birmingham, UK. (poster).
- Sheng Guo, Daniel T. Reed, David Brampton, **Ruixia Liu** and David Book, Borohydrides as potential hydrogen storage materials, *International Hydrogen Research Showcase,* 2011, 13 – 15th of April 2011, Birmingham, UK. (poster).